



# Sub-10 nm nano-structured carbohydrate-based block copolymer thin films for organic photovoltaic applications

Yoko Otsuka

## ► To cite this version:

Yoko Otsuka. Sub-10 nm nano-structured carbohydrate-based block copolymer thin films for organic photovoltaic applications. Theoretical and/or physical chemistry. Université Grenoble Alpes, 2017. English. NNT : 2017GREAV024 . tel-01830370

**HAL Id: tel-01830370**

**<https://theses.hal.science/tel-01830370>**

Submitted on 5 Jul 2018

**HAL** is a multi-disciplinary open access archive for the deposit and dissemination of scientific research documents, whether they are published or not. The documents may come from teaching and research institutions in France or abroad, or from public or private research centers.

L'archive ouverte pluridisciplinaire **HAL**, est destinée au dépôt et à la diffusion de documents scientifiques de niveau recherche, publiés ou non, émanant des établissements d'enseignement et de recherche français ou étrangers, des laboratoires publics ou privés.

## THÈSE

Pour obtenir le grade de

### **DOCTEUR DE LA COMMUNAUTE UNIVERSITE GRENOBLE ALPES**

Spécialité : **Chimie Physique Moléculaire et Structurale**

Arrêté ministériel : 7 août 2006

Présentée par

**Yoko OTSUKA**

Thèse dirigée par **Redouane BORSALI**

préparée au sein du **Centre de Recherche sur les  
Macromolécules Végétales (CERMAV)**  
et du **Centre de Technique du Papier (CTP)**

dans l'**École Doctorale Chimie et Sciences du Vivant**

### **Films minces nanostructurés de domaines sub-10 nm à partir de copolymères biosourcés pour des applications dans le photovoltaïque organique**

Thèse soutenue publiquement le « **4 janvier 2017** »,  
devant le jury composé de :

**M. Patrice RANNOU**

Directeur de Recherche au CNRS, SPrAM (Président)

**M. Martin BRINKMANN**

Directeur de Recherche au CNRS, ICS (Rapporteur)

**M. Eric CLOUTET**

Directeur de Recherche au CNRS, LCPO (Rapporteur)

**M. Redouane BORSALI**

Directeur de Recherche au CNRS, CERMAV (Directeur de thèse)





# ACKNOWLEDGEMENTS

I would like to express my profound gratitude and sincere thanks to my supervisor Dr. Redouane Borsali (Research professor, CNRS) for giving me an opportunity to have excellent research experience in CERMAV. I appreciate all of his help, encouragement and support throughout my thesis not only professionally and scientifically but also personally. I cannot thank him enough but please accept my heartfelt gratitude; Merci beaucoup, Arigatou, Obrigado, Lacoste, and 10 ants Redouane!

I would like to thank Dr. Patrice Rannou for acting as a chair of thesis committee and Dr. Martin Brinkmann and Dr. Eric Cloutet for referring this thesis manuscript. I would equally like to extend my thanks to the members of the comité de suivi de thèse, Prof. Guy Royal and Dr. Thierry Baron, for their insightful comments.

My sincere appreciation goes to my co-supervisors Dr. Davy Soysouvanh from Centre Technique du Papier and Dr. Sami Halila for their fruitful discussions and suggestions during my research work. Sami is not only my co-supervisor but also one of the most cheerful colleagues in our group. It was very pleasant to chat with him during coffee breaks. It is great pleasure to express my sincere thanks to my collaborator Dr. Patrice Rannou, who has rich experience in the field of semiconducting polymers and optoelectronics and has given me valuable suggestions and many scientific ideas.

Special thanks are given to Soraia Zaioncz for her contribution on the synthesis of azido-functionalized maltoheptaose and characterization of the products. I am equally thankful to Laurent Goujon who has been working together in the close scientific project for his valuable discussions and very helpful French lessons.

This thesis work would not have been completed without help of Dr. Yoshiharu Nishiyama. I deeply and sincerely appreciate his unlimited help, valuable discussions, insightful advices. He gave me always plenty of his precious time for discussions. I admire him for his intelligence, wide knowledge, and great attitude not only as a researcher but also as an educator.



I would like to acknowledge the financial support from CNRS, Université Grenoble Alpes, PolyNat Carnot Institute (N° CARN 007-01), Labex ARCANÉ (project number ANR-11-LABX-003) and the European Union's Seventh Framework Programme (FP7/2007-2013) under grant agreement n° 603519.

I am extremely grateful to Cyrille Rochas for his help in the SAXS measurements, Robert Pecora for his kind help in English correction of my publication, Jean-Luc Putaux and Christine Lancelon-Pin for their excellent help in TEM and SEM, Yu Ogawa for his enormous amount of help, valuable discussions, and encouragement, Isabelle Jeacomine for her nice teaching in NMR, Marie-France Metral for her kindness and many technical supports, Eric Bayma for his kind help in TGA, Pierre Sailler for his great help in DSC, Laure Fort for her splendid help in Mass spectrometry, and Takuya Isono for his fruitful discussions. My sincere thanks to Isabelle Caldara, Martine Morales, and Sandrine Coindet for their great helps in the administrative work which allowed me working in the best conditions.

I am really grateful to our group members, Fred, Christophe, Noémi, Félix, sympathetic PhD students, hard-working Post-docs, lovely master students, and many others for their enormous kindness. The precious time I spend with them making these years an unforgettable memory.

Thanks must go to my Japanese friends in Grenoble, especially Aubert family, Rémy, Mari, and Lucas who give invaluable supports on a daily basis. They are like my second family in France. Arigatou!

I would like to thank my precious family in Japan; my parents, my parents-in-law, my brother, and my grandparents, for their endless love and moral support despite a long distance. Last but not least, my wordless gratitude must be dedicated to my dearest husband, Issei who stands always with me, gives me infinite love, encouragement, and support. Without his immense help and patience, I would not have been able to complete this long and tough PhD work. And of course my sweet sons, Ryosei and Kaisei, you are my little treasures who bring me supreme happiness everyday with your big smiles even at difficult times particularly these last few months.

My sincere thanks to many other people who supported me throughout everything. I wish to thank everyone from the bottom of my heart.

# Sub-10 nm Nano-Structured Carbohydrate-based Block Copolymer Thin Films for Organic Photovoltaic Applications

## Abstract

Nanoscale patterning through self-assembly of block copolymers is one of the promising bottom-up strategies for controlling active layer morphology in organic photovoltaics. In this thesis, a new class of carbohydrate-based semiconducting block copolymers consisting of  $\pi$ -conjugated regioregular poly(3-hexylthiophene) (P3HT) and oligosaccharides were synthesized and self-organized into sub-10 nm scale periodic nanostructures. Two different diblock copolymers, *i.e.* P3HT-*block*-peracetylated maltoheptaose (P3HT-*b*-AcMal<sub>7</sub>) and P3HT-*block*-maltoheptaose (P3HT-*b*-Mal<sub>7</sub>) were synthesized via "click" reaction between end-functionalized oligosaccharide and P3HT moieties. A comprehensive investigation of their self-assembly behavior by AFM, TEM, and X-ray scattering analyses revealed that the P3HT-*b*-AcMal<sub>7</sub> diblock copolymer has the ability to self-assemble into sub-10 nm scale lamellar structure, which is the ideal morphology of the active layer in organic photovoltaics and one of the smallest domain sizes achieved by self-assembly of P3HT-based block copolymers, via thermal annealing. Nano-patterned film made of P3HT was attained by selective chemical etching of AcMal<sub>7</sub> block from microphase-separated P3HT-*b*-AcMal<sub>7</sub> template without affecting the original lamellar structure. The resultant void where the etched-out AcMal<sub>7</sub> block existed will be filled with electron acceptor compounds such as [6,6]-phenyl-C<sub>61</sub>-butyric acid methyl ester (PC<sub>61</sub>BM) for photovoltaic application as a perspective of this thesis. The results and knowledge obtained in this study are expected to provide further advances and innovation in organic photovoltaics.

Key words: Carbohydrate-based block copolymers,  $\pi$ -conjugated polymers, oligosaccharides, sub-10 nm scale self-assembly, organic photovoltaics.

# **Films Minces Nano-Structurés de Domaines sub-10 nm à partir de Copolymères biosourcé pour des Applications dans le Photovoltaïque Organique**

## Résumé

La structuration par auto-assemblage à l'échelle nanométrique de copolymères à blocs est l'une des stratégies « bottom-up » prometteuses pour contrôler la morphologie de la couche active de cellules photovoltaïques organiques. Dans cette thèse, une nouvelle classe de copolymère constitué d'un bloc semi-conducteur  $\pi$ -conjugué poly(3-hexylthiophène) (P3HT) régiorégulier et d'un bloc oligosaccharidique a été synthétisée et a montré une auto-organisation en nanostructures périodiques de domaine inférieure à 10 nm. Deux systèmes de copolymères à blocs ont été synthétisés, le P3HT-*bloc*-maltoheptaose peracétylé (P3HT-*b*-AcMal<sub>7</sub>) et le P3HT-*bloc*-maltoheptaose (P3HT-*b*-Mal<sub>7</sub>), via une réaction de chimie "clic" entre les segments oligosaccharidiques et P3HT fonctionnalisés en extrémité. Une étude exhaustive sur leur comportement d'auto-assemblage par des analyses AFM, TEM et de diffusion des rayons X a révélé que le copolymère à bloc P3HT-*b*-AcMal<sub>7</sub> montre une propension à s'auto-assembler par recuit thermique en structures lamellaires avec une résolution inférieure à 10 nm, c'est-à-dire la morphologie et la taille idéale pour la couche active d'une cellule photovoltaïque organique. De plus, ce système présente l'une des plus petites tailles de domaines réalisées par l'auto-assemblage de copolymères à blocs à base de P3HT. Un réseau lamellaire composé uniquement du P3HT a été obtenu par gravure chimique sélective du bloc sacrificiel AcMal<sub>7</sub> à partir d'un film nano-organisé de P3HT-*b*-AcMal<sub>7</sub> et ceci sans affecter la structure lamellaire initiale. Les domaines vides du AcMal<sub>7</sub> gravé pourront être remplis par un composé accepteur d'électrons tel que le [6,6]-phényl-C<sub>61</sub>-butanoate de méthyle (PC<sub>61</sub>BM) pour l'application photovoltaïque comme perspective de cette thèse. Les résultats et les connaissances acquises dans cette étude devraient permettre d'augmenter les performances des prochaines générations de cellules photovoltaïques organiques.

Mots-clés: copolymères biosourcés, polymères  $\pi$ -conjugués, oligosaccharides, auto-assemblage à des échelles inférieures à 10 nm, photovoltaïque organique.

## List of Figures

<b>Figure 1.1</b> Schematic image of typical device architecture of an organic solar cell.....	15
<b>Figure 1.2</b> Schematic illustration of charge generation mechanism in organic solar cells.....	16
<b>Figure 1.3</b> Energy diagram of organic solar cell.....	17
<b>Figure 1.4</b> Active layer morphologies of organic thin film solar cells.....	18
<b>Figure 1.5</b> Structure of the first reported bilayer heterojunction organic solar cell in 1986.....	19
<b>Figure 1.6</b> Bulk heterojunction organic solar cell reported by Yu and Heeger <i>et al.</i> in 1995....	20
<b>Figure 1.7</b> (a) Chemical structure of polyacetylene and (b) schematic image of charge carrier formation by doping.....	22
<b>Figure 1.8</b> Chemical structures of common organic semiconductors.....	22
<b>Figure 1.9</b> Chemical structure of poly(3-hexylthiophene).....	23
<b>Figure 1.10</b> Regiochemistry of P3HT isomers.....	24
<b>Figure 1.11</b> Chemical structure of phenyl-C <sub>61</sub> -butyric acid methyl ester (PC <sub>61</sub> BM).....	32
<b>Figure 1.12</b> Schematic illustrations of different types of block copolymer architectures.....	33
<b>Figure 1.13</b> (a) Theoretical phase diagram of AB diblock copolymer in the weak segregation limit predicted by the self-consistent mean-field theory, depending on volume fraction of A block ( $f_A$ ) and the product of $\chi N$ , where $\chi$ is the Flory-Huggins interaction parameter and $N$ is the total degree of polymerization: S, S', CPS, and CPS' = spheres, C and C' = cylinders, G = gyroid, and L = lamellae. (b) Experimental phase diagram of polyisoprene- <i>block</i> -poly styrene, where represents the volume fraction of polyisoprene. (c) Schematic image of equilibrium morphologies of AB diblock copolymers.....	35
<b>Figure 1.14</b> Phase diagram for weakly segregated PPV- <i>b</i> -PI block copolymer system. (a) Maier-Saupé interaction $\mu N$ vs volume fraction of coil segment and (b) Flory-Huggins interaction $\chi N$ vs volume fraction of coil segment. (c) Chemical structure of PPV- <i>b</i> -PI.....	37
<b>Figure 1.15</b> Schematic representation of the thermoresponsive self-assembly of PNIPAM- <i>b</i> -oligosaccharides.....	39
<b>Figure 1.16</b> (a) Schematic representation of sugar-based block copolymer thin film fabrication	

with 5-10 nm features. (b) Chemical structure of maltoheptaose-*block*-polystyrene (Mal<sub>7</sub>-*b*-PS). (c) AFM images of Mal<sub>7</sub>-*b*-PS thin films; control of horizontal and perpendicular 10 nm cylinders by varying the composition of annealing co-solvents.....41

**Figure 1.17** Classification of block copolymers (BCPs) on the basis of their structure and role in photovoltaic applications.....42

**Figure 1.18** (a) Chemical structure of the first reported P3HT-based block copolymers and (b) AFM phase image of the “nanowire” morphology in P3HT-*b*-PS thin film casted from toluene.....43

**Figure 1.19** (a) Chemical structure of poly(3-hexylthiophene)-*block*-poly(*L*-lactide) (P3HT-*b*-PLLA) and its schematic representation. The procedure for the preparation of donor-acceptor nanostructures; (b) ordering of the P3HT-*b*-PLLA, (c) selective removal of PLLA, and (d) backfilling with C<sub>60</sub> hydroxide. (e) The random structure consisted of P3HT and C<sub>60</sub> without ordering.....45

**Figure 1.20** Schematic illustration of the formation of an active layer having a well-defined lamellar structure.....49

**Figure 2.1** (a) MALDI-TOF MS spectrum of ethynyl-P3HT **P1** and (b) magnified part in the range of 21 repeating units.....62

**Figure 2.2** <sup>1</sup>H NMR spectrum of ethynyl-P3HT **P1** in CDCl<sub>3</sub>.....68

**Figure 2.3** <sup>13</sup>C NMR spectrum of ethynyl-P3HT **P1** in CDCl<sub>3</sub>.....69

**Figure 2.4** (a) <sup>1</sup>H-<sup>13</sup>C HSQC spectrum of ethynyl-P3HT **P1** in CDCl<sub>3</sub> and (b) magnified part in the range of 3.0–0.5 ppm in the x-axis and 35–10 ppm in the y-axis.....70

**Figure 2.5** (a) <sup>1</sup>H-<sup>13</sup>C HMBC spectrum of ethynyl-P3HT **P1** in CDCl<sub>3</sub> and (b) magnified part in the range of 3.0–0.5 ppm in the x-axis and 35–10 ppm in the y-axis.....71

**Figure 2.6** SEC trace of ethynyl-P3HT **P1**.....72

**Figure 2.7** MALDI-TOF MS spectrum of ethynyl-P3HT **P1**.....73

**Figure 2.8** SEC trace of pentynyl-P3HT **P2**.....79

**Figure 2.9** <sup>1</sup>H NMR spectrum of pentynyl-P3HT **P2** in CDCl<sub>3</sub>.....80

**Figure 2.10** (a) MALDI-TOF MS spectrum of pentynyl-P3HT **P2** and (b) magnified part in the range of 22 repeating units.....82

<b>Figure 2.11</b> $^1\text{H}$ NMR spectra of (a) H/Br capped P3HT and (b) ethynyl-P3HT <b>P3</b> .....	85
<b>Figure 2.12</b> (a) MALDI-TOF MS spectra of H/Br-capped P3HT and (b) magnified part in the range of 17-18 repeating units.....	87
<b>Figure 2.13</b> (a) MALDI-TOF MS spectra of ethynyl-P3HT <b>P3</b> and (b) magnified part in the range of 22-23 repeating units.....	88
<b>Figure 2.14</b> Comparison of the SEC traces of ethynyl-P3HT prepared by post-polymerization functionalization method (solid line) and <i>in situ</i> functionalization method (dotted line).....	89
<b>Figure 2.15</b> $^1\text{H}$ NMR spectra of (a) Mal <sub>7</sub> and (b) Mal <sub>7</sub> -N <sub>3</sub> in D <sub>2</sub> O.....	91
<b>Figure 2.16</b> FT-IR spectra of (a) Mal <sub>7</sub> and (b) Mal <sub>7</sub> -N <sub>3</sub> .....	92
<b>Figure 2.17</b> MALDI-TOF MS spectrum of Mal <sub>7</sub> -N <sub>3</sub> in positive mode.....	93
<b>Figure 2.18</b> $^1\text{H}$ NMR spectra of (a) Mal <sub>7</sub> and (b) Mal <sub>7</sub> -NAC-C <sub>2</sub> H <sub>2</sub> -N <sub>3</sub> in D <sub>2</sub> O.....	95
<b>Figure 2.19</b> FT-IR spectra of (a) Mal <sub>7</sub> and (b) Mal <sub>7</sub> -NAC-C <sub>2</sub> H <sub>4</sub> -N <sub>3</sub> .....	95
<b>Figure 2.20</b> MALDI-TOF MS spectrum of Mal <sub>7</sub> -NAC-C <sub>2</sub> H <sub>4</sub> -N <sub>3</sub> in positive mode.....	96
<b>Figure 2.21</b> (a) SEC traces of ethynyl-P3HT <b>P1</b> (black line) and the resulting product of run 1 (blue line). (b) FT-IR spectra of (i) ethynyl-P3HT <b>P1</b> , (ii) Mal <sub>7</sub> -N <sub>3</sub> , and (iii) reaction mixture of run1.....	99
<b>Figure 2.22</b> SEC traces of the PS-N <sub>3</sub> (dotted line), the penthynyl-P3HT <b>P2</b> (broken line), and the reaction mixture (solid line) of “click” reaction performed in (a) THF and (b) mixed solvent of THF/DMF.....	104
<b>Figure 2.23</b> FT-IR spectra of (a) ethynyl-P3HT <b>P1</b> , (b) Mal <sub>7</sub> -N <sub>3</sub> , (c) AcMal <sub>7</sub> -N <sub>3</sub> , (d) P3HT <sub>P1</sub> - <i>b</i> -AcMal <sub>7</sub> and (e) P3HT <sub>P1</sub> - <i>b</i> -Mal <sub>7</sub> .....	106
<b>Figure 2.24</b> SEC traces of ethynyl-P3HT <b>P1</b> (black line), P3HT <sub>P1</sub> - <i>b</i> -AcMal <sub>7</sub> (red line).....	108
<b>Figure 2.25</b> Chemical structures of the matrices tested for the MALDI-TOF MS analysis.....	109
<b>Figure 2.26</b> $^1\text{H}$ NMR spectra of (a) ethynyl-P3HT <b>P1</b> , (b) AcMal <sub>7</sub> -N <sub>3</sub> , (c) P3HT <sub>P1</sub> - <i>b</i> -AcMal <sub>7</sub> block copolymer and (d) P3HT <sub>P1</sub> - <i>b</i> -Mal <sub>7</sub> block copolymer in CDCl <sub>3</sub> .....	112
<b>Figure 2.27</b> $^1\text{H}$ -DOSY spectrum of P3HT <sub>P1</sub> - <i>b</i> -AcMal <sub>7</sub> .....	113
<b>Figure 2.28</b> MALDI-TOF MS spectra of P3HT <sub>P1</sub> - <i>b</i> -AcMal <sub>7</sub> obtained by using (a) dithranol	

and (c) DHB as a matrix, and magnified part in the range of (b) 23 repeating units in the spectrum a (encircled area with green dotted line), (d) 22 repeating units of unreacted P3HT **P1** (encircled area with blue dotted line) and (e) 22 repeating units of P3HT<sub>P1</sub>-*b*-AcMal<sub>7</sub> (encircled area with red dotted line) in the spectrum c.....114

**Figure 2.29** <sup>13</sup>C NMR spectra of (a) ethynyl-P3HT **P1** in CDCl<sub>3</sub>, (b) Mal<sub>7</sub>-N<sub>3</sub> in D<sub>2</sub>O, (c) P3HT<sub>P1</sub>-*b*-Mal<sub>7</sub> block copolymer in CDCl<sub>3</sub> and (d) <sup>13</sup>C CP/MAS NMR spectrum of P3HT<sub>P1</sub>-*b*-Mal<sub>7</sub> block copolymer.....115

**Figure 3.1** General procedures for the preparation of the polymer thin films for AFM and TEM measurements.....121

**Figure 3.2** Dependence of the (a) concentration of a polymer solution and (b) spin speed on the film thickness (solvent: CHCl<sub>3</sub>).....122

**Figure 3.3** AFM phase images of as-cast films for (a) P3HT<sub>P1</sub>-*b*-Mal<sub>7</sub>, (b) P3HT<sub>P1</sub>-*b*-AcMal<sub>7</sub>, and (c) ethynyl-P3HT **P1** and TEM images of as-cast films for (d) P3HT<sub>P1</sub>-*b*-Mal<sub>7</sub>, (e) P3HT<sub>P1</sub>-*b*-AcMal<sub>7</sub>, and (f) ethynyl-P3HT **P1**. Scale bars indicate 200 nm. SAXS profiles of pristine bulk samples for (g) P3HT<sub>P1</sub>-*b*-Mal<sub>7</sub>, (h) P3HT<sub>P1</sub>-*b*-AcMal<sub>7</sub>, and (i) ethynyl-P3HT **P1**.....125

**Figure 3.4** Equipment for vapor solvent annealing.....127

**Figure 3.5** AFM phase images of (a) as-cast P3HT<sub>P1</sub>-*b*-Mal<sub>7</sub> thin film and solvent vapor annealed P3HT<sub>P1</sub>-*b*-Mal<sub>7</sub> thin films with different solvent compositions of (b) THF/H<sub>2</sub>O = 10/0, (c) THF/H<sub>2</sub>O = 8/2, (d) THF/H<sub>2</sub>O = 6/4, (e) THF/H<sub>2</sub>O = 4/6, (f) THF/H<sub>2</sub>O = 2/8, and (g) THF/H<sub>2</sub>O = 0/10 (annealing time: 24h). Scale bars indicate 200 nm.....127

**Figure 3.6** Representative AFM phase images of P3HT<sub>P1</sub>-*b*-Mal<sub>7</sub> thin films after solvent vapor annealing for 24 h with (a) anisole and (b) CHCl<sub>3</sub>/MeOH = 1/1.....129

**Figure 3.7** Representative AFM phase image of P3HT<sub>P1</sub>-*b*-AcMal<sub>7</sub> thin film after solvent annealing under the vapor produced from mixture of THF/H<sub>2</sub>O = 1/1 for 24h.....130

**Figure 3.8** AFM phase images of as-cast films for (a) P3HT<sub>P1</sub>-*b*-Mal<sub>7</sub>, (b) P3HT<sub>P1</sub>-*b*-AcMal<sub>7</sub>, (c) ethynyl-P3HT **P1**, and thermally annealed films at 220 °C for 10 min for (d) P3HT<sub>P1</sub>-*b*-Mal<sub>7</sub>, (e) P3HT<sub>P1</sub>-*b*-AcMal<sub>7</sub>, (f) ethynyl-P3HT **P1**. SAXS profiles of neat samples in bulk (dotted line) and thermally annealed bulk samples (solid line) at 220 °C for 10 min for (g) P3HT<sub>P1</sub>-*b*-Mal<sub>7</sub>, (h) P3HT<sub>P1</sub>-*b*-AcMal<sub>7</sub> and (i) ethynyl-P3HT **P1**.....133

**Figure 3.9** TEM images of (a) as-spun and (b) thermally annealed (220 °C for 10 min) P3HT<sub>P1</sub>-*b*-AcMal<sub>7</sub> thin films. Fourier transform image of TEM image is given as the inset.....134

<b>Figure 3.10</b> TEM images of P3HT <sub>P1</sub> - <i>b</i> -AcMal <sub>7</sub> films obtained after thermal annealing at (a) 100 °C, (b) 170 °C, (c) 180 °C, and (d) 220 °C for 10 min. Fast Fourier transform (FFT) images and electron diffraction patterns are given bottom left and bottom right side of each TEM image, respectively.....	138
<b>Figure 3.11</b> TEM images of (a) P3HT <sub>P1</sub> - <i>b</i> -AcMal <sub>7</sub> and (b) P3HT <sub>P3</sub> - <i>b</i> -AcMal <sub>7</sub> thin films obtained after thermal annealing at 220 °C for 10 min. Insets represent fast Fourier transform (FFT) images. SAXS profiles of (c) P3HT <sub>P1</sub> - <i>b</i> -AcMal <sub>7</sub> and (d) P3HT <sub>P3</sub> - <i>b</i> -AcMal <sub>7</sub> bulk samples obtained after thermal annealing at 220 °C for 10 min.....	140
<b>Figure 3.12</b> An ideal structure for the active layer morphology of organic thin film solar cells.....	141
<b>Figure 3.13</b> Microtome procedure.....	142
<b>Figure 3.14</b> TEM images of the cross-section of thermally annealed P3HT <sub>P3</sub> - <i>b</i> -AcMal <sub>7</sub> films (annealing condition: 220 °C for 10 min). (a) Low magnification image of the air/film interface, (b) magnified image of the encircled area with dotted line in (a), and (c) low magnification image of the PTFE substrate/film interface.....	143
<b>Figure 3.15</b> Two-dimensional GISAXS pattern of P3HT <sub>P3</sub> - <i>b</i> -AcMal <sub>7</sub> thin film ( <i>ca.</i> 35 nm) annealed at 200 °C for 10 min.....	144
<b>Figure 3.16</b> Schematic images of possible packing models for lamellar structure of the P3HT- <i>b</i> -AcMal <sub>7</sub> , where orange and red lines represent the P3HT and AcMal <sub>7</sub> segments. (a) monolayer, non-interdigitated AcMal <sub>7</sub> packing (side-by-side arrangement), (b) monolayer, interdigitated AcMal <sub>7</sub> packing, and (c) bilayer, non-interdigitated AcMal <sub>7</sub> packing.....	145
<b>Figure 3.17</b> Schematic illustrations of (a) expected arrangement estimated based on geometrical parameters, (b) hypothetical arrangement and density assuming P3HT segments are aligned parallel to the AcMal <sub>7</sub> segments, and (c) expected arrangement estimated based on space-filling (density) argument.....	150
<b>Figure 4.1</b> TGA curves of ethynyl-P3HT, P3HT- <i>b</i> -AcMal <sub>7</sub> and P3HT- <i>b</i> -Mal <sub>7</sub> .....	157
<b>Figure 4.2</b> TGA curves of AcMal <sub>7</sub> (red line) and Mal <sub>7</sub> (blue line).....	158
<b>Figure 4.3</b> DSC heating thermogram of AcMal <sub>7</sub> during heating cycle with a heating rate of 10 °C/min after cooling cycle with a cooling rate of 20 °C/min.....	161
<b>Figure 4.4</b> DSC thermograms of ethynyl-P3HT <b>P3</b> (black line), P3HT <sub>P3</sub> - <i>b</i> -AcMal <sub>7</sub> (red line) and P3HT <sub>P3</sub> - <i>b</i> -Mal <sub>7</sub> (blue line) obtained during first cooling run and second heating run	



with a heating and cooling rate of 10 °C/min. Small changes around 90 °C found for the all samples are probably artifacts derived from the apparatus used.....162

**Figure 4.5** DSC heating thermograms of (a) ethynyl-P3HT **P3**, (b) P3HT<sub>P3</sub>-*b*-AcMal<sub>7</sub>, and (c) P3HT<sub>P3</sub>-*b*-Mal<sub>7</sub> obtained during heating cycles with a heating rate of 10 °C/min after cooling cycle with different cooling rate.....164

**Figure 4.6** (a) DSC thermograms of ethynyl-P3HT **P1** during 1st heating, 1st cooling, and 2nd heating cycles with a heating rate of 10 °C/min and cooling rate of 2.5 °C/min. (b) SAXS profiles of ethynyl-P3HT **P1** bulk sample taken during *in situ* heating, holding, and cooling measurement.....168

**Figure 4.7** (a) DSC thermograms of P3HT<sub>P1</sub>-*b*-AcMal<sub>7</sub> during 1st heating, 1st cooling, and 2nd heating cycles with a heating rate of 10 °C/min and cooling rate of 2.5 °C/min. (b) SAXS profiles of P3HT<sub>P1</sub>-*b*-AcMal<sub>7</sub> bulk sample taken during *in situ* heating, holding, and cooling measurement.....170

**Figure 4.8** (a) Evolution of *d*-spacing of P3HT<sub>P1</sub>-*b*-AcMal<sub>7</sub> during *in situ* measurement. (b) Schematic illustration of P3HT<sub>P1</sub>-*b*-AcMal<sub>7</sub> conformation, where orange and red lines represent P3HT and AcMal<sub>7</sub> segments, respectively.....171

**Figure 4.9** (a) Evolution of ordered domains size of P3HT<sub>P1</sub>-*b*-AcMal<sub>7</sub> during *in situ* measurement. (b) TEM image of P3HT<sub>P1</sub>-*b*-AcMal<sub>7</sub> thin film obtained after thermal annealing at 220 °C for 10 min.....173

**Figure 4.10** Schematic illustration of the hierarchical semi-crystalline structure of P3HT.....175

**Figure 4.11** Projection of the P3HT crystal structure along *c* axes and the unit cell proposed by Brinkmann *et al.*.....176

**Figure 4.12** WAXS profiles of (a) P3HT homopolymers and (b) P3HT-*b*-AcMal<sub>7</sub> block copolymers measured at room temperature. Black and blue profiles represent P1 and P3 series, *i.e.* ethynyl-P3HT **P1**/P3HT<sub>P1</sub>-*b*-AcMal<sub>7</sub> and ethynyl-P3HT **P3**/P3HT<sub>P3</sub>-*b*-AcMal<sub>7</sub>, respectively. Positions of strong reflections estimated based on the unit cell proposed by Brinkmann *et al.* were depicted with gray dashed lines together with corresponding Miller indices. All reflection positions were plotted with purple marks.....178

**Figure 4.13** Comparison between before (black) and after (red) thermal annealed bulk samples. (a) ethynyl-P3HT **P3** and (b) P3HT<sub>P3</sub>-*b*-AcMal<sub>7</sub>. Positions of strong reflections estimated based on the unit cell proposed by Brinkmann *et al.* were depicted with gray dashed lines together with corresponding Miller indices. All reflection positions were plotted with purple marks.....180

**Figure 4.14** Comparison of diffraction patterns between as-prepared bulk samples of (a) ethynyl-P3HT **P3** and (b) P3HT<sub>P3</sub>-*b*-AcMal<sub>7</sub>.....181

<b>Figure 4.15</b> (a) WAXS profiles of P3HT <sub>P1</sub> - <i>b</i> -AcMal <sub>7</sub> bulk sample and variation of (b) $d_{100}$ and (c) crystallite size during <i>in situ</i> heating and cooling process.....	184
<b>Figure 4.16</b> (a) WAXS profiles of P3HT <sub>P3</sub> - <i>b</i> -AcMal <sub>7</sub> bulk sample and variation of (b) $d_{200}$ and (c) $d_{020/002}$ during <i>in situ</i> heating process from 30 to 200 °C.....	185
<b>Figure 5.1</b> Film thickness of the P3HT (red circle) and AcMal <sub>7</sub> (black circle) as a function of etching time.....	193
<b>Figure 5.2</b> Weight loss profiles obtained by thermogravimetry of sulfuric acid-impregnated AcMal <sub>7</sub> (black line) and P3HT (red line) powders as a function of time during heating process from room temperature to 100 °C with heating rate at 10 °C/min following isothermal heat treatment at 100 °C.....	196
<b>Figure 5.3</b> FT-IR spectra of the P3HT <sub>P3</sub> - <i>b</i> -AcMal <sub>7</sub> films (a) before etching and after sulfuric acid etching at 100 °C for (b) 30 min and (c) 1h. The film was prepared by spin-coating on Si wafer with the thickness of <i>ca.</i> 250 nm.....	197
<b>Figure 5.4</b> TEM image of the P3HT <sub>P3</sub> - <i>b</i> -AcMal <sub>7</sub> thin film, obtained after sulfuric acid etching at 100 °C for 1h.....	199
<b>Figure 5.5.</b> MALDI-TOF MS spectrum of PC <sub>61</sub> BA in the negative mode.....	204
<b>Figure 5.6</b> FT-IR spectra of (a) PC <sub>61</sub> BM, (b) PC <sub>61</sub> BA, (c) PC <sub>61</sub> B-Cl, and (d) ethynyl-PC <sub>61</sub> BAm.....	204
<b>Figure 5.7</b> <sup>1</sup> H NMR spectrum of (a) PC <sub>61</sub> BM in CDCl <sub>3</sub> and (b) ethynyl-PC <sub>61</sub> BAm in THF- <i>d</i> <sub>8</sub> .....	205
<b>Figure 5.8</b> MALDI-TOF MS spectrum of ethynyl-PC <sub>61</sub> BAm in negative mode.....	206
<b>Figure 5.9</b> SEC traces of PC <sub>61</sub> BM, ethynyl-PC <sub>61</sub> BAm, AcMal <sub>7</sub> -N <sub>3</sub> , and AcMal <sub>7</sub> -C <sub>61</sub> recorded by UV detector.....	208
<b>Figure 5.10</b> FT-IR spectra of (a) ethynyl-PC <sub>61</sub> BAm, (b) AcMal <sub>7</sub> -N <sub>3</sub> , and (c) AcMal <sub>7</sub> -C <sub>61</sub> .....	209
<b>Figure 5.11</b> MALDI-TOF MS spectrum of AcMal <sub>7</sub> -C <sub>61</sub> in positive mode.....	210
<b>Figure 5.12</b> <sup>1</sup> H-DOSY spectrum of (a) AcMal <sub>7</sub> -N <sub>3</sub> , (b) ethynyl-PC <sub>61</sub> BAm, and (c) AcMal <sub>7</sub> -C <sub>61</sub> (solvent: toluene- <i>d</i> <sub>8</sub> ).....	211

**Figure 5.13** TEM images of thermally annealed thin films of (a) P3HT<sub>P3</sub>-*b*-AcMal<sub>7</sub> and the blend of P3HT<sub>P3</sub>-*b*-AcMal<sub>7</sub> and PC<sub>61</sub>BM with donor: acceptor ratio of (b) 1:0.1, (c) 1:0.5 and (d) 1:1 (annealing condition: 210 °C for 10 min).....213

**Figure 5.14** TEM images of the cross section of thermally annealed P3HT<sub>P3</sub>-*b*-AcMal<sub>7</sub>: PC<sub>61</sub>BM blend film (1:1) (annealing condition: 220 °C for 10 min) at the interface of PTFE substrate/film.....213

**Figure 5.15** TEM images of thermally annealed thin films of (a) P3HT<sub>P3</sub>-*b*-AcMal<sub>7</sub> and the blend of P3HT<sub>P3</sub>-*b*-AcMal<sub>7</sub> and AcMal<sub>7</sub>-C<sub>61</sub> with donor: acceptor ratio of (b) 1:0.1, (c) 1:0.5 and (d) 1:1 (annealing condition: 210 °C for 10 min).....214

**Figure 5.16** Schematic representation of nanostructure of the blend film of P3HT-*b*-AcMal<sub>7</sub> and AcMal<sub>7</sub>-C<sub>61</sub>.....215

**Figure 5.17** WAXS profiles of the thermally annealed bulk samples of the single substance of (a) P3HT<sub>P3</sub>-*b*-AcMal<sub>7</sub> and (e) AcMal<sub>7</sub>-C<sub>61</sub>, and the thermally annealed bulk samples of the blend of P3HT-*b*-AcMal<sub>7</sub> and AcMal<sub>7</sub>-C<sub>61</sub> with donor:acceptor ratio of (b) 1:0.1, (c) 1:0.5, and (d) 1:1 (Annealing condition: 210 °C for 10 min).....216

**Figure 5.18** Methodology used for evaluation of the mixed state of P3HT-*b*-AcMal<sub>7</sub> and AcMal<sub>7</sub>-C<sub>61</sub>.....218

**Figure 5.19** WAXS profiles (black) and combined spectra (red) of the thermally annealed samples of the blend of P3HT-*b*-AcMal<sub>7</sub> and AcMal<sub>7</sub>-C<sub>61</sub> with donor/acceptor ratio of (a) 1/0.1, (b) 1/0.5, and (c) 1/1 (Annealing condition: 210 °C for 10 min). The combined spectra were normalized with respect to integrated area of corresponding WAXS profiles.....218

## List of Schemes

<b>Scheme 1.1</b> Synthesis of regioregular poly(3-alkylthiophene-2,5-diyl)s via (a) McCullough method and (b) Rieke method.....	25
<b>Scheme 1.2</b> Synthesis of regioregular (HT-HT > 99 %) poly(3-hexylthiophene-2,5-diyl) via the GRIM polymerization.....	27
<b>Scheme 1.3</b> Synthesis of P3HT initiated from ethynyl-functionalized Ni-based initiator.....	29
<b>Scheme 1.4</b> Synthesis of end-functionalized P3HT via <i>in situ</i> end-capping strategy. A below figure shows classification of the Grignard reagents which tend to afford mono- or bis-capped P3HT as the major product.....	30
<b>Scheme 1.5</b> Effect of the unsaturated additive, LiCl, and temperature on the end-group composition of tolyl-magnesium bromide quenched P3HT reported by Pickel <i>et al.</i> .....	31
<b>Scheme 2.1</b> The alkyne-terminated P3HT synthesized by the <i>in situ</i> end-functionalization method.....	59
<b>Scheme 2.2</b> Proposed interaction between Ni catalyst and unsaturated group of additives.....	60
<b>Scheme 2.3</b> Synthesis of ethynyl-functionalized P3HT <b>P1</b> by the combination of modified Grignard metathesis polymerization and <i>in situ</i> functionalization.....	60
<b>Scheme 2.4</b> (a) Chain growth reaction of the GRIM polymerization and (b) proposed mechanism of by-products formation process during the termination reaction.....	64
<b>Scheme 2.5</b> Proposed mechanism for the homo-dimerization of the polymers (route A).....	76
<b>Scheme 2.6</b> Proposed mechanism for the homo-dimerization of the polymers (route B).....	77
<b>Scheme 2.7</b> Synthesis of pentynyl-functionalized P3HT <b>P2</b> by the combination of modified Grignard metathesis polymerization and <i>in situ</i> functionalization.....	78
<b>Scheme 2.8</b> Synthesis of ethynyl-functionalized P3HT <b>P3</b> via modified Grignard metathesis polymerization and post-polymerization functionalization with Stille reaction.....	84
<b>Scheme 2.9</b> Azido-functionalized maltoheptaoses synthesized in this study.....	90

<b>Scheme 2.10</b> Direct synthesis of azido-functionalized maltoheptaose Mal <sub>7</sub> -N <sub>3</sub> .....	90
<b>Scheme 2.11</b> Synthesis of azido-functionalized maltoheptaose Mal <sub>7</sub> -N <sub>3</sub> -C <sub>2</sub> H <sub>4</sub> -N <sub>3</sub> .....	94
<b>Scheme 2.12</b> Attempts to direct click reaction between alkyne-functionalized P3HT and azido-functionalized Mal <sub>7</sub> .....	97
<b>Scheme 2.13</b> (a) Reaction conditions of Glaser coupling and Huisgen type CuAAC “click” reaction. (b) Mechanism of Glaser reaction.....	102
<b>Scheme 2.14</b> Experiments to verify the hypothesis: “click” reaction between azido-functionalized polystyrene (PS-N <sub>3</sub> ) and pentynyl-P3HT <b>P2</b> in (a) THF and (b) mixed solvent of THF/DMF.....	103
<b>Scheme 2.15</b> Strategy used for the synthesis of P3HT- <i>b</i> -Mal <sub>7</sub> block copolymer: (a) synthesis of azido end-functionalized peracetylated maltoheptaose (AcMal <sub>7</sub> -N <sub>3</sub> ) and (b) “click” reaction of ethynyl-P3HT with AcMal <sub>7</sub> -N <sub>3</sub> and followed by deacetylation of sugar block.....	105
<b>Scheme 5.1</b> Synthesis of <i>N</i> -propargyl (6,6)-phenyl C <sub>61</sub> butyramido (ethynyl-PC <sub>61</sub> BAm).....	201
<b>Scheme 5.2</b> Synthesis of fullerene-conjugated AcMal <sub>7</sub> .....	207

## List of Tables

<b>Table 1.1</b> P3AT-based block copolymers reported in literature.....	46-47
<b>Table 2.1</b> Summary of characterizations of the ethynyl-P3HT <b>P1</b> .....	61
<b>Table 2.2</b> Structural assignments of peaks observed in MALDI-TOF MS spectrum of ethynyl-P3HT <b>P1</b> .....	63
<b>Table 2.3</b> $^1\text{H}$ and $^{13}\text{C}$ NMR chemical shifts corresponding to the regioisomers in P3HT.....	66
<b>Table 2.4</b> Structural assignments of peaks observed in MALDI-TOF MS spectrum of pentynyl-P3HT <b>P2</b> .....	83
<b>Table 2.5</b> Structural assignments of peaks observed in MALDI-TOF MS spectrum of H/Br-capped P3HT.....	87
<b>Table 2.6</b> Structural assignments of peaks observed in MALDI-TOF MS spectrum of ethynyl-P3HT <b>P3</b> .....	88
<b>Table 2.7</b> Characterization details of the synthesized P3HTs in this study.....	89
<b>Table 2.8</b> Structural assignments of peaks observed in MALDI-TOF MS spectrum.....	93
<b>Table 2.9</b> Structural assignments of peaks observed in MALDI-TOF MS spectrum.....	96
<b>Table 2.10</b> Solubility of P3HT and Mal <sub>7</sub> .....	98
<b>Table 2.11</b> Summary of the direct click reaction experiments described in this chapter.....	100
<b>Table 2.12</b> Summary of solubility tests done on P3HT, AcMal <sub>7</sub> and Mal <sub>7</sub> .....	107
<b>Table 2.13</b> Characterization details of the synthesized glycoconjugated block copolymers in this study.....	116
<b>Table 3.1</b> Molecular properties of P3HT- <i>b</i> -AcMal <sub>7</sub> and P3HT- <i>b</i> -Mal <sub>7</sub> .....	136
<b>Table 3.2</b> Experimental structural parameters for P3HT <sub>P3</sub> - <i>b</i> -AcMal <sub>7</sub> and ethynyl-P3HT <sub>P3</sub> .....	146
<b>Table 3.3</b> Structural parameters of P3HT and AcMal <sub>7</sub> .....	149

<b>Table 4.1</b> Thermal properties of ethynyl-P3HT homopolymer, P3HT- <i>b</i> -AcMal <sub>7</sub> , and P3HT- <i>b</i> -Mal <sub>7</sub> obtained by TGA analysis.....	158
<b>Table 4.2</b> Thermal properties of ethynyl-P3HT homopolymer, P3HT- <i>b</i> -AcMal <sub>7</sub> , and P3HT- <i>b</i> -Mal <sub>7</sub> obtained by DSC analysis.....	162
<b>Table 4.3</b> Thermal properties of ethynyl-P3HT homopolymer, P3HT- <i>b</i> -AcMal <sub>7</sub> , and P3HT- <i>b</i> -Mal <sub>7</sub> obtained by DSC analysis.....	165
<b>Table 4.4</b> Molecular parameters of P3HT homopolymer and P3HT- <i>b</i> -AcMal <sub>7</sub> .....	174
<b>Table 4.5</b> Predicted and experimental <i>d</i> -spacings.....	181
<b>Table 5.1</b> Structural assignments of peaks observed in MALDI-TOF MS spectrum of AcMal <sub>7</sub> -C <sub>61</sub> .....	210

# TABLE OF CONTENTS

---

**ABSTRACT**

**RESUME (Français)**

**LIST OF FIGURES / SCHEMES / TABLAS**

<b>TABLE OF CONTENTS</b>	<b>1</b>
<b>GENERAL INTRODUCTION</b>	<b>4</b>
<b>INTRODUCTION GENERALE (Français)</b>	<b>8</b>
 <b>CHAPTER I:</b>	 <b>13</b>
<b>BACKGROUND AND REVIEW OF LITERATURES</b>	
I.1 Organic photovoltaic cells	14
I.1.1 Principles of energy generation process	15
I.1.2 History and development of active layer architectures	18
I.2. Organic semiconductor compounds	21
I.2.1 Poly (3-hexylthiophene) (P3HT)	23
I.2.1-1 Regioregularity	23
I.2.1-2 Synthesis of regioregular P3HT	25
I.2.1-3 End functionalization of P3HT using GRIM method	28
I.2.2 Fullerene and fullerene derivatives	32
I.3 Block copolymers	33
I.3.1 Self-assembly of block copolymers	33
I.3.2 Carbohydrate containing block copolymers	38
I.3.3 Block copolymers for organic photovoltaic	42
I.4 Motivation and aim of the thesis	48
I.5 References	50
 <b>CHAPTER II:</b>	 <b>57</b>
<b>SYNTHESIS AND STRUCTURAL CHARACTERIZATION OF SEMICONDUCTING GLYCOCONJUGATED DIBLOCK COPOLYMERS</b>	
II.1 Introduction	58
II.2 Synthesis of alkyne-terminated P3HT	59
II.2.1 <i>in situ</i> end-functionalization	59
II.2.2 Post-polymerization modification of Br-end-P3HT	84



II.3 Synthesis of azido-functionalized maltoheptaose (Mal <sub>7</sub> -N <sub>3</sub> )	90
II.4 Synthesis of P3HT- <i>b</i> -oligosaccharide block copolymers	97
II.4.1 Attempts to direct click reaction between alkyne-P3HT and Mal <sub>7</sub> -N <sub>3</sub>	97
II.4.2 Alternative attempts to the click reaction between alkyne-P3HT and acetylated maltoheptaose (AcMal <sub>7</sub> )	105
II.5 Conclusion	117
II.6 References	118
<b>CHAPTER III:</b>	<b>119</b>
<b>STUDY OF THE SELF-ASSEMBLY BEHAVIORS AND MORPHOLOGIES OF THE SEMICONDUCTING GLYCOCONJUGATED DIBLOCK COPOLYMERS</b>	
III.1 Introduction	120
III.2 Sample preparation	121
III.2.1.1 Thin film samples for AFM and TEM measurements	121
III.2.1.2 Bulk samples for SAXS measurements	123
III.3 Morphologies of as-cast samples	124
III.4 Self-organization via solvent annealing	126
III.5 Self-organization via thermal annealing	131
III.6 Molecular Packing Model	145
III.7 Conclusion	152
III.8 References	153
<b>CHAPTER IV:</b>	<b>155</b>
<b><i>in situ</i> EVALUATION OF THERMALLY INDUCED STRUCTURAL EVOLUTION OF THE SEMICONDUCTING GLYCOCONJUGATED DIBLOCK COPOLYMERS</b>	
IV.1 Introduction	156
IV.2 Thermal properties	157
IV.2.1 Thermogravimetric analysis (TGA)	157
IV.2.2 Differential scanning calorimetry (DSC)	159
IV.3 Step-wise heating and cooling SAXS measurements	166
IV.4 Step-wise heating and cooling WAXS measurements	174
IV.5 Conclusion	186
IV.6 References	187

<b>CHAPTER V:</b>	<b>189</b>
<b>APPROACHES TOWARD APPLICATION OF THE SEMICONDUCTING GLYCOCONJUGATED DIBLOCK COPOLYMERS TO PHOTOVOLTAIC CELLS</b>	
V.1 Introduction	190
V.2 Selective etching of oligosaccharidic block	191
V.2.1 Plasma etching	191
V.2.2 Wet etching by concentrated sulfuric acid	194
V.3 Synthesis and characterization of fullerene-conjugated oligosaccharide	200
V.3.1 Synthesis of alkyne-functionalized fullerene derivative	201
V.3.2 Synthesis of fullerene-conjugated AcMal <sub>7</sub> (AcMal <sub>7</sub> -C <sub>61</sub> )	207
V.3.3 Morphologies of the blend of P3HT- <i>b</i> -AcMal <sub>7</sub> :AcMal <sub>7</sub> -C <sub>61</sub>	212
V.4 Conclusion	219
V.5 References	220
 <b>CHAPTER VI:</b>	 <b>221</b>
<b>EXPERIMENTAL SECTION</b>	
VI.1 Synthesis	222
VI.1.1 Materials	222
VI.1.2 Instruments	222
VI.1.3 Synthesis of P3HT- <i>b</i> -oligosaccharide block copolymers	223
VI.1.4 Synthesis of fullerene-conjugated AcMal <sub>7</sub>	230
VI.2 Characterization	232
VI.2.1 Thermal properties	232
VI.2.2 AFM and TEM measurements	233
VI.2.3 SAXS and WAXS measurements	234
VI.3 Selective etching of oligosaccharidic block	235
VI.3.1 Plasma etching	235
VI.3.2 Wet etching by concentrated sulfuric acid	235
VI.4 References	236
 <b>GENERAL CONCLUSION</b>	 <b>238</b>

# GENERAL INTRODUCTION

Organic photovoltaic solar cells (OPVs) have emerged as a challenging new research field during the past few decades. Compared with classical inorganic systems, OPVs have many advantages, such as mechanical flexibility, applicability for “roll-to-roll” processing, low-cost productivity, mass productivity, *etc.*<sup>1-4</sup> However, the demonstrated power conversion efficiency of OPVs is limited to few percent, mainly due to the short exciton lifetime, poor mobility, and recombination of the charge carriers. These shortcomings are strongly influenced by the active layer morphology and the crystallinity of the  $\pi$ -conjugated materials used. One of the promising approaches to improve the efficiency is to design and control the active layer morphology between the donor and acceptor materials on a 10 – 15 nm scale that corresponds to the exciton diffusion length.<sup>5</sup> In particular, the periodic lamellar structure in which the electron donor and acceptor compounds are mutually interpenetrating is considered to be an ideal structure because this structure makes it possible to (i) suppress the exciton decay, (ii) provide the shortest charge transportation pathway, (iii) reduce charge trap sites, and (iv) promote charge separation of excitons by enlarging the interface contact area.<sup>6,7</sup>

The self-assembly of  $\pi$ -conjugated block copolymers has drawn considerable attention as a powerful approach to achieve ideal morphologies for applications in organic electronics.<sup>8-10</sup> The self-assembly behavior of A-B type diblock copolymer is regulated by the degree of polymerization ( $N$ ), the volume fraction of each block ( $\phi$ ), and the Flory-Huggins interaction parameter ( $\chi$ ), which quantify the thermodynamic driving force for microphase separation. In the case of flexible coil-coil type diblock copolymers, the strength of segregation of the two blocks is proportional to  $\chi N$ , that is, block copolymers are predicted to order into diverse morphologies as a function of  $\phi$  when  $\chi N$  is larger than a critical value (10.5 when  $\phi = 0.5$ ).<sup>11</sup> Therefore, block copolymers having high  $\chi$  and low  $N$  values, so-called “high  $\chi$ –low  $N$  block polymers”<sup>12</sup>, have attracted significant interest to realize phase separation with much smaller features than one could ever achieve using “low  $\chi$ ” block copolymers such as polystyrene-*block*-poly(methyl methacrylate).<sup>13,14</sup> For such purpose, the physico-chemistry and self-assembly of glycopolymer group in CERMAV directed by R. Borsali has synthesized a variety of glycoconjugated block copolymers consisting of oligosaccharides as one of the block components that self-organized

into sub-10 nm scale periodic structures such as spheres, cylinders, and lamellae.<sup>15–20</sup> The strong incompatibility, *i.e.* high  $\chi$ , between oligosaccharidic and synthetic polymer blocks arisen from their hydrophilicity-hydrophobicity imbalance that is further enhanced sterically by the “rod”-like structure of the oligosaccharidic blocks is the key to achieve such a small domain features. This concept can be extended to OPVs. High performance photovoltaic devices can be envisioned by taking advantage of the microphase segregation of new optoelectronically active semiconducting (electron-donating functional) glycoconjugated block copolymers. Once the expected nanostructure is obtained via self-organization of the block copolymer, the sacrificial oligosaccharidic segment will be removed, and the resultant cavity will be replaced with an electron accepting compounds to achieve the ultimate ideal structure in which the donor and acceptor compounds are alternately arranging in sub-10 nm scale.

To achieve the aforementioned objective, this thesis is mainly focused on the synthesis of the new class of semiconducting glycoconjugated diblock copolymers and their self-assembly behaviors. The thesis is divided into five chapters.

**Chapter 1** gives an introduction to OPVs and self-assembly of block copolymers to explain fundamental theory behind this project.

**Chapter 2** describes the synthesis and characterization of a novel diblock copolymers consisting of  $\pi$ -conjugated regioregular poly (3-hexylthiophene) (P3HT) and oligosaccharide. Two different diblock copolymers, *i.e.* P3HT-*block*-peracetylated maltoheptaose (P3HT-*b*-AcMal<sub>7</sub>) and P3HT-*block*-maltoheptaose (P3HT-*b*-Mal<sub>7</sub>) were synthesized. Comprehensive characterization of the obtained diblock copolymers via various analytical techniques are described in detail.

**Chapter 3** describes a morphological study of the synthesized diblock copolymers. Thermal annealing and solvent vapor annealing, which are the two most practical methods to facilitate or accelerate self-organizations of block copolymers, were applied on the both P3HT-*b*-AcMal<sub>7</sub> and P3HT-*b*-Mal<sub>7</sub> diblock copolymers. Their morphologies were carefully investigated by means of atomic force microscope (AFM), transmission electron microscope (TEM), and small-angle X-ray scattering (SAXS) measurements. It was found that the P3HT-*b*-AcMal<sub>7</sub> diblock copolymer has a potential ability to self-assemble into well-defined lamellar structure in sub-10 nm scale through thermal annealing. A molecular packing model for the self-assembled P3HT-*b*-AcMal<sub>7</sub> was also discussed based on the experimental results and theoretical crystal structure.

**Chapter 4** describes thermal properties and thermally-induced structural evolution of the semiconducting glycoconjugated diblock copolymers. The structural changes were investigated by *in situ* step-wise heating and cooling measurements of infrared spectroscopy (IR), small- and wide-angle X-ray scattering (SAXS/WAXS).

In **Chapter 5**, two concrete approaches towards application of the synthesized block copolymer to OPVs are presented. First, selective etching of the oligosaccharide segment (AcMal<sub>7</sub>) from self-assembled P3HT-*b*-AcMal<sub>7</sub> film was attempted via dry and wet etching process to provide ultimate desired architecture. Secondly, fullerene-conjugated oligosaccharide (AcMal<sub>7</sub>-C<sub>61</sub>) was synthesized with the aim of controlling a location of acceptor moiety and stabilizing the morphology.

**Chapter 6** contains the detailed experimental methods performed in this work.

## References

- (1) Nelson, J. *Mater. Today* **2011**, *14* (10), 462–470.
- (2) Heeger, A. J. *Adv. Mater.* **2014**, *26* (1), 10–28.
- (3) Huang, Y.; Kramer, E. J.; Heeger, A. J.; Bazan, G. C. *Chem. Rev.* **2014**, *114* (14), 7006–7043.
- (4) Mayer, A. C.; Scully, S. R.; Hardin, B. E.; Rowell, M. W.; McGehee, M. D. *Mater. Today* **2007**, *10* (11), 28–33.
- (5) Shaw, P. E.; Ruseckas, A.; Samuel, I. D. W. *Adv. Mater.* **2008**, *20* (18), 3516–3520.
- (6) Coakley, K. M.; McGehee, M. D. *Chem. Mater.* **2004**, *16* (23), 4533–4542.
- (7) Shah, M.; Ganesan, V. *Macromolecules* **2010**, *43* (1), 543–552.
- (8) Segalman, R. a.; McCulloch, B.; Kirmayer, S.; Urban, J. J. *Macromolecules* **2009**, *42* (23), 9205–9216.
- (9) Darling, S. B. *Energy Environ. Sci.* **2009**, *2* (12), 1266.
- (10) Botiz, I.; Darling, S. B. *Macromolecules* **2009**, *42* (21), 8211–8217.
- (11) Bates, F. S.; Fredrickson, G. H. *Annu. Rev. Phys. Chem.* **1990**, *41* (1), 525–557.
- (12) Sinturel, C.; Bates, F. S.; Hillmyer, M. A. *ACS Macro Lett.* **2015**, *4* (9), 1044–1050.
- (13) Russell, T.; Jr, R. H.; Seeger, P. *Macromolecules* **1990**, *23* (3), 890–893.
- (14) Xu, T.; Kim, H. C.; DeRouchey, J.; Seney, C.; Levesque, C.; Martin, P.; Stafford, C. M.; Russell, T. P. *Polymer* **2001**, *42* (21), 9091–9095.
- (15) Aissou, K.; Otsuka, I.; Rochas, C.; Fort, S.; Halila, S.; Borsali, R. *Langmuir* **2011**, *27* (7), 4098–4103.
- (16) Cushen, J. D.; Otsuka, I.; Bates, C. M.; Halila, S.; Fort, S.; Rochas, C.; Easley, J. A.; Rausch, E. L.; Thio, A.; Borsali, R.; Willson, C. G.; Ellison, C. J. *ACS Nano* **2012**, *6* (4), 3424–3433.
- (17) Otsuka, I.; Isono, T.; Rochas, C.; Halila, S.; Fort, S.; Satoh, T.; Kakuchi, T.; Borsali, R. *ACS Macro Lett.* **2012**, *1* (12), 1379–1382.
- (18) Otsuka, I.; Tallegas, S.; Sakai, Y.; Rochas, C.; Halila, S.; Fort, S.; Bsiesy, A.; Baron, T.; Borsali, R. *Nanoscale* **2013**, *5* (7), 2637–2641.
- (19) Isono, T.; Otsuka, I.; Kondo, Y.; Halila, S.; Fort, S.; Rochas, C.; Satoh, T.; Borsali, R.; Kakuchi, T. *Macromolecules* **2013**, *46* (4), 1461–1469.
- (20) Togashi, D.; Otsuka, I.; Borsali, R.; Takeda, K.; Enomoto, K.; Kawaguchi, S.; Narumi, A. *Biomacromolecules* **2014**, *15* (12), 4509–4519.

# INTRODUCTION GENERAL (FR)

Au cours des dernières décennies, le photovoltaïque organique (PVO) a émergé, ouvrant un nouveau champ de recherche stimulant. Par rapport aux systèmes inorganiques classiques, le PVO présente de nombreux avantages, tels que la flexibilité mécanique, l'applicabilité pour un système d'impression "roll-to-roll" (à rouleaux), la production à faible coût, la production de masse, etc.<sup>1-4</sup> Cependant, l'efficacité démontrée de la conversion de puissance du PVO est limitée à quelques pour cent, principalement en raison de la courte durée de vie des excitons, de leur faible mobilité, et de la recombinaison des porteurs de charge. Ces insuffisances sont fortement influencées par la morphologie de la couche active et la cristallinité des matériaux  $\pi$ -conjugués utilisés. Une des approches prometteuses pour améliorer l'efficacité est de concevoir et de contrôler, à une échelle de 10-15 nm, la morphologie de la couche active qui est constituée d'un matériau donneur et d'un matériau accepteur d'électrons. Cette échelle de 10-15 nm correspond à la longueur de diffusion des excitons au sein des matériaux  $\pi$ -conjugués.<sup>5</sup> La structure lamellaire périodique, dans lequel le donneur et accepteur sont interpénétrés, est considérée comme une structure idéale parce qu'elle permet de (i) limiter la décroissance d'excitons, (ii) fournir la voie de transport de charges aux électrodes la plus courte, (iii) réduire les sites responsables de pièges, et (iv) promouvoir la séparation de charge des excitons en augmentant la surface de l'hétérojonction entre le donneur et l'accepteur d'électrons.<sup>6,7</sup>

L'auto-assemblage de copolymères à blocs  $\pi$ -conjugués a attiré une attention considérable comme une approche sûre pour obtenir une morphologie idéale pour les applications en électronique organique.<sup>8-10</sup> L'auto-assemblage de copolymères diblocs de type AB est régulée par le degré de polymérisation ( $N$ ), la fraction volumique de chaque bloc ( $\phi$ ), et le paramètre d'interaction de Flory-Huggins ( $\chi$ ) qui quantifie la force thermodynamique entraînant la séparation de phases des blocs A et B à l'échelle nanométrique. Dans le cas des copolymères flexibles, dit "coil-coil", la force de séparation des deux blocs est proportionnelle à  $\chi N$ . Ces copolymères à blocs s'auto-assemblent en diverses morphologies en fonction de  $\phi$  lorsque  $\chi N$  est supérieur à une valeur critique (10.5 lorsque  $\phi = 0.5$ ).<sup>11</sup> Par conséquent, des copolymères à blocs ayant un haut  $\chi$  et de faibles valeurs  $N$ , dits «copolymères à blocs à haut  $\chi$  – bas  $N$ »<sup>12</sup>, ont suscité un vif intérêt pour réaliser une séparation de phase à une échelle beaucoup plus petite que ce qu'il pouvait être

obtenu en utilisant des copolymères à blocs à «bas  $\chi$ », tels que le polystyrène-*bloc*-poly(méthacrylate de méthyle)<sup>13,14</sup> Dans ce but, à l'équipe de physicochimie et auto-assemblage des glycopolymères du CERMAV dirigé par R. Borsali a synthétisé une variété de copolymères à blocs glycoconjugués dont l'un des blocs est constitué d'un oligosaccharide et qui s'auto-organisent en structures shériques, cylindriques ou lamellaires de périodicité inférieure à 10 nm.<sup>15-20</sup> La forte incompatibilité (haut  $\chi$ ) entre les blocs oligosaccharidiques et synthétiques, provenant de leur hydrophobicité opposée (oligosaccharides hydrophiles et polymères synthétiques hydrophobes), est accentuée par la structure "rod" des blocs oligosaccharidiques, et est la clé pour réaliser de tels domaines nanométriques. Ce concept peut être étendu au PVO. Des dispositifs photovoltaïques ayant de hautes performances peuvent être envisagés en tirant parti de la séparation de phase à l'échelle nanométrique du nouveau semi-conducteur copolymère à bloc glycoconjugué. Une fois la nanostructure obtenue par auto-organisation du copolymère à bloc, le segment oligosaccharidique sacrificiel est enlevé et la cavité résultante sera remplacée par un accepteur d'électrons pour obtenir la structure idéale finale dans laquelle les composés donneurs et accepteurs seront alternativement organisés à une échelle inférieure à 10 nm.

Pour atteindre l'objectif mentionné ci-dessus, cette thèse s'est concentré principalement sur la synthèse de la nouvelle classe des copolymères diblocs glycoconjugués semi-conducteurs et leurs comportements d'auto-assemblage. La thèse est divisée en cinq chapitres.

Le **chapitre 1** introduit les notions et théories fondamentales pour comprendre les systèmes photovoltaïques organiques et l'auto-assemblage des copolymères à blocs.

Le **chapitre 2** détaille la synthèse et la caractérisation d'un nouveau copolymère dibloc constitué d'un polymère  $\pi$ -conjugué régiorégulier, le poly(3-hexylthiophène) (P3HT), et d'un oligosaccharide. Deux copolymères diblocs différents, à savoir les P3HT-*bloc*-maltoheptaose peracétylé (P3HT-*b*-AcMal<sub>7</sub>) et P3HT-*bloc*-maltoheptaose (P3HT-*b*-Mal<sub>7</sub>) ont été synthétisés.

Le **Chapitre 3** décrit l'étude morphologique des copolymères diblocs synthétisés. Des recuits thermiques et des recuits par vapeur de solvants, les deux méthodes les plus utilisées pour entraîner ou accélérer l'auto-organisation des copolymères à blocs, ont été employés sur le P3HT-*b*-AcMal<sub>7</sub> et le P3HT-*b*-Mal<sub>7</sub>. Leurs morphologies ont été soigneusement étudiées par microscopie à force atomique (AFM), microscopie électronique à transmission (MET), et diffusion des rayons X aux petits angles (SAXS). Dans le cas de l'auto-assemblage du P3HT-*b*-



AcMal<sub>7</sub>, un modèle d'arrangement moléculaire a également été proposé sur la base des résultats expérimentaux et de la structure cristalline théorique du P3HT.

Le **chapitre 4** porte sur l'étude des changements structuraux des copolymères à blocs glycoconjugués lors des traitements thermiques. Leur changements structuraux ont été étudiées par une méthode de chauffage *in situ* et refroidissement progressive en utilisant des mesures de spectroscopie infrarouge (IR) et diffusion des rayons X aux petits et grands angles (SAXS / WAXS).

Dans le **chapitre 5**, deux approches concrètes vers l'application PVO sont présentées. Tout d'abord, la gravure sélective à sec ou en milieu humide des domaines oligosaccharides (AcMal<sub>7</sub>) des films auto-assemblés de P3HT-*b*-AcMal<sub>7</sub> a été examinée. Puis, un nouveau matériau d'oligosaccharide conjugué avec fullerène (AcMal<sub>7</sub>-C<sub>61</sub>) a été synthétisé dans le but de contrôler la position du fullerène par rapport à celle du P3HT-*b*-AcMal<sub>7</sub>.

Le **chapitre 6** contient le détail des méthodes expérimentales utilisé dans ce travail.

## References

- (1) Nelson, J. *Mater. Today* **2011**, *14* (10), 462–470.
- (2) Heeger, A. J. *Adv. Mater.* **2014**, *26* (1), 10–28.
- (3) Huang, Y.; Kramer, E. J.; Heeger, A. J.; Bazan, G. C. *Chem. Rev.* **2014**, *114* (14), 7006–7043.
- (4) Mayer, A. C.; Scully, S. R.; Hardin, B. E.; Rowell, M. W.; McGehee, M. D. *Mater. Today* **2007**, *10* (11), 28–33.
- (5) Shaw, P. E.; Ruseckas, A.; Samuel, I. D. W. *Adv. Mater.* **2008**, *20* (18), 3516–3520.
- (6) Coakley, K. M.; McGehee, M. D. *Chem. Mater.* **2004**, *16* (23), 4533–4542.
- (7) Shah, M.; Ganesan, V. *Macromolecules* **2010**, *43* (1), 543–552.
- (8) Segalman, R. a.; McCulloch, B.; Kirmayer, S.; Urban, J. J. *Macromolecules* **2009**, *42* (23), 9205–9216.
- (9) Darling, S. B. *Energy Environ. Sci.* **2009**, *2* (12), 1266.
- (10) Botiz, I.; Darling, S. B. *Macromolecules* **2009**, *42* (21), 8211–8217.
- (11) Bates, F. S.; Fredrickson, G. H. *Annu. Rev. Phys. Chem.* **1990**, *41* (1), 525–557.
- (12) Sinturel, C.; Bates, F. S.; Hillmyer, M. A. *ACS Macro Lett.* **2015**, *4* (9), 1044–1050.
- (13) Russell, T.; Jr, R. H.; Seeger, P. *Macromolecules* **1990**, *23* (3), 890–893.
- (14) Xu, T.; Kim, H. C.; DeRouchey, J.; Seney, C.; Levesque, C.; Martin, P.; Stafford, C. M.; Russell, T. P. *Polymer* **2001**, *42* (21), 9091–9095.
- (15) Aissou, K.; Otsuka, I.; Rochas, C.; Fort, S.; Halila, S.; Borsali, R. *Langmuir* **2011**, *27* (7), 4098–4103.
- (16) Cushen, J. D.; Otsuka, I.; Bates, C. M.; Halila, S.; Fort, S.; Rochas, C.; Easley, J. A.; Rausch, E. L.; Thio, A.; Borsali, R.; Willson, C. G.; Ellison, C. J. *ACS Nano* **2012**, *6* (4), 3424–3433.
- (17) Otsuka, I.; Isono, T.; Rochas, C.; Halila, S.; Fort, S.; Satoh, T.; Kakuchi, T.; Borsali, R. *ACS Macro Lett.* **2012**, *1* (12), 1379–1382.
- (18) Otsuka, I.; Tallegas, S.; Sakai, Y.; Rochas, C.; Halila, S.; Fort, S.; Bsiesy, A.; Baron, T.; Borsali, R. *Nanoscale* **2013**, *5* (7), 2637–2641.
- (19) Isono, T.; Otsuka, I.; Kondo, Y.; Halila, S.; Fort, S.; Rochas, C.; Satoh, T.; Borsali, R.; Kakuchi, T. *Macromolecules* **2013**, *46* (4), 1461–1469.
- (20) Togashi, D.; Otsuka, I.; Borsali, R.; Takeda, K.; Enomoto, K.; Kawaguchi, S.; Narumi, A. *Biomacromolecules* **2014**, *15* (12), 4509–4519.



## **CHAPTER I:**

# **BACKGROUND AND REVIEW OF LITERATURES**

## I.1 Organic photovoltaic cells

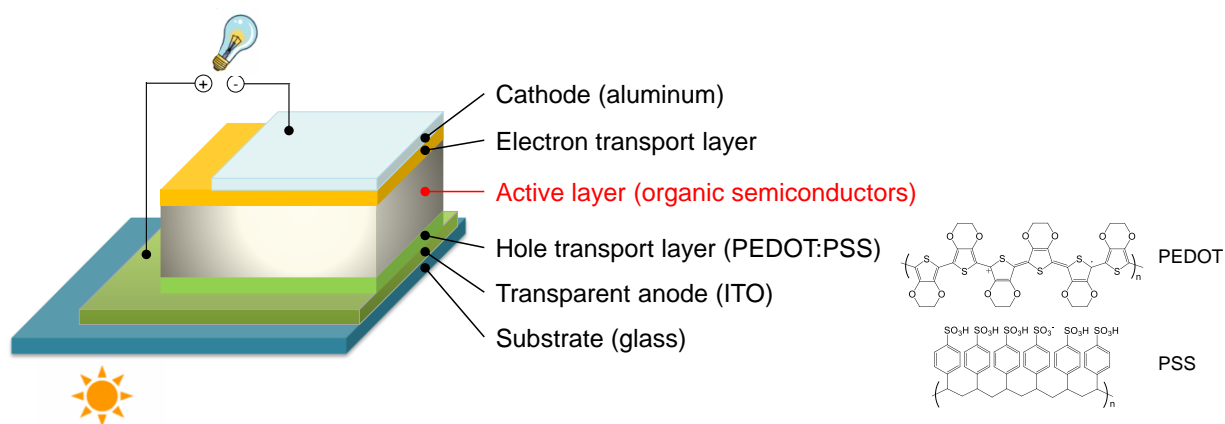
The continuous economic development and growth of human population demand much more additional energy supply year after year. In modern society, the primary sources of our energy are provided from fossil fuels such as petroleum, coal, and natural gas. Given that these resources are finite and produce a large amount of greenhouse effect gases, alternative energy technologies based on renewable energy resources are expected. Solar energy is one of the most abundant and clean energies on planet. Therefore the photovoltaic technology, which enables harness sunlight by converting the solar energy into usable electric energy, has attracted growing interest as a key solution to realize a sustainable society. Today, the most conventional solar cells are based on inorganic crystalline silicon. Power conversion efficiency of the silicon-based solar cells now reached up to 25 %. Despite significant improvement in efficiencies over the past decades, this technology still suffers from a trade-off between efficiency and cost. Expensive manufacturing cost and material cost itself inhibit widespread use of inorganic solar systems.

Organic thin film solar cells have emerged as a promising next-generation solar cell system to meet the global demand toward low-cost renewable energy sources. Organic photovoltaic cells are a class of photovoltaic that use organic semiconducting materials as a photoelectric conversion layer. Compared to conventional inorganic solar cells, organic solar cells are particularly attractive due to their solution-based processability, low production cost, mechanical flexibility, light weight, and semi-transparency. The use of organic materials enables a large-scale device production onto flexible substrate via cost-effective fabrication process such as roll-to-roll, screen, and inkjet printing techniques.<sup>1-9</sup> In addition, it is advantageous that the organic materials can be tuned their chemical, physical, and electric properties according to the need through chemical modification, resulting in unlimited possibilities. These attractive advantages of the organic photovoltaic cells make them very intriguing technologies by opening up new market opportunities (*e.g.* portable, wearable, and foldable devices) which have never realized by using the existing photovoltaic technologies. Although the performance of the organic photovoltaic cells has increased steadily and reached near 11.7 %, <sup>10</sup> efficiency limitation and long-term reliability remain issues to be addressed for the commercialization of this technology. Hence, the organic photovoltaic is an ongoing area of research.

### I.1.1 Principles of energy generation process

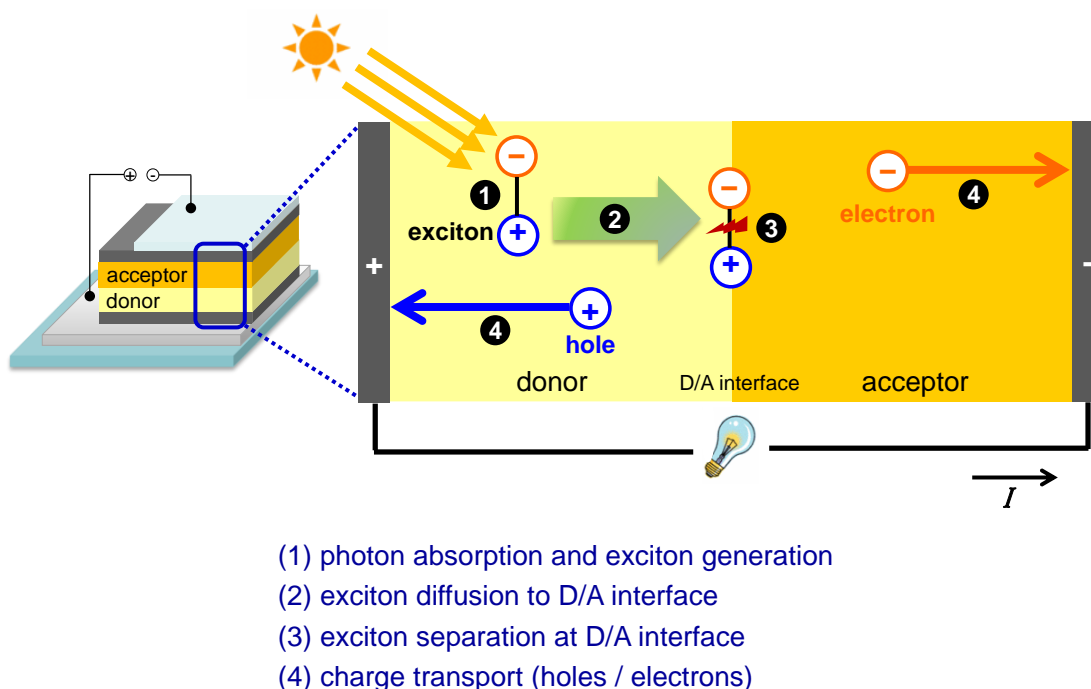
One of the major differences between organic and inorganic semiconductors is charge carriers. Whereas inorganic semiconductors generate free electrons and holes upon irradiation of light, organic semiconductors produce a tightly bound electron-hole pair, so-called exciton. A relatively low dielectric constant of organic materials results in a strong Coulomb force between the electron and the hole, thus, a strong driving force such as electric field is required to separate exciton into two free charge carriers.

The conventional architecture of an organic thin film solar cell is shown in Figure 1.1. The device has a sandwich configuration in which a photoelectric conversion layer (active layer) is placed between two different electrodes, typically indium-tin oxide (ITO) and low work function metal such as aluminum and magnesium, and calcium. The ITO, which is a transparent conductive electrode with high work function, plays the role of collecting charge carriers (holes) as well as taking in external light.



**Figure 1.1** Schematic image of typical device architecture of an organic solar cell.

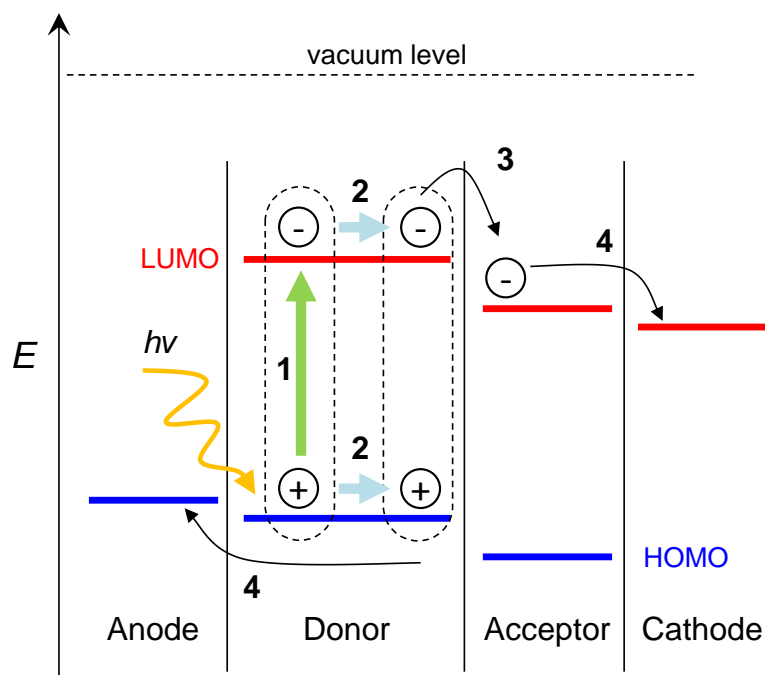
The photoelectric conversion process in organic solar cells is schematically illustrated in Figure 1.2. It can be described by the following four steps. When the OPV device is exposed to the light, the donor material absorbs a photon and generates an exciton (bound electron-hole pair) (step1: exciton generation). Then exciton diffuse to the interface of donor and acceptor materials (step2: exciton diffusion). At the donor-acceptor interface the electron is transferred from donor to acceptor while the positively charged hole remains in the donor material (step3: exciton dissociation). Finally the generated free charge carriers are transported through the donor (hole-transporting material) and acceptor (electron transporting material) to the appropriate electrodes (step 4: charge transport). In this way, the incident photons can be converted into practical electronic power.



**Figure 1.2** Schematic illustration of charge generation mechanism in organic solar cells.

The photoelectric conversion mechanism can be also explained by using an energy diagram as shown in Figure 1.3. Upon absorption of a photon in the donor material, an electron is excited from the highest occupied molecular orbital (HOMO) to the lowest unoccupied molecular orbital (LUMO) and the generated exciton migrates to the donor-acceptor interface. At the interface, the internal electric field arising from the energetic mismatch of the molecular orbitals and difference

in work function of the anode and cathode provide a driving force to split the exciton into free charge carriers. It is reported that the higher HOMO-LUMO gap between the LUMO of acceptor compound and HOMO of donor compound tends to provide higher open-circuit voltage ( $V_{oc}$ ). However, if the LUMO level of acceptor compound is too close to the LUMO level of donor compound, it prevents efficient exciton dissociation.

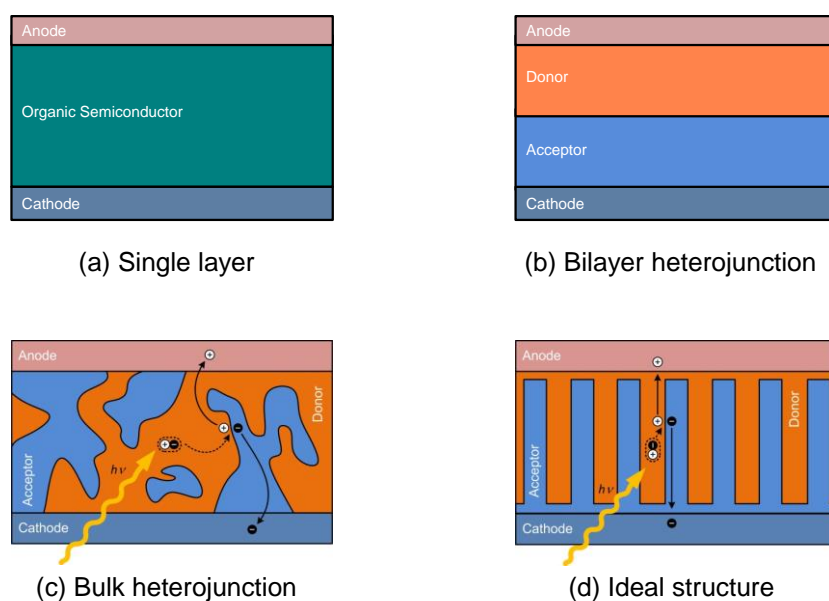


**Figure 1.3** Energy diagram of organic solar cell.



### I.1.2 History and development of active layer architectures

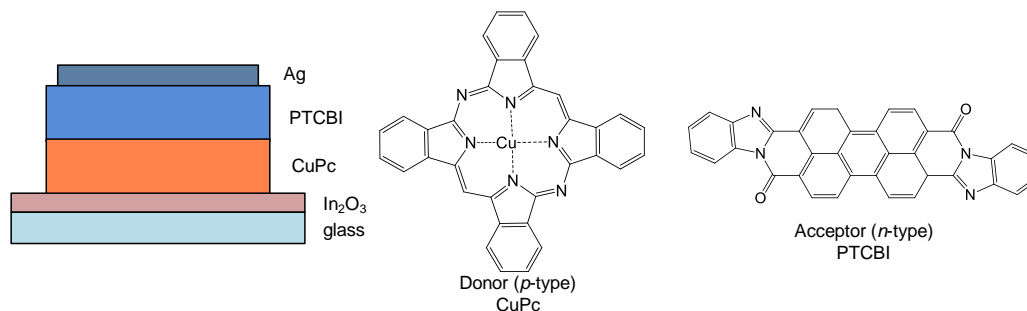
In the early organic solar cells, the device structure was based on a single organic semiconductor layer sandwiched between two different electrodes (Figure 1.4a). Although the difference in work function between two electrodes provides an electric field, this electric field was not sufficient to separate the photogenerated excitons efficiently because of a high exciton binding energy in the organic semiconductor. Therefore, power conversion efficiency has been limited below 0.1%.



**Figure 1.4** Active layer morphologies of organic thin film solar cells.

A first breakthrough was made by C. W. Tang in 1986.<sup>11</sup> He first introduced bilayer concept, in which *p*-type and *n*-type organic semiconductor layers were interposed between the two electrodes (Figure 1.4b and 1.5). Copper phthalocyanine (CuPc) and perylene tetracarboxylic bisimide derivatives (PTCBI) were used as donor and acceptor compounds, respectively. Power conversion efficiency greatly increased up to *ca.* 1%. However, the efficiency of the bilayer heterojunction was still limited due to the exciton diffusion length (5-20 nm). The excitons generated away from the donor-acceptor interface more than exciton diffusion length cannot

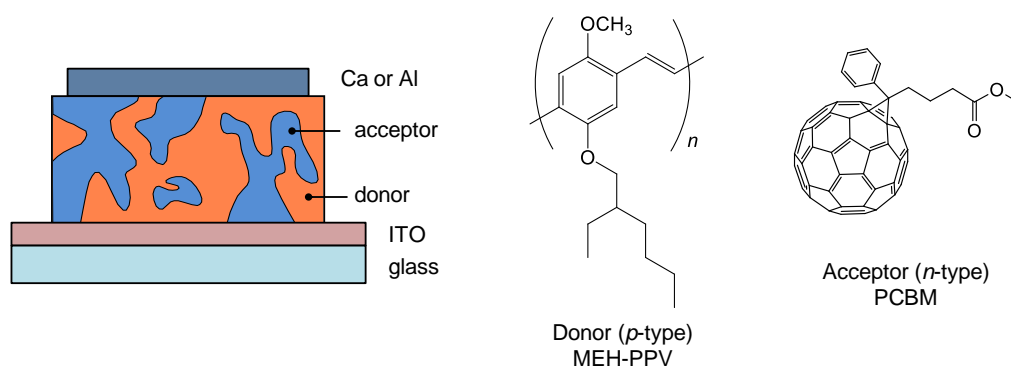
contribute to the photoelectric conversion but they will recombine by emitting a photon or decay before reaching to the interface.



**Figure 1.5** Structure of the first reported bilayer heterojunction organic solar cell in 1986.<sup>11</sup>

In 1992, Sariciftci *et al.* first showed an evidence of potential application of the buckminsterfullerene (C<sub>60</sub>) for acceptor by demonstrating the ultrafast photoinduced electron transfer from *p*-type conducting polymer to fullerene.<sup>12</sup> The time scale for charge transfer is sub-picosecond that is more than 10<sup>3</sup> times faster than the decay time of exciton. However, low solubility of the pristine fullerene in most of organic solvents has limited high concentration dissolution of the fullerene, thus, efficiencies remained below 1 %. After Wudl *et al.* reported soluble fullerene derivatives such as phenyl-C<sub>61</sub>-butyric acid methyl ester (PCBM),<sup>13</sup> next breakthrough came in 1995. A revolutionary development in organic solar cells was achieved by Yu and Heeger *et al.* by using a blend system consisting of organic donor compound of poly(2-methoxy-5-(2'-ethyl-hexyloxy)-1,4-phenylene vinylene) (MEH-PPV) and soluble fullerene derivatives, in which a bicontinuous network of donor and acceptor is created, so-called bulk heterojunction (Figure 1.4c and 1.6).<sup>14</sup> External power conversion efficiency (EPCE) reached up to 1.5 %. The significant improvement in the efficiency of bulk heterojunction device is attributed to a much larger donor-acceptor interface compared with bilayer heterojunction, which eventually leads efficient dissociation of excitons. The use of soluble fullerene derivatives enabled homogeneous blends and the optimization of the blend ratio of the donor and acceptor.

Since the early report of solar cells based on single layer, the field of polymer-fullerene solar cells has undergone a fast and dynamic development. Currently, one of the well-established state-of-the-art in organic photovoltaics is the bulk heterojunction solar cells based on the blend of poly(3-hexylthiophene) (P3HT) and fullerene derivatives where the reported efficiencies are about 5-6 %. Owing to a large number of extensive studies, it can be said that the EPCE of this prototype has reached almost the limit. To improve efficiency further toward 10 %, another innovative breakthrough is needed.



**Figure 1.6** Bulk heterojunction organic solar cell reported by Yu and Heeger *et al.* in 1995.<sup>14</sup>

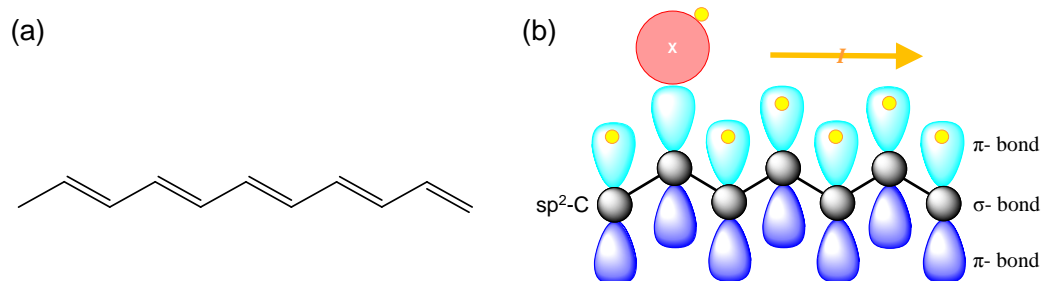
In the polymer-fullerene blend, a precise control of the blend morphology with good reproducibility is still challenging because the active layer is prepared via solution processing. As described above, a large interfacial area and small domain size between donor and acceptor compounds are favorable to enhance the dissociation of excitons, but if both compounds are too finely dispersed in the active layer with uncontrolled manner, it eventually prevent the charge carriers from reaching the electrodes without recombination. This inevitable trade-off cannot be solved by current bulk heterojunction active layer.

A periodic lamellar structure in which the electron donor and acceptor compounds are mutually interpenetrating as shown in Figure 1.4d is considered to be an ideal structure because this structure makes it possible to (i) suppress the exciton decay, (ii) provide the shortest charge transportation pathway, (iii) reduce charge trap sites, and (iv) promote charge separation of excitons by enlarging the interface contact area.

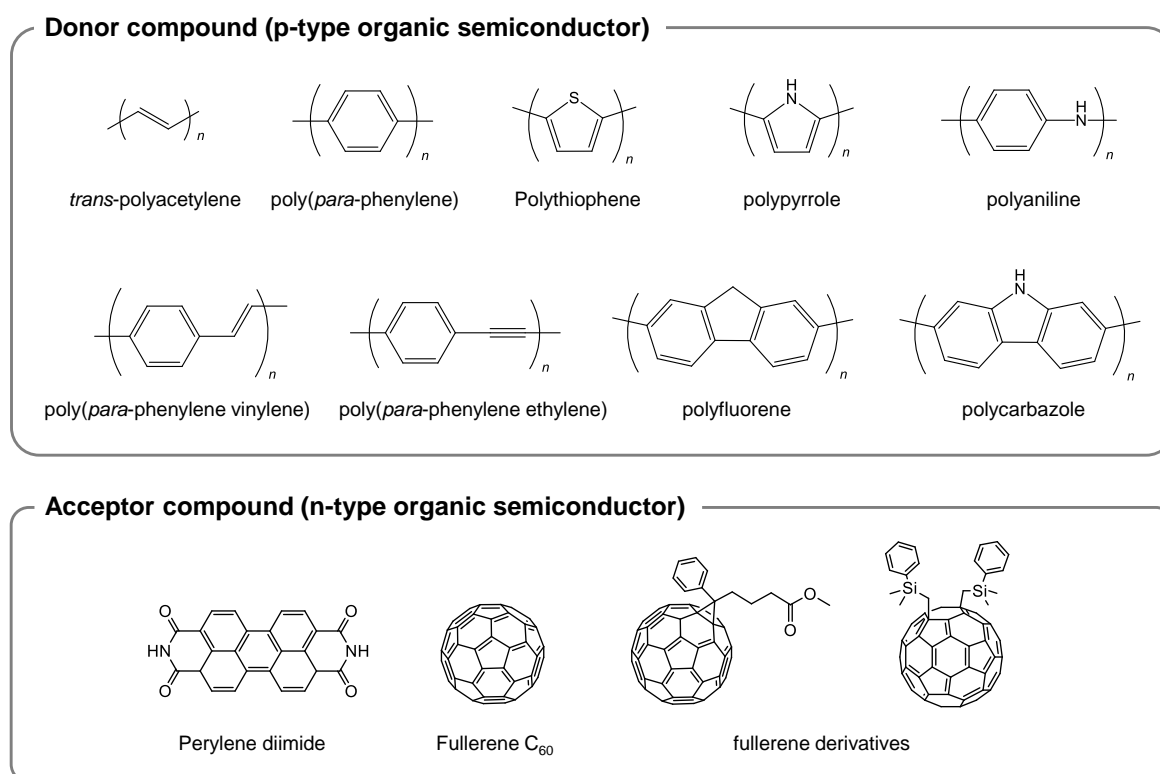
## I.2 Organic semiconductor compounds

In general, organic compounds are regarded as insulators because they do not have free electrons like metals. But some organic compounds exhibit electronic properties similar to inorganic conductors owing to their distinctive structure. In 1977, Shirakawa *et al.* has first reported that polyacetylene demonstrated conductivity about  $10^3 \text{ Scm}^{-1}$  by doping with  $\text{I}_2$ .<sup>15</sup> The polyacetylene, which is the simplest conjugated polymer consisting of long chain carbon skeleton with alternating single and double bonds based on  $\text{sp}^2$ -hybridized carbon atoms, shows high electrical conductivity upon doping owing to a highly delocalized  $\pi$ -conjugated system with large electronic polarizability (Figure 1.7). Since then, intensive research has been devoted in the field of organic conducting polymers. Organic semiconductor can be divided into *p*-type and *n*-type on the basis of the main charge carriers. The *p*-type organic semiconductors transport holes as a dominant charge carrier. The  $\pi$ -conjugated polymers based on aromatic rings play the leading role in the development of *p*-type materials due to their processability, thermal stability, and ease of chemical modifications. The energy levels of these polymers can be tuned by various molecular design strategies. Some of the principal families of *p*-type organic materials are presented in Figure 1.8. On the other hand, in case of the *n*-type organic semiconductors which transport electrons as a dominant charge carrier, there are not many choices compared with *p*-type materials. Perylene diimide derivatives and fullerene derivatives are some of the few examples of *n*-type materials (Figure 1.8).

This section describes a brief description of two organic semiconductors used for this thesis, that is, poly (3-hexylthiophene) (P3HT) (*p*-type) and phenyl- $\text{C}_{61}$ -butyric acid methyl ester ( $\text{PC}_{61}\text{BM}$ ) (*n*-type). The first subsection provides an overview of the chemistry of P3HT as well with particular emphasis on the synthetic strategies for polymerization of regioregular P3HT and end-functionalization of P3HT which are some of the principal part of this thesis.



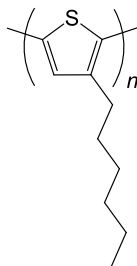
**Figure 1.7** (a) Chemical structure of polyacetylene and (b) schematic image of charge carrier formation by doping.



**Figure 1.8** Chemical structures of common organic semiconductors.

### I. 2.1 Poly(3-hexylthiophene) (P3HT)

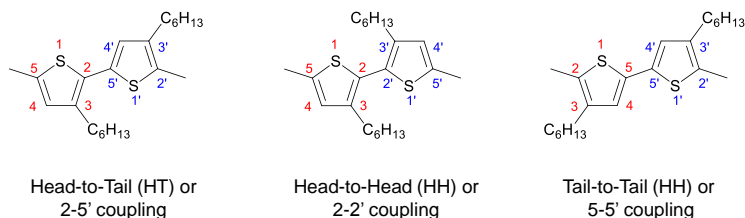
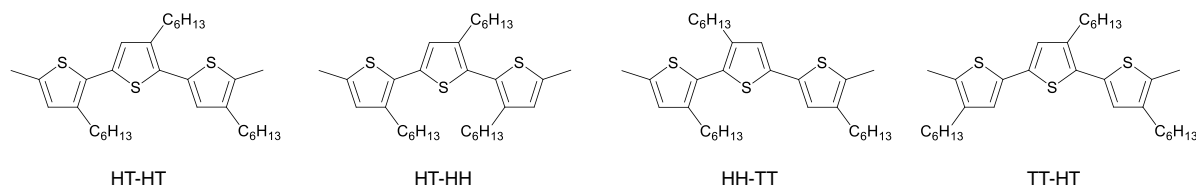
Poly(3-alkylthiophene)s (P3AT)s are one of the most important representative  $\pi$ -conjugated polymers used as electron-donating compounds (*p*-type organic semiconductor) in the organic electronics. Among them, poly(3-hexylthiophene) (P3HT) has attracted considerable attention due to its excellent characteristics such as solution processability, thermal and environmental stability, synthetic versatility, and electronic properties, etc.<sup>16,17</sup> Nowadays, a combination of P3HT and phenyl-C<sub>61</sub>-butyric acid methyl ester (PC<sub>61</sub>BM) is one of the most widely studied blend systems for the active layer of organic thin-film solar cells.



**Figure 1.9** Chemical structure of poly(3-hexylthiophene).

#### I.2.1-1 Regioregularity

It has been demonstrated in the literature that the optoelectronic properties of the P3HT including hole mobility, band gap, and UV absorption range, that are crucial characteristics for the optoelectronic applications, are strongly influenced by regioregularity of the polymer.<sup>18–20</sup> The regiochemistry of P3HT can be represented as shown in Figure 1.10. Since a monomer unit of 3-hexylthiophene has an asymmetric chemical structure, when two monomers are coupled between 2- and 5- positions, it leads to the following three dyad configurations; head-to-tail (HT), head-to-head (HH) and tail-to-tail (TT) couplings. Besides, these dyads can combine each other to generate four triad regioisomers, *i.e.* HT-HT, HT-HH, HH-TT, and TT-HT. In the case where the coupling reaction proceeds in an uncontrolled manner, resulting polythiophene includes all regioisomeric linkages. This sequence is referred to as a regiorandom or regiorregular P3HT. On

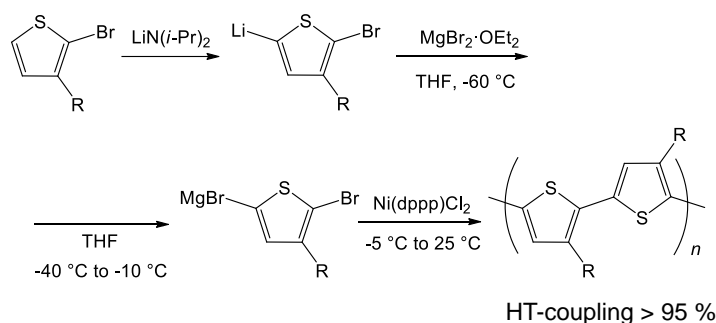
dyadtriad**Figure 1.10** Regiochemistry of P3HT isomers.

the other hands, the regioregular P3HT contains almost exclusivity HT linkage. Consequently, a low energy coplanar conformation with highly  $\pi$ -conjugated sequence can be obtained. Other linkages are considered as defects, because they induce distortion in the polymer backbone due to steric repulsion and deteriorate the effective conjugation length. The regioregularity plays an important role in the improvement of crystallinity, molecular packing and charge transport property. Therefore, a considerable number of studies have been conducted on the synthesis of the HT-coupled regioregular P3HT over the past decade. Currently, the Grignard metathesis (GRIM) method described below is the most commonly employed method for the synthesis of regioregular P3HT.

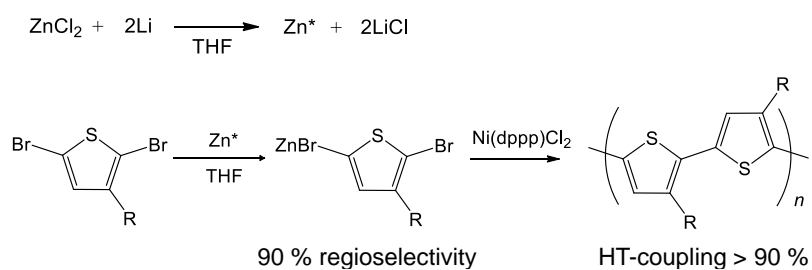
### I.2.1-2 Synthesis of regioregular P3HT

In 1992, the synthesis of regioregular P3AT was first reported by McCullough *et al.*<sup>21</sup> In this method, 2-bromo-5-bromomagnesio-3-alkylthiophene monomers, which are prepared via lithiation and transmetallation of 2-bromo-3-hexylthiophene monomer, are polymerized with Ni catalyst; [1,2-bis(diphenylphosphino)propane] dichloronickel(II) (Ni(dppp)Cl<sub>2</sub>). The reaction proceeds via Kumada cross-coupling<sup>22</sup> and provides a P3AT with 95-100 % HT-coupled regioregularity (Scheme 1.1a). Shortly thereafter, Rieke *et al.* also reported the synthesis of regioregular P3HT by using Ni-catalyzed cross-coupling reaction similar to the McCullough method except for the preparation of reactive monomer.<sup>23</sup> In this method, 2,5-dibromo-3-hexylthiophene was reacted with highly reactive Rieke zinc (Zn\*), which prepared by a reduction of anhydrous metal with an alkali metal,<sup>24</sup> to give the polymerizable organozinc monomer with 90 % regioselectivity. Accordingly, the polymerization with Ni catalyst results in well-defined P3HT with high regioregularity (Scheme 1.1b). Whereas the both method provide regioregular P3ATs, the need of delicate operations like temperature control (cryogenic temperature) and preparation of highly reactive Rieke metal have limited a large-scale production.

(a) McCullough method



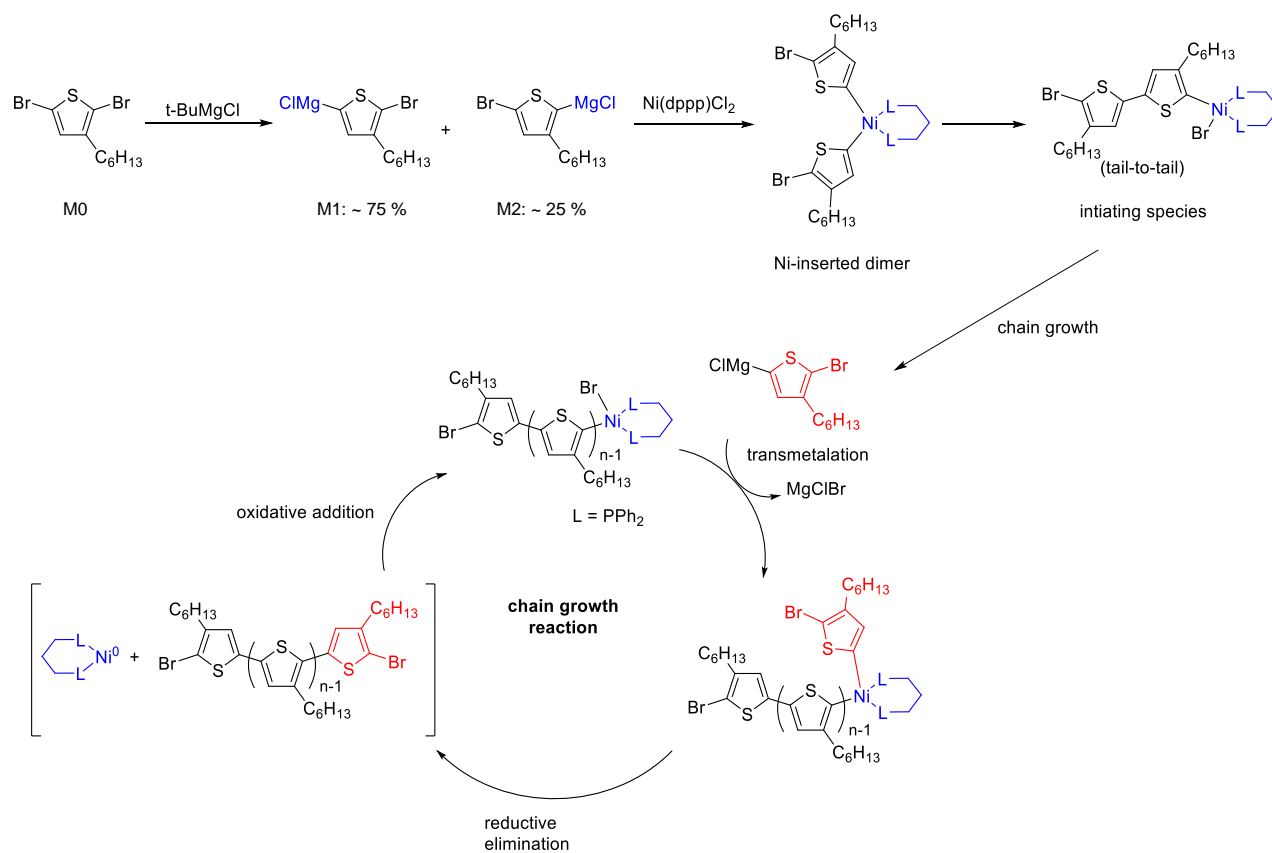
(b) Rieke method



**Scheme 1.1** Synthesis of regioregular poly(3-alkylthiophene-2,5-diyl)s via (a) McCullough method and (b) Rieke method.



In 1999, McCullough *et al.* developed the Grignard metathesis (GRIM) polymerization (Scheme 1.2),<sup>25,26</sup> followed by the improvement by Yokozawa *et al.*<sup>27</sup> One of the most important improvements of this method compared to the earlier ones is that neither cryogenic temperature nor highly reactive metal is required. Whole polymerization process including an active Grignard monomer formation proceeds in a one-pot at room temperature. In this method, 2,5-dibromo-3-hexylthiophene is employed as starting material to generate active Grignard monomer via halogen-metal exchange reaction with *t*-butyl magnesium chloride. Due to the absent of chemical selectivity of the two bromine substituted monomer precursor, two regioisomers of the active Grignard monomer (monomer M1 and M2) are generated with a ratio of *ca.* M1: M2 = 75 : 25. Upon addition of Ni catalyst, first, nickel-inserted dimer is formed with tail-to-tail conformation. Then, chain growth reaction proceeds via multiple cycles of transmetalation, reductive elimination, and intramolecular oxidative addition while forming mainly a head-to-head sequence. During the chain growth reaction, regioisomer M1 is exclusively incorporated into the polymer chain whereas the more sterically hindered M2 is not consumed. As a result, the P3HT with a high HT regioregularity can be obtained. Nowadays the GRIM polymerization is the most commonly utilized versatile method for synthesizing regioregular P3ATs with well-defined molecular weight and narrow dispersity.



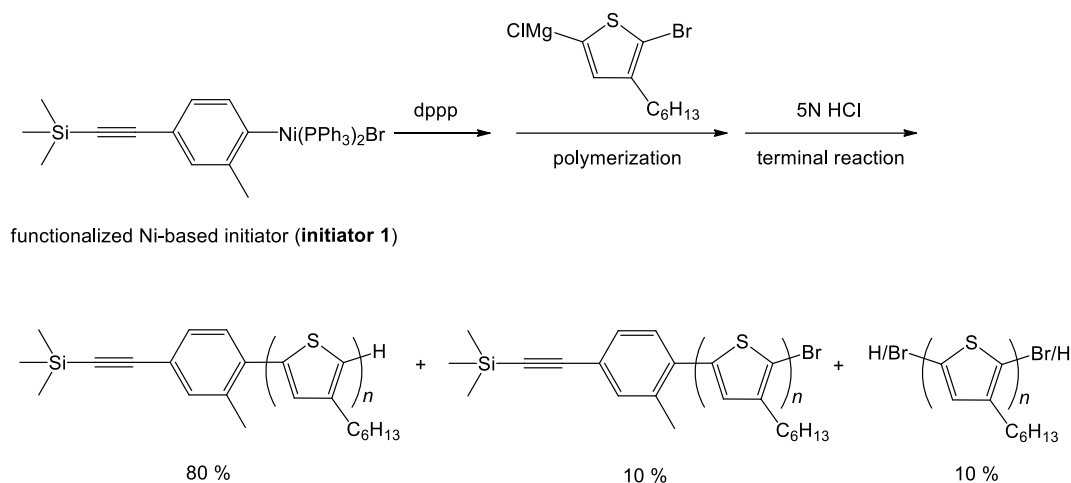
**Scheme 1.2** Synthesis of regioregular (HT-HT > 99 %) poly(3-hexylthiophene-2,5-diyl) via the GRIM polymerization.

### I.2.1-3 End functionalization of P3HT using the GRIM method

Owing to the development of the GRIM polymerization method, it became possible to synthesize end-functionalized regioregular P3ATs. These polymers have triggered intense interest in designing novel polymeric architectures, multifunctional polymers, and hybrid materials including block copolymer. Therefore a precise control of end composition and functionality of P3ATs is one of the important tasks. There are mainly three synthetic strategies for preparation of end-functionalized regioregular P3HTs; (i) use of functionalized Ni-based initiators, (ii) post-polymerization modification, and (iii) *in situ* functionalization. Each strategy has some advantages and disadvantages.

#### (i) use of functionalized Ni-based initiators

In this strategy, specially prepared Ni-catalyst bearing a functional group is used as an external initiator instead of Ni(dppp)Cl<sub>2</sub> to introduce a desired functional group at the  $\alpha$ -chain end of the polymer. Koeckelberghs *et al.* reported the synthesis of functionalized Ni catalysts and their successful use in synthesizing of regioregular P3ATs with different end-functional groups.<sup>28</sup> For example, they prepared a Ni-based initiator equipped with a trimethylsilyl ethynyl group (**initiator 1**) and employed it for the P3HT polymerization as an initiator (Scheme 1.3). As a results, the P3HT having a functional group corresponding to the chemical structure of the **initiator 1** was successfully obtained without decomposition of **initiator 1** with 90 % purity. The remaining 10 % was determined as P3HT having proton and/or bromine at both chain-ends, indicating that polymerization was not initiated from **initiator 1** but initiated from residual Ni<sup>2+</sup> salts contaminated in the **initiator 1** as impurities. Although this approach is considered as useful and straightforward way for preparing a wide variety of end-functionalized conjugated polymers, the impurities and instability of the Ni-based external initiators can be obstacles for the precise control of end-functionality. Since a new initiator must be synthesized for each desired functionalization, this synthetic route is not that common.



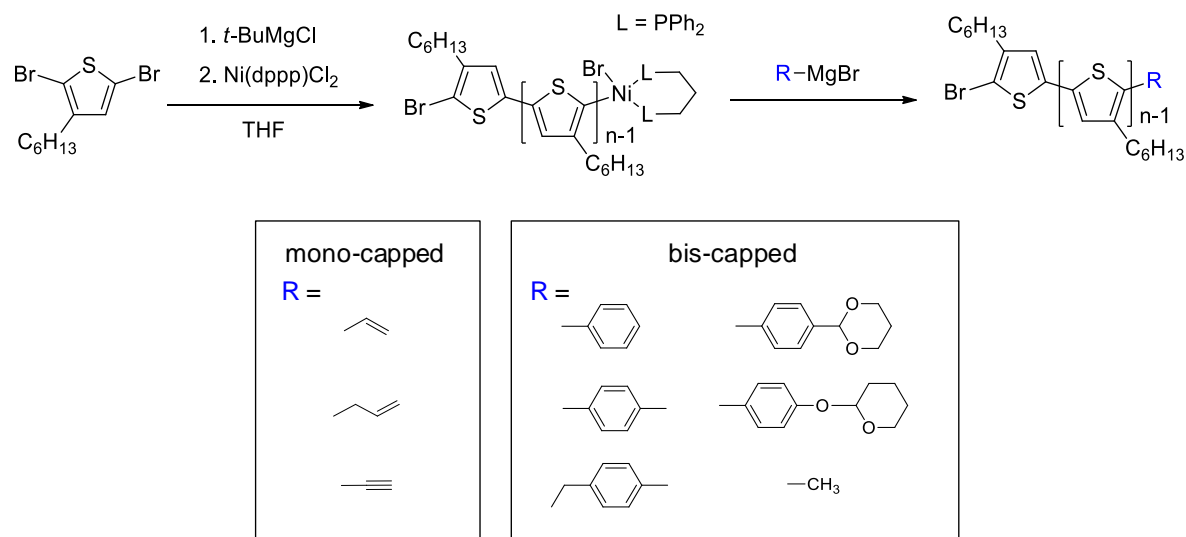
**Scheme 1.3** Synthesis of P3HT initiated from ethynyl-functionalized Ni-based initiator.

(ii) post-polymerization modification

Generally, the P3ATs polymerized via GRIM method have a bromo group at  $\alpha$ -chain end when the reaction is quenched by hydrochloric acid. Therefore, a selective and quantitative introduction of functional groups onto the  $\alpha$ -end of the polymer is possible by substituting the bromine to desired functional group after polymerization. So far a variety of P3AT having different end-structures has been synthesized via Suzuki-Miyaura coupling, Stille coupling, Sonogashira coupling, and so on.<sup>29–33</sup> Although this approach is versatile, the final product often contains non-functionalized polymer as a minor product. It is because that a small amount of polymer having no bromine at both chain ends can be formed during the termination reaction with hydrochloric acid. In addition, requirements of multiple reaction steps and specific coupling reagents must also be considered when the synthetic strategy will be envisioned.

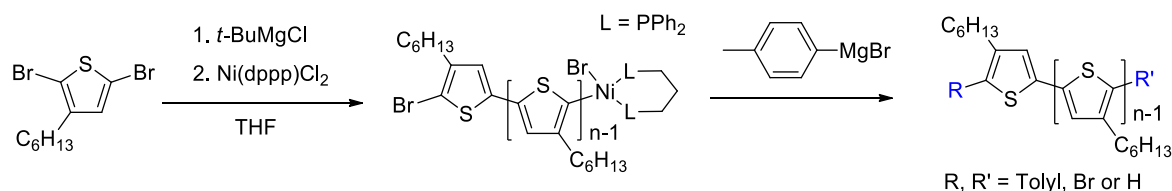
(iii) *in situ* functionalization

Owing to the "living" nature of the GRIM polymerization, the functionalization to the polymer chain-end is possible by adding a second Grignard reagent bearing functional group during the terminal reaction step. This versatile and facile method allows the introduction of a variety of different terminal functional groups to the P3HT. However, a composition of terminal groups and the degree of end-functionalization are significantly influenced by a nature of the Grignard reagents used for quenching. McCullough *et al.* first reported the synthesis of end-functionalized regioregular P3HT via this *in situ* functionalization approach by using different types of Grignard reagents, such as aryl, alkyl, allyl, vinyl, and so on, and observed that unsaturated Grignard reagents had a trend to yield mono-functionalized polymers whereas others provided mainly bis-functional polymers (Scheme 1.4).<sup>19</sup> It is proposed that unsaturated Grignard reagent could stabilize the Ni catalyst by forming a stable  $\pi$ -complex with  $\text{Ni}^0$  and prevent the oxidative addition of  $\text{Ni}^0$  to the  $\alpha$ -chain end. However, the resulting products were often afforded as a mixture of mono-, bis-, and non-functionalized polymers.



**Scheme 1.4** Synthesis of end-functionalized P3HT via *in situ* end-capping strategy. A below figure shows classification of the Grignard reagents which tend to afford mono- or bis-capped P3HT as the major product.

Based on above fact, Pickel *et al.* recently demonstrated an extended strategy by utilizing the stabilizing effect of the unsaturated bonds to control the end-functionality. The authors showed that the addition of olefins (1-pentene, styrene) prior to addition of Grignard reagent could stabilize Ni catalyst.<sup>34</sup> In addition, they described the effect of temperature and another chemical additive of LiCl on the end-functionality. Whereas LiCl has been known as a reagent which increase the rate of metal-halogen exchange reaction of 2,5-dibromo-3-hexylthiophene and the yield of the metathesis polymerization, they revealed that LiCl plays a role to suppress the formation of the bis-functional product as well. For instant, when the functionalization with tolyl-magnesium bromide was done at 0°C in the presence of both LiCl and styrene, yield of the mono-capped P3HT significantly increased from 11 % to 72 % (Scheme 1.5). While this approach allowed better end group control, it is still difficult to completely restrain the formation of bis-functionalized polymer.



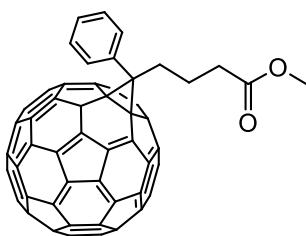
additive	LiCl	temperature	mono-capped	bis-capped	non-capped
			%	%	%
-	-	r.t.	11	85	4
1-pentene	-	r.t.	31	60	9
1-pentene	Yes	r.t.	44	42	14
1-pentene	Yes	0 °C	52	27	21
styrene	Yes	0 °C	72	20	8

**Scheme 1.5** Effect of the unsaturated additive, LiCl, and temperature on the end-group composition of tolyl-magnesium bromide quenched P3HT reported by Pickel *et al.*<sup>34</sup>

In this thesis, two synthetic strategies; (ii) post-polymerization modification method and (iii) *in situ* end-functionalization method, were employed to prepare mono-functionalized P3HTs with "clickable" alkyne group as building blocks for the synthesis of block copolymers.

## I. 2.2 Fullerene and fullerene derivatives

Generally, many of  $\pi$ -conjugated polymers having a planar structure are electron donating materials because they readily undergo oxidation. On the other hand, organic compounds with a high electron affinity are much rare. Buckminsterfullerene  $C_{60}$  is a one of the good electron acceptor compound with a variety of interesting chemical and physical properties. The fullerene can reversibly accept up to six electrons<sup>35</sup> owing to its triply-degenerate low-lying LUMO (1.5-2.0 eV). It is known that polymer-fullerene blends exhibit a remarkably fast photoinduced electron transfer from  $\pi$ -conjugated polymer to fullerene whereas a back electron transfer (charge recombination) is much slower.<sup>12,36,37</sup> This electronically interesting characteristic is derived from an unique spherical structure of fullerene consisted of sixty chemically equivalent carbons. The fullerene can delocalize an accepted electron over the entire molecule and results in a metastable charge-separated state. In addition, the spherical structure is thought to be advantageous for the formation of crystalline domain of fullerene, which is favorable to charge transport, by segregating from another electron donating polymer domain due to a large difference in molecular shape (in most cases, donor compounds are planar molecule). For above reasons, the fullerene is considered as one of the most reasonable acceptors for organic solar cells. However, since pristine fullerene exhibits very poor solubility in most of the commonly used organic solvents, the application of fullerene in optoelectronic devices has been limited. Therefore, various substituents have been introduced onto fullerene to improve solubility. Among those solution processable fullerene derivatives, phenyl- $C_{61}$ -butyric acid methyl ester (PC<sub>61</sub>BM) is at present the most extensively studied and commonly used electron accepting compound.



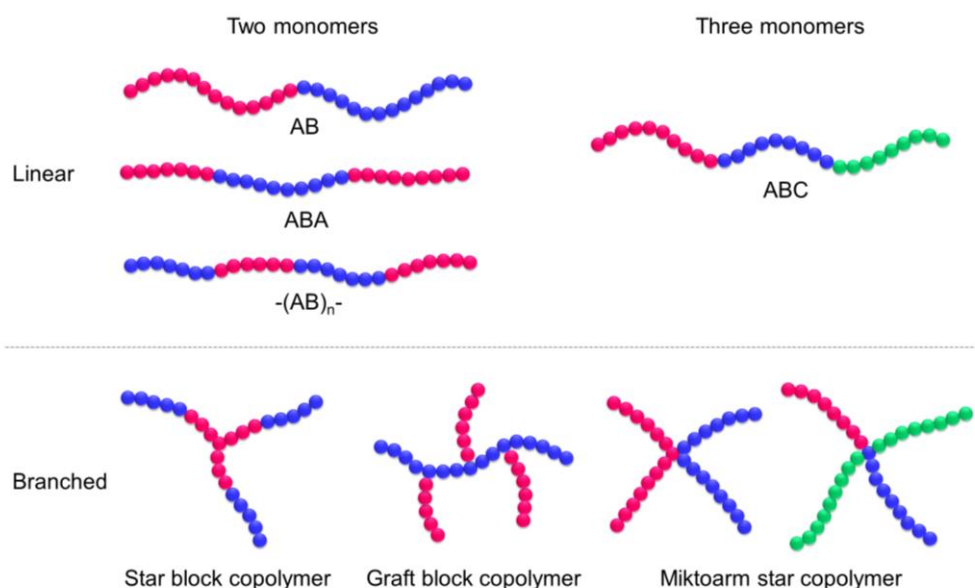
**Figure 1.11** Chemical structure of phenyl- $C_{61}$ -butyric acid methyl ester (PC<sub>61</sub>BM).

### I.3 Block copolymers

To date, the self-assembly nature of block copolymers has attracted considerable attention as one of the promising bottom-up strategies for controlling an active layer morphology at the nanometer scale. This section outlines the self-assembly behavior of block copolymers in the solid-state and gives a brief review of carbohydrate-containing block copolymers and semiconducting block copolymers that have been specifically designed for optoelectronic applications.

#### I.3.1 Self-assembly of block copolymers

Block copolymers are a specific class of copolymer well-known for their ability to self-assemble into a variety of periodic structures at micro-, meso-, or nanometer length scale. The block copolymers consist of two or more chemically distinct polymeric blocks that are covalently tethered each other. Depending on the number of monomer types and molecular architectures, almost limitless number of block copolymers can be configured as shown in Figure 1.12. Among them, phase behavior of AB diblock copolymers, *i.e.* the simplest configuration, has been most widely studied from theoretical and experimental point of views.<sup>38–42</sup>



**Figure 1.12** Schematic illustrations of different types of block copolymer architectures.



## Coil-coil diblock copolymers

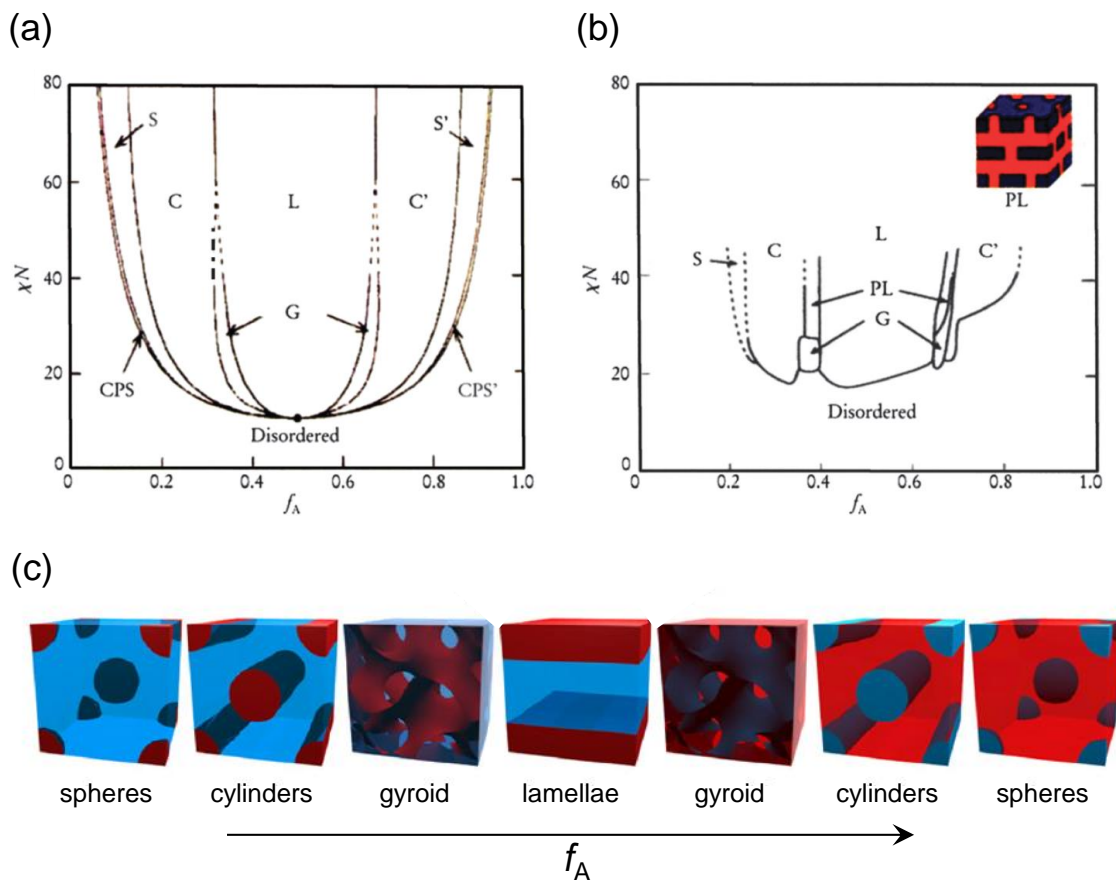
The microphase separation of AB type of diblock copolymers is driven by chemical incompatibility between A and B blocks. As immiscible polymer blends which are not covalently connected exhibit a macroscopic phase separation, A and B blocks of the diblock copolymer also tend to segregate. However, the covalent linkage of block copolymer inhibits such macrophase separation and leads to diverse periodic nano-structures, such as spheres, cylinders, lamellae, and bicontinuous gyroids, *etc.* (Figure 1.13c)<sup>43</sup> depending on the counterbalance of interfacial energy between A and B domains, elastic free energy of polymer chains, and bending elastic energy associated with the interfacial curvature of block copolymers.

The phase behavior of diblock copolymer can be parameterized by three experimentally controllable factors: (i) the volume fractions of each block,  $f_A$  and  $f_B$  ( $f_A + f_B = 1$ ), (ii) the total degree of polymerization,  $N$  ( $N = N_A + N_B$ ), and (iii) Flory-Huggins interaction parameter,  $\chi$  which represents the degree of incompatibility between A and B blocks. The first two factors can be adjusted through synthetic conditions and the  $\chi$  parameter is determined by the combination of A-B blocks.<sup>44</sup> Figure 1.13a and 1.13b show a theoretical phase diagram of diblock copolymer predicted by the self-consistent mean-field theory and an experimental phase diagram of model diblock copolymer, polystyrene-*block*-polyisoprene (PS-*b*-PI), respectively.<sup>44</sup> These diagrams bear a very close resemblance. These diagrams indicate that microphase separation can occur when the  $\chi N$  exceeds critical value of order-to-disorder transition. The critical  $\chi N$  for the symmetric diblock copolymer (*i.e.*  $f_A = f_B = 0.5$ ) is predicted as 10.5. The  $\chi$  parameter is generally inversely proportional to temperature as expressed by following formula;

$$\chi = \frac{z}{2k_B T} (2\varepsilon_{AB} - \varepsilon_{AA} - \varepsilon_{BB})$$

where  $z$  is the number of nearest neighbor monomers per repeat unit in the polymer,  $k_B$  is the Boltzman constant,  $\varepsilon_{AB}$ ,  $\varepsilon_{AA}$ , and  $\varepsilon_{BB}$  are interaction energies per monomer unit between A-B, A-A, and B-B monomers, respectively. Thus, it should be noted that the phase behavior of block copolymers is strongly affected by the temperature as well. An increase in the temperature would cause a disordered structure at the low  $\chi N$  regime, since the  $\chi$  parameter decreases in accordance with the temperature.

The microdomain size of  $D$  can be theoretically described with the degree of polymerization  $N$  depending on the magnitude of the segregation. In the strong segregation limit (SSL) where the  $\chi N$  is sufficiently large ( $\chi N \gg 10$ ), the domain size is given as  $D \propto \chi^{1/6} N^{2/3}$ . This 2/3 power law has been verified experimentally using model block copolymer systems such as polystyrene-*block*-isoprene by several research groups.<sup>40,45–48</sup> In the weak segregation limit (WSL) where the  $\chi N$  is in the vicinity of order-to-disorder transition ( $\chi N \approx 10$ ), the  $D$  scales as the dimension of a random coil,  $D \propto N^{1/2}$ .



**Figure 1.13** (a) Theoretical phase diagram of AB diblock copolymer in the weak segregation limit predicted by the self-consistent mean-field theory, depending on volume fraction of A block ( $f_A$ ) and the product of  $\chi N$ , where  $\chi$  is the Flory-Huggins interaction parameter and  $N$  is the total degree of polymerization: S, S', CPS, and CPS' = spheres, C and C' = cylinders, G = gyroid, and L = lamellae.<sup>44</sup> (b) Experimental phase diagram of polyisoprene-*block*-polystyrene, where represents the volume fraction of polyisoprene.<sup>44</sup> (c) Schematic image of equilibrium morphologies of AB diblock copolymers.<sup>43</sup>

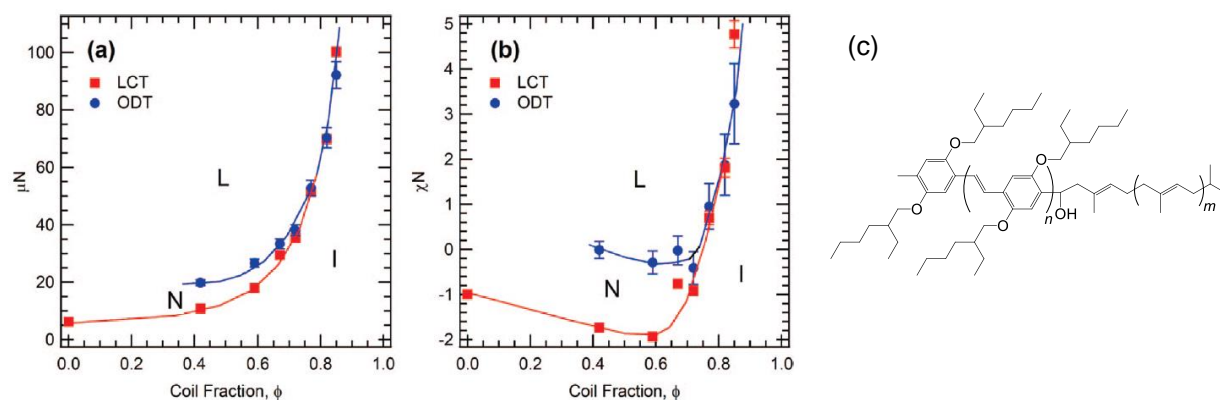
Nowadays, downsizing of the microphase-separated domains is a very attractive topic especially in the field of microelectronics industry. Given the facts that there is a minimum value of  $\chi N$  necessary to maintain the microphase separation ( $\chi N > 10.5$ ), to make the domain size as small as possible (*i.e.* low  $N$  value), the high  $\chi$  value that is high enough to compensate for the drop in  $N$  value is required. To this end, we have developed a new class of carbohydrate containing "natural-synthetic" hybrid block copolymer systems ("high  $\chi$ -low  $N$ " system<sup>49</sup>) and achieved sub-10 nm scale features size. The description about recent results of our research concerning the "high  $\chi$ -low  $N$ " block copolymer system will be presented in the next section (Chapter I.3.2).

## Rod-coil block copolymers

If one of the coil blocks is replaced by a  $\pi$ -conjugated semiconducting polymer (rigid block) for the purpose of photovoltaic applications to which this thesis aims, the phase behavior of this class of *rod-coil* block polymers is more complicated than classical coil-coil block copolymer system because strong rod-rod interactions such as  $\pi$ - $\pi$  interaction will be introduced.

To describe the equilibrium phase behavior of rod-coil block copolymers, two additional parameters, the Maier-Saupé interaction ( $\mu N$ ) and the conformation asymmetry ( $\varepsilon$ ), should be taken into account in addition to Flory-Huggins interaction  $\chi N$  and the volume fraction of the segments  $f$ .<sup>50-55</sup> The Maier-Saupé interaction  $\mu N$  represents the strength of rod-rod interaction (liquid crystalline interactions). The geometrical asymmetry  $\varepsilon$ , defined as a ratio of the radius of gyration of the coil and the rod length, has been introduced to describe the influence of the topological disparity between the rod and coil segments on the phase separation behavior. Since the both rod and coil blocks are covalently linked each other they must share the same interfacial area even though their occupied volumes are very different. Such size mismatch can create an internal frustration and may have significant impact on the curvature of the equilibrium microphase structure. These two additional parameters  $\mu N$  and  $\varepsilon$  often affect the microphase boundaries. The self-assembly behavior of rod-coil block copolymers have been investigated from experimental and theoretical perspectives by several research groups.<sup>50,52,56-58</sup> For instance, Segalman *et al.* performed a series of studies on a weakly segregated model system, poly(2,5-di(2'-ethylhexyloxy)-1,4-phenylenevinylene-*block*-isoprene (PPV-*b*-PI), and provided a phase diagram of conjugated rod-coil block copolymer as shown in Figure 1.14.<sup>54,55,59,60</sup> This phase

diagram shows qualitative difference from that of classical coil-coil block copolymer system as we previously seen in Figure 1.13a.



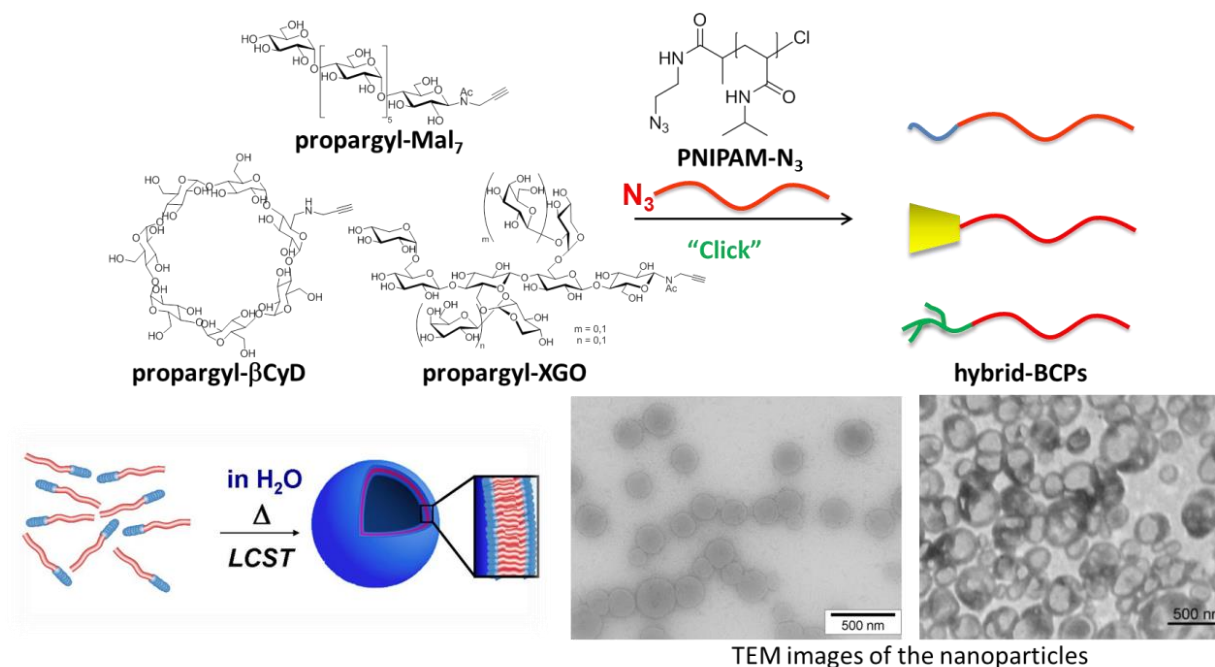
**Figure 1.14** Phase diagram for weakly segregated PPV-*b*-PI block copolymer system. (a) Maier-Saupé interaction  $\mu N$  vs volume fraction of coil segment and (b) Flory-Huggins interaction  $\chi N$  vs volume fraction of coil segment. (c) Chemical structure of PPV-*b*-PI.<sup>55</sup>

### I.3.2 Carbohydrate containing block copolymers

There have been numerous studies on the self-assembly of block copolymers consisting of petroleum-based synthetic polymers so far. In recent years, the next generation of block copolymers, which are partially composed of natural biomacromolecules, has attracted growing interest due to their potential applications in multidisciplinary fields, such as nanoparticles for molecular deliveries, biosensors, surface modifications, lithographic masks etc. Poly/oligo-saccharides (carbohydrates) are, among other natural resources, one of the most abundant raw materials obtained from “biomass” that show biodegradability, biocompatibility, and biorecognition property. However, the number of studies on the poly/oligo-saccharide-based block copolymers is still much less than that on the fully petroleum-based block copolymers because of some difficulties in the synthesis, such as arduous tasks for the functionalization of saccharides, incompatibility between the synthetic and saccharidic polymer blocks, and laborious purification steps.

In the early 1960s, Ceresa have first demonstrated a synthesis of block copolymers containing carbohydrates (cellulose derivatives and starch) by using mechanical rupture of the polysaccharides chain to generated free radicals that initiated the copolymerization with polymerizable monomer.<sup>61</sup> Since this pioneer research, a variety of synthetic strategies to prepare carbohydrate containing block copolymers have been developed.<sup>62–67</sup> A comprehensive review on the synthesis and application of polysaccharide-containing block copolymers is available.<sup>68</sup>

Because of the amphiphilic nature of the poly/oligo-saccharide-based hybrid block copolymers, recent work highlights their ability to self-assemble into nanoparticles in the solution-state, namely glyconanoparticles, with a variety of morphologies (spherical micelles, cylinder micelles, polymersomes, etc.). For instance, our research group reported a number of self-assemblies of carbohydrate-based block copolymers such as polystyrene- $\beta$ -cyclodextrin,<sup>69</sup> poly(*N*-isopropylacrylamide)-*block*-oligosaccharides (Figure 1.15),<sup>70</sup> maltoheptaose-*block*-peracetylated maltoheptaose,<sup>71</sup> polystyrene-*block*-maltoheptaose,<sup>72</sup> poly(methylmetacrylate)-*block*-maltoheptaose,<sup>73,74</sup> and polycaprolactone-*block*-xyloglucan,<sup>75</sup> etc.

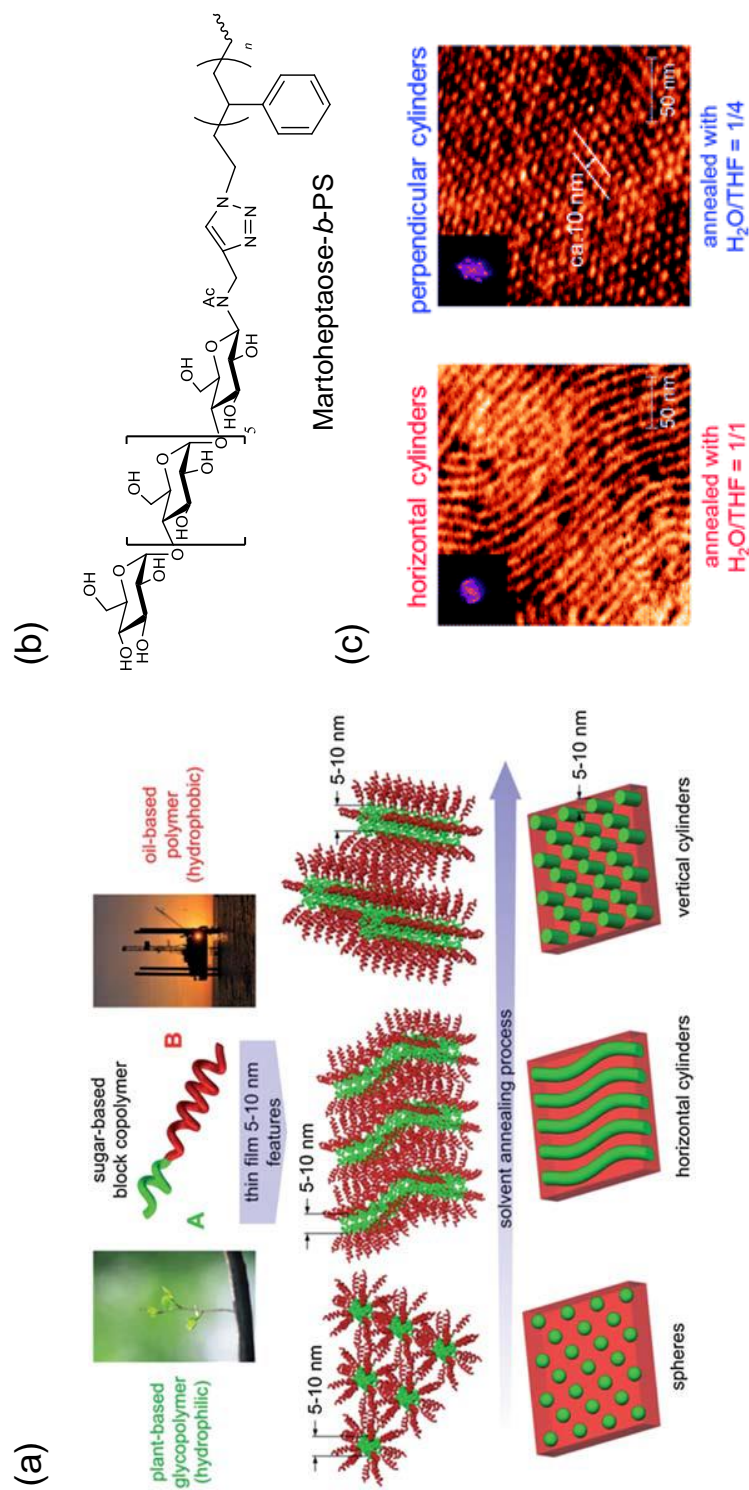


**Figure 1.15** Schematic representation of the thermoresponsive self-assembly of PNIPAM-*b*-oligosaccharides.<sup>70</sup>

It is only recently that the self-assemblies of the poly/oligo-saccharides-based “hybrid” block copolymers were investigated in the thin film state. Because of the contrasting characters between the natural poly-/oligosaccharidic blocks and the synthetic polymer blocks, these hybrid block copolymers should have much higher  $\chi$  parameter than the petroleum derived conventional block copolymers. This remarkable nature of these hybrid block copolymers will lead to form less than 10 nm scale periodically ordered nanostructures, which is below the current limit of the patterning obtained from the petroleum derived block copolymer systems to date. To this end, our group have first demonstrated that the novel hybrid block copolymers consisting of oligosaccharides and polystyrene having small  $N$  (less than kDa) can self-organize into well-ordered periodic structures with 10 nm scale domain spacing due to their high  $\chi$  parameter between natural oligosaccharidic block and synthetic polystyrene block.<sup>76</sup> Indeed, this high  $\chi$  parameter is due to the hydrophobicity/hydrophilicity imbalance which is further enhanced sterically by the rod-like nature of the oligosaccharide blocks, as compared to coil-coil block copolymer systems made from petroleum. After this pioneering study, a variety of poly-/oligosaccharide-based block copolymers were synthesized and self-organized into various

periodic phases in sub-10 nm scale in our group and others. Figure 1.16 presents one of the representative studies on the self-assembly of the poly/oligo-saccharide-based block copolymer system. In this study, it has been demonstrated facile method to control the orientation of the periodic nanostructure derived from phase separation of the oligosaccharide-containing hybrid block copolymer by simply varying composition of annealing co-solvents.<sup>77</sup> The thin films of the block copolymer, maltoheptaose-*block*-polystyrene (Mal<sub>7</sub>-*b*-PS), were annealed under vapor produced from mixtures of THF and water with different weight fractions. When the thin films annealed with pure water (Mal<sub>7</sub>-selective solvent) and THF (PS-selective solvent) showed poorly ordered spherical morphologies due to trapped micelles and reverse micelles, respectively. Annealing the films under vapors from the mixture of THF and water led well-ordered hexagonally-packed cylindrical (Hex) morphologies. Notably, perpendicular orientation of the cylinders relative to the substrate was obtained when the film was annealed with the mixture of THF and water with similar weight fraction of PS and Mal<sub>7</sub> blocks. Under this atmosphere, both Mal<sub>7</sub> and PS blocks should migrate equally to the polymer-vapor interface, resulting in the Hex domain oriented perpendicular to the surface. On the other hand, annealing with the mixture with lower weight fraction of THF than the weight fraction of PS block in the block copolymer showed horizontally oriented cylinders, because Mal<sub>7</sub> blocks prefer to migrate to the polymer-vapor interface more than PS blocks.

Although several types of carbohydrate-containing block copolymers have been developed, the application of these self-organized systems for photovoltaic has yet to be attempted. This thesis is intended to control the active layer morphology via self-assembly of the block copolymer. Since small domain size properly matched with the exciton diffusion length (5-20 nm) is required for the organic photovoltaics, the used of the "high  $\chi$ -low  $N$ " block copolymer systems should be of particular interest for not only control the morphology but also reduce in domain size.

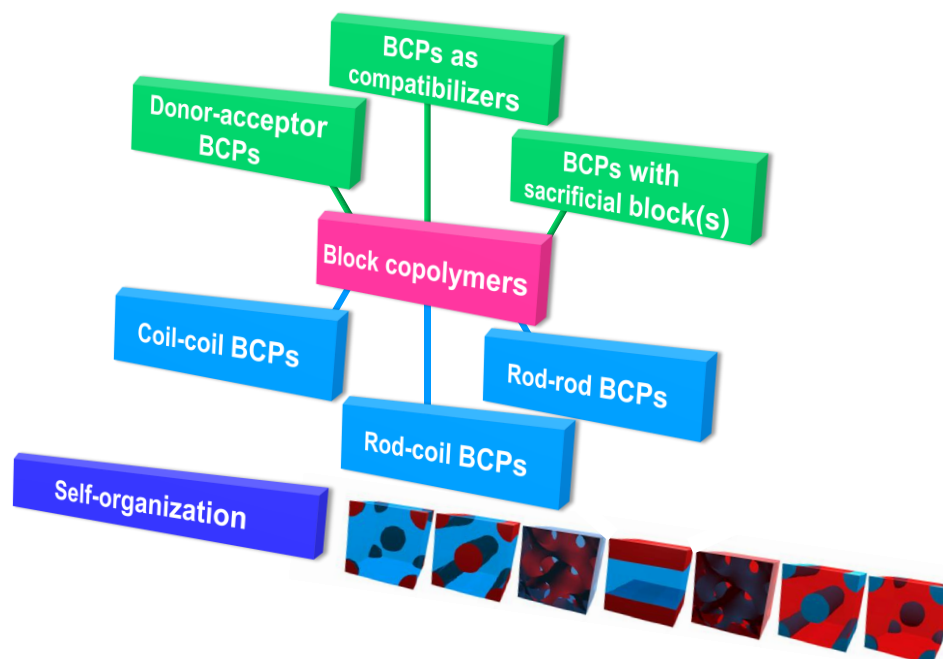


**Figure 1.16** (a) Schematic representation of sugar-based block copolymer thin film fabrication with 5-10 nm features. (b) Chemical structure of maltoheptaose-*block*-polystyrene (Mal<sub>7</sub>-*b*-PS). (c) AFM images of Mal<sub>7</sub>-*b*-PS thin films; control of horizontal and perpendicular 10 nm cylinders by varying the composition of annealing co-solvents.<sup>77</sup>



### I.3.3 Block copolymers for organic photovoltaics

Many reviews on the topic of block copolymers for the optoelectronic applications have been reported by several authors.<sup>78–83</sup> A wide variety of block copolymers in terms of types of  $\pi$ -conjugated blocks, molecular architectures, and granted functions have been synthesized and used for different purposes. Brief classification of these block copolymers is given in Figure 1.17.

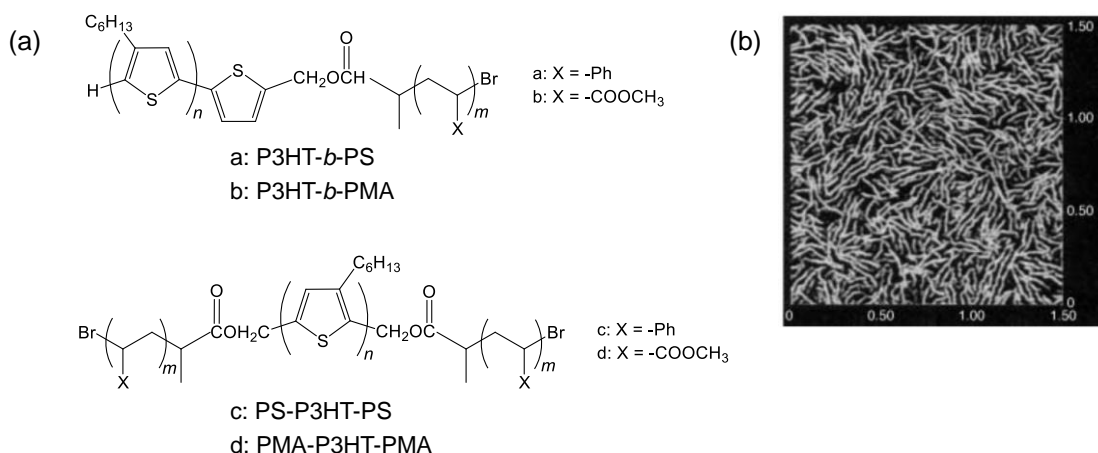


**Figure 1.17** Classification of block copolymers (BCPs) on the basis of their structure and role in photovoltaic applications.<sup>83</sup>

### P3HT-containing block copolymers

P3HT is one of the most attractive candidates as an electrically active block due to its excellent electrical properties, established polymerization method (Chapter I.2.1-2) and the existence of various synthetic routes for preparing block copolymers (Chapter I.2.1-3). A variety of studies on the synthesis and characterization of block copolymers containing P3HT has been reported so far. The first synthesis of the P3HT-based rod-coil block copolymers was reported by McCullough *et al.*<sup>84</sup> A-B and A-B-A type of di- and tri-block copolymers consisting of P3HT (as B block) and polystyrene or poly(methyl acrylate) (as A block) were successfully synthesized via atom transfer

polymerization (ATRP) of A blocks from end-functionalized P3HT-based ATRP macro-initiators (Figure 1.18a and BCP1 in Table 1.1). The synthesized block copolymers displayed nanowire morphology as shown in Figure 1.18b.



**Figure 1.18** (a) Chemical structure of the first reported P3HT-based block copolymers and (b) AFM phase image of the “nanowire” morphology in P3HT-*b*-PS thin film casted from toluene.<sup>84</sup>

Other than the above, numerous P3HT-based block copolymers have been reported, such as P3HT-*b*-Poly(methyl methacrylate) (BCP2 in Table 1.1),<sup>85</sup> P3HT-*b*-poly(acrylic acid) (BCP3),<sup>86,87</sup> P3HT-*b*-polyisoprene (BCP4),<sup>88</sup> P3HT-*b*-polylactide (BCP5),<sup>89,90</sup> P3HT-*b*-poly(4-vinylpyridine) (BCP6),<sup>91</sup> , P3HT-*b*-poly(ethylene oxide) (BCP7),<sup>92</sup> 4-vinyltriphenylamine (PVTPA) containing triblock copolymer, *i.e.* PVTPA-*b*-P3HT-*b*-PVTPA (BCP8),<sup>93</sup> P3HT-*b*-poly(9,9-dioctylfluorene) (BCP9),<sup>94</sup> and so on. However, most of them exhibited solely nanofibril morphology, which is often found for the P3HT homopolymer, irrespective of the volume fraction of the each blocks. In the block copolymer systems having crystalline segment as one block, like P3HT-containing block copolymers, the ultimate morphology is determined by the competition between crystallization and phase separation. Thus, the nanofibril morphologies observed in the above-mentioned reports indicates that the structure formation of these block copolymers were entirely dictated by the strong crystallization of P3HT segment. To direct the counterbalance between crystallization and phase separation toward the phase separation, the use

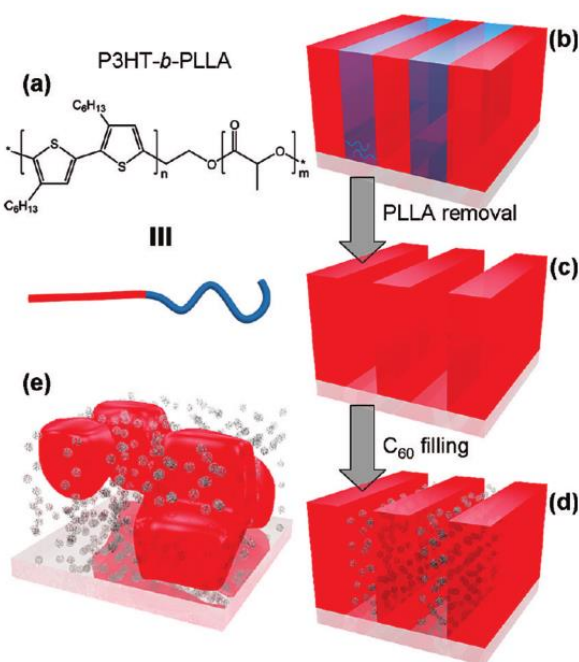
of appropriate block copolymer system having sufficiently high segregation strength (high  $\chi$ ) or suppression of the  $\pi$ - $\pi$  interaction of the P3HT main chains are thought as reasonable approaches.

In this context, several research groups have attempted chemical modifications of alkyl side-chain of the P3AT to reduce its rod-rod interaction and some of them have successfully demonstrated a variety of phase-separated structures other than the nanofibril morphology (representative works are presented in the Table 1.1 (BCP10-12)).<sup>95-99</sup> For instance, Segalman *et al.* reported that poly(3-(2'-ethyl)-hexylthiophene)-*block*-polylactide (P3EHT-*b*-PLA) (BCP 11) bearing a bulkier branched alkyl side chain could self-organize into various periodic phase-separated structures including lamellae and cylinders depending on the volume fraction of the P3EHT.<sup>96</sup> This enriched phase behavior was attributed to the introduction of a branch to the side chain accompanying by a decrease of crystallization temperature of P3EHT (weakening rod-rod interaction). Whereas the reported P3EHT-*b*-PLA block copolymers retained the good charge transport property comparable to the P3HT homopolymer, the low thermal stability of the block copolymers (melting point: P3HT ( $\approx 220$  °C)  $\gg$  P3EHT-*b*-PLA ( $\approx 90$  °C)) is not considered to be suitable for photovoltaic applications.

In this regard, the P3HT serves still desirable candidate as one block of the semiconducting block copolymers designed for organic electronic applications due to its balanced properties including high charge carrier mobility, proper band gap, good solubility, and thermal stability *etc.* However, to the best of my knowledge, there are only a few reports on the self-assembly of the P3HT-based block copolymers showing the well-ordered phase separated structures probably due to the strong rod-rod interaction of the P3HT (BCP 13-16).<sup>100-105</sup>

Finally, two early works which have demonstrated the elegant way to prepare the nano-patterned P3AT networks via selective decomposition of the sacrificial block should be presented. This strategy is analogous to the concept of this thesis. First example was reported by Hillmyer *et al.*<sup>89</sup> In this work, Poly(3-dodecylthiophene)-*b*-polylactide (P3DDT-*b*-PLA) (BCP5) block copolymer, in which the PLA segment is biodegradable and can be easily decomposed by chemical etching, were synthesized and used as a structure-directing agent. Upon etching of the PLA block with alkaline solution, a nanoporous structure made of P3DDT was obtained although a microphase-separated periodic structure has not been attained with this block copolymer system ( $M_{n,P3DDT} = 12,500$  kg/mol,  $f_{PLA} = 0.12-0.17$ ). Later on, Botiz and Darling<sup>106</sup> demonstrated the nano

patterning of the active materials by using a commercially available P3HT-*b*-poly(*L*-lactide) block copolymer ( $M_{n,P3HT} = 3300$ ,  $M_{n,PLLA} = 4100$ ) via similar method as Hillmyer *et al.* (Figure 1.19). This block copolymer showed lamellar structure and after selective removal of PLLA block, the ordered nanostructure composed of only P3HT was obtained. Then, active material fullerene hydroxide ( $C_{60}(OH)_{22-26}$ ) was filled in the empty space by dip-coating. Although these pioneer works has demonstrated the validity of this approach, no comprehensive study on the phase behavior of the block copolymers, crystal state of the  $\pi$ -conjugated block confined in the microdomains, and electronic properties that are crucial factors for the photovoltaic applications has been conducted.



**Figure 1.19** (a) Chemical structure of poly(3-hexylthiophene)-*block*-poly(*L*-lactide) (P3HT-*b*-PLLA) and its schematic representation. The procedure for the preparation of donor-acceptor nanostructures; (b) ordering of the P3HT-*b*-PLLA, (c) selective removal of PLLA, and (d) backfilling with  $C_{60}$  hydroxide. (e) The random structure consisted of P3HT and  $C_{60}$  without ordering.<sup>106</sup>

**Table 1.1** P3AT-based block copolymers reported in literature

	chemical structure		synthetic pathway <sup>a</sup>	morphology	ref.
BCP1	<p>a: X = -Ph b: X = -COOCH<sub>3</sub></p>	P3HT- <i>b</i> -PS P3HT- <i>b</i> -PMA	(1) P3HT-based macroinitiator (method ii) (2) ATRP	nanofiber	78
BCP2		P3HT- <i>b</i> -PMMA	(1) P3HT-based macroinitiator (method ii & iii) (2) ATRP	nanofiber	79
BCP3		P3HT- <i>b</i> -PAA	(1) P3HT-based macroinitiator (method ii & iii) (2) ATRP	nanofiber	80, 81
BCP4		P3HT- <i>b</i> -PI	(1) P3HT-based macroinitiator (method ii & iii) (2) NMP	nanofiber	82
BCP5	<p>R = C<sub>6</sub>H<sub>13</sub> or C<sub>12</sub>H<sub>25</sub></p>	P3HT- <i>b</i> -PLA P3DDT- <i>b</i> -PLA	(1) P3HT-based macroinitiator (method ii & iii) (2) ROP of D,L-lactide	—	83, 84
BCP6		P3HT- <i>b</i> -P4VP	(1) Alkyne-functionalized P3HT (method iii) (2) Synthesis of P3HT-based macroinitiator via Click reaction followed by NMP of 4-vinylpyridine	nanofiber	85
BCP7		P3HT- <i>b</i> -PEO	(1) Alkyne-functionalized P3HT (method iii) (2) Click reaction with azido-functionalized PEO	nanofiber	86
BCP8	<p>PVTPA-<i>b</i>-P3HT-<i>b</i>-PVTPA</p>		(1) 1,1-diphenylethylene-capped P3HT (method iii) (2) Coupling reaction with living anionic PVTPA	nanofiber	87
BCP9		P3HT- <i>b</i> -PF	(1) Alkyne-functionalized P3HT (method iii) (2) Click reaction with azido-functionalized PF	nanofiber	88

Table 1.1 (continue)

	chemical structure	synthetic pathway <sup>a</sup>	morphology	ref.
BCP10		(1) P3DDT macroinitiator (method ii) (2) Anionic coupling reaction with living PMMA	fibril, lamellae, cylinder, sphere	91, 93
BCP11		(1) OH-capped P3EHT macroinitiator (method ii) (2) ROP of D,L-lactide	fibril, lamellae ( $d = 29-40$ nm), cylinder ( $d = 19-25$ nm), micelle ( $d = 52$ nm)	90
BCP12		(1) Alkyne-functionalized P3HT (method iii) (2) Click reaction with azido-functionalized PEO	lamellae, gyroid (melt)	92
BCP13		(1) Azide-functionalized hexyl chain containing P3HT (GRIM) (2) Click reaction with alkyne-terminated P2VP	fibril ( $L = 12.5$ ), lamellae ( $d = 18$ nm), cylinder ( $d = 21-25$ nm), sphere ( $d = 26-27$ nm)	94
BCP14		(1) Dibromo groups-containing P3HT (method ii) (2) Anionic coupling reaction with living PMMA	fibril, lamellae, cylinder, sphere	95
BCP15		(1) P3HT-based macroinitiator (method ii & iii) (2) Anionic polymerization of 2-vinyl pyridine	fibril, lamellae ( $d = 13-15$ nm), cylinder ( $d = 15-20$ nm), sphere, gyroid (melt)	96-98
BCP16		(1) P3HT-based macroinitiator (method ii & iii) (2) NMP	lamellae ( $d = 42$ nm), Cylinder ( $d = 57$ nm)	99

<sup>a</sup>(1) indicates a type of synthesized P3HT. Synthetic strategy used for preparation of P3HT having functional group are shown in parentheses. Method i, ii, and iii refer to the end-functionalization method described in the chapter I,2,1-3, i.e. (i) use of functionalized Ni-based initiators, (ii) post-polymerization modification, and (iii) *in situ* functionalization. (2) stands for strategy used for incorporation of second block. Abbreviations refer to; ATRP = atom transfer radical polymerization, NMP = nitroxide-mediated polymerization, and ROP = ring-opening polymerization.

## I.4 Motivation and aim of the thesis

This thesis aims at the realization of a conceptually ideal active layer structure for organic photovoltaic cells by using carbohydrate-based “high  $\chi$ ” block copolymers. As described in the above sections, in respect of rational design for the organic photovoltaic active layers, it is essential to control several structures at multiple length scales simultaneously.

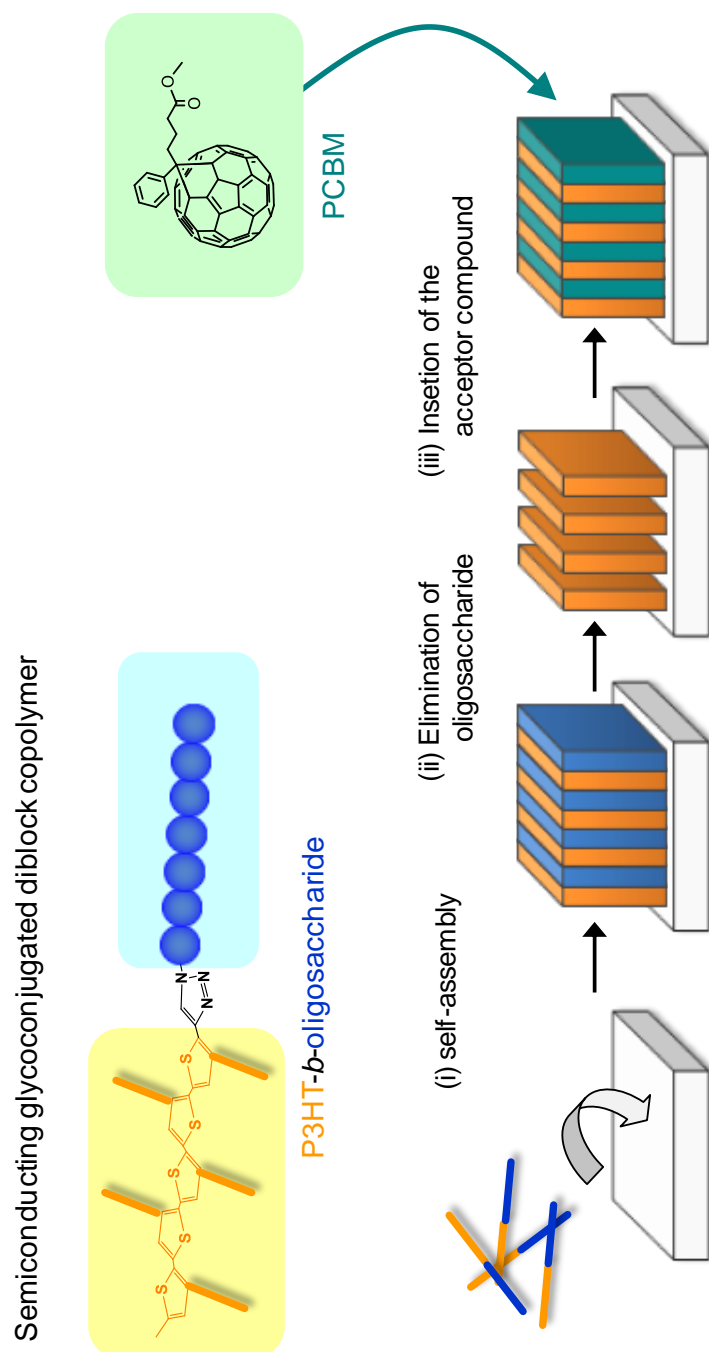
(i) At the 100 nm to micron scale, the donor and acceptor domains must form continuous pathways toward the respective electrodes to collect charge carriers efficiently with reduced probability of the holes-electron recombination.

(ii) At the nanometer scale, the electron donating and accepting materials must be uniformly arraying mutually over the whole active layer, ideally with the each domain size comparable to the exciton diffusion length (10-15 nm), to guarantee that generated exciton reaches the donor-acceptor interface within its lifetime prior to radiative and/or non-radiative decays.

(iii) At the angstrom scale, the crystal structure of semi-conducting compound and its orientation must be optimized to enhance the charge carrier transport.

Based on these prerequisites and our latest research developments on the carbohydrate-based “high  $\chi$ ” block copolymers system, a novel class of organic semiconductor containing glycoconjugated block copolymers, P3HT-*b*-oligosaccharide, is rationally designed and used as a structurally controllable template. The overall strategy to achieve the ultimate active layer is schematically illustrated in Figure 1.20. Once the expected nanostructure is obtained, the sacrificial oligosaccharidic segment will be eliminated, and the resultant cavity will be filled with an electron accepting compounds to give the well-defined donor-acceptor network in which the both compounds are alternately arranging in the sub-10 nm scale.

The research in this thesis will mainly focus on the synthesis and characterization of the novel semiconducting glycoconjugated block copolymers and the fundamental investigation of their self-assembly behaviors. A particular emphasis will be placed on the crystal structure of the semiconducting segment, as well as on the mechanism of phase separation. A preliminary investigation on the selective elimination of the oligosaccharide block is also conducted.



**Figure 1.20** Schematic illustration of the formation of an active layer having a well-defined lamellar structure.



## I.5 References

- (1) Brabec, C. J. *Sol. Energy Mater. Sol. Cells* **2004**, 83 (2–3), 273–292.
- (2) Brabec, C. J.; Padinger, F.; Hummelen, J. C.; Janssen, R. A. J.; Sariciftci, N. S. *Synth. Met.* **1999**, 102 (1–3), 861–864.
- (3) Krebs, F. C.; Spanggaard, H.; Kjær, T.; Biancardo, M.; Alstrup, J. *Mater. Sci. Eng. B* **2007**, 138 (2), 106–111.
- (4) Lungenschmied, C.; Dennler, G.; Neugebauer, H.; Sariciftci, S. N.; Glatthaar, M.; Meyer, T.; Meyer, A. *Sol. Energy Mater. Sol. Cells* **2007**, 91 (5), 379–384.
- (5) Niggemann, M.; Zimmermann, B.; Haschke, J.; Glatthaar, M.; Gombert, A. *Thin Solid Films* **2008**, 516 (20), 7181–7187.
- (6) Hauch, J. A.; Schilinsky, P.; Choulis, S. A.; Childers, R.; Biele, M.; Brabec, C. J. *Sol. Energy Mater. Sol. Cells* **2008**, 92 (7), 727–731.
- (7) Blankenburg, L.; Schultheis, K.; Schache, H.; Sensfuss, S.; Schrödner, M. *Sol. Energy Mater. Sol. Cells* **2009**, 93 (4), 476–483.
- (8) Tipnis, R.; Bernkopf, J.; Jia, S.; Krieg, J.; Li, S.; Storch, M.; Laird, D. *Sol. Energy Mater. Sol. Cells* **2009**, 93 (4), 442–446.
- (9) Krebs, F. C. *Sol. Energy Mater. Sol. Cells* **2009**, 93 (9), 1636–1641.
- (10) Zhao, J.; Li, Y.; Yang, G.; Jiang, K.; Lin, H.; Ade, H.; Ma, W.; Yan, H. *Nat. Energy* **2016**, 1 (2), 15027.
- (11) Tang, C. W. *Appl. Phys. Lett.* **1986**, 48 (2), 183–185.
- (12) Sariciftci, N. S.; Smilowitz, L.; Heeger, A. J.; Wudl, F. *Science* **1992**, 258 (5087), 1474–1476.
- (13) Knight, B. W.; Wudl, F. *J. Org. Chem.* **1995**, 60 (21), 532–538.
- (14) Yu, G.; Gao, J.; Hummelen, J. C.; Wudl, F.; Heeger, A. J. *Science* **1995**, 270 (5243), 1789–1791.
- (15) Fridman. *J. Chem. Soc. Chem. Commun.* **1977**, No. 16, 578–580.

- (16) McCullough, R. D. *Adv. Mater.* **1998**, *10* (2), 93–116.
- (17) Peet, J.; Heeger, A. J.; Bazan, G. C. *Acc. Chem. Res.* **2009**, *42* (11), 1700–1708.
- (18) Wang, G.; Swensen, J.; Moses, D.; Heeger, A. J. *J. Appl. Phys.* **2003**, *93* (10), 6137–6141.
- (19) Jeffries-El, M.; Sauvé, G.; McCullough, R. D. *Macromolecules* **2005**, *38* (25), 10346–10352.
- (20) Chang, J. F.; Sun, B.; Breiby, D. W.; Nielsen, M. M.; Sölling, T. I.; Giles, M.; McCulloch, I.; Sirringhaus, H. *Chem. Mater.* **2004**, *16* (23), 4772–4776.
- (21) McCullough, R. D.; Lowe, R. D. *J. Chem. Soc. Chem. Commun* **1992**, No. 70, 70–72.
- (22) Tamao, K.; Sumitani, K.; Kumada, M. *J. Am. Chem. Soc.* **1972**, *94* (12), 4374–4376.
- (23) Chen, T. A.; Rieke, R. D. *J. Am. Chem. Soc.* **1992**, *114* (25), 10087–10088.
- (24) Rieke, R. D. *Acc. Chem. Res.* **1977**, *10* (8), 301–306.
- (25) Loewe, R. S.; Khersonsky, S. M.; McCullough, R. D. *Adv. Mater.* **1999**, *11* (3), 250–253.
- (26) Loewe, R. S.; Ewbank, P. C.; Liu, J.; Zhai, L.; McCullough, R. D. *Macromolecules* **2001**, *34* (13), 4324–4333.
- (27) Miyakoshi, R.; Yokoyama, A.; Yokozawa, T. *J. Am. Chem. Soc.* **2005**, *127* (49), 17542–17547.
- (28) Smeets, A.; Van Den Bergh, K.; De Winter, J.; Gerbaux, P.; Verbiest, T.; Koeckelberghs, G. *Macromolecules* **2009**, *42* (20), 7638–7641.
- (29) Liu, J.; McCullough, R. D. *Macromolecules* **2002**, *35*, 9882–9889.
- (30) Lohwasser, R. H.; Thelakkat, M. *Macromolecules* **2010**, *43* (18), 7611–7616.
- (31) Mognier, S. J.; Brochon, C.; Cloutet, E.; Fleury, G.; Cramail, H.; Hadziioannou, G. *Macromol. Rapid Commun.* **2012**, *33* (8), 703–709.
- (32) Park, J.; Moon, H. C.; Kim, J. K. *J. Polym. Sci. Part A Polym. Chem.* **2013**, *51* (10), 2225–2232.
- (33) Langeveld-voss, B. M. W.; Janssen, R. A. J.; Spiering, A. J. H.; Dongen, J. L. J. Van; Vonk, E. C.; Claessens, H. A. *Chem. Commun.* **2000**, 81–82.

- (34) Kochemba, W. M.; Kilbey, S. M.; Pickel, D. L. *J. Polym. Sci. Part A Polym. Chem.* **2012**, *50* (14), 2762–2769.
- (35) L. Echegoyen, F. Diederich, L. E. E. *Chem. Phys. Technol.* **2000**, No. John Wiley & Sons; Inc.; New York, 1–51.
- (36) N.S. Sariciftci, A.J. Heeger, in: H. S. N. *Handb. Org. Conduct. Mol. Polym.* **1997**, *1* (Chapter 8).
- (37) Brabec, C. J.; Zerza, G.; Cerullo, G.; De Silvestri, S.; Luzzati, S.; Hummelen, J. C.; Sariciftci, S. *Chem. Phys. Lett.* **2001**, *340* (3–4), 232–236.
- (38) Helfand, E. *Macromolecules* **1975**, *8* (4), 552–556.
- (39) Leibler, L. *Macromolecules* **1980**, *13* (10), 1602–1617.
- (40) Hashimoto, T.; Shibayama, M.; Kawai, H. *Macromolecules* **1980**, *13* (5), 1237–1247.
- (41) Ohta, T.; Kawasaki, K. *Macromolecules* **1986**, *19* (10), 2621–2632.
- (42) Bates, F. S.; Fredrickson, G. H. *Annu. Rev. Phys. Chem.* **1990**, *41* (1), 525–557.
- (43) Darling, S. B. *Prog. Polym. Sci.* **2007**, *32* (10), 1152–1204.
- (44) Bates, F. S.; Fredrickson, G. H. *Phys. Today* **1999**, *52* (2), 32.
- (45) Sivaniah, E.; Hayashi, Y.; Matsubara, S.; Kiyono, S.; Hashimoto, T.; Fukunaga, K.; Kramer, E. J.; Mates, T. *Macromolecules* **2005**, *38* (5), 1837–1849.
- (46) Matsushita, Y.; Mori, K.; Saguchi, R.; Nakao, Y.; Noda, I.; Nagasawa, M. *Macromolecules* **1990**, *23* (19), 4313–4316.
- (47) Hadziioannou, G.; Skoulios, A. *Macromolecules* **1982**, *15* (6), 258–262.
- (48) Coulon, G.; Russell, T. P.; Deline, V. R.; Green, P. F. *Macromolecules* **1989**, *22* (6), 2581–2589.
- (49) Sinturel, C.; Bates, F. S.; Hillmyer, M. A. *ACS Macro Lett.* **2015**, *4* (9), 1044–1050.
- (50) Holyst, R.; Schick, M. *J. Chem. Phys.* **1992**, *96* (1), 730.
- (51) Matsen, M. W.; Barrett, C. J. *J. Chem. Phys.* **1998**, *109* (10), 4108–4118.
- (52) Singh, C.; Goulian, M.; Liu, A. J.; Fredrickson, G. H. *Macromolecules* **1994**, *27* (11), 2974–2986.

- (53) Pryamitsyn, V.; Ganesan, V. *J. Chem. Phys.* **2004**, *120* (12), 5824.
- (54) Olsen, B. D.; Segalman, R. A. *Macromolecules* **2006**, *39* (20), 7078–7083.
- (55) Olsen, B. D.; Shah, M.; Ganesan, V.; Segalman, R. A. *Macromolecules* **2008**, *41* (18), 6809–6817.
- (56) Semenov, a. N.; Vasilenko, S. V. *J. Exp. Theor. Phys.* **1986**, *63* (1), 70–79.
- (57) Reenders, M.; Ten Brinke, G. *Macromolecules* **2002**, *35* (8), 3266–3280.
- (58) Sary, N.; Rubatat, L.; Brochon, C.; Hadziioannou, G.; Ruokolainen, J.; Mezzenga, R. *Macromolecules* **2007**, *40*, 6990–6997.
- (59) Olsen, B. D.; Segalman, R. A. *Macromolecules* **2005**, *38* (24), 10127–10137.
- (60) Olsen, B. D.; Segalman, R. A. *Macromolecules* **2007**, *40* (19), 6922–6929.
- (61) Ceresa, R. J. *Polymer (Guildf)*. **1961**, *2*, 213–219.
- (62) Ziegast, G.; Pfannemüller, B. *Carbohydr. Res.* **1987**, *160* (C), 185–204.
- (63) Pfannemuller, B.; Schmidt, M.; Ziegast, G.; Matsuo, K. *Macromolecules* **1984**, *17* (4), 710–716.
- (64) Loos, K.; Stadler, R. *Macromolecules* **1997**, *30* (24), 7641–7643.
- (65) Loos, K.; Müller, A. H. E. *Biomacromolecules* **2002**, *3* (2), 368–373.
- (66) Houga, C.; Meins, J.-F. Le; Borsali, R.; Taton, D.; Gnanou, Y. *Chem. Commun.* **2007**, No. 29, 3063.
- (67) Bosker, W. T. E.; Ágoston, K.; Cohen Stuart, M. A.; Norde, W.; Timmermans, J. W.; Slaghek, T. M. *Macromolecules* **2003**, *36* (6), 1982–1987.
- (68) Schatz, C.; Lecommandoux, S. *Macromol. Rapid Commun.* **2010**, *31* (19), 1664–1684.
- (69) Giacomelli, C.; Schmidt, V.; Putaux, J. L.; Narumi, A.; Kakuchi, T.; Borsali, R. *Biomacromolecules* **2009**, *10* (2), 449–453.
- (70) Otsuka, I.; Travelet, C.; Halila, S.; Fort, S.; Pignot-Paintrand, I.; Narumi, A.; Borsali, R. *Biomacromolecules* **2012**, *13* (5), 1458–1465.
- (71) De Medeiros Modolon, S.; Otsuka, I.; Fort, S.; Minatti, E.; Borsali, R.; Halila, S. *Biomacromolecules* **2012**, *13* (4), 1129–1135.

- (72) Otsuka, I.; Osaka, M.; Sakai, Y.; Travelet, C.; Putaux, J. L.; Borsali, R. *Langmuir* **2013**, 29 (49), 15224–15230.
- (73) Zepon, K. M.; Otsuka, I.; Bouilhac, C.; Muniz, E. C.; Soldi, V.; Borsali, R. *Biomacromolecules* **2015**, 16 (7), 2012–2024.
- (74) Zepon, K. M.; Otsuka, I.; Bouilhac, C.; Muniz, E. C.; Soldi, V.; Borsali, R. *Langmuir* **2016**, 32 (18), 4538–4545.
- (75) Petrelli, A.; Borsali, R.; Fort, S.; Halila, S. *Chem. Commun.* **2016**, 52, 12202.
- (76) Aissou, K.; Otsuka, I.; Rochas, C.; Fort, S.; Halila, S.; Borsali, R. *Langmuir* **2011**, 27 (7), 4098–4103.
- (77) Otsuka, I.; Tallegas, S.; Sakai, Y.; Rochas, C.; Halila, S.; Fort, S.; Bsiesy, A.; Baron, T.; Borsali, R. *Nanoscale* **2013**, 5 (7), 2637–2641.
- (78) Segalman, R. a.; McCulloch, B.; Kirmayer, S.; Urban, J. J. *Macromolecules* **2009**, 42 (23), 9205–9216.
- (79) Botiz, I.; Darling, S. B. *Mater. Today* **2010**, 13 (5), 42–51.
- (80) De Cuendias, A.; Hiorns, R. C.; Cloutet, E.; Vignau, L.; Cramail, H. *Polym. Int.* **2010**, 59 (11), 1452–1476.
- (81) Liu, C. L.; Lin, C. H.; Kuo, C. C.; Lin, S. T.; Chen, W. C. *Prog. Polym. Sci.* **2011**, 36 (5), 603–637.
- (82) Topham, P. D.; Parnell, A. J.; Hiorns, R. C. *J. Polym. Sci. Part B Polym. Phys.* **2011**, 49 (16), 1131–1156.
- (83) Yassar, A.; Miozzo, L.; Gironda, R.; Horowitz, G. *Prog. Polym. Sci.* **2013**, 38 (5), 791–844.
- (84) Liu, J.; Sheina, E.; Kowalewski, T.; McCullough, R. D. *Angew. Chem. Int. Ed.* **2002**, 41 (2), 329.
- (85) Iovu, M. C.; Zhang, R.; Cooper, J. R.; Smilgies, D. M.; Javier, A. E.; Sheina, E. E.; Kowalewski, T.; McCullough, R. D. *Macromol. Rapid Commun.* **2007**, 28 (17), 1816–1824.

- (86) Craley, C. R.; Zhang, R.; Kowalewski, T.; McCullough, R. D.; Stefan, M. C. *Macromol. Rapid Commun.* **2009**, *30* (1), 11–16.
- (87) Li, Z.; Ono, R. J.; Wu, Z.-Q.; Bielawski, C. W. *Chem. Commun.* **2011**, *47* (1), 197–199.
- (88) Lim, H.; Chao, C.-Y.; Su, W.-F. *Macromolecules* **2015**, *48* (10), 3269–3281.
- (89) Boudouris, B. W.; Frisbie, C. D.; Hillmyer, M. A. *Macromolecules* **2008**, *41* (1), 67–75.
- (90) Grancharov, G.; Coulembier, O.; Surin, M.; Lazzaroni, R.; Dubois, P. *Macromolecules* **2010**, *43* (21), 8957–8964.
- (91) Lohwasser, R. H.; Thelakkat, M. *Macromolecules* **2012**, *45* (7), 3070–3077.
- (92) He, L.; Pan, S.; Peng, J. *J. Polym. Sci. Part B Polym. Phys.* **2016**, *54* (5), 544–551.
- (93) Higashihara, T.; Ueda, M. *Macromolecules* **2009**, *42* (22), 8794–8800.
- (94) Smith, K. A.; Lin, Y. H.; Dement, D. B.; Strzalka, J.; Darling, S. B.; Pickel, D. L.; Verduzco, R. *Macromolecules* **2013**, *46* (7), 2636–2645.
- (95) Ho, V.; Boudouris, B. W.; Segalman, R. A. *Macromolecules* **2010**, *43* (19), 7895–7899.
- (96) Ho, V.; Boudouris, B. W.; McCulloch, B. L.; Shuttle, C. G.; Burkhardt, M.; Chabiny, M. L.; Segalman, R. A. *J. Am. Chem. Soc.* **2011**, *133* (24), 9270–9273.
- (97) Moon, H. C.; Bae, D.; Kim, J. K. *Macromolecules* **2012**, *45* (12), 5201–5207.
- (98) Patel, S. N.; Javier, A. E.; Beers, K. M.; Pople, J. A.; Ho, V.; Segalman, R. A.; Balsara, N. P. *Nano Lett.* **2012**, *12* (9), 4901–4906.
- (99) Lin, S. H.; Wu, S. J.; Ho, C. C.; Su, W. F. *Macromolecules* **2013**, *46* (7), 2725–2732.
- (100) Kim, H. J.; Paek, K.; Yang, H.; Cho, C. H.; Kim, J. S.; Lee, W.; Kim, B. J. *Macromolecules* **2013**, *46* (21), 8472–8478.
- (101) Park, J.; Choi, C.; Hyun, S.; Moon, H. C.; Vincent Joseph, K. L.; Kim, J. K. *Macromolecules* **2016**, *49* (2), 616–623.
- (102) Dai, C. A.; Yen, W. C.; Lee, Y. H.; Ho, C. C.; Su, W. F. *J. Am. Chem. Soc.* **2007**, *129* (36), 11036–11038.
- (103) Lee, Y.-H.; Yen, W.-C.; Su, W.-F.; Dai, C.-A. *Soft Matter* **2011**, *7* (21), 10429.

- (104) Lee, Y.-H.; Yang, Y.-L.; Yen, W.-C.; Su, W.-F.; Dai, C.-A. *Nanoscale* **2014**, 6 (4), 2194–2200.
- (105) Lohwasser, R. H.; Gupta, G.; Kohn, P.; Sommer, M.; Lang, A. S.; Thurn-Albrecht, T.; Thelakkat, M. *Macromolecules* **2013**, 46 (11), 4403–4410.
- (106) Botiz, I.; Darling, S. B. *Macromolecules* **2009**, 42 (21), 8211–8217.

## **CHAPTER II:**

# **SYNTHESIS AND STRUCTURAL CHARACTERIZATION OF SEMICONDUCTING GLYCOCONJUGATED DIBLOCK COPOLYMERS**



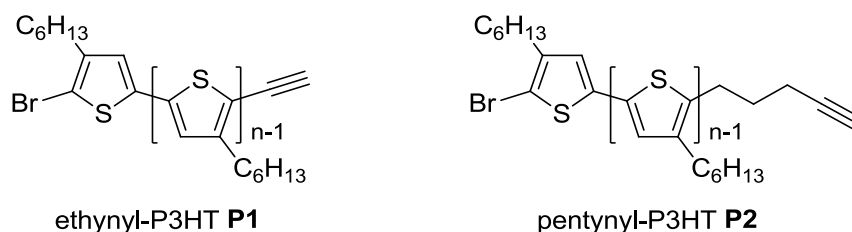
## II.1 Introduction

It is well-known that the device performance of bulk heterojunction solar cells, where the active layer consists of a mixture of the donor and acceptor compounds, is highly dependent on the morphology of the active layer. However, despite many efforts, morphological control of the active layer at nanoscale needs yet to be addressed to improve the performance of the bulk heterojunction solar cells. A periodic lamellar structure in which the electron donor and acceptor compounds are mutually interpenetrating in sub-20 nm scale is considered to be an ideal structure from the point of view of efficient charge separation and charge collection. One of the promising bottom-up approaches for designing the ideal structure is the use of the self-assembly nature of block copolymers. Recently, our research group (physico-chemistry and self-assembly of glycopolymer group in CERMAV) has developed a new class of carbohydrate-containing block copolymer system, referred to as “high  $\chi$ -low  $N$ ” system, and achieved one of the smallest feature sizes ever reached to date (see Chapter I.3.2). This remarkable progress in downsizing of self-assembled domain spacing is attributed to the distinctive characteristics of the carbohydrates, such as high hydrophilicity, strong polarizability, and rigid structure, *etc.* In this context, novel block copolymers composed of electronically active  $\pi$ -conjugated polymer and oligosaccharides were designed for patterning of the active materials (electron donors and acceptors) into well-ordered periodic nanostructures in sub-20 nm scale with the help of self-assembly of “high  $\chi$ ” block copolymers.

In this chapter, the synthesis of novel diblock copolymers consisting of maltoheptaose and  $\pi$ -conjugated regioregular HT-coupled poly(3-hexylthiophene-2,5-diyl) (P3HT) is described. P3HT is one of the promising and widely explored polymeric semiconductor owing to its excellent properties such as high carrier mobility and solution processability. Maltoheptaose is a linear oligosaccharide composed of seven  $\alpha$ -1,4-linked D-glucopyranosyl units. A series of oligosaccharide-containing block copolymers were generally prepared via the following three steps: (i) synthesis of alkyne end-functionalized regioregular P3HT with well-defined molar mass by modified Grignard metathesis (GRIM) polymerization, (ii) synthesis of azido-functionalized oligosaccharides by direct anomeric azidation, and (iii) coupling the alkyne end-capped P3HT block and the azido endo-capped malto-oligosaccharide block via copper (I) catalyzed 1,3-dipolar cycloaddition.

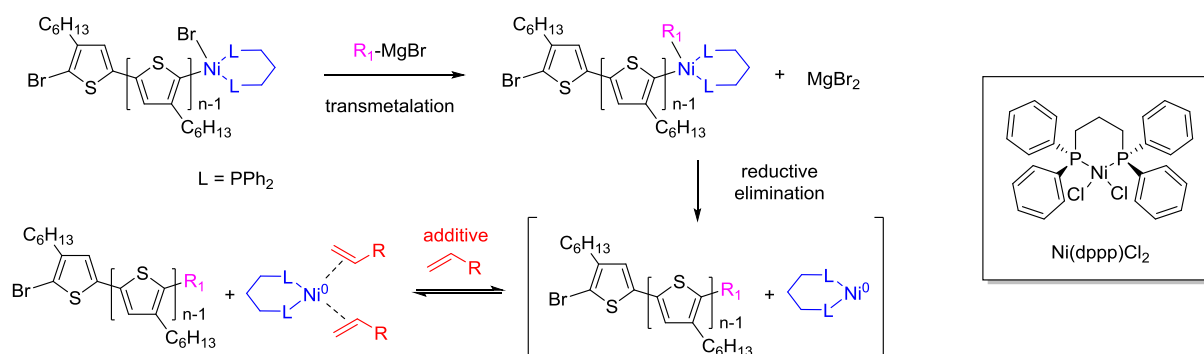
## II.2 Synthesis of alkyne-terminated P3HT

### II.2.1 *in situ* end-functionalization



**Scheme 2.1** The alkyne-terminated P3HT synthesized by the *in situ* end-functionalization method.

As a first step, two types of the alkyne-terminated P3HTs, *i.e.* ethynyl-P3HT **P1** and pentynyl-P3HT **P2**, were prepared by one-pot synthesis combining the modified Grignard metathesis polymerization (GRIM) and the *in situ* functionalization with alkyne-functionalized Grignard reagent (scheme 2.1). These two polymers were selected to investigate how the steric hindrance and electron density distribution at terminal alkyne group effect on the reactivity of subsequent copper-catalyzed azide-alkyne cycloaddition (CuAAC "click" reaction). As already mentioned in the previous chapter, GRIM polymerization follows a living mechanism.<sup>1</sup> Therefore, addition of other Grignard reagents at the end of polymerization will terminate the reaction and provide end-capped regioregular P3HTs with desired functional groups. Although this method is simple and versatile, the precise control of the end-group functionalities has been difficult because of the existing various quenching routes eventually provide different types of end-group. Recently, Pickel *et al.* reported that the additives containing unsaturated groups such as allyl, vinyl, or alkynyl groups could prevent further oxidative addition of Ni<sup>0</sup> to the  $\alpha$ -chain end, which causes undesired end-functionalization, including bis-end-functionalized products, by forming a stable  $\pi$ -complex between Ni<sup>0</sup> and the unsaturated group (Scheme 2.2).<sup>2</sup> Thus, in this study, we used 1-hexene as an unsaturated additive to increase the yield of monofunctional P3HT by controlling the end-capping process.

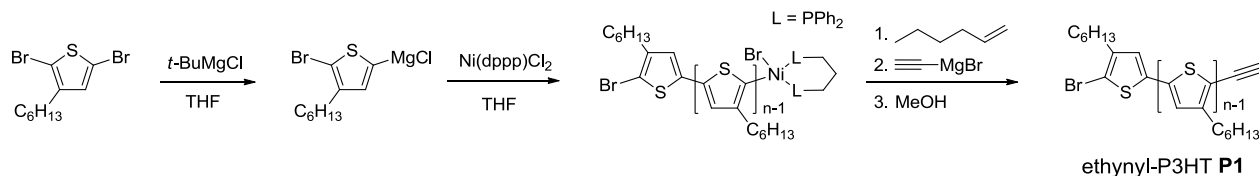


**Scheme 2.2** Proposed interaction between Ni catalyst and unsaturated group of additives.

In a general experiment of end-capping reaction, the molar ratio of the monomer [M] and Ni catalyst [Ni] was fixed as [M] / [Ni] = 25 / 1 to provide P3HT with a number-average molecular weight  $M_n$  of ca. 4000 g/mol. This target molecular weight was estimated based on our previous studies on the self-assembly, in which we revealed that oligosaccharide-containing high  $\chi$  block copolymers systems self-organize into sub-10 nm scale morphologies such as spheres, cylinders, and lamellae when using synthetic blocks with molecular weights in the 2000-5000 g/mol range.

## Ethynyl-P3HT **P1**

First, ethynyl-P3HT **P1** was synthesized according to scheme 2.3. Prior to termination step, the reaction mixture was cooled to 0 °C and then an excess of 1-hexene (*ca.* 1000 equiv.) was added to the mixture. The termination reaction and functionalization were carried out in a one-shot addition of ethynylmagnesium bromide. The mixture was stirred for 3 min and then poured into



**Scheme 2.3** Synthesis of ethynyl-functionalized P3HT **P1** by the combination of modified Grignard metathesis polymerization and *in situ* functionalization.

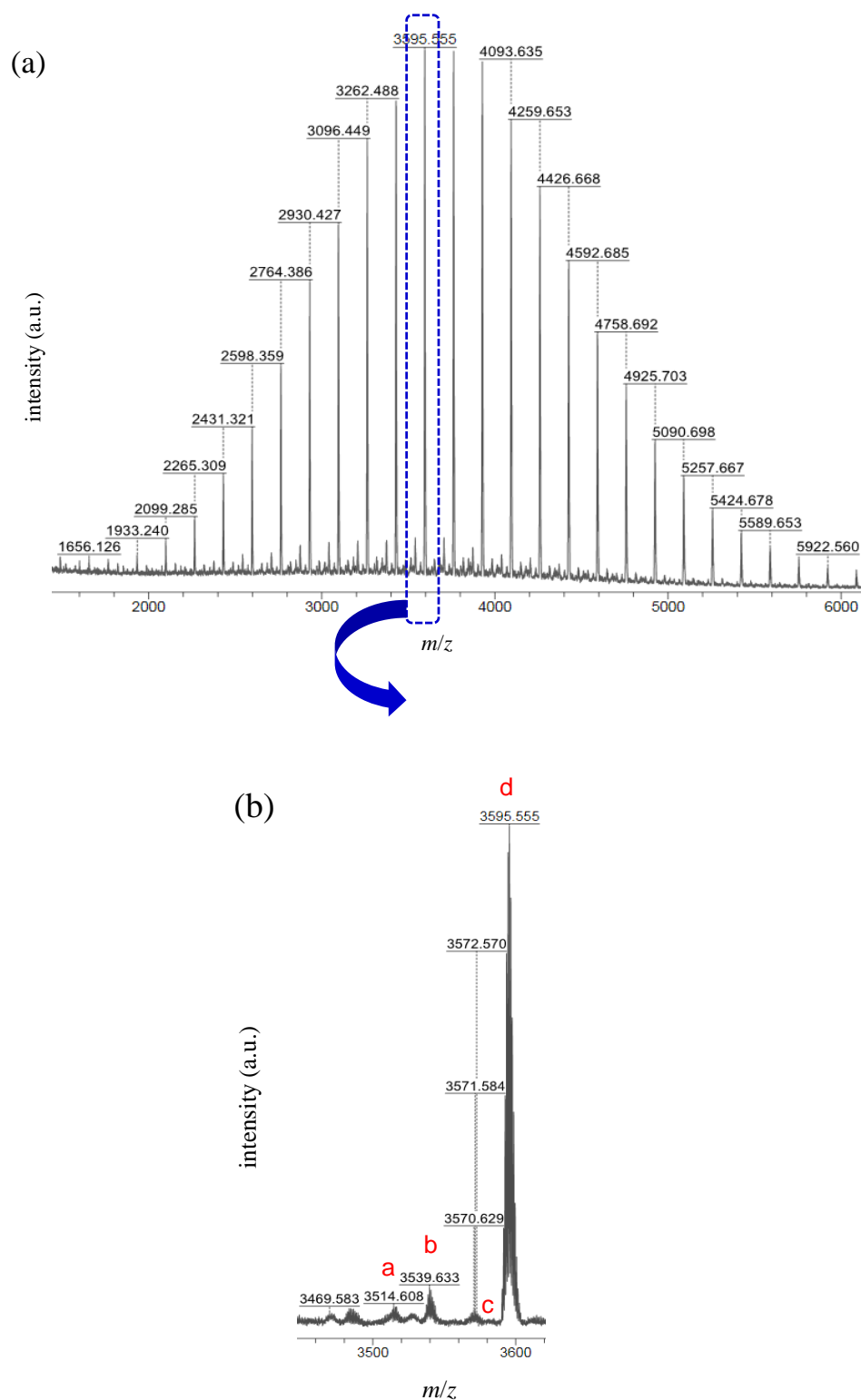
cold MeOH for quenching. The obtained polymer was purified by precipitation in cold methanol and characterized by MALDI-TOF MS,  $^1\text{H}$  NMR, and SEC. The characteristics of the polymer are summarized in Table 2.1.

**Table 2.1** Summary of characterizations of the ethynyl-P3HT **P1**

entry	polymer	$M_{n, \text{SEC, P3HT}}^a$	$M_{n, \text{SEC, P3HT}}^b$	$M_{\text{p, MALDI, P3HT}}^c$	$\bar{D}^a$	% HT <sup>d</sup>	end-functionality <sup>e</sup>		
		[non-corrected]	[corrected]				( $M_{\text{w}} / M_{\text{n}}$ )	(%)	mono
		(g/mol)	(g/mol)	(g/mol)			-endcapped	-endcapped	-endcapped
P1	ethynyl-P3HT	5330	3490	3596	1.35	> 95	91	7	2

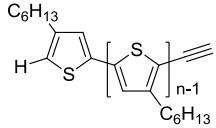
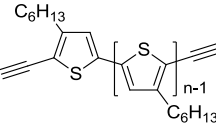
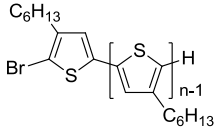
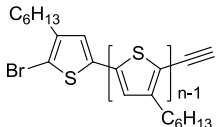
<sup>a</sup> Number average molecular weight determined by SEC in THF based on PS standards. <sup>b</sup> Corrected SEC value using the Mark - Houwink - Sakurada constants:  $a_{\text{P3HT}}$  and  $K_{\text{P3HT}}$  are 0.96 and  $2.28 \times 10^{-3}$  ( $\text{cm}^3/\text{g}$ ), respectively. <sup>c</sup> Molecular weight at the peak maximum determined by MALDI-TOF MS. <sup>d</sup> HT coupling regioregularity determined by  $^1\text{H}$  NMR spectroscopy. <sup>e</sup> Degree of polymer chain-end functionalities determined by MALDI-TOF MS.

The end-group composition of P3HT was determined by MALDI-TOF MS analysis. As shown in Figure 2.1, MALDI-TOF MS spectrum of the ethynyl-P3HT **P1** contained four series of peaks separated with an interval of 166 g/mol corresponding to the 3HT unit. Structural assignments of each peak are tabulated in Table 2.2. As expected, the series of the most intense peaks were identified as monofunctional P3HT terminated with an alkyne group at the  $\omega$ -end and one bromine function at the  $\alpha$ -end. For example, the peak at  $m/z = 3595.56$  g/mol (magnified part is shown in Figure 2.1b) is corresponding to the 21-mer of P3HT with an alkyne and a bromine end group;  $(\text{M.W. of 3HT}) \times 21 + (\text{M.W. of alkyne}) + (\text{M.W. of bromine}) + \text{H}^+ = 3596.64$ . The relative abundance of this species was estimated from peak intensity ratio to be 88 %. Similarly, the other small amount of by-products were assigned to be bis-end-functionalized P3HT having alkyne/alkyne groups (7 %), mono-functionalized P3HT having alkyne/H groups (3 %), and non-functionalized P3HT having H/Br (2 %) end groups. Hence, the *in situ* end-functionalization of P3HT via the GRIM method in the presence of 1-hexene led to monofunctionalized ethynyl-P3HT with 91 % purity.



**Figure 2.1** (a) MALDI-TOF MS spectrum of ethynyl-P3HT **P1** and (b) magnified part in the range of 21 repeating units.

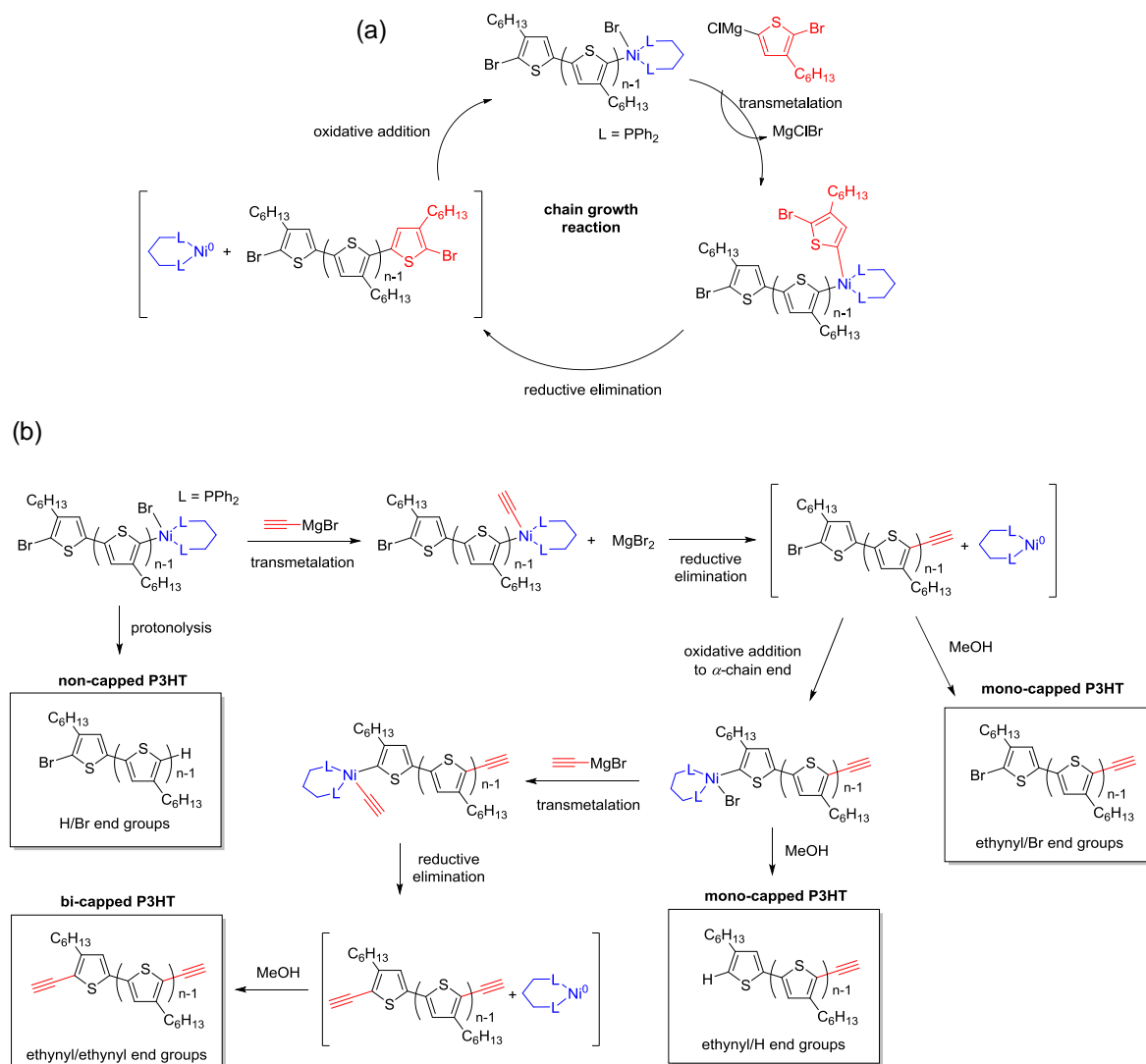
**Table 2.2** Structural assignments of peaks observed in MALDI-TOF MS spectrum of ethynyl-P3HT **P1**

peak code <sup>a</sup>	structure	added ion	n <sup>b</sup>	mass ( <i>m/z</i> )		abundance ratio
				calculated	observed	
a		H <sup>+</sup>	21	3518.73	3514.61	3%
b		H <sup>+</sup>	21	3542.73	3539.63	7%
c		H <sup>+</sup>	21	3572.64	3572.57	2%
d		H <sup>+</sup>	21	3596.64	3595.56	88%

<sup>a</sup> Peak codes are shown in Figure 2.1. <sup>b</sup> Degree of polymerization at the peak maximum.

Elucidation: generation mechanism of by-products

Although significant improvement has been made with regard to the control of the end-group functionalities by using unsaturated additives, we found that it is still difficult to provide P3HTs with perfectly controlled terminal structure. Here, we describe about the generation mechanism of by-products based on the report of Pickel *et al.*<sup>2</sup> and consider possible solutions. As shown in



scheme 2.4(a), the chain propagation reaction of the GRIM polymerization proceeds via multiple

cycles including i) transmetalation between Ni catalyst associated with a  $\omega$ -chain end and activated Grignard monomer (2-bromo-5-magnesioclho-3-hexylthiophene), ii) reductive elimination of Ni catalyst, and iii) intramolecular oxidative addition of Ni catalyst into C-Br bond at the polymer chain end. In the ideal case, when a second Grignard reagent, *i.e.* ethynylmagnesium bromide, is added to the mixture, end-capping reaction will occur at only  $\omega$ -end through a transmetalation with Ni catalyst and subsequent reductive elimination, resulting in a mono-functional P3HT. However, the actual reaction does not proceed as simply as this way. For instance, in cases where the regenerated  $\text{Ni}^0(\text{dppp})$  reaches to the  $\alpha$ -chain end via "chain-walking", it may cause undesired second oxidative addition to the  $\alpha$ -end, resulting in the formation of by-product having a functional group at both chain-ends. Likewise, the P3HT having an alkyne group at the  $\omega$ -end and a hydrogen at the  $\alpha$ -end would be generated as a result of oxidative addition of Ni catalyst to the  $\alpha$ -end followed by quenching with proton, that occurs at the same time as or after the end-capping reaction at  $\omega$ -chain end with ethynylmagnesium bromide. On the other hand, the polymer having no functional group, *i.e.* P3HT-H/Br, will be afforded when the active  $\omega$ -end associated with Ni catalyst undergoes protonolysis prior to the end-capping reaction with an ethynylmagnesium bromide. Therefore, to attain the selective synthesis of mono-functional P3HT more precisely, it seems effective to further stabilize Ni catalyst with alternative stabilizer for the enhancement of the reactivity of Grignard reagent (capping agent) with polymer chain-end.

Further structural characterization of ethynyl-P3HT **P1** was carried out by the analysis of the  $^1\text{H}$  NMR spectrum as shown Figure 2.2. The proton resonance signal at 3.53 ppm (signal x in Figure 2.2) was assigned to the alkyne proton ( $-\text{C}\equiv\text{CH}$ ), indicating successful introduction of alkyne functional group to the polymer chain.

Additional information regarding the regioregularity can be obtained from the NMR spectra. As described in the Chapter I.2.1-1, there are four possible triad configurations for the 3-substituted polythiophenes. These regioisomers are distinguishable by means of  $^1\text{H}$  and  $^{13}\text{C}$  NMR spectroscopy thanks to their chemical environment differences. The assignments of the  $^1\text{H}$  and  $^{13}\text{C}$  chemical shifts corresponding to the various regioisomers are well-documented in the



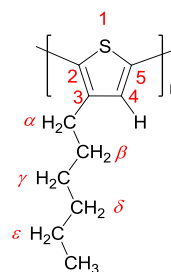
literature<sup>3</sup> and summarized in Table 2.3. The regioregularity defined by the percentage of head-to-tail (HT) linkage can be determined by integration of the <sup>1</sup>H NMR signals.

**Table 2.3** <sup>1</sup>H and <sup>13</sup>C NMR chemical shifts corresponding to the regioisomers in P3HT

dayad		chemical shift $\delta$ (ppm)	
		HT	HH
<sup>1</sup> H NMR	CH <sub>2</sub> ( $\alpha$ )	2.80	2.58
	CH <sub>2</sub> ( $\beta$ )	1.72	1.63

triad		chemical shift $\delta$ (ppm)			
		HT-HT	HT-HH	HH-TT	TT-HT
<sup>1</sup> H NMR	H4	6.98	7.02	7.05	7.00
<sup>13</sup> C NMR	C2	130.5	129.7	127.2	128.3
	C3	139.9	140.3	143.4	142.8
	C4	128.6	127.3	125.1	126.6
	C5	133.7	134.7	136.8	135.7



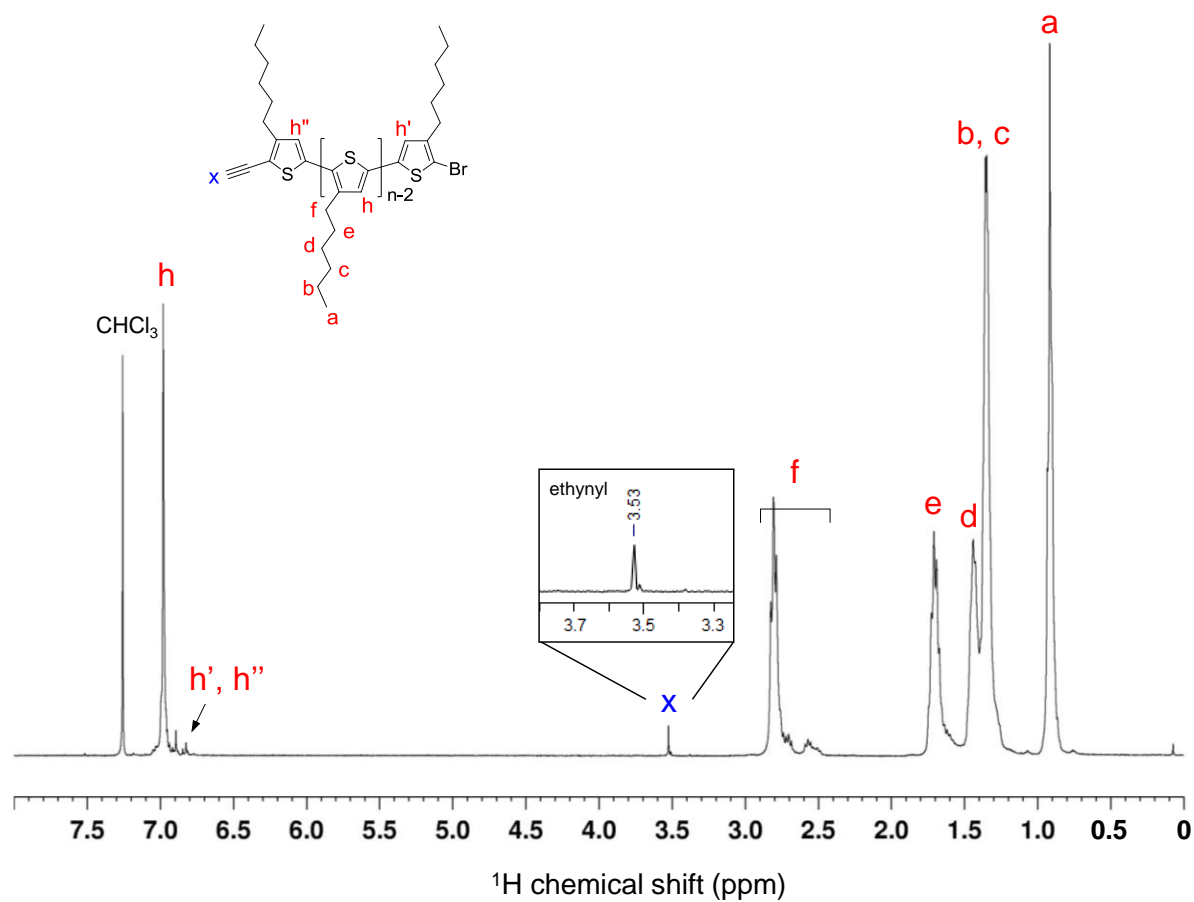
For instance, the HT-HT regioregularity was estimated to be 95 % by comparing integral ratio of the signals corresponding to  $\alpha$ -methylene protons, that is, the signal at 2.80 ppm due to HT linkage and the signals around 2.48-2.75 ppm due to head-to-head (HH) linkages (signal f in Figure 2.2).

Figure 2.3 shows <sup>13</sup>C NMR spectrum of ethynyl-P3HT **P1**. Unfortunately, no characteristic signal due to the terminal alkyne carbon ( $\text{-C}\equiv\text{CH}$ ), which is generally found in the range of 60-90 ppm, was obtained. However other detectable carbon signals clearly suggest the P3HT structure. Carbon resonances observed in the range of 140-128 ppm were assigned to the HT-HT coupled thiophene ring and six carbon resonances observed at higher magnetic field region from 30 to 14 ppm were attributed to the hexyl chain of P3HT.

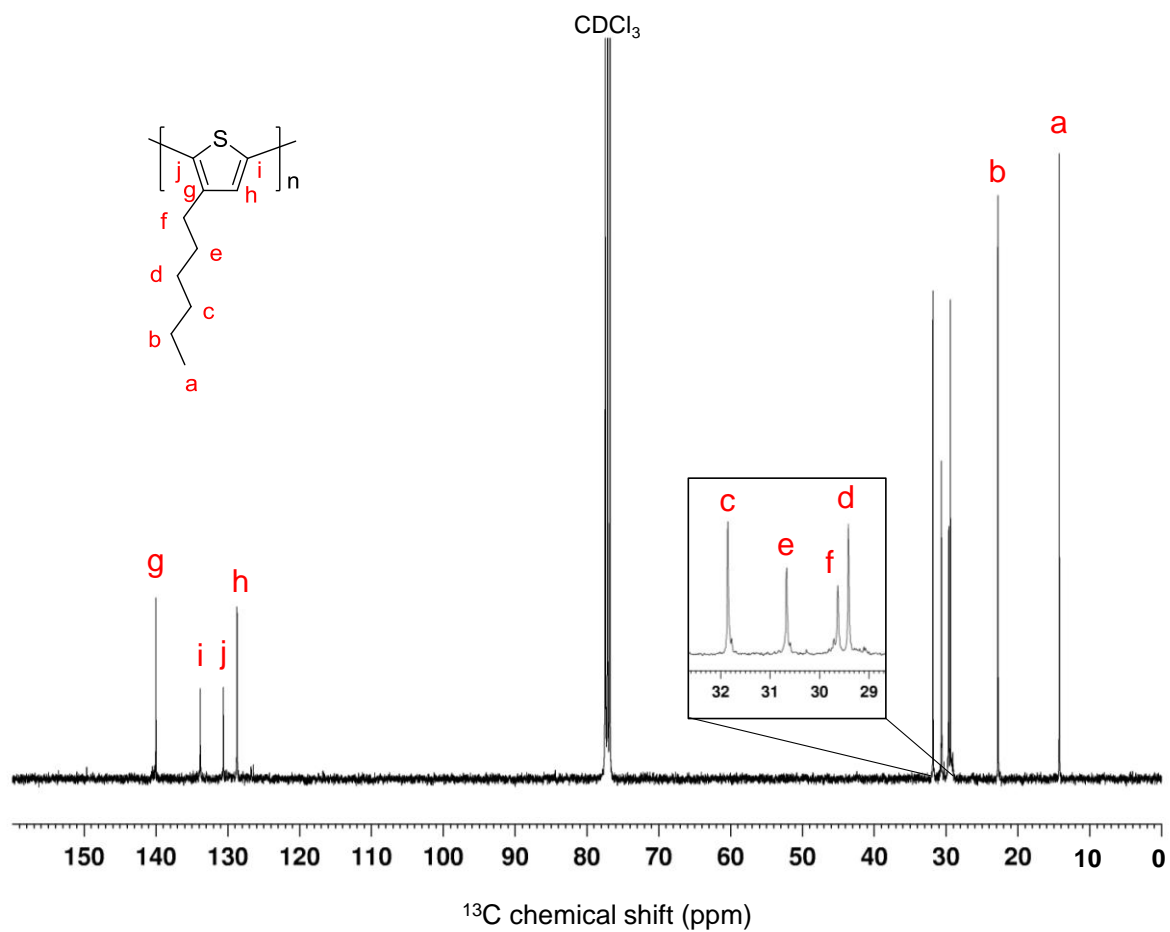
One should keep in mind that reported assignments are sometimes contradictory. Indeed, different assignments of the  $^{13}\text{C}$  signals, especially for the hexyl side chain of P3HT, were observed in the literatures probably due to the fact that the  $^{13}\text{C}$  chemical shifts of the hexyl chain does not follow the molecular arrangement order. Thus, to obtain reliable structural information, two-dimensional NMR studies, including heteronuclear single-quantum correlation (HSQC), heteronuclear multiple-bond correlation (HMBC) spectroscopy and diffusion ordered spectroscopy (DOSY), were performed. The signal assignments were then additionally confirmed by comparison with the literature data.

The structural determination of the product was facilitated by the  $^1\text{H}$ - $^{13}\text{C}$  HSQC and  $^1\text{H}$ - $^{13}\text{C}$  HMBC experiment. The  $^1\text{H}$ - $^{13}\text{C}$  HSQC provides cross peaks due to the connection between a proton and directly bonded carbon. The  $^1\text{H}$ - $^{13}\text{C}$  HMBC is a long range correlation experiment which gives information about the connection between protons and carbons attached two or three bonds away. Figure 2.4 and 2.5 show the  $^1\text{H}$ - $^{13}\text{C}$  HSQC and  $^1\text{H}$ - $^{13}\text{C}$  HMBC spectra of the ethynyl-P3HT **P1**, respectively, together with the assignment of some peaks.

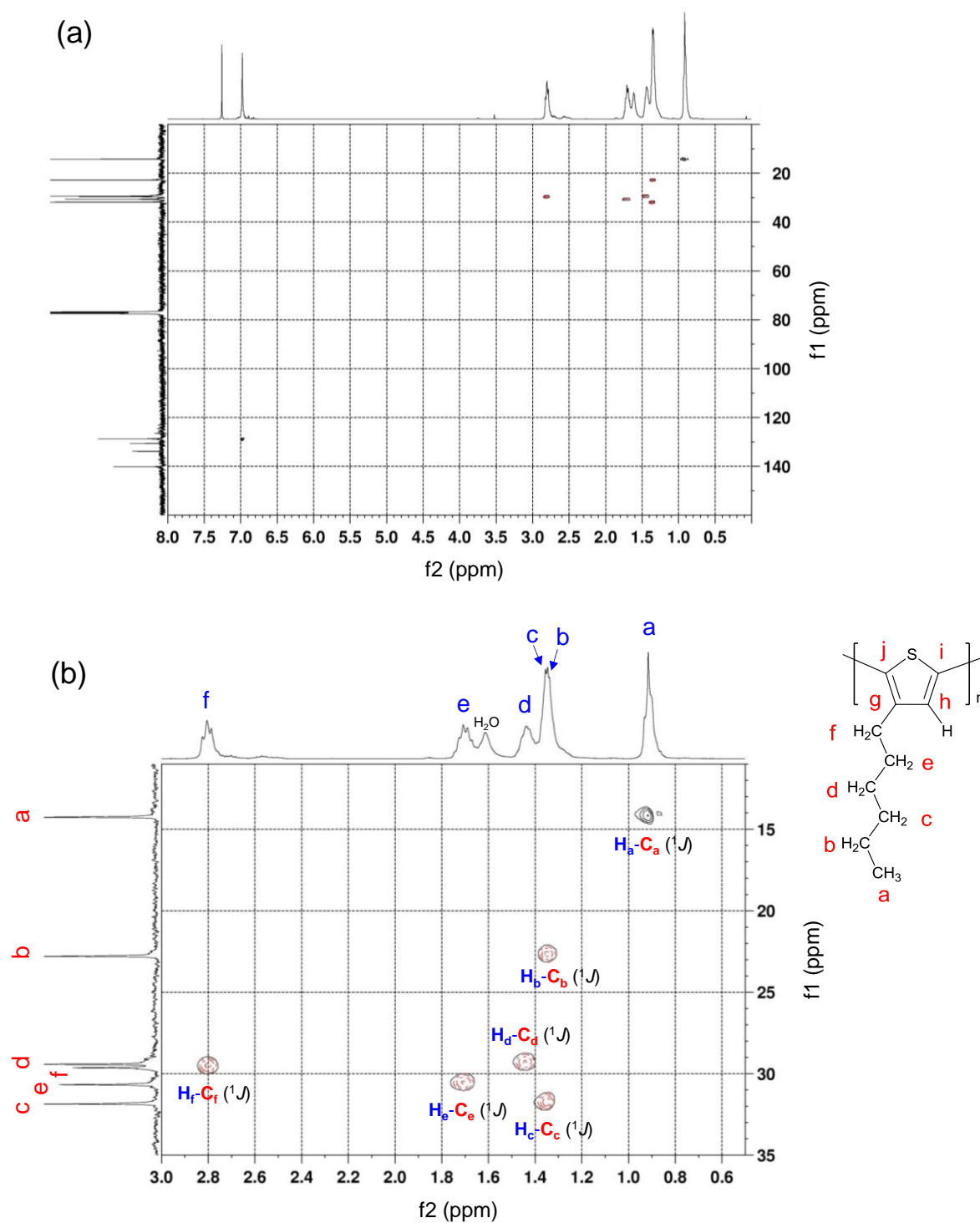
From HSQC spectrum, a carbon signal at 30.7 ppm correlated with the proton due to  $\beta$ -methylene was straightforwardly identified as  $\beta$ -carbon. Likewise, carbon signals at 29.6 ppm and 29.4 ppm correlated with the proton of  $\alpha$ -methylene and  $\gamma$ -methylene were attributed to  $\alpha$ -carbon and  $\gamma$ -carbon, respectively. Moreover, three cross peaks at the coordinate (1.44 ppm, 31.9 ppm), (1.35 ppm, 31.9 ppm), and (0.92 ppm, 31.9 ppm) in the HMBC spectrum enabled identify a peak at 31.9 ppm as a carbon signal corresponding to  $\delta$ -carbon. Thus, we could confirm all  $^{13}\text{C}$  NMR assignments of the hexyl chain by means of HSQC and HMBC experiments as following: C ( $\alpha$ ) = 29.6 ppm, C ( $\beta$ ) = 30.7 ppm, C ( $\gamma$ ) = 31.9 ppm, C ( $\delta$ ) = 31.9 ppm, C ( $\epsilon$ ) = 22.8 ppm,  $\text{CH}_3$  = 14.3 ppm.



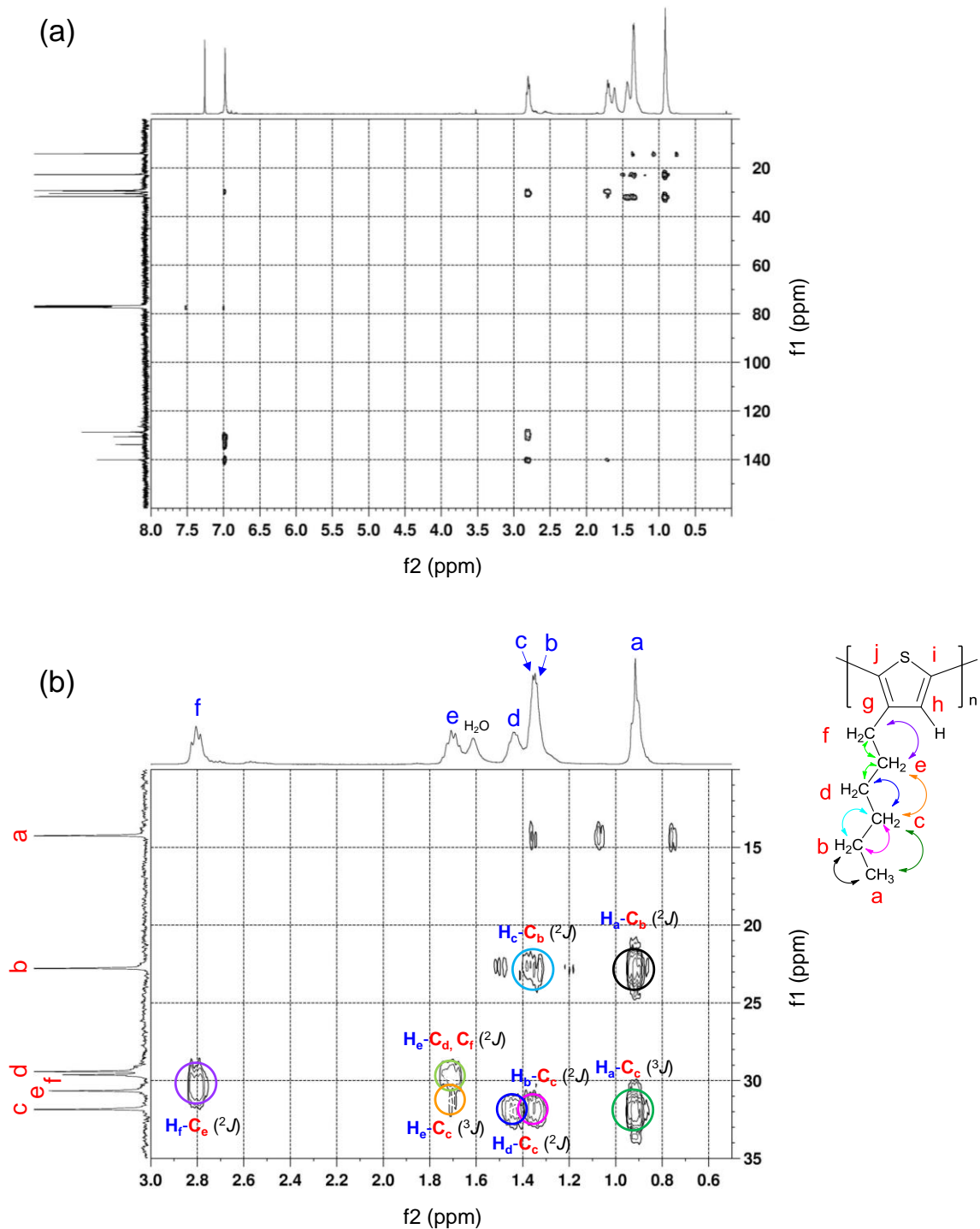
**Figure 2.2**  $^1\text{H}$  NMR spectrum of ethynyl-P3HT **P1** in  $\text{CDCl}_3$ .



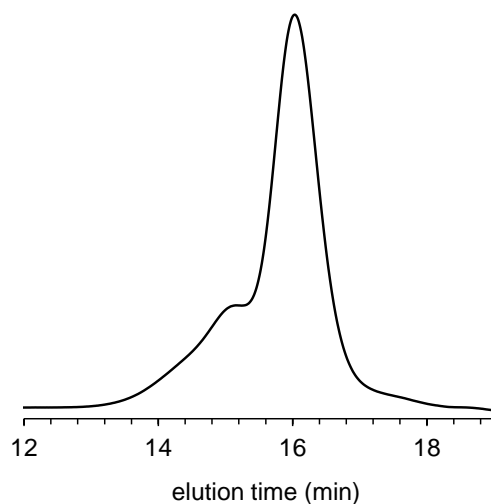
**Figure 2.3**  $^{13}\text{C}$  NMR spectrum of ethynyl-P3HT **P1** in  $\text{CDCl}_3$ .



**Figure 2.4** (a)  $^1\text{H}$ - $^{13}\text{C}$  HSQC spectrum of ethynyl-P3HT **P1** in  $\text{CDCl}_3$  and (b) magnified part in the range of 3.0–0.5 ppm in the x-axis and 35–10 ppm in the y-axis.



**Figure 2.5** (a)  $^1\text{H}$ - $^{13}\text{C}$  HMBC spectrum of ethynyl-P3HT **P1** in  $\text{CDCl}_3$  and (b) magnified part in the range of 3.0–0.5 ppm in the x-axis and 35–10 ppm in the y-axis.



**Figure 2.6** SEC trace of ethynyl-P3HT **P1** recorded by UV detector.

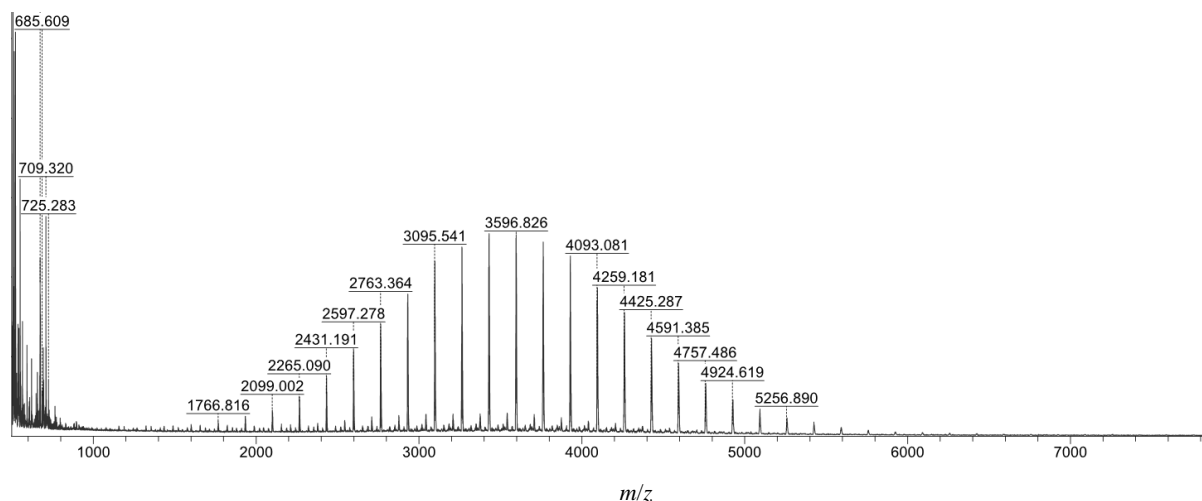
The number-average molecular weight ( $M_{n, SEC}$ ) and the dispersity  $D$  ( $M_w/M_n$ ) of ethynyl-P3HT **P1** were determined to be 5330 g/mol and 1.35, respectively by SEC (Table 2.9 and Figure 2.6) based on polystyrene standards. Here, it should be noted that the molecular weight of P3HT determined by SEC using polystyrene standards are overestimated compared to the real value because of the stiffness of the  $\pi$ -conjugated polymer backbones and the large difference in the hydrodynamic volume between P3HT and polystyrene in the THF eluent. Therefore, the SEC data were evaluated by using the calibration curve which was corrected by following equation (Eq 2.1)

$$\log M_2 = \left( \frac{1}{1+a_2} \right) \log \left( \frac{K_1}{K_2} \right) + \frac{1+a_1}{1+a_2} \log M_1 \quad (\text{Eq 2.1})$$

where  $K_1$ ,  $a_1$  and  $M_1$  are known as Mark-Houwink-Sakurada (MHS) constants and known molecular weight of polystyrene (PS standard) and  $K_2$ ,  $a_2$  and  $M_2$  represent known MHS constants and corrected molecular weight of the P3HT. The MHS constants in THF at 25 °C for polystyrene and P3HT were taken from the literature as  $K_{PS} = 1.29 \times 10^{-2} \text{ cm}^3/\text{g}$ ,  $a_{P3HT} = 0.713$ ,  $K_{P3HT} = 2.28 \times 10^{-3} \text{ cm}^3/\text{g}$ , and  $a_{P3HT} = 0.96$ , respectively.<sup>4</sup> The corrected  $M_n$  value was calculated to be 3490 g/mol, which is in good agreement with the maximum value (3596 g/mol) of the weight distribution in the MALTDI-TOF-MS spectrum. Another fact requiring special attention is a shoulder found in high molecular weight region in the SEC trace. The estimated molecular

weight at the shoulder is almost twice compared to that of the main peak, suggesting that a small amount of chain-chain coupling between P3HTs has occurred in the course of the polymerization or purification. The high molecular fraction was not isolated in this study but a complementary information about the chemical structure of this impurities may be obtained by mass spectrometry. Unfortunately, only a low mass distribution could be detected in the MALDI-TOF MS spectra as shown in Figure 2.7 (full-scan mass spectrum of Figure 2.1a) because of the difficult ionization of the relatively high molecular dimerized P3HTs.

Indeed, the dimerization phenomenon is often seen when the P3HTs are synthesized via GRIM method.<sup>5-7</sup> Nevertheless, very few attempts have been made to characterize the exact structure of dimerized polymer and elucidate its generation mechanism so far. Here, two possible pathways for dimerized polymer formation and the consequent structures are described.



**Figure 2.7** MALDI-TOF MS spectrum of ethynyl-P3HT **P1**.



Elucidation: generation mechanism of dimerized P3HTsRoute A

The most likely pathway is depicted in Scheme 2.5b. Once the mono-ethynyl-P3HT (PT1) is formed, the introduced alkyne group may react with unreacted Grignard reagent, *i.e.* ethynylmagnesium bromide or 5-bromo-2-chloromagnesium-3-hexylthiophene (M2), and transform into alkynyl Grignard reagent (PT2). Here, M2 is a regioisomer of 2-bromo-5-chloromagnesium-3-hexylthiophene (M1), which is a minor product of halogen-metal exchange reaction of M0 with *t*-BuMgCl (yield: M1 = 75%, M2 = 25%). Nevertheless, M2 does not participate in a polymerization due to steric hindrance whereas M1 is selectively consumed during the chain growth reaction. Thereby, a small amount of M2 is remaining in the reaction medium. The PT2 will subsequently react with Ni-associated P3HT (PT3) followed by reductive elimination of the catalyst and finally dimerized P3HT having no functional group at both chain ends (PT4) is formed. Moreover, if the PT4 undergoes further oxidative addition of Ni catalyst (condition where R = Br), the dimerized P3HT having an alkyne functional group (PT5) would be generated via a transmetalation of Grignard reagent to the  $\alpha$ -chain end and subsequent reductive elimination (Scheme 2.5c).

Route B

Another possible pathway is shown in Scheme 2.6. This route is based on the dimerization mechanism for the classical GRIM polymerization of P3HT without *in situ* end-functionalization step. The dimerization phenomenon has been firstly recognized when non-functional P3HTs were synthesized via GRIM method. So far, it has been revealed that the quenching reagents have significant influence on the molecular weight distribution of the resulting polymer. For instance, Yokozawa *et al.*<sup>8</sup> reported successful synthesis of P3HT having monomodal distribution by using hydrochloric acid as a quenching reagent whereas bimodal distributed P3HT in which dimerized polymer was included was afforded when water was used as quenching reagent. They proposed that the slow quenching rate of water causes disproportionation of the P3HT-Ni(dppp)-Br complex followed by reductive elimination and eventually provides dimerized polymer. In the present study, the reaction is terminated with Grignard reagent to afford end-capped polymer followed by addition of excess methanol. Therefore, the circumstance in the termination step is quite different from such case. However, it cannot be denied the possibility that dimerization

proceeds via disproportionation mechanism. Predicted structure of the dimerized polymer generated through the disproportionation pathway is given as PT6 in the Scheme 2.6a. If the PT6 undergoes another oxidative addition of Ni catalyst, the dimerized P3HT having an alkyne functional group (PT7) might be generated (Scheme 2.6b).

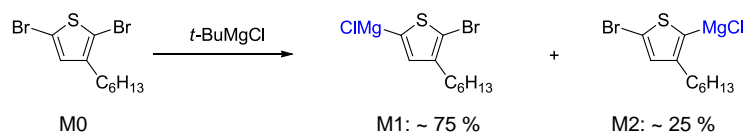
As seen thus far, chemical structure of the dimerized polymer is roughly categorized into two types based on the terminal structure; P3HT having either no functional group (PT4 and PT6) or one functional group (PT5 and PT7) at polymer ends.

However, it seems that there is little possibility of the formation of PT5 and PT7. The first reason is low probability of the occurrence of oxidative addition of Ni catalyst to the  $\alpha$ -chain end itself. The proportion of yielded bis-end-functionalized P3HT estimated by MALDI-TOF MS was only 7% even in the case of single P3HT chain (not dimerized one). Furthermore, in case of dimerized polymer, the oxidative addition to the  $\alpha$ -chain end seems more difficult because Ni catalyst must “chain-walk” along the extended polymer chain until reaching to a chain-end.

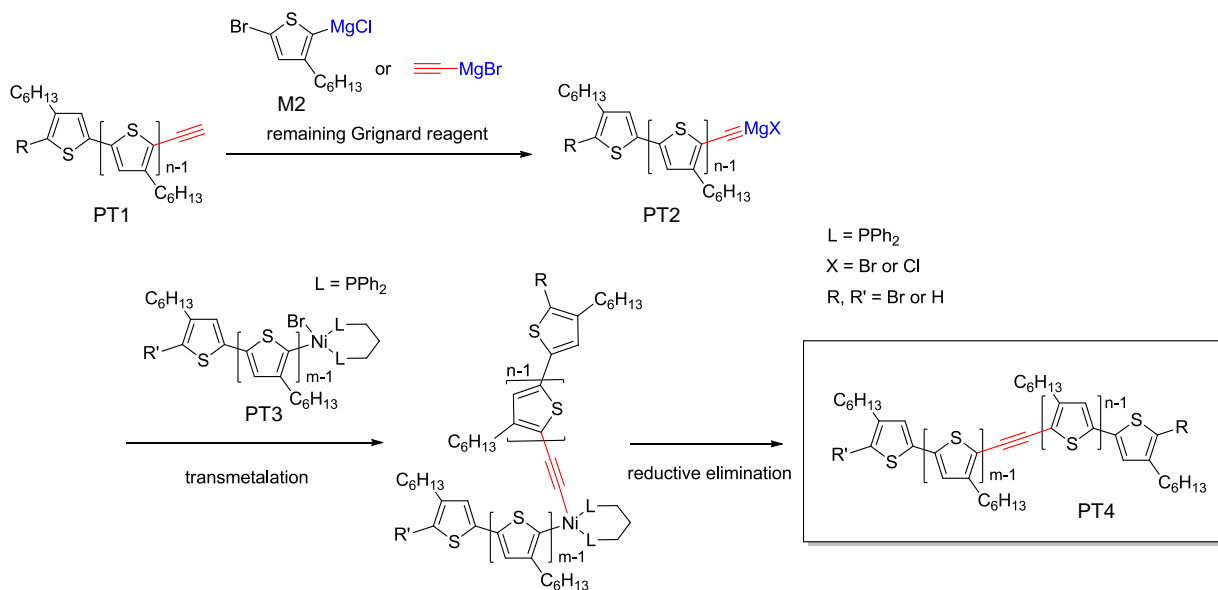
Thus, most likely structure of dimerized polymer is proposed as PT4.

**route A**

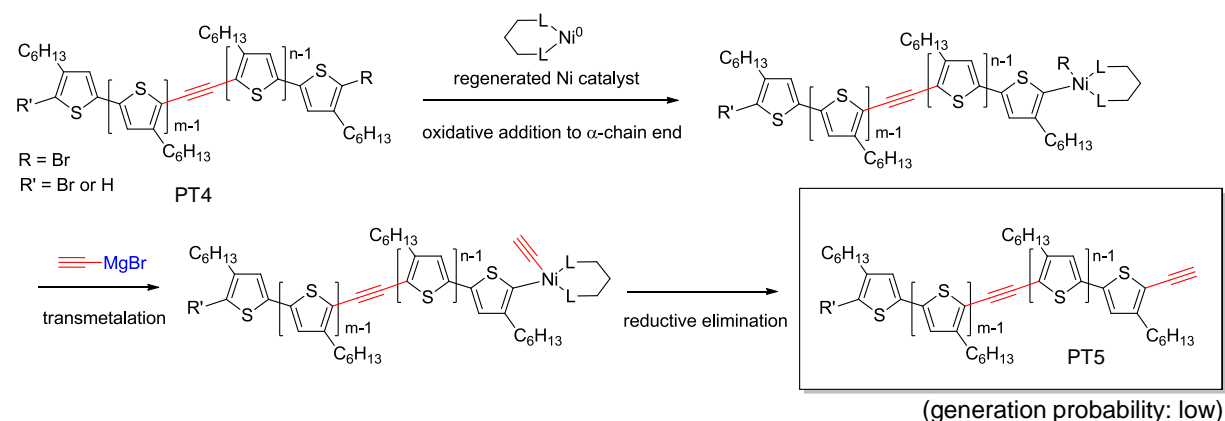
(a) formation of the Grignard monomer



(b) formation of the dimerized polymer with no functional group at chain ends

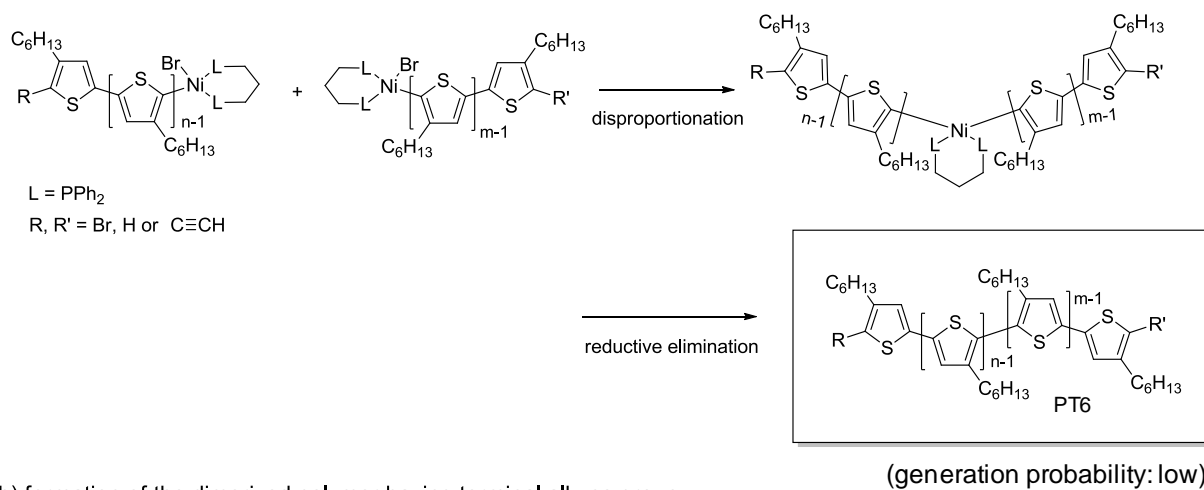


(c) formation of the dimerized polymer having terminal alkyne group

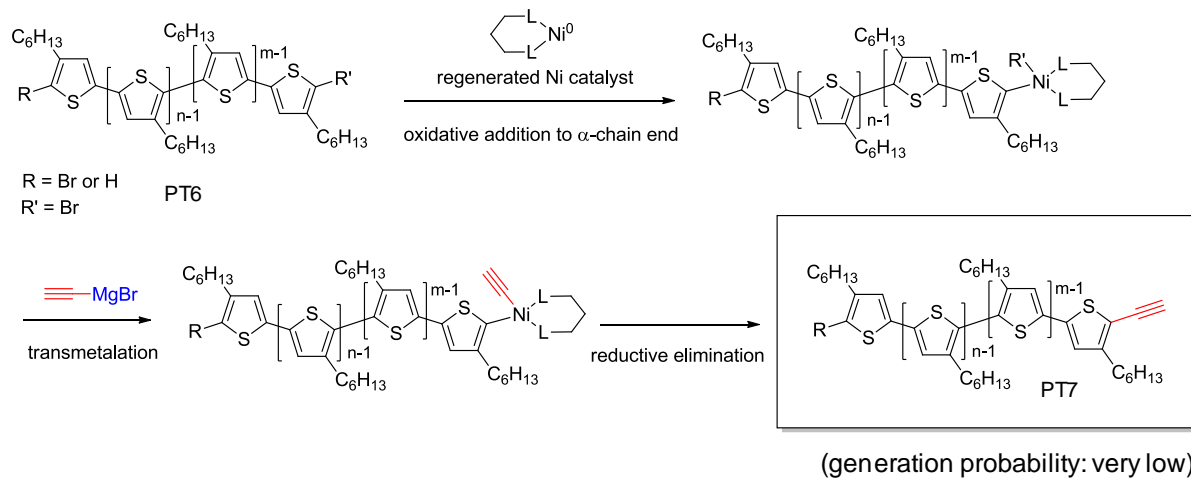
**Scheme 2.5** Proposed mechanism for the homo-dimerization of the polymers (route A).

**route B**

(a) formation of the dimerized polymer with no functional group at chain ends



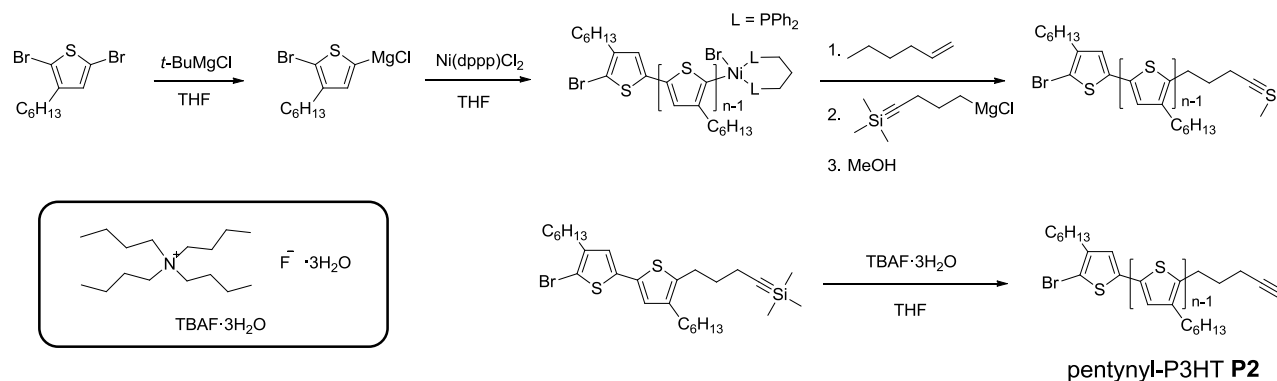
(b) formation of the dimerized polymer having terminal alkyne group

**Scheme 2.6** Proposed mechanism for the homo-dimerization of the polymers (route B).

## Pentynyl-P3HT **P2**

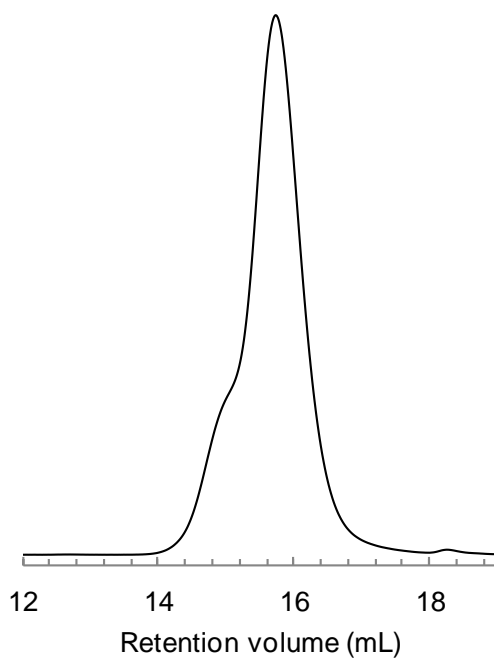
In order to investigate the effect of the structure neighboring an alkyne group on the reactivity of subsequent CuAAC click reaction, another type of alkyne-functionalized P3HT which contains an alkyl spacer between polymer chain and alkyne group was prepared. In a similar way as the synthesis of ethynyl-P3HT **P1**, pentynyl-P3HT **P2** was prepared using the *in situ* functionalization method.

As shown Scheme 2.7, end-capping reaction was conducted with (5-chloromagnesio-1-pentynyl) trimethylsilane in the presence of 1000 equiv. of 1-hexene. After purification, deprotection of trimethylsilane group was performed with TBAF·3H<sub>2</sub>O to afford pentynyl-P3HT **P2** as dark purple solid. The resulting compound was analyzed by MALDI-TOF MS, <sup>1</sup>H NMR, and SEC.

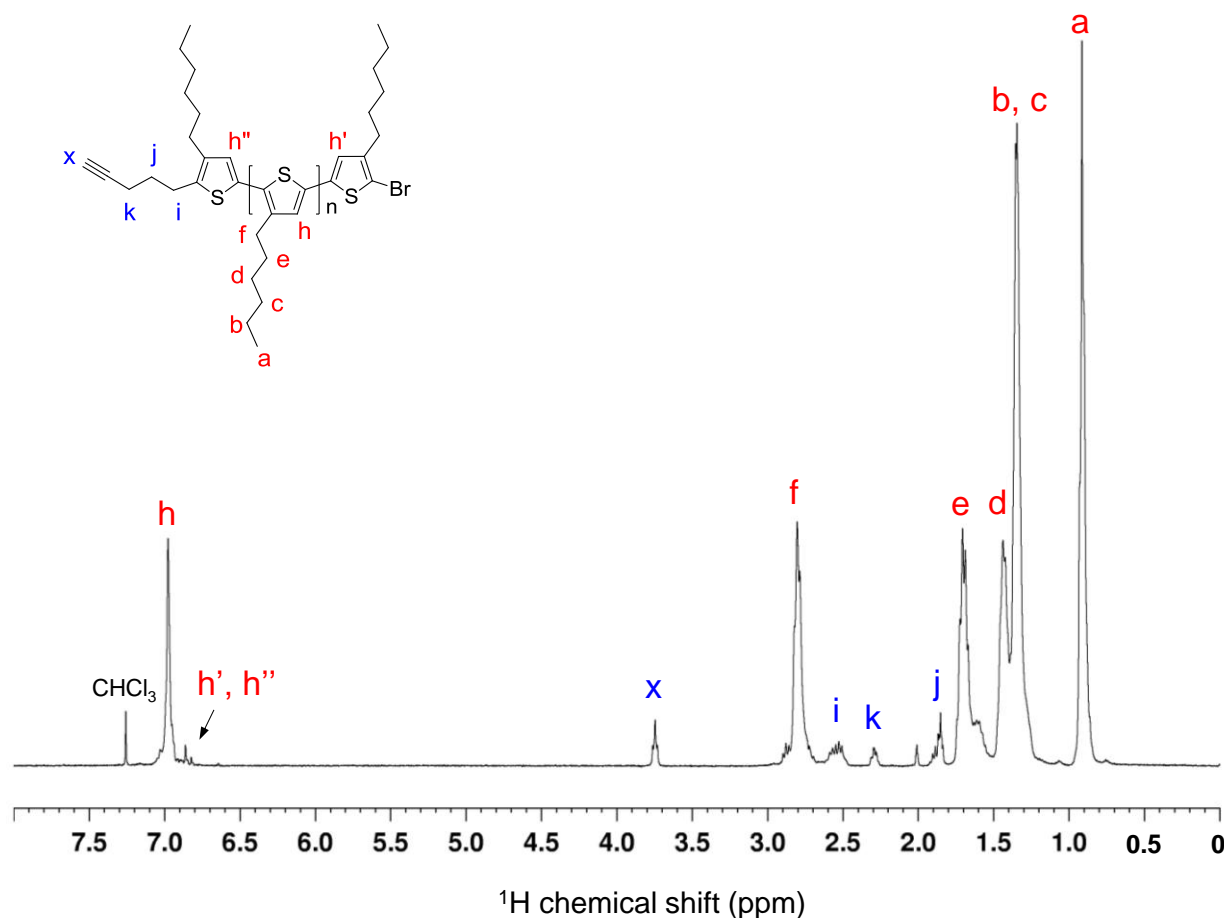


**Scheme 2.7** Synthesis of pentynyl-functionalized P3HT **P2** by the combination of modified Grignard metathesis polymerization and *in situ* functionalization.

SEC trace of the obtained product showed monomodal distribution with a negligible shoulder at higher molecular weight region as shown Figure 2.8. As mentioned above, this small shoulder is probably due to a chain-chain coupling between the polymers because the molecular weight corresponding to the shoulder peak is found nearly twice with respect to those of main peak. The number-average molecular weight ( $M_{n, SEC}$ ) and the dispersity  $D$  ( $M_w/M_n$ ) of pentynyl-P3HT **P2** were determined to be 3689 g/mol and 1.20, respectively based on polystyrene standards.



**Figure 2.8** SEC trace of pentynyl-P3HT **P2** recorded by UV detector.

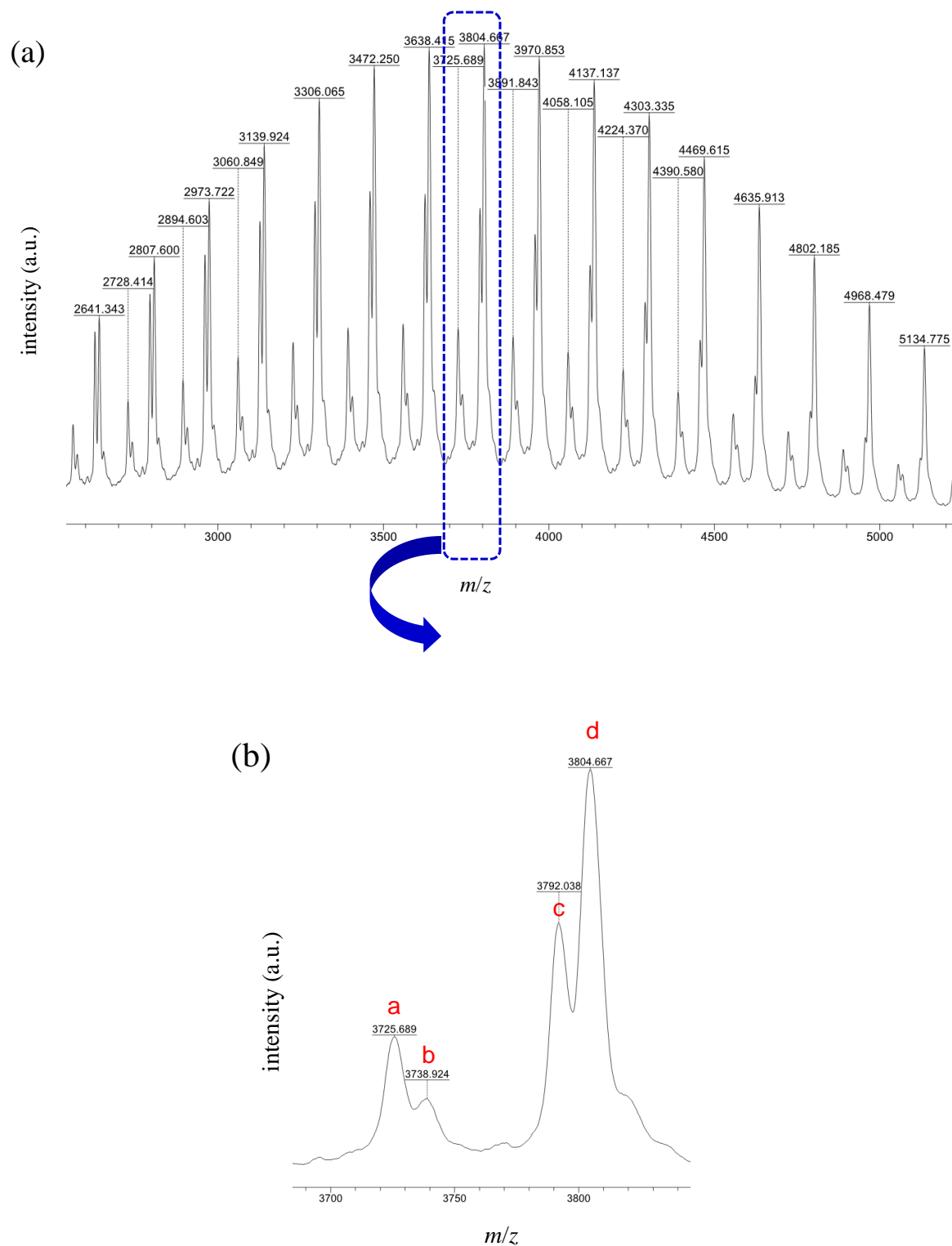


**Figure 2.9**  $^1\text{H}$  NMR spectrum of pentynyl-P3HT **P2** in  $\text{CDCl}_3$ .

The chemical structure of the product was confirmed by  $^1\text{H}$  NMR analysis as shown Figure 2.9. The proton resonance signal at 3.53 ppm assignable to the alkyne proton ( $-\text{C}\equiv\text{CH}$ ) (signal x) and the other signals at 2.3 ppm (signal k), 1.9 ppm (signal j), and 2.5 ppm (signal i) corresponding to the  $\text{CH}_2$  protons of the pentynyl group indicate successful introduction of pentynyl functional group to the polymer chain. HT-HT coupled regioregularity was determined to be 92 % from integral ratio of the signals corresponding to  $\alpha$ -methylene protons, that is, the signal at 2.80 ppm due to HT linkage and the signals around 2.48-2.75 ppm due to head-to-head (HH) linkages.

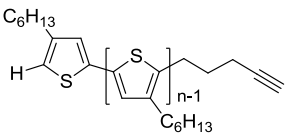
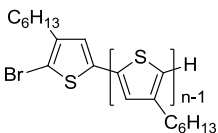
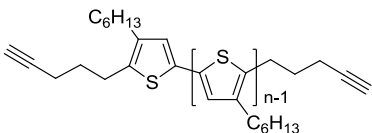
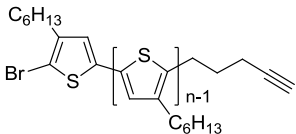
Finally, the end-group composition of P3HT was determined by MALDI-TOF MS analysis. As shown in Figure 2.10, MALDI-TOF MS spectrum of the pentynyl-P3HT **P2** contained four series of peaks separated with an interval of 166 g/mol corresponding to the 3HT unit. Structural assignments of each peak are tabulated in Table 2.4. The major peak series was attributed to the targeted mono-functional P3HT terminated with a pentynyl group at the  $\omega$ -end and bromine at the  $\alpha$ -end with 45 % abundance ratio. Other sub-peaks were identified to be bis-end-functionalized P3HT having pentynyl/pentynyl groups (29 %), mono-functionalized P3HT having pentynyl/H groups (16 %), and non-functional P3HT having H/Br (10 %) end groups. Hence, total amount of mono-functionalized pentynyl-P3HTs that can yield the targeting diblock copolymers was estimated to be 61 %. It is noticeable that while the formation of mono-functional P3HTs were predominant, considerable amount of by-products were generated with this reaction, suggesting that the end-capping reaction proceeded in rather uncontrollable manner compared to the above-mentioned ethynyl-P3HT **P1** experiment. Taking into consideration the mechanism of the formation of by-products, it is reasonable to assume that an increase in amount of non-functional polymer is caused by the low reactivity of Grignard reagent used here. Because the by-product having H/Br end groups (non-functional P3HT) would be afforded when the deactivation of the active chain end occurs in preference to the end-capping reaction with Grignard reagent, (5-chloromagnesio-1-pentynyl) trimethylsilane in this case. On the other hand, an increase in the yield of bis-end-functionalized P3HT is difficult to interpret because diffusion of the Ni catalyst to the  $\alpha$ -chain end would not be affected by the quenching reagent thanks to the excessive addition of 1-hexene which plays a role in stabilizing Ni catalyst. In any case, there is still plenty of room for optimization of the reaction conditions to improve the yield of mono-functionalized P3HT.





**Figure 2.10** (a) MALDI-TOF MS spectrum of pentynyl-P3HT **P2** and (b) magnified part in the range of 22 repeating units.

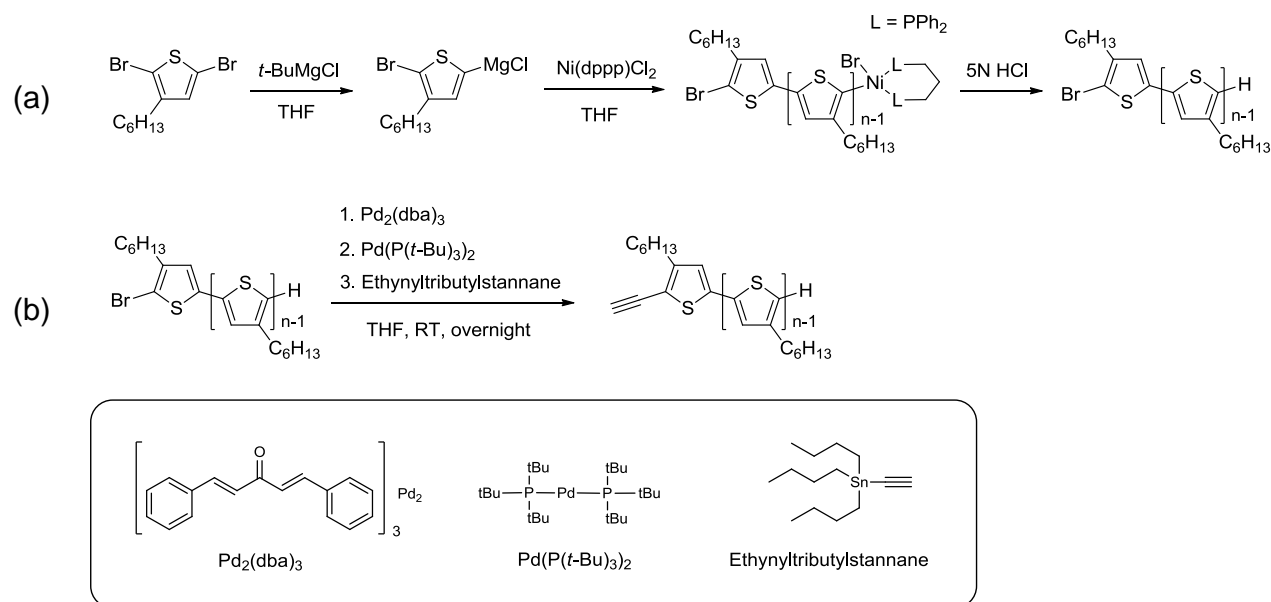
**Table 2.4** Structural assignments of peaks observed in MALDI-TOF MS spectrum of pentynyl-P3HT **P2**

peak code <sup>a</sup>	structure	added ion	n <sup>b</sup>	mass ( <i>m/z</i> )		abundance ratio
				calculated	observed	
a		H <sup>+</sup>	22	3724.86	3725.69	16%
b		H <sup>+</sup>	22	3737.72	3738.92	10%
c		H <sup>+</sup>	22	3792.91	3792.04	29%
d		H <sup>+</sup>	22	3804.77	3804.67	45%

<sup>a</sup> Peak codes are shown in Figure 2.10. <sup>b</sup> Degree of polymerization at the peak maximum.

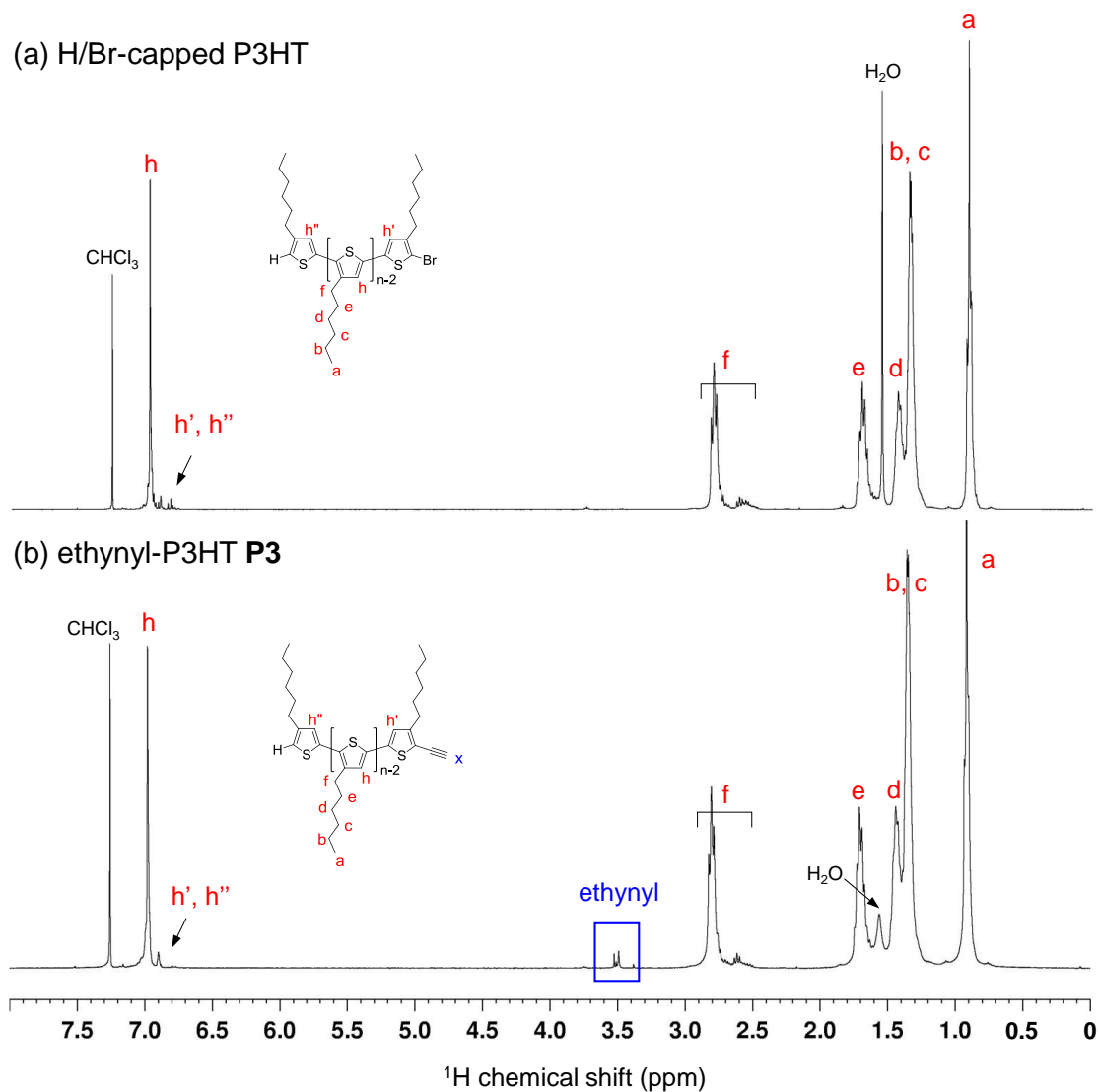
## II.2.2 Post-polymerization modification of Br end-capped P3HT

As describe in above section, the *in situ* functionalization method tends to provide P3HTs with a small amount of high molecular weight impurities presumably originated from alkyne-alkyne homocoupling of P3HT. This dimerization may take place during the end-capping process in the intricate reaction mixture including reactive ethynyl-capped polymer (target product), unreacted Grignard monomers and Ni catalyst. To circumvent this unstable reaction environment and suppress undesired by-product, herein, another synthetic strategy, post-polymerization modification method, was conducted. This method involves two synthetic steps; (i) synthesis of regioregular P3HT bearing a bromine at  $\alpha$ -end and a hydrogen at  $\omega$ -end (Br/H-P3HT) (Scheme 2.8a) and (ii) cross-coupling reaction onto terminal bromine of the Br/H-P3HT with organotin compound (this reaction is referred to Stille reaction) (Scheme 2.8b). In addition to the reduction in probability of the dimerization of P3HT another principal advantage of this method is the ability to purify the stable Br/H-P3HT before coupling reaction via Soxhlet extraction.



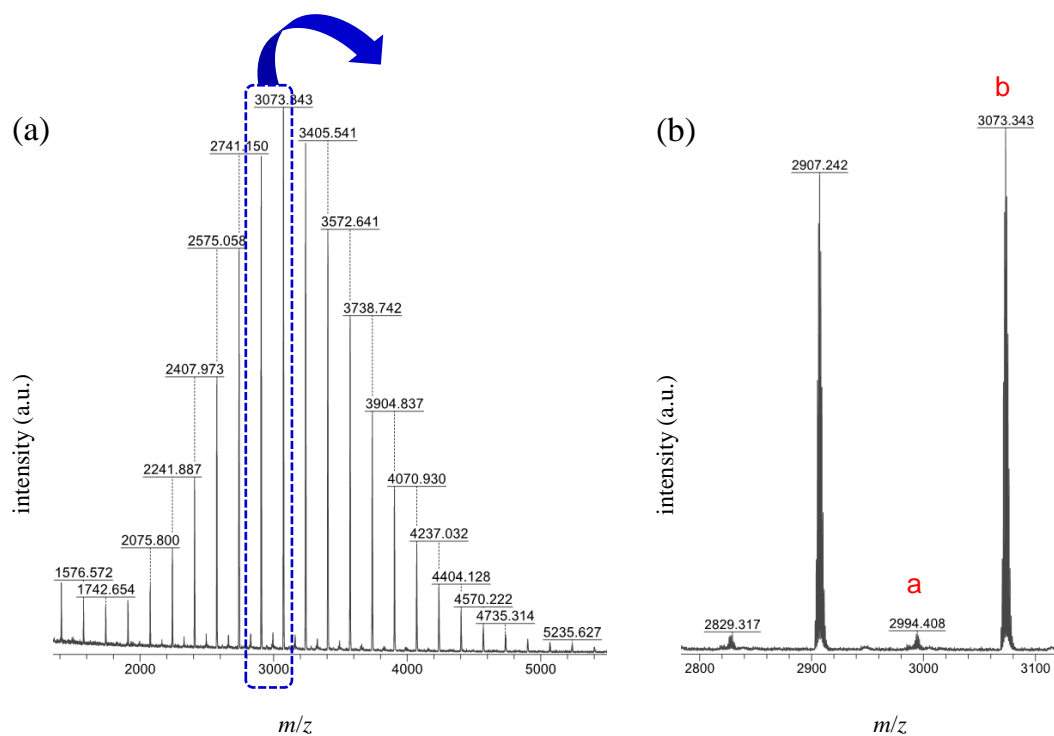
**Scheme 2.8** Synthesis of ethynyl-functionalized P3HT **P3** via modified Grignard metathesis polymerization and post-polymerization functionalization with Stille reaction.

The Br/H-P3HT was prepared via GRIM polymerization followed by quenching with 5 N of hydrochloric acid. The stable Br/H-P3HT was then subjected to consecutive Soxhlet extractions against methanol, hexane, and dichloromethane to afford low dispersity polymers. Finally, Stille cross coupling was carried out in the presence of palladium catalyst between the purified Br/H-P3HT (dichloromethane fraction) and ethynylbutylstannane to give the ethynyl-P3HT **P3**.



**Figure 2.11**  $^1\text{H}$  NMR spectra of (a) H/Br capped P3HT and (b) ethynyl-P3HT **P3**.

Figure 2.11a and 2.11b shows  $^1\text{H}$  NMR spectra of the precursor polymer (Br/H-P3HT), and ethynyl-P3HT **P3**. After the end-functionalization, an appearance of a new peak at 3.53 ppm was observed, indicating a successful introduction of the ethynyl group. The regioregularity was estimated to be more than 94 % for the both polymers. The end-group composition of the polymers was determined by MALDI-TOF MS analysis. Figure 2.12 shows MALDI-TOF MS spectrum of the Br/H-capped P3HT. Two series of the peaks with an interval of 166 g/mol corresponding to the 3HT unit was observed. Structural assignments of the peaks were tabulated in Table 2.5. The major peak series was attributed to the P3HT terminated with Br atom at the  $\alpha$ -end and hydrogen at the  $\omega$ -end with 97 % abundance ratio. The other minor peaks were identified to be the P3HT bearing H atom at both chain-ends (abundance ratio: 3 %). After the cross-coupling reaction, the major peak series entirely shifted toward lower molecular weight region by 55 g/mol corresponding to the difference in molecular weight between bromine and ethynyl group, whereas the minor peaks remained at identical position, indicating that the terminal bromine was selectively converted into ethynyl functional group. Abundance ratios were determined to be 85 % for the target product (ethynyl-P3HT) and 15 % for the by-product (H/H-P3HT). The reason of this increase in the amount of H/H-P3HT from 3 to 15 % is unclear at the moment. Figure 2.14 presents the SEC trace of the ethynyl-P3HT **P3** together with that of the ethynyl-P3HT **P1** which was synthesized by *in situ* end-functionalization method. The shoulder corresponding to the dimerized polymer observed in the SEC trace of the ethynyl-P3HT **P3** was significantly smaller than that of the ethynyl-P3HT **P1**. Furthermore, after Soxhlet extraction process, the ethynyl-P3HT **P3** showed much narrower molecular weight distribution compared with the ethynyl-P3HT **P1** ( $D_{\text{P3}}$  (1.07) <  $D_{\text{P1}}$ (1.35)). Hence, it was found that the post-polymerization modification method is remarkably effective for the reduction in yield of the dimerized P3HT, narrowing of the molecular weight distribution, and elimination of the bis-functional P3HT. Detailed characteristics of the alkyne-functionalized P3HTs synthesized in this study are summarized in Table 2.7.

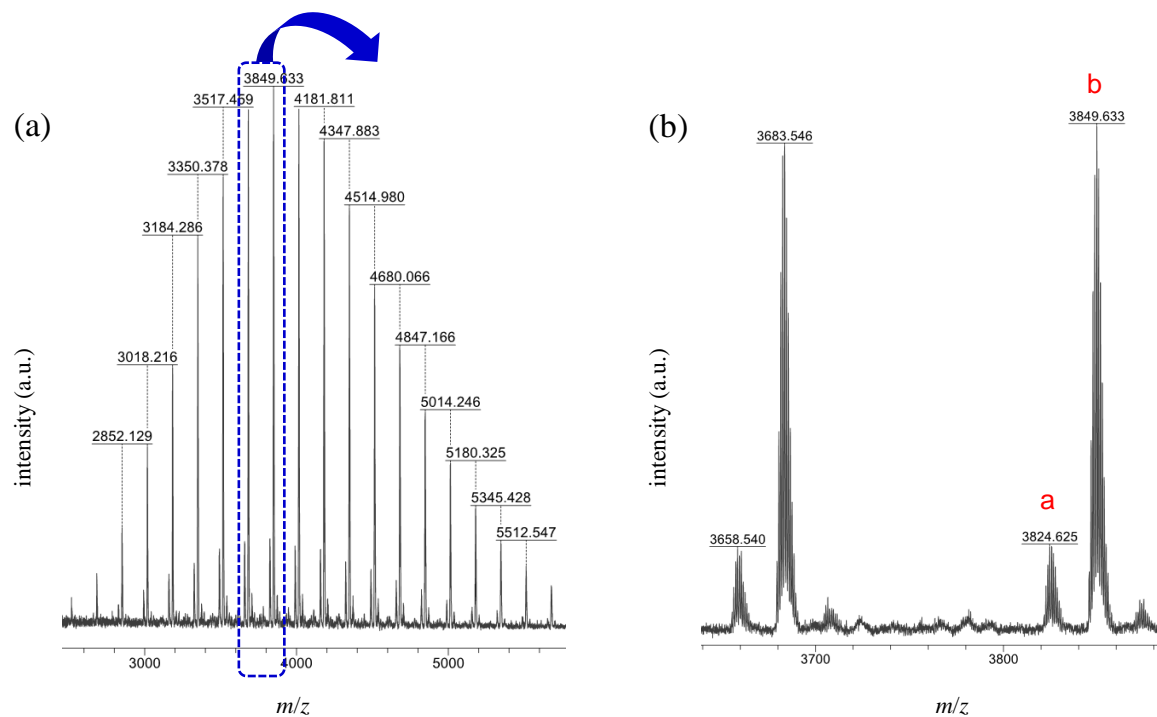


**Figure 2.12** (a) MALDI-TOF MS spectra of H/Br-capped P3HT and (b) magnified part in the range of 17-18 repeating units.

**Table 2.5** Structural assignments of peaks observed in MALDI-TOF MS spectrum of H/Br-capped P3HT

peak code <sup>a</sup>	structure	added ion	n <sup>b</sup>	mass (m/z)		abundance ratio
				calculated	observed	
a		H <sup>+</sup>	18	2994.49	2994.41	3%
b		H <sup>+</sup>	18	3074.40	3073.34	97%

<sup>a</sup> Peak codes are shown in Figure 2.12. <sup>b</sup> Degree of polymerization at the peak maximum.

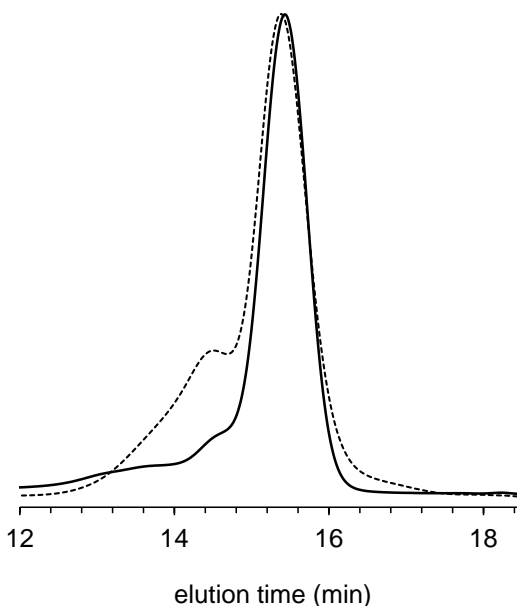


**Figure 2.13** (a) MALDI-TOF MS spectra of ethynyl-P3HT **P3** and (b) magnified part in the range of 22-23 repeating units.

**Table 2.6** Structural assignments of peaks observed in MALDI-TOF MS spectrum of ethynyl-P3HT **P3**

peak code <sup>a</sup>	structure	added ion	n <sup>b</sup>	mass (m/z)		abundance ratio
				calculated	observed	
a		H <sup>+</sup>	23	3826.90	3824.63	15%
b		H <sup>+</sup>	23	3850.90	3849.63	85%

<sup>a</sup>Peak codes are shown in Figure 2.13. <sup>b</sup>Degree of polymerization at the peak maximum.



**Figure 2.14** Comparison of the SEC traces of ethynyl-P3HT prepared by post-polymerization functionalization method (solid line) and *in situ* functionalization method (dotted line), respectively.

**Table 2.7** Characterization details of the synthesized P3HTs in this study

entry	polymer	protocol	$M_{p, \text{MALDI, P3HT}}^a$ (g/mol)	$\bar{D}^b$ ( $M_w / M_n$ )	% HT <sup>c</sup> (%)	end-functionality <sup>d</sup>			
						functional group	mono-endcapped	bis-endcapped	non-endcapped
P1	ethynyl-P3HT	<i>in situ</i> functionalization	3596	1.35	> 95	ethynyl	91	7	2
P2	pentynyl-P3HT	<i>in situ</i> functionalization	3805	1.20	> 92	pentynyl	61	29	10
P3	ethynyl-P3HT	post-polymerization functionalization	3850	1.07	> 94	ethynyl	85	0	15

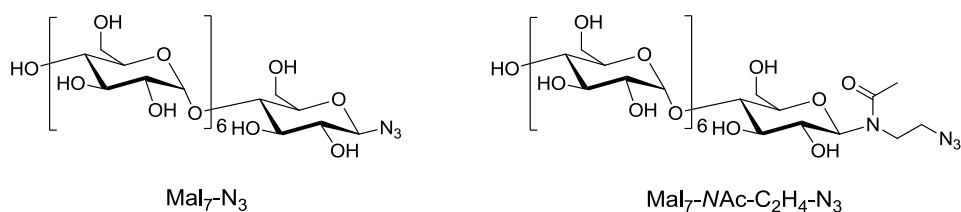
<sup>a</sup> Molecular weight at the peak maximum determined by MALDI-TOF MS. <sup>b</sup> Dispersity determined by SEC in THF based on PS standards.

<sup>c</sup> HT coupled regioregularity determined by <sup>1</sup>H NMR spectroscopy. <sup>d</sup> Degree of polymer chain-end functionalities determined by MALDI-TOF MS.



### II.3 Synthesis of azido-functionalized maltoheptaose

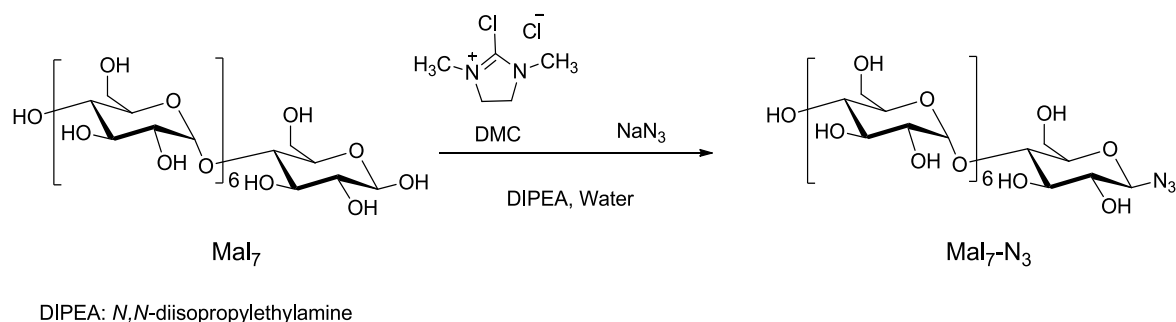
To introduce a “clickable” function to the oligosaccharide, two types of azido-functionalized maltoheptaose, *i.e.* Mal<sub>7</sub>-N<sub>3</sub> and Mal<sub>7</sub>-Nac-C<sub>2</sub>H<sub>4</sub>-N<sub>3</sub> (Scheme 2.9), were prepared by the direct anomeric azidation and *N*-acetylation method, respectively.



**Scheme 2.9** Azido-functionalized maltoheptaoses synthesized in this study.

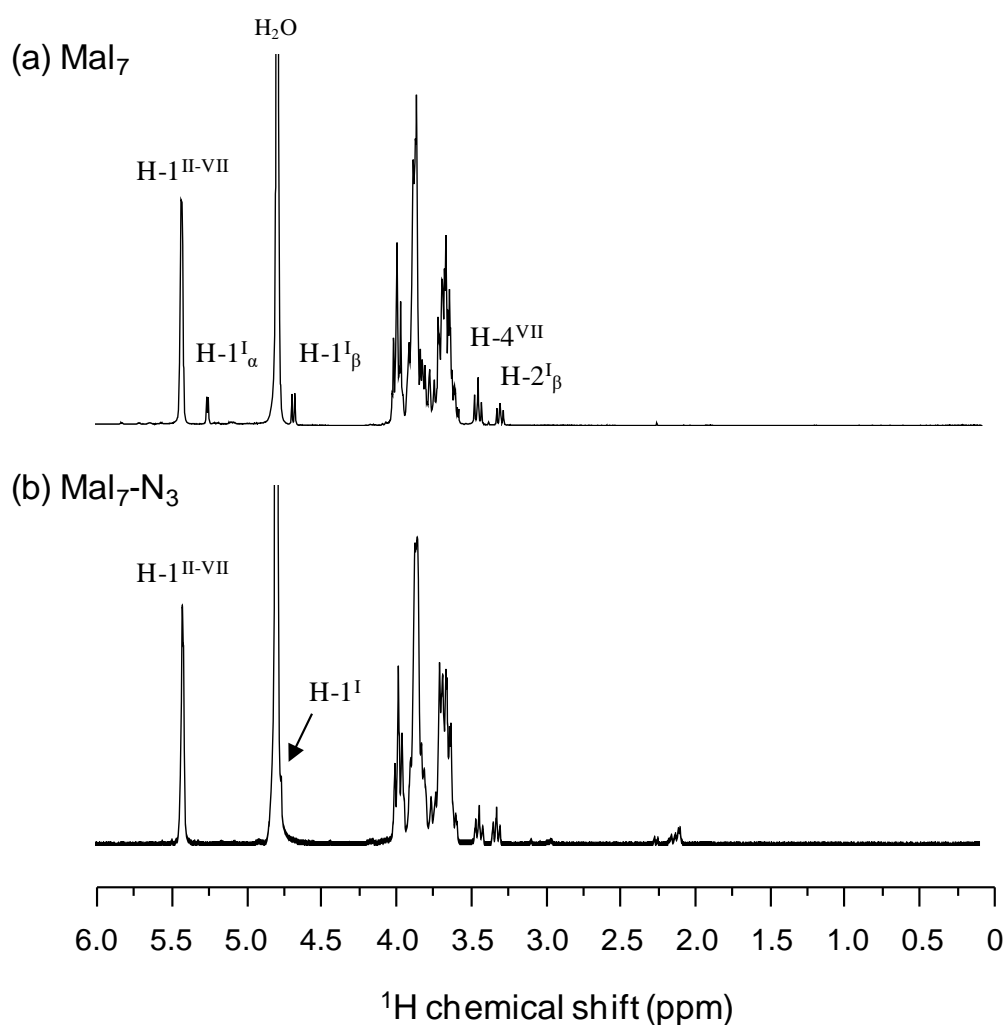
#### Mal<sub>7</sub>-N<sub>3</sub>

In general, selective functionalization of sugars at anomeric position requires multiple-steps involving protection and deprotection of hydroxyl groups. Therefore, the total chemical process becomes laborious and time-consuming. To overcome this shortcoming, Shoda *et al.* have developed a one-step functionalization method for unprotected sugars by using 2-chloro-1,3-dimethylimidazolium chloride (DMC) as a selective activation agent of the anomeric hydroxyl group.<sup>9</sup> In the present study, this strategy was applied with minor modification to prepare the azido-functionalized maltoheptaose (Mal<sub>7</sub>-N<sub>3</sub>) (Scheme 2.10).



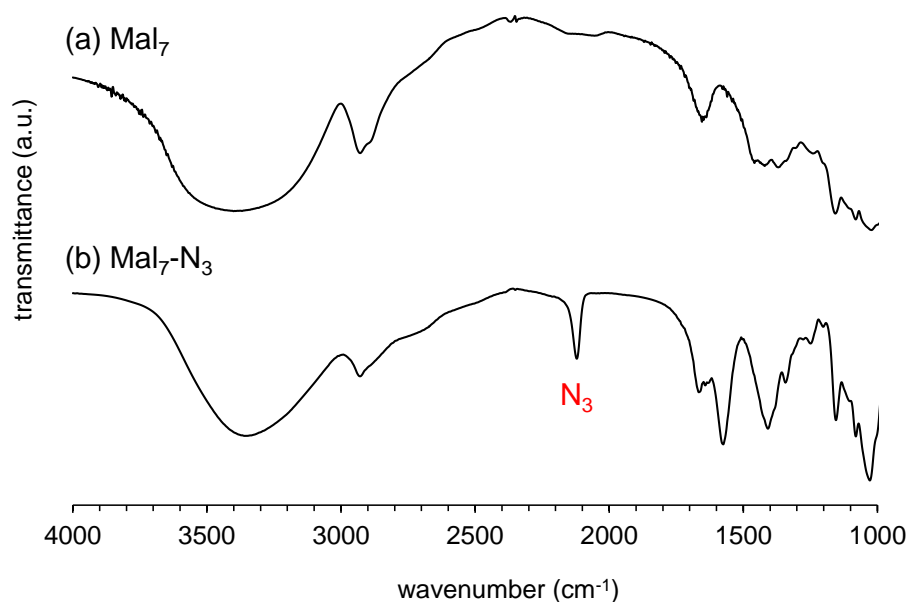
**Scheme 2.10** Direct synthesis of azido-functionalized maltoheptaose Mal<sub>7</sub>-N<sub>3</sub>.

To an aqueous solution of maltoheptaose (1 equiv.) and  $\text{NaN}_3$  (250 equiv.), DMC (25 equiv.) and DIPEA (75 equiv.) were added, and the mixture was stirred at room temperature until the TLC (eluent: acetonitrile/water = 7/3) showed complete disappearance of the starting material. The mixture was first dialyzed against water using a dialysis membrane, and then freeze-dried to afford  $\text{Mal}_7\text{-N}_3$  as a white solid (yield: 80 %). The resulting product was then characterized by  $^1\text{H}$  NMR, MALDI TOF MS and FT-IR.

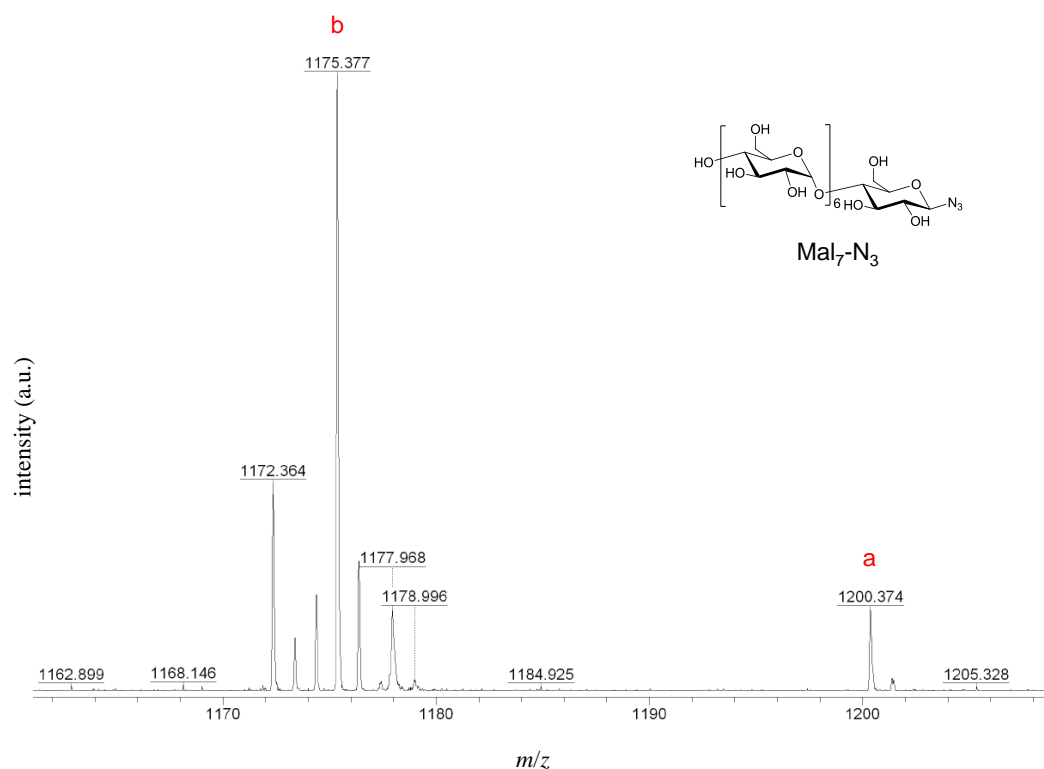


**Figure 2.15**  $^1\text{H}$  NMR spectra of (a)  $\text{Mal}_7$  and (b)  $\text{Mal}_7\text{-N}_3$  in  $\text{D}_2\text{O}$ .

The  $^1\text{H}$  NMR spectrum of the product exhibited a signal at 4.7 ppm assignable to the anomeric proton of the  $\text{Mal}_7\text{-N}_3$  (Figure 2.15). The structure of the product was further investigated by MALDI TOF MS analysis. As shown Figure 2.17 and Table 2.8, two characteristics adduct ion peaks with  $\text{Na}^+$  are found at  $m/z = 1200$  and  $1175$  which correspond to the molecular ion peak of the targeted compound ( $\text{Mal}_7\text{-N}_3 + \text{Na}^+$ ) and its fragment ion ( $\text{Mal}_7\text{-NH}_2 + \text{Na}^+$ ). The FT-IR spectrum of the product exhibits a clear evidence of the successful introduction of an azido group by detecting the characteristic peak of azido group at *ca.*  $2100\text{ cm}^{-1}$  (Figure 2.16). On the basis of these results, we confirmed the formation of targeted  $\text{Mal}_7\text{-N}_3$ .



**Figure 2.16** FT-IR spectra of (a)  $\text{Mal}_7$  and (b)  $\text{Mal}_7\text{-N}_3$ .



**Figure 2.17** MALDI-TOF MS spectrum of Mal<sub>7</sub>-N<sub>3</sub> in positive mode.

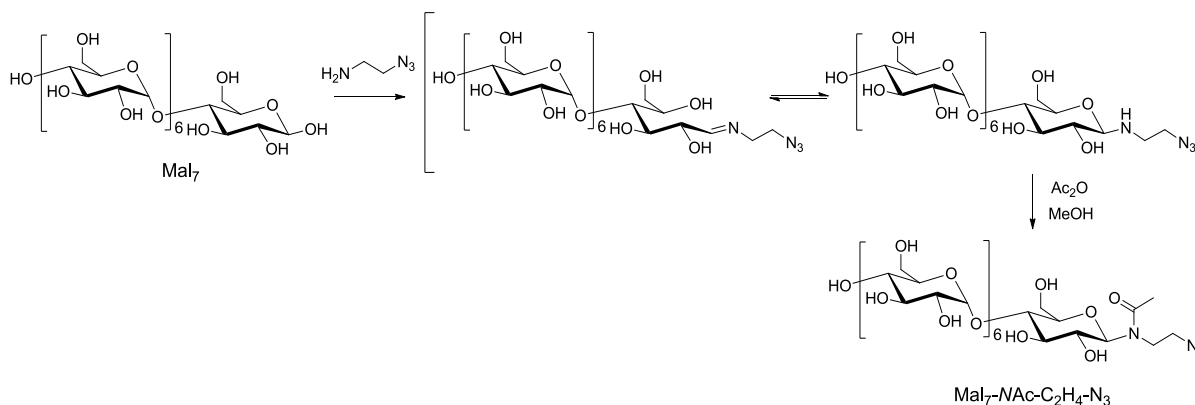
**Table 2.8** Structural assignments of peaks observed in MALDI-TOF MS spectrum

peak code <sup>a</sup>	structure	added ion	mass ( <i>m/z</i> )	
			calculated	observed
a		Na <sup>+</sup>	1200.38	1200.37
b		Na <sup>+</sup>	1174.39	1175.37

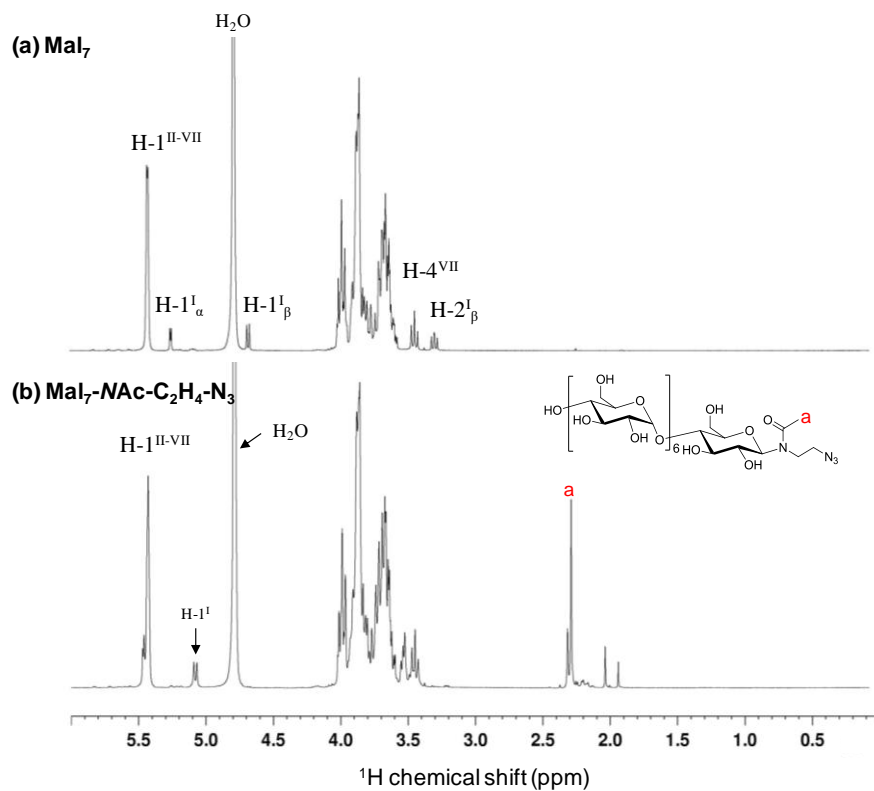
<sup>a</sup> Peak codes are shown in Figure 2.17.

**Mal<sub>7</sub>-NAc-C<sub>2</sub>H<sub>4</sub>-N<sub>3</sub>**

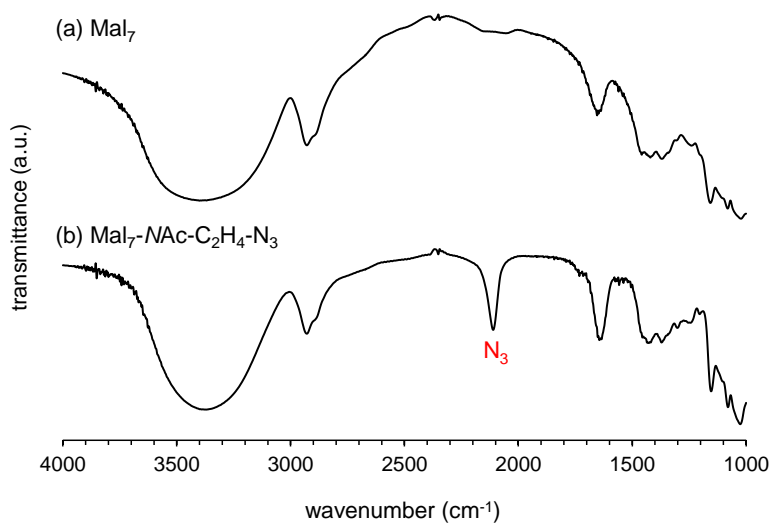
To study an effect of the structure around the azido functional group on the reactivity of the click reaction, another type of azido-functionalized maltoheptaose, *N*-(β-Maltoheptaosyl)-*N*-(2-azidoethyl)-acetoamide (Mal<sub>7</sub>-NAc-C<sub>2</sub>H<sub>4</sub>-N<sub>3</sub>), was synthesised as shown Scheme 2.11. Maltoheptaose was suspended in neat 2-azidoethylamine at room temperature until the TLC shows complete disappearance of the starting material. The unstable reaction intermediate was converted to the stable compound by *N*-acetylation to afford *N*-(β-Maltoheptaosyl)-*N*-(2-azidoethyl)-acetoamide as a white solid. Figure 2.18 shows <sup>1</sup>H NMR spectra of the obtained product and starting material. The spectrum of the product displayed the characteristic signals at 5.1 ppm and 2.3 ppm corresponding to the anomeric proton and *N*-acetyl proton. In addition, the FT-IR spectrum of the product showed a characteristic absorption peak around 2100 cm<sup>-1</sup> corresponding to the azido group, suggesting successful introduction of azido functional group to the maltoheptaose (Figure 2.19). In order to identify the chemical structure, MALDI-TOF MS measurement was conducted (Figure 2.20 and Table 2.9). In the positive ion mode, we found two MALDI-TOF MS characteristic peaks corresponding to the target compound with potassium ion ([M+K]<sup>+</sup>; *m/z* 1301) and sodium ion ([M+Na]<sup>+</sup>; *m/z* 1285). In addition, two other peaks derived from the fragmentation of the product were also observed as potassium adduct (*m/z* 1275) and sodium adduct (*m/z* 1259). Therefore, it was confirmed that the obtained product was the targeted Mal<sub>7</sub>-NAc-C<sub>2</sub>H<sub>4</sub>-N<sub>3</sub>.



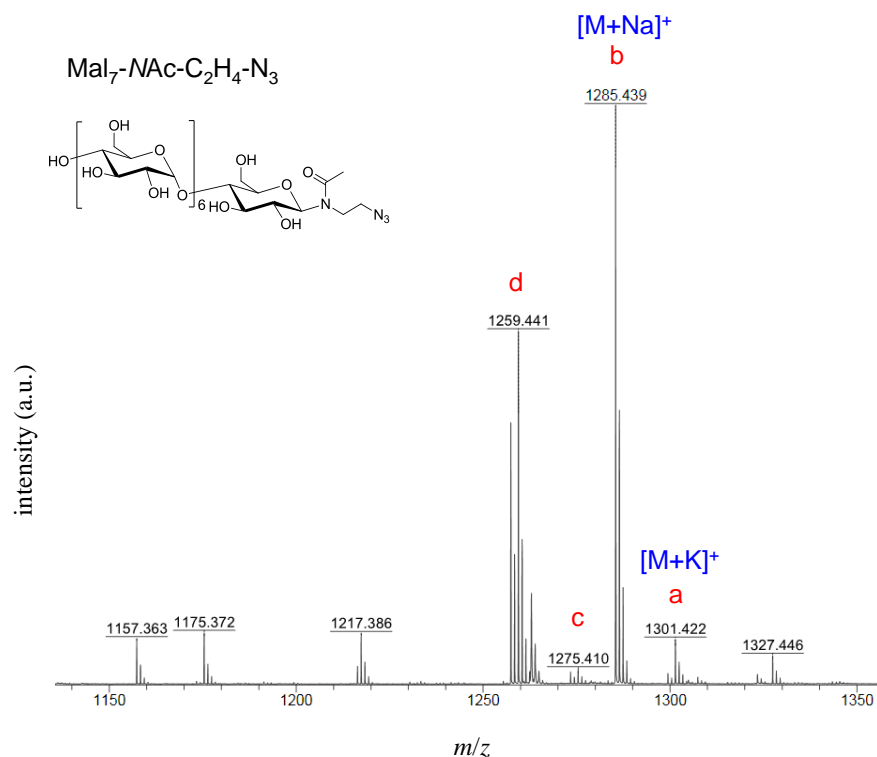
**Scheme 2.11** Synthesis of azido-functionalized maltoheptaose Mal<sub>7</sub>-NAc-C<sub>2</sub>H<sub>4</sub>-N<sub>3</sub>.



**Figure 2.18**  $^1\text{H}$  NMR spectra of (a)  $\text{Mal}_7$  and (b)  $\text{Mal}_7\text{-NAc-C}_2\text{H}_4\text{-N}_3$  in  $\text{D}_2\text{O}$ .



**Figure 2.19** FT-IR spectra of (a)  $\text{Mal}_7$  and (b)  $\text{Mal}_7\text{-NAc-C}_2\text{H}_4\text{-N}_3$ .



**Figure 2.20** MALDI-TOF MS spectrum of Mal<sub>7</sub>-NAc-C<sub>2</sub>H<sub>4</sub>-N<sub>3</sub> in positive mode.

**Table 2.9** Structural assignments of peaks observed in MALDI-TOF MS spectrum

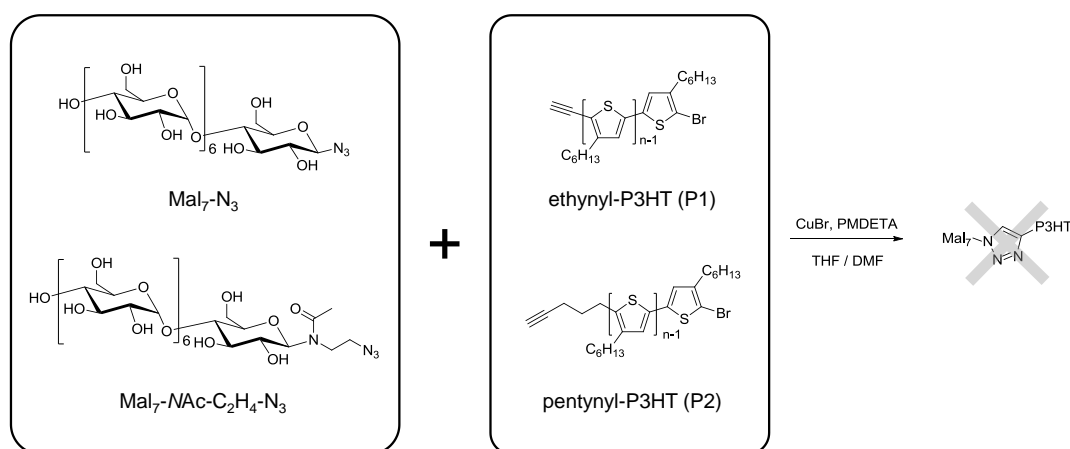
peak code <sup>a</sup>	structure	added ion	mass ( <i>m/z</i> )	
			calculated	observed
a		K <sup>+</sup>	1301.40	1301.42
b		Na <sup>+</sup>	1285.43	1285.44
c		K <sup>+</sup>	1275.41	1275.41
d		Na <sup>+</sup>	1259.44	1259.44

<sup>a</sup> Peak codes are shown in Figure 2.20.

## II.4 Synthesis of P3HT-*b*-oligosaccharide block copolymers

### II.4.1 Attempts to direct click reaction between alkyne-P3HT and Mal<sub>7</sub>-N<sub>3</sub>


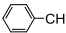
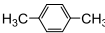
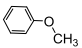
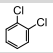
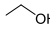
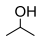
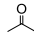
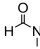
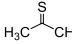
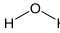
Attempts to couple between obtained P3HT and maltoheptaose molecular bricks were then carried out in order to prepare P3HT-*b*-Mal<sub>7</sub>. First, a direct coupling reaction of ethynyl-P3HT **P1** with Mal<sub>7</sub>-N<sub>3</sub> was performed by copper-catalyzed azide-alkyne cycloaddition, the so-called CuAAC "click" reaction, using CuBr and PMDETA as a catalytic system (Scheme 2.12). A major concern for this reaction was the choice of solvent. Since the solubilities of the individual segments, hydrophobic P3HT and the hydrophilic maltoheptaose moiety, are very different, no common single solvent for both moieties was found (Table 2.10). Indeed, we already encountered a similar difficulty concerning a solubility in our previous study on the synthesis of ABA-type triblock copolymers consisting of hydrophilic maltoheptaose (A block) and hydrophobic polystyrene (B block) via CuAAC click reaction. This problem was eventually resolved by mixing THF and DMF which are good solvents for polystyrene and maltoheptaose block, respectively. The target polymer has been successfully obtained. Based on this result, a similar condition was applied to the present reaction. According to the solubility test, the composition of the mix solvent for this system was optimized to be THF/DMF = 4/1 (see Table 2.10).



**Scheme 2.12** Attempts to direct click reaction between alkyne-functionalized P3HT and azido-functionalized Mal<sub>7</sub>.



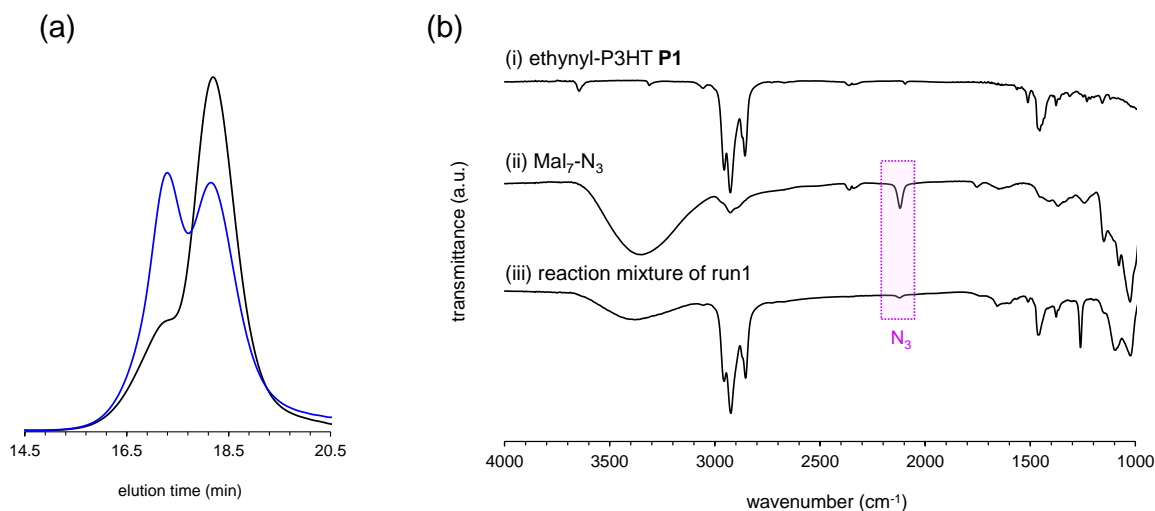
**Table 2.10** Solubility of P3HT and Mal<sub>7</sub>

		b.p.	m.p.	solubility in water	dipole moment	P3HT	Mal <sub>7</sub>
<b>Heteroaromatics</b>							
THF		66 °C	-108 °C	miscible	1.63 D	+	—
<b>Aromatics</b>							
toluene		111 °C	-95 °C	0.52 g/L (20°C)	0.36 D	+	—
p-xylene		138 °C	13 °C	insoluble	0.07 D	+	—
anisole		154 °C	-37 °C	insoluble	1.38 D	+	—
<b>Halogenated aromatics</b>							
o-dichlorobenzene		181 °C	-17 °C	insoluble	2.5 D	+	—
<b>Halogenated alkanes</b>							
chloroform	CHCl <sub>3</sub>	61 °C	64 °C	8.09 g/L (20°C)	1.15 D	+	—
dichloromethane	CH <sub>2</sub> Cl <sub>2</sub>	40 °C	-97 °C	17.5 g/L (25°C)	1.6 D	+	—
<b>Alcohols</b>							
methanol	CH <sub>3</sub> OH	65 °C	-98 °C	miscible	1.69 D	—	+
ethanol		78 °C	-114 °C	miscible	1.69 D	—	—
isoproryl alcohol		83 °C	-89 °C	miscible	1.66 D	—	—
<b>Polar sovents</b>							
acetone		56 °C	-95 °C	miscible	2.91 D	—	—
DMF		152-154 °C	-61 °C	miscible	3.86 D	—	+
DMSO		189 °C	19 °C	miscible	4.3 D	—	+
water		100 °C	0 °C	—	1.85 D	—	+
<b>Mix sovents</b>							
THF/DMF = 1/1						—	+
THF/DMF = 2/1						—	+
THF/DMF = 4/1						+	+

+: soluble, -: insoluble

In a typical experiment, Mal<sub>7</sub>-N<sub>3</sub> and PMDETA were added to a flask A and dissolved in DMF. In another flask B, end-functionalized P3HT and CuBr were added and dissolved in THF. Both mixtures were purged with argon for at least 5 min. The content of flask A was transferred to flask B via cannula under argon atmosphere. The reaction mixture was stirred at 40 °C for several days. The extent of reaction was monitored by SEC and FT-IR.

Figure 2.21b shows an example of the FT-IR spectra of the reaction intermediate (run 1 in Table 2.11). In the spectrum of the reaction mixture (Figure 2.21b.iii), a significant decrease of the spectral intensity of a characteristic peak at 2120 cm<sup>-1</sup> due to Mal<sub>7</sub> azido group is observed, suggesting a partial consumption of the azido group during the reaction. Also, SEC trace of the resulting product (blue line in Figure 2.21a) indicates that a portion of starting material was converted to higher molecular weight compound. From these results, the obtained product was initially supposed as the target block copolymer, *i.e.* P3HT<sub>P1</sub>-*b*-Mal<sub>7</sub>. Thus, to achieve complete conversion of ethynyl-P3HT **P1** to the desired block copolymer, the reaction condition was optimized by changing various parameters, such as catalytic system, reactant ratio, reaction time, and temperature, *etc.* Table 2.11 summarizes the all experiments carried out. However, no significant improvement was observed in all cases. Almost a half amount of ethynyl-P3HT **P1** charged was always remaining as unreacted substance.



**Figure 2.21** (a) SEC traces of ethynyl-P3HT **P1** (black line) and the resulting product of run 1 (blue line) recorded by UV detector. (b) FT-IR spectra of (i) ethynyl-P3HT **P1**, (ii) Mal<sub>7</sub>-N<sub>3</sub>, and (iii) reaction mixture of run1.

**Table 2.11** Summary of the direct click reaction experiments described in this chapter

run	P3HT	sugar	catalyst	[sugar] / [P3HT] <sub>final</sub> <sup>a</sup>	[catalyst]/[P3HT] <sub>final</sub> <sup>a</sup>	solvent	temperature (°C)	reaction time
1	ethynyl-P3HT <b>P1</b>	Mal- <sub>7</sub> -N <sub>3</sub>	CuBr / PMDETA	1.3 equiv.	3 equiv.	THF / DMF	40 °C	17 days
2	ethynyl-P3HT <b>P1</b>	Mal- <sub>7</sub> -N <sub>3</sub>	CuBr / PMDETA	1.3 equiv.	3 equiv.	THF / DMF	80 °C microwave <sup>b</sup>	3h
3	ethynyl-P3HT <b>P1</b>	Mal- <sub>7</sub> -N <sub>3</sub>	CuI·P(OEt) <sub>3</sub> / PMDETA	1.3 equiv.	3 equiv.	THF / DMF	40 °C	7 days
4	ethynyl-P3HT <b>P1</b>	Mal- <sub>7</sub> -N Ac-C <sub>2</sub> H <sub>4</sub> -N <sub>3</sub>	CuBr / PMDETA	2.8 equiv.	2 equiv.	THF / DMF	40 °C	10 days
5	ethynyl-P3HT <b>P1</b>	Mal- <sub>7</sub> -N Ac-C <sub>2</sub> H <sub>4</sub> -N <sub>3</sub>	CuBr / PMDETA	1.8 equiv.	3 equiv.	THF / DMF	40 °C	13 days
6	pentynyl-P3HT <b>P2</b>	Mal- <sub>7</sub> -N Ac-C <sub>2</sub> H <sub>4</sub> -N <sub>3</sub>	CuBr / PMDETA	2.3 equiv.	3 equiv.	THF / DMF	40 °C	11 days

General conditions: Initial molar ratio of [sugar]/[P3HT] and [catalyst]/[P3HT] were 1.3 and 1.5 equiv., respectively. Initial volume ratio of mixed solvent THF/DMF was 4/1.

<sup>a</sup> Sugar and catalyst were added in several times. [catalyst]/[P3HT]<sub>final</sub> and [catalyst]/[P3HT]<sub>final</sub> indicate the final molar ratio of the sugar to the polymer chain and the catalyst to the polymer chain, respectively. <sup>b</sup> Reaction was conducted under microwave irradiation.

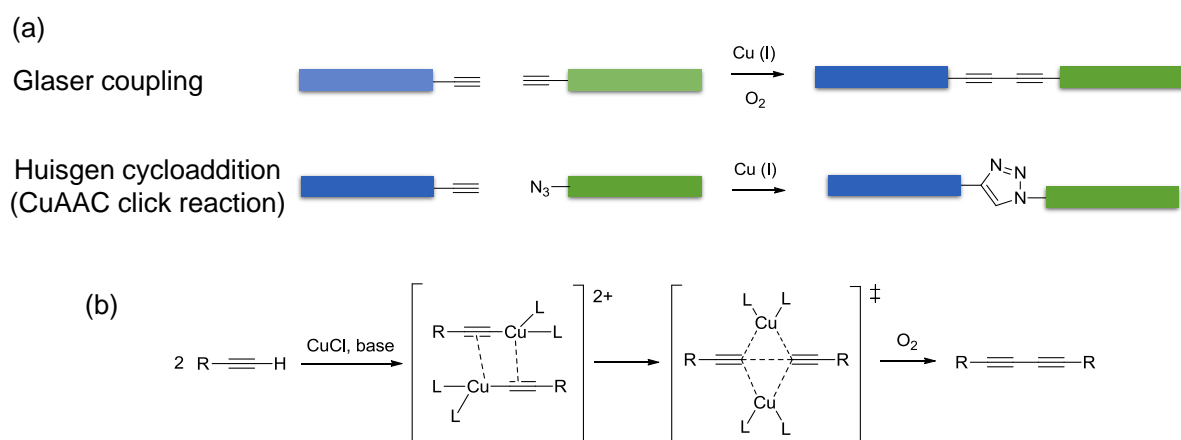
According to Cloutet and Vignau *et al.*, the electronic and steric environment around the alkynyl group is a crucial parameter for "click" reaction.<sup>10</sup> In this report, they have prepared two different alkyne-functionalized P3HTs, *i.e.* ethynyl-P3HT and  $\alpha,\omega$ -pentynyl-P3HT, and attempted to synthesize poly(3-hexylthiophen)-*block*-polystyrene block copolymer via CuAAC "click" reaction. However, they have succeeded in acquiring the block copolymer with only  $\alpha,\omega$ -pentynyl-P3HT which is connected with a functional group three bonds away from polymer backbone. This result was explained from the viewpoint of a reactivity of the functional group. Since a triple bond of ethynyl group can conjugate with  $\pi$ -conjugated P3HT main chain, it would be stabilized by delocalization of electrons; thereby the reactivity will be reduced. Thus the "click" reaction did not work. On the other hand, in the case of the  $\alpha,\omega$ -pentynyl-P3HT, the coupling reaction worked well because the  $\alpha,\omega$ -pentynyl-P3HT is free from harmful influence of  $\pi$ -conjugated system thanks to an alkyl spacer between triple bond and main chain.

On the basis of this report, the click reaction between pentynyl-P3HT **P2** and Mal<sub>7</sub>-NAC-C<sub>2</sub>H<sub>4</sub>-N<sub>3</sub> was then attempted under the same condition as run 1. Introducing a spacer to both blocks was expected to be sterically and electronically more favorable for "click" reaction. Even so, we were again unsuccessful in achieving complete conversion of starting material to a higher molecular compound. SEC trace of the resulting product showed bimodal molar mass distribution similar to those of run 1 (Figure 2.21a).

By reconsideration of all above data, it became apparent that the resulting products were not the target block copolymers but dimerized P3HTs. Especially by close inspection of the SEC traces, it was found that the molecular weight of the obtained product was nearly twice with respect to that of starting material, suggesting the occurrence of chain-chain coupling of the polymer. Recently, Heise *et al.* reported that the Glaser coupling would take place as a side reaction during the Huisgen-type "click" reaction in the specific conditions.<sup>11,12</sup> They perceived this finding in the course of the study on the surface functionalization of macroporous polymer by using "click" reaction. Various alkyne-functionalized substances were examined to react with azido-functionalized surface. It was found that the reaction did not proceed when the high molecular weight polymer (alkyne-functionalized polystyrene) was used, whereas low molecular weight alkynes were successfully coupled with the azido-functionalized surface. Homo-coupling of the alkyne-functionalized polystyrene rather occurred instead of the "click" reaction. It was

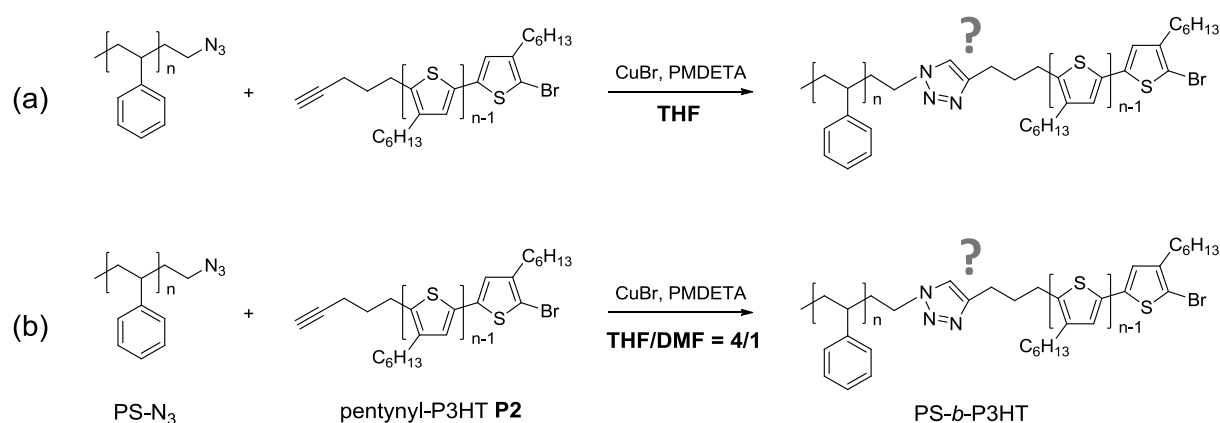
presumed that the poor accessibility of the alkyne group to the hindered azide group located on the surface is a contributing factor of the impediment of the “click” reaction.

The Glaser reaction is a class of homo-coupling reaction between terminal alkynes that generates symmetric diyne via oxidative homo-coupling. The reaction is mediated by copper catalyst (ex. copper(I) chloride and copper(I) bromide) and proceeded under basic condition in the presence of oxygen. Namely, the Glaser coupling occurs under very similar conditions as the Huisgen-type CuAAC “click” reaction (Scheme 2.13). Therefore, it is reasonable to assume that the Glaser coupling preferentially occurred in the current system even though the CuAAC “click” reaction is generally more predominant and proceeds faster than any other reaction with high selectivity under ideal conditions. The primary cause of this failure may be lack of the solubility of the two segments. In the mixed solvent of THF and DMF (THF/DMF = 4/1), it seemed that the both blocks were macroscopically soluble but microscopically insoluble. An insufficient accessibility to the reactive terminal groups prevented the pathway to the azide-alkyne cycloaddition, but rather giving the way toward the Glaser coupling because the Glaser coupling can proceed efficiently even in the solid-state. The oxygen which is a necessary condition for the Glaser coupling may be contaminated when the additional chemical reagents and solvent were added to the mixture in the course of the long reaction. From this viewpoint, one may say that performing the reaction under the homogeneous medium could be the answer to solve this undesired side reaction.



**Scheme 2.13** (a) Reaction conditions of Glaser coupling and Huisgen type CuAAC “click” reaction. (b) Mechanism of Glaser reaction.

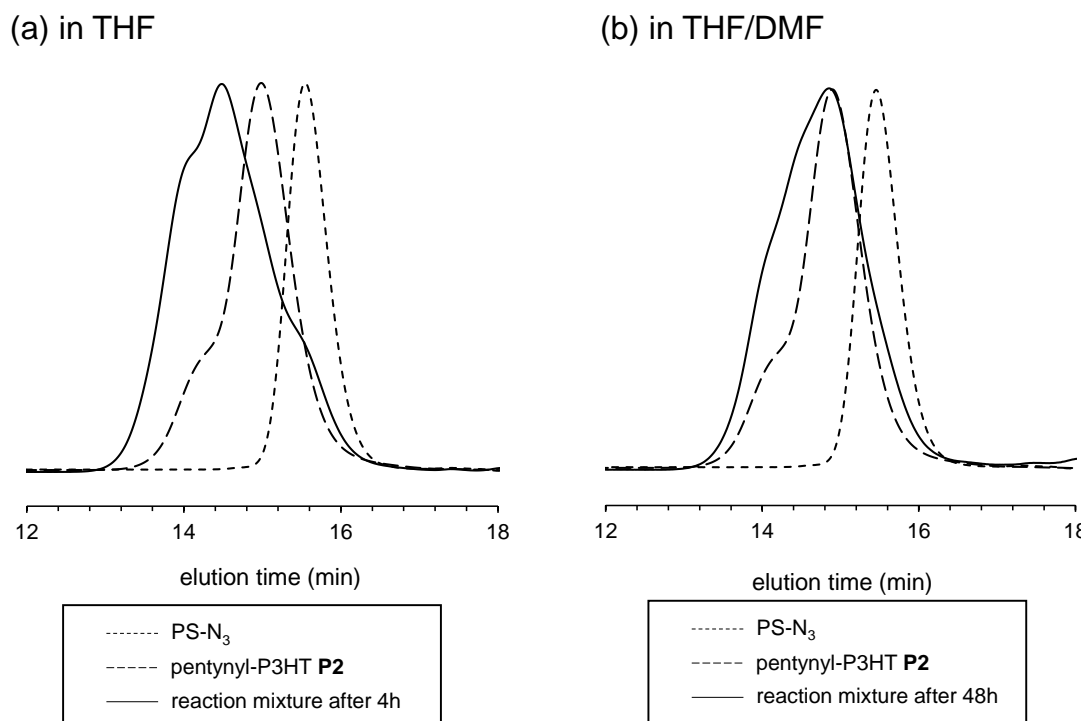
In order to verify the above hypothesis, the effect of the solvent on the reactivity was examined by using a model system as depicted in Scheme 2.14. Azido-functionalized polystyrene was applied as an alternative reactant to couple with penthynyl-P3HT **P2**. The rationale behind this choice was that the polystyrene is soluble in the both DMF and THF and it facilitates an interpretation of the P3HT reactivity.



**Scheme 2.14** Experiments to verify the hypothesis: “click” reaction between azido-functionalized polystyrene (PS-N<sub>3</sub>) and penthynyl-P3HT **P2** in (a) THF and (b) mixed solvent of THF/DMF.

The “click” reactions were carried out in the two different solvent, either (a) THF or (b) mix solvent of THF/DMF (4/1) at room temperature. In both cases, a slightly excess amount of azido-functional polystyrene was added to ensure the accomplishment of the reaction. The reaction progress was monitored by SEC and FT-IR without isolating the resulting product. Figure 2.22a shows SEC traces of the model reaction (a) in which the both penthynyl-P3HT **P2** and azido-functional polystyrene segments were perfectly dissolved in THF. As expected, a clear shift of the main peak toward high molecular weight range from the initial peak corresponding to the P3HT was observed in only 4 hours, suggesting a successful formation of the target block copolymers. By contrast, in the case of model reaction (b), as Figure 2.22b displayed, no

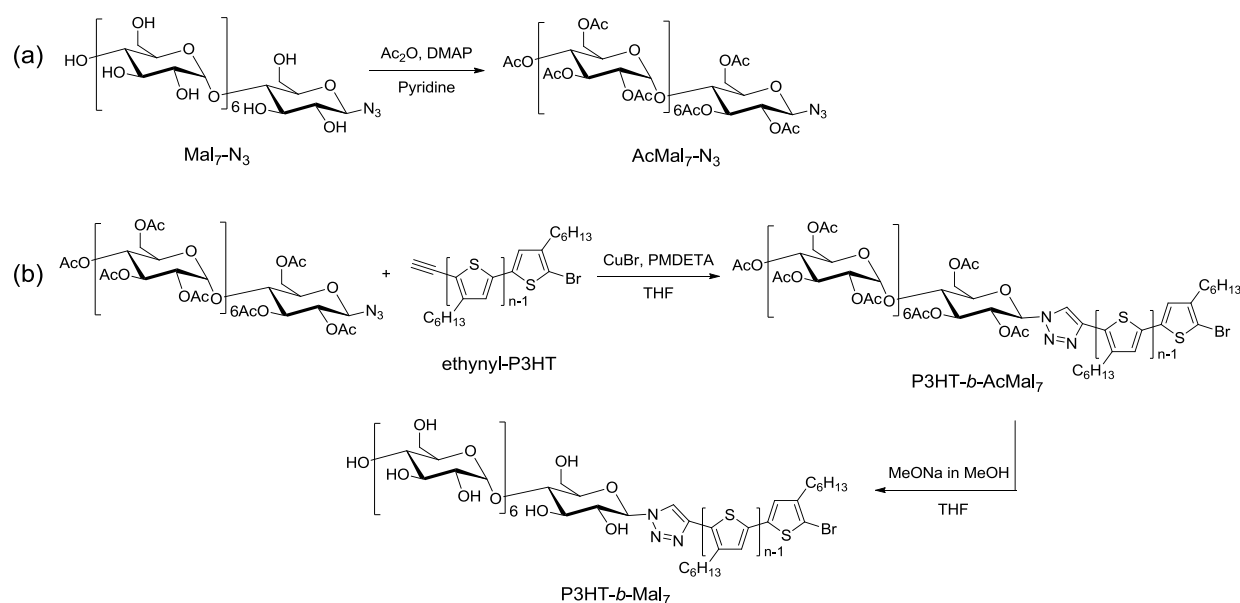
significant peak shift was observed even after 48h. These results clearly shows that the direct click reaction between alkyne-functionalized P3HT and Mal<sub>7</sub>-N<sub>3</sub> did not proceed not because lack of reactivity of the alkyne-P3HT but because the heterogeneity of the reaction system.



**Figure 2.22** SEC traces of the PS-N<sub>3</sub> (dotted line), the pentynyl-P3HT **P2** (broken line), and the reaction mixture (solid line) of “click” reaction performed in (a) THF and (b) mixed solvent of THF/DMF.

## II.4.2 Alternative attempts to the click reaction between alkyne-P3HT and acetylated maltoheptaose (AcMal<sub>7</sub>)

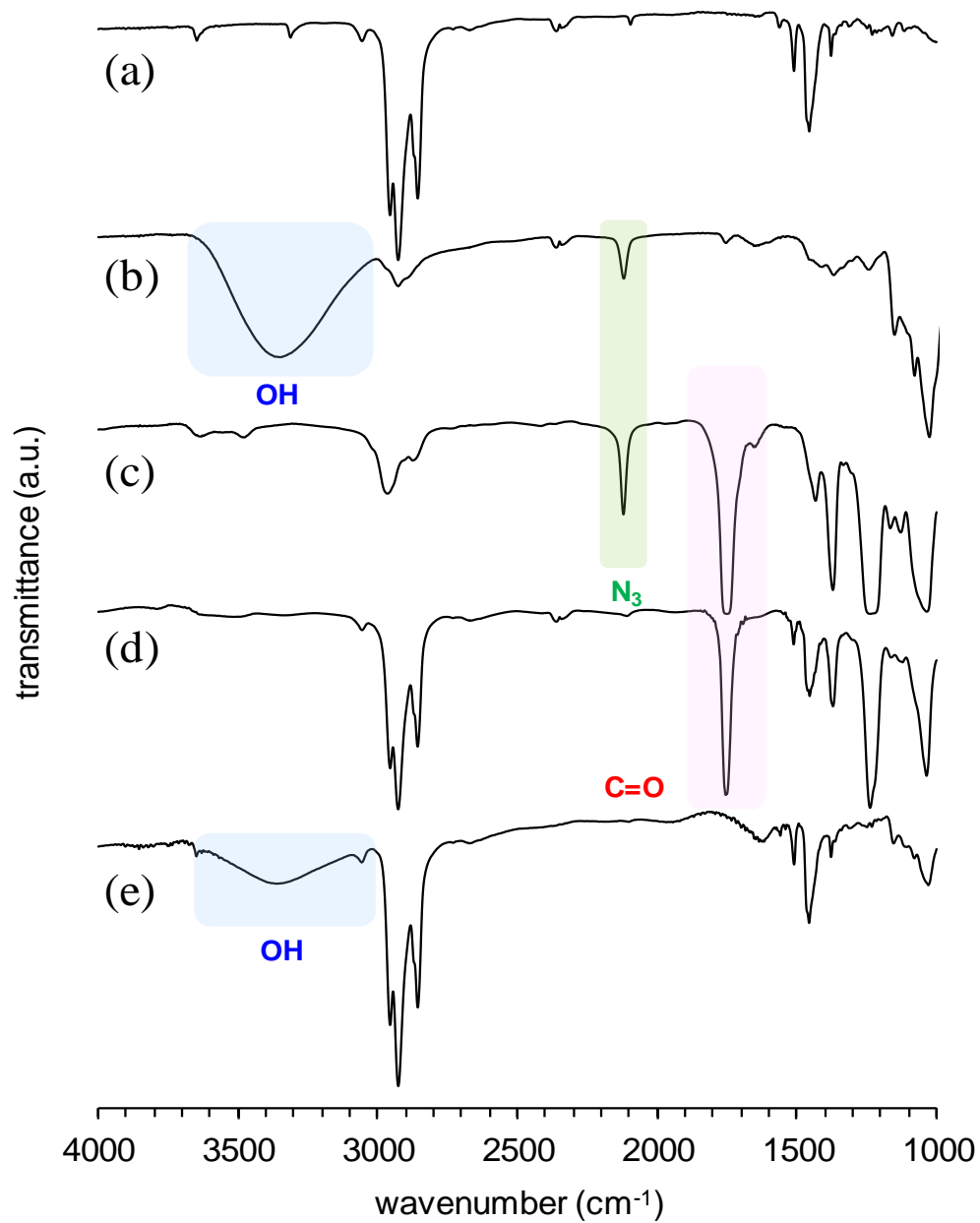
On the basis of above satisfactory evidence, it was decided to acetylate the hydroxyl groups of Mal<sub>7</sub>-N<sub>3</sub> with the aim to change the solubility to perform the CuAAC “click” reaction in a homogenous state. The synthetic path towards diblock copolymers composed of P3HT and oligosaccharides was modified as shown in Scheme 2.15.



**Scheme 2.15** Strategy used for the synthesis of P3HT-*b*-Mal<sub>7</sub> block copolymer: (a) synthesis of azido end-functionalized peracetylated maltoheptaose (AcMal<sub>7</sub>-N<sub>3</sub>) and (b) “click” reaction of ethynyl-P3HT with AcMal<sub>7</sub>-N<sub>3</sub> and followed by deacetylation of sugar block.

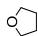
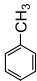
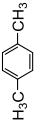
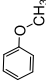
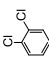

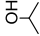
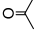
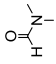
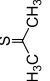
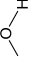
The acetylation of the hydroxyl group of Mal<sub>7</sub>-N<sub>3</sub> was performed with an acetic anhydride/pyridine mixture in the presence of DMAP as a catalyst to give peracetylated Mal<sub>7</sub>-N<sub>3</sub> (AcMal<sub>7</sub>-N<sub>3</sub>). The presence of a strong peak at 1750 cm<sup>-1</sup> corresponding to the C=O stretching in FT-IR spectrum indicated a successful substitution of acetyl groups (Figure 2.23c). The solubility of the resulting AcMal<sub>7</sub>-N<sub>3</sub> has greatly changed as expected and it becomes soluble in several organic solvents such as THF, toluene and chloroform which are also good solvent for P3HT segment (Table 2.12).





**Figure 2.23** FT-IR spectra of (a) ethynyl-P3HT **P1**, (b) Mal<sub>7</sub>-N<sub>3</sub>, (c) AcMal<sub>7</sub>-N<sub>3</sub>, (d) P3HT<sub>P1</sub>-*b*-AcMal<sub>7</sub> and (e) P3HT<sub>P1</sub>-*b*-Mal<sub>7</sub>.

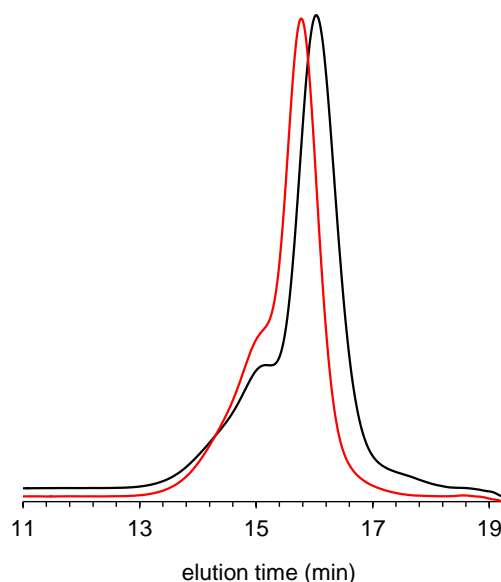
**Table 2.12** Summary of solubility tests done on P3HT, AcMal<sub>7</sub> and Mal<sub>7</sub>

	b.p.	m.p.	solubility in water	dipole moment	P3HT	AcMal <sub>7</sub>	Mal <sub>7</sub>
<b>Heteroaromatics</b>							
THF		66 °C	-108 °C	miscible	1.63 D	+	—
<b>Aromatics</b>							
toluene		111 °C	-95 °C	0.52 g/L (20°C)	0.36 D	+	—
p-xylene		138 °C	13 °C	insoluble	0.07 D	+	—
anisole		154 °C	-37 °C	insoluble	1.38 D	+	—
<b>Halogenated aromatics</b>							
o-dichlorobenzene		181 °C	-17 °C	insoluble	2.5 D	+	—
<b>Halogenated alkanes</b>							
chloroform	CHCl <sub>3</sub>	61 °C	64 °C	8.09 g/L (20°C)	1.15 D	+	—
dichloromethane	CH <sub>2</sub> Cl <sub>2</sub>	40 °C	-97 °C	17.5 g/L (25°C)	1.6 D	+	—
<b>Alcohols</b>							
methanol	CH <sub>3</sub> OH	65 °C	-98 °C	miscible	1.69 D	+	+
ethanol		78 °C	-114 °C	miscible	1.69 D	+	—
isopropyl alcohol		83 °C	-89 °C	miscible	1.66 D	—	—
<b>Polar solvents</b>							
acetone		56 °C	-95 °C	miscible	2.91 D	+	—
DMF		152-154 °C	-61 °C	miscible	3.86 D	+	+
DMSO		189 °C	19 °C	miscible	4.3 D	+	+
water		100 °C	0 °C	—	1.85 D	—	+

+: soluble, -: insoluble

The coupling reaction of ethynyl-P3HT **P1** and AcMal<sub>7</sub>-N<sub>3</sub> was subsequently performed in THF at room temperature by using CuBr and PMDETA as a catalytic system (Scheme 2.15b). The resulting product was characterized by SEC, <sup>1</sup>H NMR, and IR analyses.

The SEC trace of the product (red line in Figure 2.24) indicated a clear shift toward the higher molecular weight region compared to that of ethynyl-P3HT **P1** (black line in Figure 2.24). Here, it is worth noting that a small shoulder corresponding to the dimerized P3HT observed in the SEC trace of starting polymer remains the same position after coupling reaction, indicating that the dimerized P3HT does not contain functional groups at both chain ends. This result is coherent with what previously discussed about the dimerization mechanism.



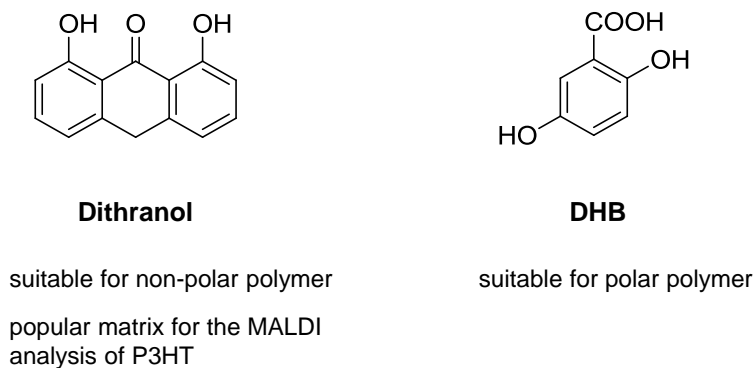
**Figure 2.24** SEC traces of ethynyl-P3HT **P1** (black line), P3HT<sub>P1</sub>-*b*-AcMal<sub>7</sub> (red line) recorded by UV detector.

<sup>1</sup>H NMR spectrum of the product showed characteristic signals assignable to the protons of P3HT **P1** and AcMal<sub>7</sub> as well as the signal corresponding to the proton on the triazole ring at 7.77 ppm (signal y in Figure 2.26c). The complete disappearance of the signal at 3.53 ppm corresponding to an alkyne proton (-C≡CH) indicated that all functional alkyne groups were consumed during the reaction.

To verify the covalent attachment of the AcMal<sub>7</sub> to the polymer, diffusion-ordered spectroscopy (DOSY) experiments were also performed. DOSY is one of the reliable two-dimensional NMR technique representing chemical shifts on the x-axis and diffusion coefficients on the y-axis. With this method, it is possible to separate NMR signals from the overlapping spectra of a mixture as a function of diffusion coefficients of each component which are related to their hydrodynamic radius. As shown Figure 2.27, <sup>1</sup>H DOSY NMR spectrum of the product displayed that proton signals related to the P3HT and AcMal<sub>7</sub> segments as well as triazole ring aligned on the same horizontal line (diffusion coefficient:  $D = 3.8 \times 10^{-10} \text{ m}^2/\text{s}$ ), indicating that both blocks are covalently linked.

In the IR spectrum of resulting product (Figure 2.23d), the peak at  $2120 \text{ cm}^{-1}$  due to the azido group of AcMal<sub>7</sub>-N<sub>3</sub> (Figure 2.23c) completely disappeared whereas the peak at  $1750 \text{ cm}^{-1}$  corresponding to the C=O stretching vibration of the acetyl group in AcMal<sub>7</sub> were clearly observed. From these results, the obtained product was identified as the targeted block copolymer P3HT<sub>P1</sub>-*b*-AcMal<sub>7</sub>.

MALDI-TOF MS spectrometry was also used to confirm the formation of the block copolymer. First, dithranol, which is one of the most popular matrices for the MALDI-TOF MS characterization of  $\pi$ -conjugated polymers, was used as a matrix (Figure 2.25). When the MALDI-TOF MS measurement was conducted on the P3HT homopolymers by using the dithranol, an appropriate result was obtained in terms of sensitivity and signal-to-noise ratio. On the other hand, when the dithranol was applied for the analysis of the block copolymer, no peak



**Figure 2.25** Chemical structures of the matrices tested for the MALDI-TOF MS analysis.

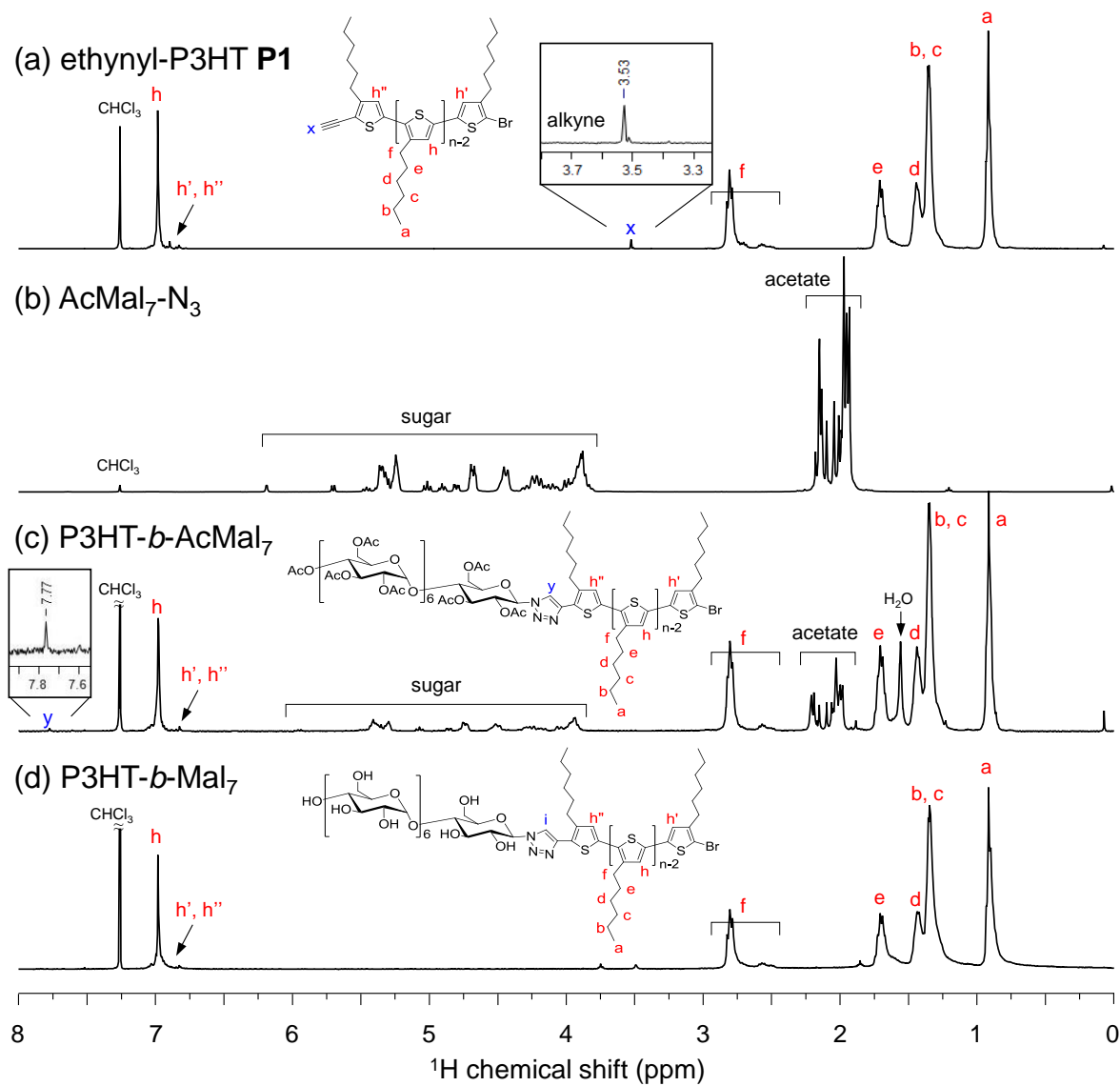
corresponding to the product was observed in the high-mass range, but only a low mass distribution corresponding to the unreacted P3HT homopolymer were detected (Figure 2.28a). Therefore, dihydroxybenzoic acid (DHB) was applied as an alternative matrix (Figure 2.25). Three series of peaks were newly detected in the high molecular weight region together with the peaks in the low mass region (Figure 2.28b). As expected, the series of peaks with highest intensity were assigned to the target block copolymer. For example, the peak at  $m/z = 5787$  g/mol corresponded theoretical value of P3HT<sub>22</sub>-*b*-AcMal<sub>7</sub> (P3HT: 22-mer) with proton;  $M+H^+ = 5788$  g/mol. The low mass distribution observed around  $m/z$  2800 was assigned to the unreacted P3HT homopolymer. The abundance ratio of residual P3HT was not negligible, whereas the SEC trace of the obtained product displayed neither peak nor shoulder corresponding to the starting material. Taking into consideration of SEC result, the relative proportion of the low mass P3HT homopolymer was significantly overestimated under the applied conditions because low mass compounds generally have a better tendency to be ionized and desorbed than high molecular analytes. Through the mass spectrometry investigation, it was revealed that the matrices used for MALDI-TOF MS have a serious influence on the resulting MS spectrum. In this respect, experiment condition for the MALDI-TOF MS should be carefully chosen and tailored through trial and error to afford accurate results.

Finally, P3HT<sub>P1</sub>-*b*-AcMal<sub>7</sub> was deacetylated with sodium methoxide in dry THF to give the block copolymer P3HT<sub>P1</sub>-*b*-Mal<sub>7</sub>. Figure 2.23d and 2.23e show the IR spectra of P3HT<sub>P1</sub>-*b*-AcMal<sub>7</sub> and its deacetylated product, respectively. The disappearance of the sharp absorption at 1750 cm<sup>-1</sup> of acetyl groups and the appearance of the broad band at 3000-3500 cm<sup>-1</sup> due to hydroxyl groups clearly indicate the deacetylation of P3HT<sub>P1</sub>-*b*-AcMal<sub>7</sub>.

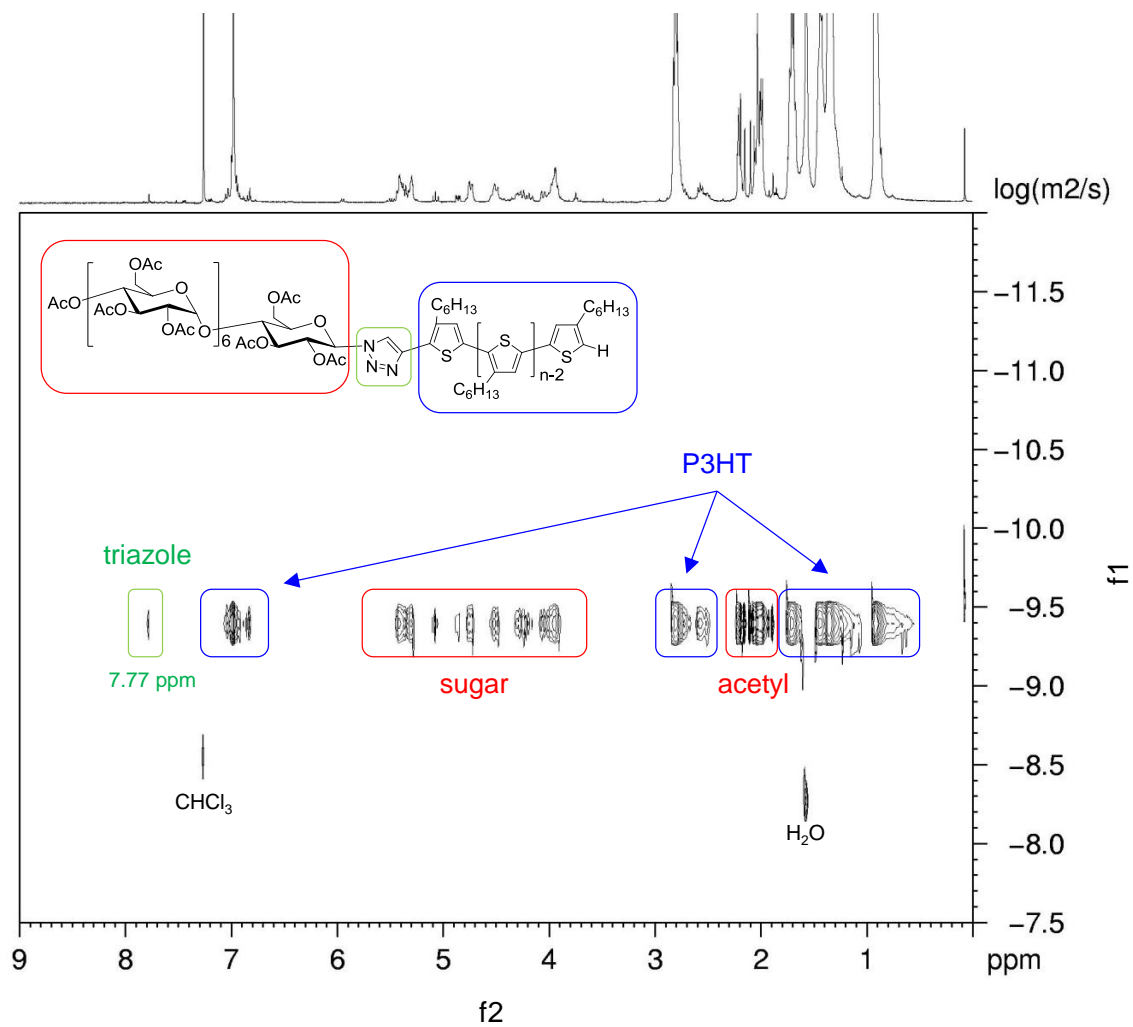
Figure 2.26d shows <sup>1</sup>H NMR spectra of the product in CDCl<sub>3</sub>. The characteristic signals assignable to the protons of P3HT were observed whereas the signals due to the protons of Mal<sub>7</sub> and the triazole ring were not observed. This is probably due to reverse micellar aggregation of the block copolymer in CDCl<sub>3</sub> owing to its amphiphilic feature where the core of the aggregates consists of hydrophilic Mal<sub>7</sub> segments and the shell consists of hydrophobic P3HT segments. This aggregation extremely limits the intramolecular mobility of Mal<sub>7</sub> and the triazole ring segments in the core, and thus, the detection of the resonance from the protons of Mal<sub>7</sub> and the triazole ring was prevented. To finally confirm the product structure, solid-state <sup>13</sup>C cross-polarization magic angle spinning (<sup>13</sup>C CP/MAS) NMR analysis of the product was performed. The spectrum is shown in Figure 2.29 together with the solution state <sup>13</sup>C NMR spectra. Similarly as the <sup>1</sup>H NMR spectra of the product in CDCl<sub>3</sub> (Figure 2.26d), the solution state <sup>13</sup>C NMR spectrum (Figure 2.29c) displays signals assignable to the <sup>13</sup>C resonance of P3HT segments whereas no signal due to Mal<sub>7</sub> and triazole segments was observed. On the other hand, the <sup>13</sup>C CPMAS measurement allowed detecting the <sup>13</sup>C resonance of both P3HT (signals 1-10) and Mal<sub>7</sub> segments (55-110 ppm) as shown in Figure 2.29d. Therefore, the obtained product can be identified as P3HT<sub>P1</sub>-*b*-Mal<sub>7</sub>.

In a similar fashion, ethynyl-P3HT **P3** was also coupled with AcMal<sub>7</sub> to give P3HT<sub>P3</sub>-*b*-AcMal<sub>7</sub> block copolymer. Subsequently, P3HT<sub>P3</sub>-*b*-AcMal<sub>7</sub> underwent deacetylation to afford P3HT<sub>P3</sub>-*b*-Mal<sub>7</sub> as a final product. These block copolymers, P3HT<sub>P3</sub>-*b*-AcMal<sub>7</sub> and P3HT<sub>P3</sub>-*b*-Mal<sub>7</sub>, showed narrower molecular weight distribution than P3HT **P1** based block copolymers thanks to a significantly low molecular weight distribution of ethynyl-P3HT **P3** homopolymer.

The characteristics of all of the obtained block copolymers are summarized in Table 2.13.

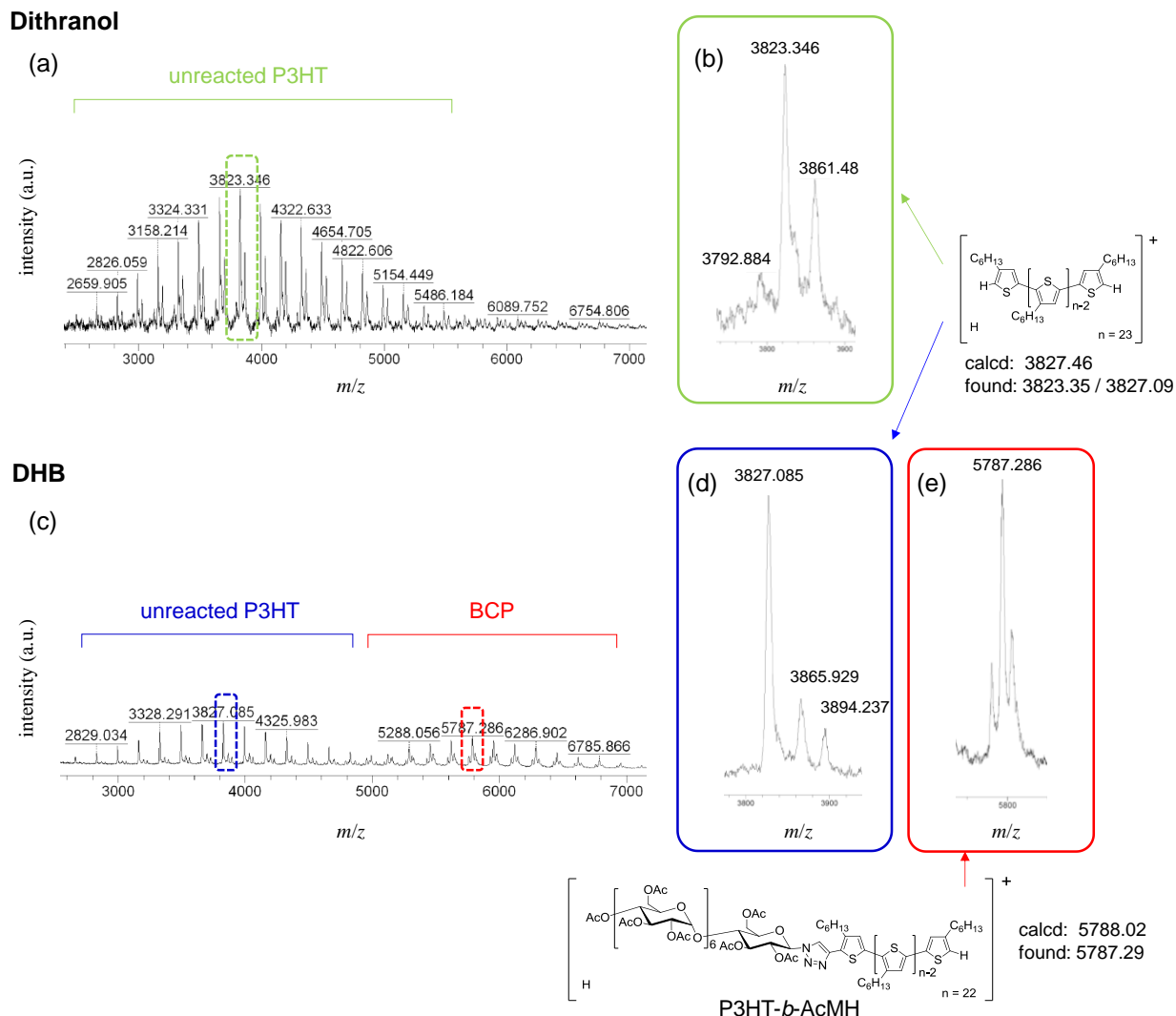


**Figure 2.26** <sup>1</sup>H NMR spectra of (a) ethynyl-P3HT **P1**, (b) AcMal<sub>7</sub>-N<sub>3</sub>, (c) P3HT<sub>P1</sub>-*b*-AcMal<sub>7</sub> block copolymer and (d) P3HT<sub>P1</sub>-*b*-Mal<sub>7</sub> block copolymer in CDCl<sub>3</sub>.

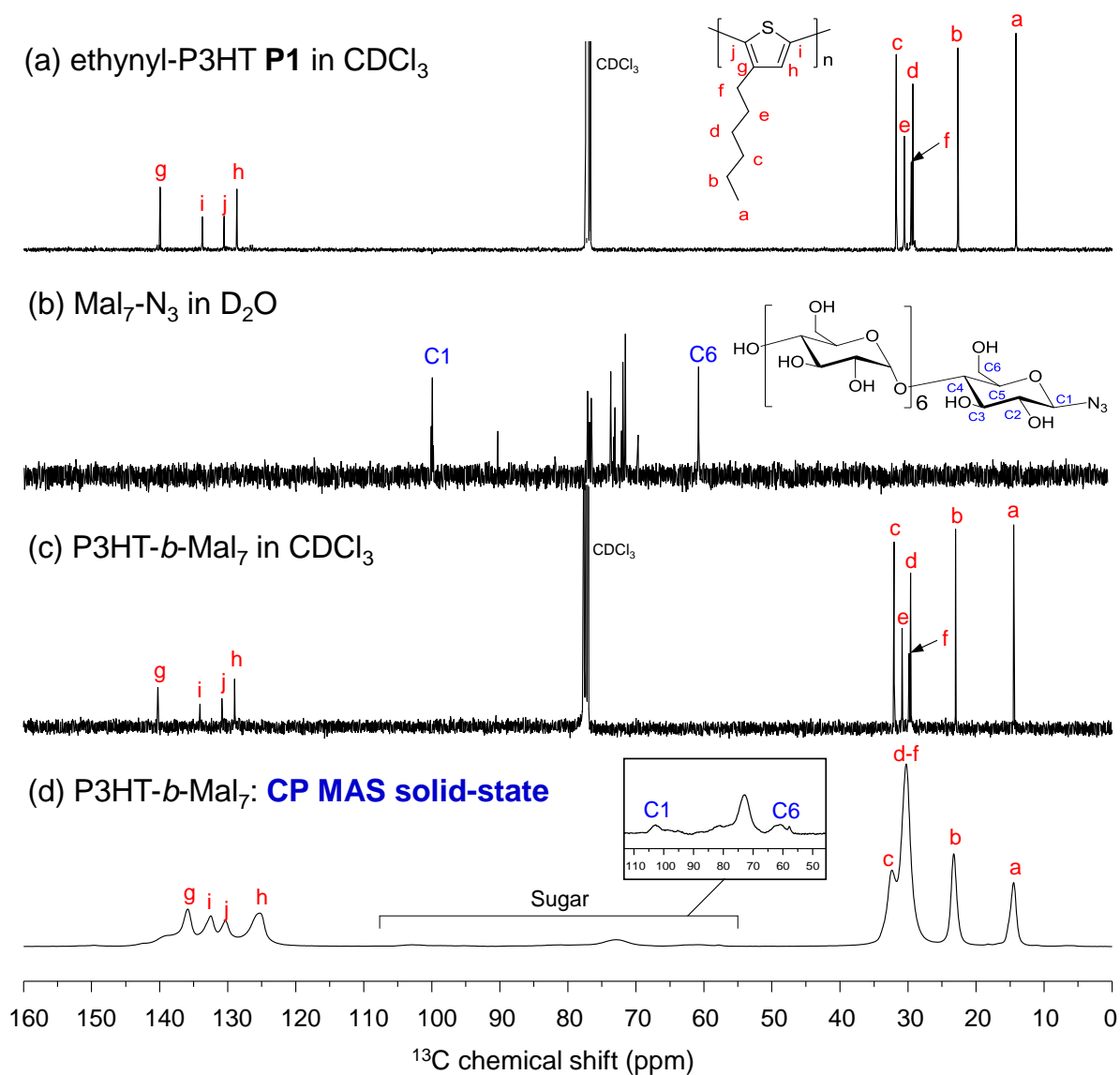


**Figure 2.27**  $^1\text{H}$ -DOSY spectrum of  $\text{P3HT}_{\text{P1}}\text{-}b\text{-AcMal}_7$ .





**Figure 2.28** MALDI-TOF MS spectra of P3HT<sub>P1</sub>-*b*-AcMal<sub>7</sub> obtained by using (a) dithranol and (c) DHB as a matrix, and magnified part in the range of (b) 23 repeating units in the spectrum a (encircled area with green dotted line), (d) 22 repeating units of unreacted P3HT **P1** (encircled area with blue dotted line) and (e) 22 repeating units of P3HT<sub>P1</sub>-*b*-AcMal<sub>7</sub> (encircled area with red dotted line) in the spectrum c.



**Figure 2.29**  $^{13}\text{C}$  NMR spectra of (a) ethynyl-P3HT **P1** in  $\text{CDCl}_3$ , (b)  $\text{Mal}_7\text{-N}_3$  in  $\text{D}_2\text{O}$ , (c)  $\text{P3HT}_{\text{P1}}\text{-}b\text{-Mal}_7$  block copolymer in  $\text{CDCl}_3$  and (d)  $^{13}\text{C}$  CP/MAS NMR spectrum of  $\text{P3HT}_{\text{P1}}\text{-}b\text{-Mal}_7$  block copolymer.

**Table 2.13** Characterization details of the synthesized glycoconjugated block copolymers in this study

sample	P3HT					sugar	block copolymer				
	polymer	$M_{\text{P, MALDI, P3HT}}^a$ (g/mol)	$M_{\text{w}}/M_{\text{n, P3HT}}^b$	end-functionality <sup>c</sup>							
				functional group	mono-endcapped	bis-endcapped	non-endcapped	% HT <sup>d</sup>	$M_{\text{sugar}}^e$ (g/mol)	$M_{\text{w}}/M_{\text{n, total}}^f$ $f_{\text{P3HT}}^g$	
P3HT <sub>P1</sub> - <i>b</i> -AcMal <sub>7</sub>	<b>P1</b>	3596	1.35	ethynyl	91	7	2	> 95 %	2060	1.29	0.64
P3HT <sub>P3</sub> - <i>b</i> -AcMal <sub>7</sub>	<b>P3</b>	3850	1.07	ethynyl	85	0	15	> 94 %		1.15	0.66
P3HT <sub>P1</sub> - <i>b</i> -Mal <sub>7</sub>	<b>P1</b>	3596	1.35	ethynyl	91	7	2	> 95 %	1136	1.39	0.79
P3HT <sub>P3</sub> - <i>b</i> -Mal <sub>7</sub>	<b>P3</b>	3850	1.07	ethynyl	85	0	15	> 94 %		–	0.80

<sup>a</sup> Molecular weight at the peak maximum determined by MALDI-TOF MS. <sup>b</sup> Dispersity of the P3HT estimated by SEC in THF based on PS standards. <sup>c</sup> Determined by MALDI-TOF MS. <sup>d</sup> HT coupling regioregularity determined by <sup>1</sup>H NMR. <sup>e</sup> Molecular weight of sugars. <sup>f</sup> Dispersity of the block copolymers estimated by SEC in THF based on PS standards. <sup>g</sup> Volume fraction of P3HT in copolymers calculated by using density values 1.16 g/cm<sup>3</sup> for P3HT, 1.36 g/cm<sup>3</sup> for Mal<sub>7</sub> and 1.20 g/cm<sup>3</sup> for AcMal<sub>7</sub>.

## II.5 Conclusion

A series of P3HT-based glyco-block copolymers, P3HT-*b*-Mal<sub>7</sub> and P3HT-*b*-AcMal<sub>7</sub>, have been successfully synthesized in good yield via the coupling reactions of the alkyne-functionalized regioregular P3HTs and the azido-functionalized AcMal<sub>7</sub> by using CuAAC "click" chemistry. Firstly, the alkyne-functionalized regioregular P3HTs were synthesized with careful attentions to quantitative alkyne end-functionalization, control of molecular weight, and regioregularity in order to attain well-defined P3HTs and corresponding block copolymers with high purity. Two different synthetic strategies were investigated. The first one is *in situ* end-functionalization and second one is post-polymerization modification method. In the first strategy, the ethynyl-P3HT with HT regioregularity of 95 % and mono-functional ratio of 91 % was obtained by using excess amount of the 1-hexene which serves as stabilizer of Ni catalyst although a small amount of dimerized P3HTs were generated during the end-functionalization that may affect the morphology of the self-assembled block copolymer films. To circumvent this undesirable dimerization, second strategy, post-polymerization modification method was carried out. The selective ethynyl-functionalization onto the Br-terminal of the stable precursor polymer resulted in a remarkable reduction in proportion of dimerized P3HT. The Soxhlet extraction process for the stable precursor polymer further allowed a lowering of dispersity *D* from 1.35 to 1.07. Secondly, maltoheptaose was selectively functionalized on its reducing end with an azido group without resorting protection/deprotection processes. When the coupling reaction was performed between the ethynyl-P3HT and Mal<sub>7</sub>-N<sub>3</sub>, the Glaser coupling have preferentially occurred rather than CuAAC reaction due to insufficient solubility of the both substances in the mixed solvent of THF and DMF. This impediment was surmounted by the acetylation of Mal<sub>7</sub>-N<sub>3</sub> to give the AcMal<sub>7</sub>-N<sub>3</sub> which has a good solubility in various organic solvents. Then, the CuAAC click reaction of the ethynyl-P3HT with AcMal<sub>7</sub>-N<sub>3</sub> in THF has proceed smoothly as expected and afforded the P3HT-*b*-AcMal<sub>7</sub> in good yield. Finally, the deacetylation of P3HT-*b*-AcMal<sub>7</sub> using sodium methoxide gave the block copolymer consisting of P3HT and Mal<sub>7</sub> (P3HT-*b*-Mal<sub>7</sub>).

## II.6 References

- (1) Miyakoshi, R.; Yokoyama, A.; Yokozawa, T. *J. Am. Chem. Soc.* **2005**, *127* (49), 17542–17547.
- (2) Kochemba, W. M.; Kilbey, S. M.; Pickel, D. L. *J. Polym. Sci. Part A Polym. Chem.* **2012**, *50* (14), 2762–2769.
- (3) McCullough, R. D. *Adv. Mater.* **1998**, *10* (2), 93–116.
- (4) Holdcroft, S. *J. Polym. Sci. Part B Polym. Phys.* **1991**, *29* (13), 1585–1588.
- (5) Lohwasser, R. H.; Gupta, G.; Kohn, P.; Sommer, M.; Lang, A. S.; Thurn-Albrecht, T.; Thelakkat, M. *Macromolecules* **2013**, *46* (11), 4403–4410.
- (6) Lohwasser, R. H.; Thelakkat, M. *Macromolecules* **2012**, *45* (7), 3070–3077.
- (7) Li, Z.; Ono, R. J.; Wu, Z.-Q.; Bielawski, C. W. *Chem. Commun.* **2011**, *47* (1), 197–199.
- (8) Miyakoshi, R.; Yokoyama, A.; Yokozawa, T. *Macromol. Rapid Commun.* **2004**, *25* (19), 1663–1666.
- (9) Tanaka, T.; Huang, W. C.; Noguchi, M.; Kobayashi, A.; Shoda, S. I. *Tetrahedron Lett.* **2009**, *50* (18), 2154–2157.
- (10) Urien, M.; Erothu, H.; Cloutet, E.; Hiorns, R. C.; Vignau, L.; Cramail, H. *Macromolecules* **2008**, *41* (19), 7033–7040.
- (11) Duxbury, C. J.; Cummins, D.; Heise, A. *J. Polym. Sci. Part A Polym. Chem.* **2009**, *47* (15), 3795–3802.
- (12) Cummins, D.; Duxbury, C. J.; Quaedflieg, P. J. L. M.; Magusin, P. C. M. M.; Koning, C. E.; Heise, A. *Soft Matter* **2009**, *5* (4), 804.

## **CHAPTER III:**

### **STUDY OF THE SELF-ASSEMBLY BEHAVIORS AND MORPHOLOGIES OF THE SEMICONDUCTING GLYCOCONJUGATED DIBLOCK COPOLYMERS**

### III.1 Introduction

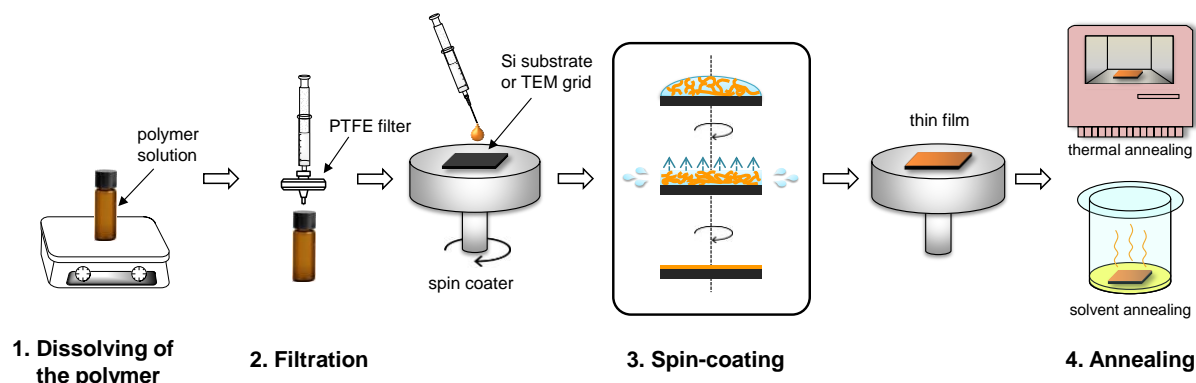
The self-assembling nature of block copolymers have attracted considerable attention as one of the promising bottom-up strategies for controlling the active layer morphology in organic photovoltaics at the nanometer scale. P3HT is one of the most attractive candidates as an optoelectronically active block due to its excellent electrical properties and thus, a variety of studies on the synthesis and characterization of block copolymers containing P3HT has been reported so far. However, to the best of my knowledge, there are only a few reports on the self-assembly of the P3HT-based block copolymers showing the well-ordered phase separated structures probably due to the strong  $\pi$ - $\pi$  interaction among P3HT chains.

This chapter describes a morphological study of the diblock copolymers, P3HT-*b*-AcMa<sub>7</sub> and P3HT-*b*-Mal<sub>7</sub>. Thermal annealing and solvent vapor annealing, which are the two most practical methods to facilitate or accelerate self-organizations of block copolymers, were applied on both block copolymers. Their morphologies were carefully investigated by means of atomic force microscopy (AFM), transmission electron microscopy (TEM), and small-angle X-ray scattering (SAXS) measurements. A molecular packing model for the self-assembled P3HT-*b*-AcMal<sub>7</sub> was also discussed based on the experimental results and theoretical crystal structure.

## III.2 Sample preparation

### III.2.1 Thin film samples for AFM and TEM measurements

Polymer thin films were prepared by spin-coating for both AFM and TEM measurements. The polymers were dissolved in organic solvents (THF,  $\text{CHCl}_3$ , dichloro methane, *o*-dichlorobenzene, and anisole, *etc.*), stirred with a magnetic stirrer for at least 3h at room temperature, then filtered through a 0.45  $\mu\text{m}$  PTFE filter prior to use. In the case of samples for AFM measurement, the solutions were deposited onto a Si wafer which was cleaned beforehand by ultrasonic treatment with ethanol. For TEM measurement, carbon-coated copper grids were used as substrate. The grid was placed on the center of a glass support fixed to the spin coater and the adequately diluted polymer solution ( $\sim 0.1$  wt%) was deposited on it. In the typical experiments, the deposition of the polymer solutions were carried out with rotation speed of 3000 rpm for 30 sec. The obtained thin films were annealed via solvent vapor annealing or/and thermal annealing under optional conditions. Annealing temperatures were given as temperature inside the oven.



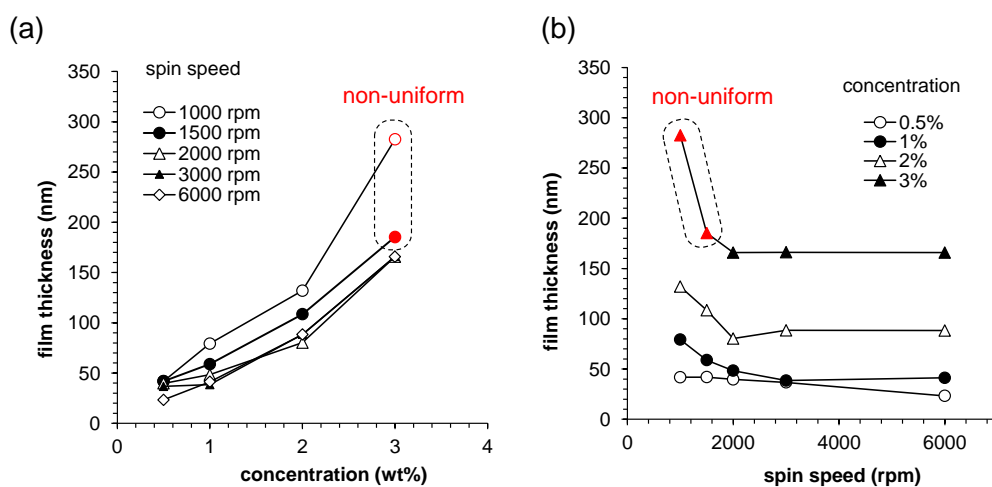
**Figure 3.1** General procedures for the preparation of the polymer thin films for AFM and TEM measurements.



## Film thickness

To find spin coating conditions that can steadily provide uniform films in a reproducible way, the effect of spin speed and concentration of the solution on both the film uniformity and thickness was first checked. In this study, spin coating duration and acceleration were fixed at 30 sec and 1000 rpm/s, respectively, and chloroform was used as a solvent. The thicknesses of the thin films were determined by measuring the depth of a scratch made on the film using AFM.

Figure 3.2a and 3.2b show the dependence of the concentration of a polymer solution and spin speed on the film thickness, respectively. From the solutions with concentrations below 2 %, uniform films were obtained at any spin speed, whereas the solution of 3 % provided non-uniform films especially at low spin speed. This is probably due to a high evaporation rate of the chloroform. With a spin speed above 2000 rpm, film thickness was independent of spin speed. On the other hand, the film thickness was almost proportional to the concentration of solution. Thus the film thickness can be easily controlled by varying the concentration in the range of 25 nm to 190 nm (the film with the thickness of 280 nm was not uniform). Therefore, the following set of parameters were used for preparation of thin films as a standard condition; concentration = 0.5 %, rotation speed = 3000 rpm, acceleration = 1000 rpm/s, and coating duration = 30 sec. These conditions always give a uniform thin film with a thickness of *ca.* 35 nm.



**Figure 3.2** Dependence of the (a) concentration of a polymer solution and (b) spin speed on the film thickness (solvent:  $\text{CHCl}_3$ ).

### II.2.2 Bulk samples for SAXS/WAXS measurements

All samples for SAXS and WAXS measurements were prepared by drop casting from concentrated polymer solution (*ca.* 3%) onto a PTFE substrate. THF was used as a solvent. The polymer solutions were filtered through a 0.45  $\mu\text{m}$  PTFE filter by using glass syringe prior to deposit. After complete evaporation of the solvent, about 10  $\mu\text{m}$ -thick films were obtained, and they were annealed under different conditions. The annealed bulk samples were then peeled off from PTFE substrate and finely crashed to put into 1.5 mm diameter glass capillaries. The capillaries were sealed with hot-melt adhesive by means of a STEINEL hot-melt glue applicator. These samples were placed in sample holders equipped with an integrated heating system. The experiments were performed using 15 keV ( $\lambda = 0.083$  nm) X-ray beam at the BM02 beamline of the European Synchrotron Radiation Facility (ESRF, Grenoble, France).

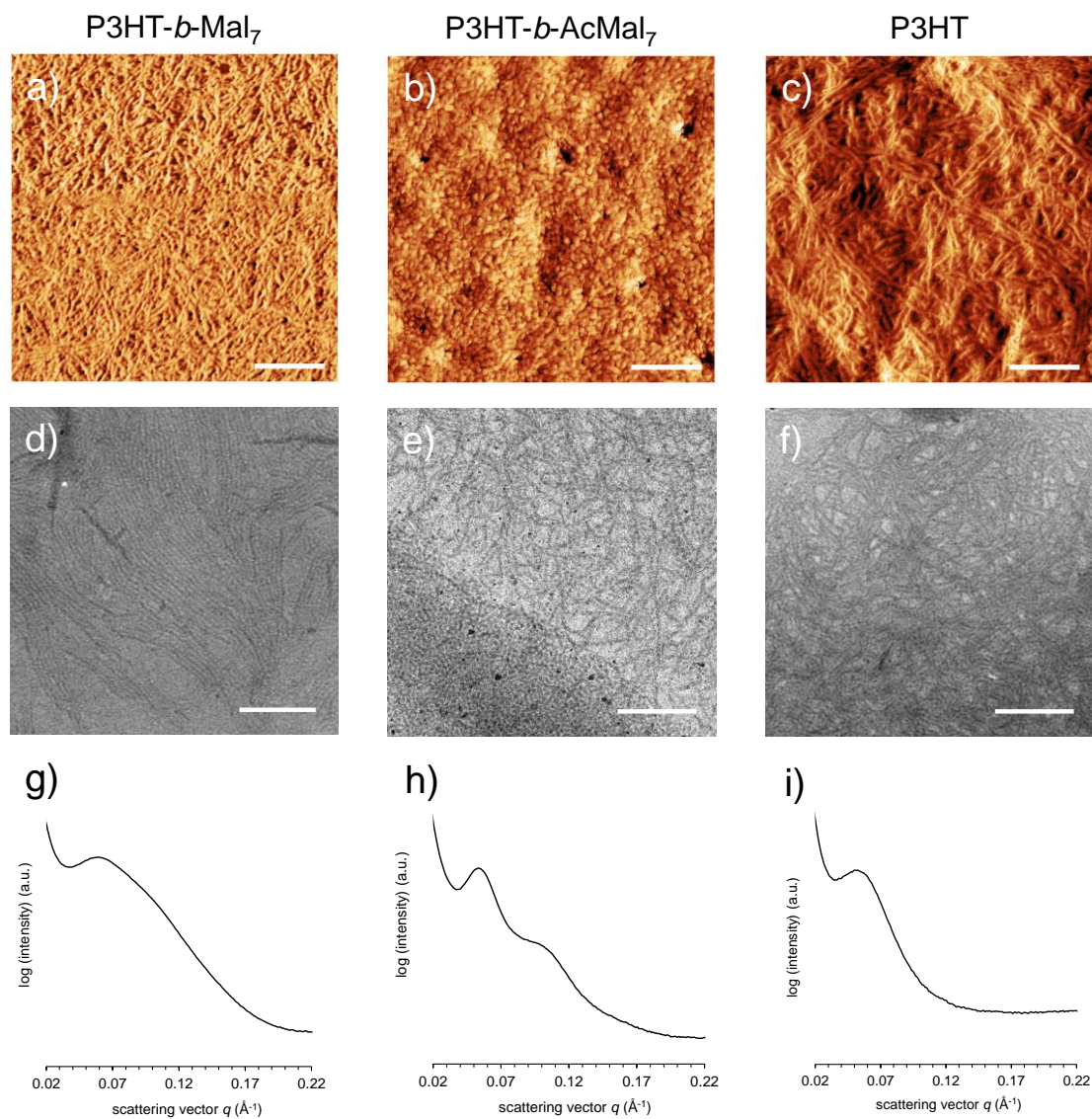
### III.3 Morphologies of the as-cast samples

As described in chapter II, we synthesized two kinds of block copolymers, P3HT-*b*-AcMal<sub>7</sub> and P3HT-*b*-Mal<sub>7</sub> with different P3HT batches, either ethynyl-P3HT **P1** or ethynyl-P3HT **P3** that were prepared by different protocols. For simplicity, representative results of the P1 series (P3HT<sub>P1</sub>-*b*-AcMal<sub>7</sub> and P3HT<sub>P1</sub>-*b*-Mal<sub>7</sub>) will be reported first, and then the morphological characteristics of the P3 series will be discussed in later section.

The self-assembly behaviors of thin film samples of P3HT<sub>P1</sub>-*b*-AcMal<sub>7</sub> and P3HT<sub>P1</sub>-*b*-Mal<sub>7</sub> were characterized by AFM and TEM and compared with the thin film sample of the ethynyl-P3HT **P1** homopolymer. The as-cast film of P3HT<sub>P1</sub>-*b*-Mal<sub>7</sub> and P3HT homopolymer showed a nanofibril structure with micrometer-scale lengths and nanoscale widths (Figure 3.3a and 3.3d (P3HT<sub>P1</sub>-*b*-Mal<sub>7</sub>) / Figure 3.3c and 3.3f (P3HT **P1**)), as is generally observed for the P3HT-based block copolymer thin films.<sup>1-5</sup> It is well-known that P3HT exhibits a fibril-like morphology because of the strong  $\pi$ - $\pi$  interactions between  $\pi$ -conjugated thiophene backbones. The P3HT used in this study also followed this trend. The SAXS profiles of P3HT<sub>P1</sub>-*b*-Mal<sub>7</sub> and P3HT homopolymer exhibit only a broad scattering peak corresponding roughly to the first-neighbor distance of the randomly oriented nanofibers (Figure 3.3g and 3.3i). Therefore, we assume that the structure formation of the P3HT<sub>P1</sub>-*b*-Mal<sub>7</sub> was entirely dictated by the strong crystallization of P3HT which is kinetically fast enough to form crystalline nanofiber structure during the solution cast process with highly volatile organic solvents (THF).

On the other hand, the as-cast film of P3HT<sub>P1</sub>-*b*-AcMal<sub>7</sub> showed a quite different morphology. The TEM image of the as spun P3HT-*b*-AcMal<sub>7</sub> film showed a heterogeneous morphology consisting of dot- and fibril-like structures (Figure 3.3e). In the AFM phase image, only globular aggregates were observed over the whole surface and characteristic fibril-like structure of the P3HT homopolymer was not observed (Figure 3.3b). This observation can be explained by the lower volume fractions of the P3HT block ( $f_{\text{P3HT}}$ ) of P3HT<sub>P1</sub>-*b*-AcMal<sub>7</sub> ( $f_{\text{P3HT}} = 0.64$ ) than that of P3HT<sub>P1</sub>-*b*-Mal<sub>7</sub> ( $f_{\text{P3HT}} = 0.79$ ). Because of the less influence of the P3HT crystallinity on the microdomain formation of P3HT<sub>P1</sub>-*b*-AcMal<sub>7</sub>, the fibril-like crystallization was rather hindered by the higher contribution of the microphase separation behavior of the block copolymer. The

less-ordered structure in the P3HT<sub>P1</sub>-*b*-AcMal<sub>7</sub> as cast film probably reflects the kinetically trapped unstable morphology.



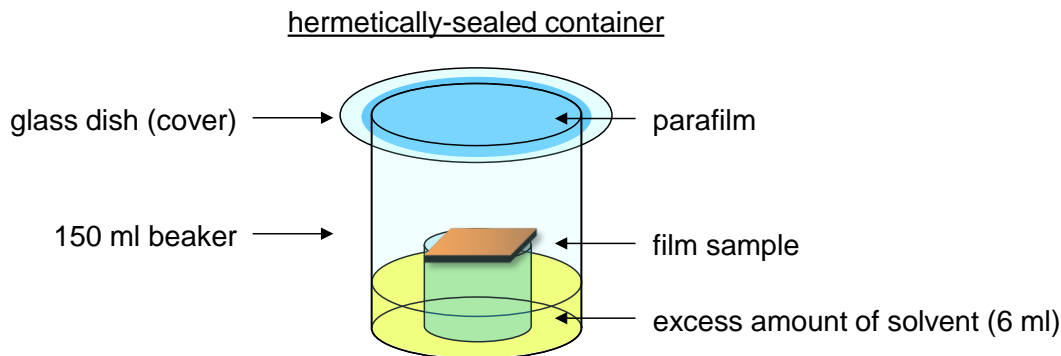
**Figure 3.3** AFM phase images of as-cast films for (a) P3HT<sub>P1</sub>-*b*-Mal<sub>7</sub>, (b) P3HT<sub>P1</sub>-*b*-AcMal<sub>7</sub>, and (c) ethynyl-P3HT **P1** and TEM images of as-cast films for (d) P3HT<sub>P1</sub>-*b*-Mal<sub>7</sub>, (e) P3HT<sub>P1</sub>-*b*-AcMal<sub>7</sub>, and (f) ethynyl-P3HT **P1**. Scale bars indicate 200 nm. SAXS profiles of pristine bulk samples for (g) P3HT<sub>P1</sub>-*b*-Mal<sub>7</sub>, (h) P3HT<sub>P1</sub>-*b*-AcMal<sub>7</sub>, and (i) ethynyl-P3HT **P1**.

### III.4 Self-organization via solvent vapor annealing

The solvent vapor annealing is one of the most commonly used practical techniques for rearranging the morphology or controlling the orientation of self-assembled structures.<sup>6-8</sup> In principle, the solvent vapor gives the polymer chains enough mobility to self-assemble into thermodynamically stable morphology. In addition to a wide variety of choices of solvents, this technique is advantageous for block copolymers having narrow working temperature window between the glass-transition and the degradation temperature. Such kind of copolymers are not suitable for thermal annealing, which is another conventional method for organizing the microphase separation.

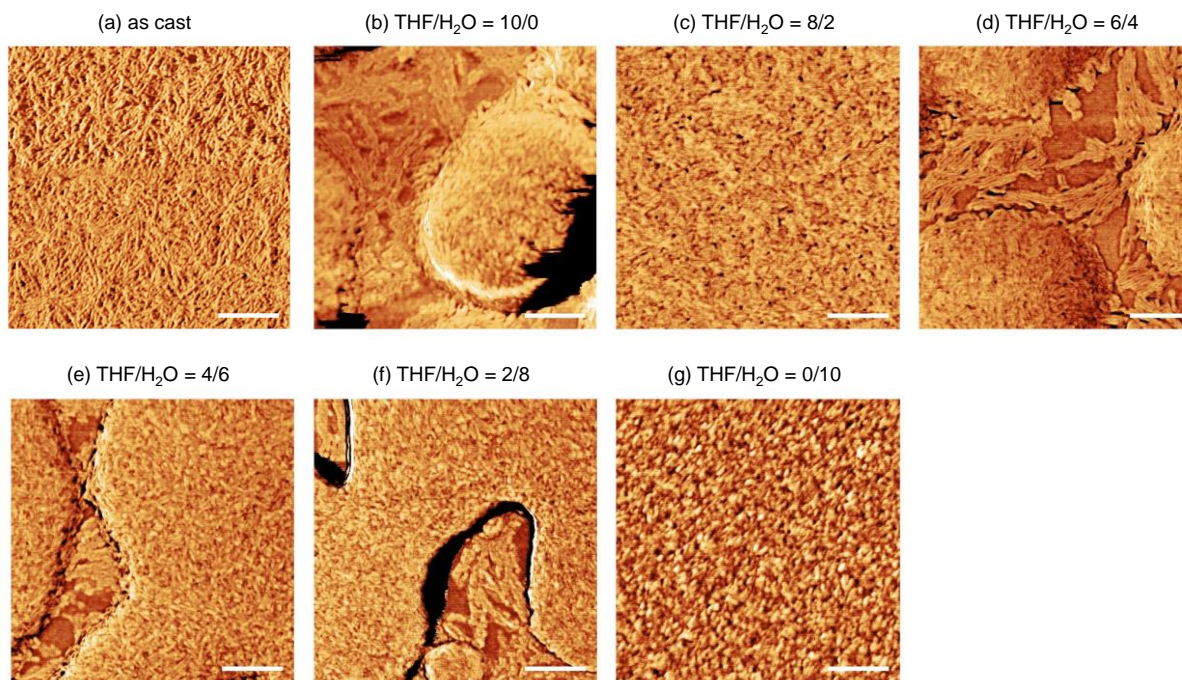
In our previous study on the carbohydrate-containing hybrid block copolymers, the solvent annealing has been effectively used to induce the phase separations and/or to control the orientation of the self-assembled microdomains.<sup>9-11</sup> For example, in the maltoheptaose-*block*-polystyrene (Mal<sub>7</sub>-*b*-PS) block copolymer system, hexagonally close-packed cylindrical morphologies with a sub-10 nm domain-spacing were obtained after solvent annealing with mixed vapor of THF and H<sub>2</sub>O.<sup>10</sup>

Based on the previous results, the solvent annealing technique was primarily applied for the P3HT<sub>P1</sub>-*b*-Mal<sub>7</sub> system by using a vapor of a co-solvent composed of THF and H<sub>2</sub>O. These two solvents were reasonably chosen in order to impart mobility to both P3HT and Mal<sub>7</sub> segments simultaneously because the THF and H<sub>2</sub>O are good solvents for the P3HT and Mal<sub>7</sub> blocks, respectively, but poor solvents for the opposites. The solvent annealing was performed in a hermetic glass container for 24 h at room temperature. A schematic image of the equipment for solvent annealing is given in Figure 3.4. The mixing ratios of THF were varied from 0 to 100 % by volume.



**Figure 3.4** Equipment for vapor solvent annealing.

**P3HT-*b*-Mal<sub>7</sub>**



**Figure 3.5** AFM phase images of (a) as-cast P3HT<sub>P1</sub>-*b*-Mal<sub>7</sub> thin film and solvent vapor annealed P3HT<sub>P1</sub>-*b*-Mal<sub>7</sub> thin films with different solvent compositions of (b) THF/H<sub>2</sub>O = 10/0, (c) THF/H<sub>2</sub>O = 8/2, (d) THF/H<sub>2</sub>O = 6/4, (e) THF/H<sub>2</sub>O = 4/6, (f) THF/H<sub>2</sub>O = 2/8, and (g) THF/H<sub>2</sub>O = 0/10 (annealing time: 24h). Scale bars indicate 200 nm.



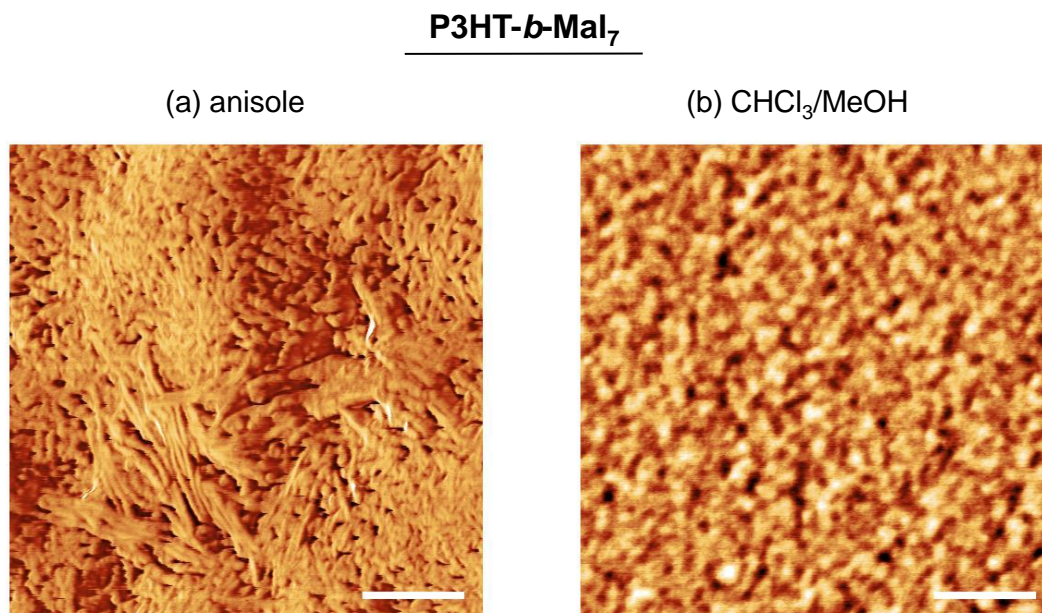
The AFM phase images of the annealed thin films are presented in Figure 3.5. All P3HT<sub>P1</sub>-*b*-Mal<sub>7</sub> thin films, which were annealed under the mixed vapors of THF and H<sub>2</sub>O with different volume fractions, showed poorly ordered short-range nanofibril morphology or disordered structures. The THF/H<sub>2</sub>O system was not favorable for realigning the nanofibrils, and instead favored shorter fragments.

Although the annealed films were macroscopically homogeneous, the AFM observation revealed that they were microscopically heterogeneous (Figure 3.5b, 3.5d, 3.5e and 3.5f). The roughness probably comes from the poor wettability of P3HT-*b*-Mal<sub>7</sub> to Si substrates, resulting in dewetting during the annealing, because the hydrophilic hydroxyl groups of the Mal<sub>7</sub> block have low affinity with relatively hydrophobic Si surface. This roughness made it difficult to observe the film surface appropriately by AFM. To change the surface energy of Si substrate, piranha solution, composed of sulfuric acid and hydrogen peroxide, was used to introduce abundant hydroxyl groups on the Si surface by hydroxylation. Indeed the contact angle of the Si surface after piranha treatment decreased to less than 5 degree from the original 45 degree. Nevertheless, no significant improvement was observed in terms of surface roughness, and morphology of the P3HT<sub>P1</sub>-*b*-AcMal<sub>7</sub> thin film casted on the hydrophilic Si substrate (data is not shown).

To induce microphase ordering, other possible parameters including the initial solvents for dissolving the polymer, the composition of the solvent for annealing, and annealing time were investigated. Figure 3.6a and 3.6b shows representative AFM phase images of the P3HT<sub>P1</sub>-*b*-Mal<sub>7</sub> thin films after vapor annealing with anisole and CHCl<sub>3</sub>/MeOH = 1/1, respectively. When the solvent annealing was performed with anisole, only a swelling phenomenon, *i.e.* increase of the nanofibril width, was observed. On the other hand, the thin film annealed with the vapor of CHCl<sub>3</sub>/MeOH exhibits featureless structure. Although various morphological changes were observed after solvent annealing, no ordered periodic structure was obtained for the P3HT<sub>P1</sub>-*b*-Mal<sub>7</sub> system.

Same type of experiments were conducted for the P3HT<sub>P1</sub>-*b*-AcMal<sub>7</sub> system as well. Nevertheless, no ordered structure was observed. An example of the obtained results is shown in Figure 3.7. The AFM phase image of the P3HT<sub>P1</sub>-*b*-AcMal<sub>7</sub> film underwent solvent annealing under the vapor of THF/H<sub>2</sub>O = 1/1 shows spherical morphology similar as that found in as-spun film (Figure 3.7).

Although the solvent annealing technique has been successfully employed for the previously reported other carbohydrate-conjugated block copolymer systems to induce the well-ordered periodic nanostructures, all attempts conducted for the both P3HT<sub>P1</sub>-*b*-Mal<sub>7</sub> and P3HT<sub>P1</sub>-*b*-AcMal<sub>7</sub> failed to achieve ordered nanostructures.

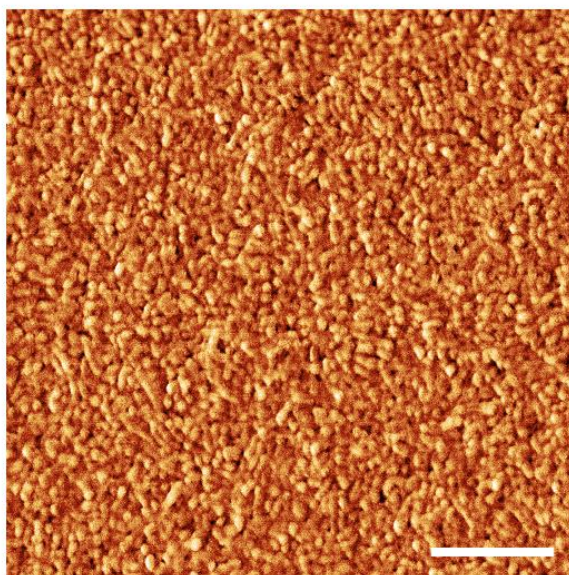


**Figure 3.6** Representative AFM phase images of P3HT<sub>P1</sub>-*b*-Mal<sub>7</sub> thin films after solvent vapor annealing for 24 h with (a) anisole and (b) CHCl<sub>3</sub>/MeOH = 1/1. Scale bars indicate 200 nm.



**P3HT-*b*-AcMal<sub>7</sub>**

THF/H<sub>2</sub>O



**Figure 3.7** Representative AFM phase image of P3HT<sub>P1</sub>-*b*-AcMal<sub>7</sub> thin film after solvent annealing under the vapor produced from mixture of THF/H<sub>2</sub>O = 1/1 for 24h. Scale bar indicates 200 nm.

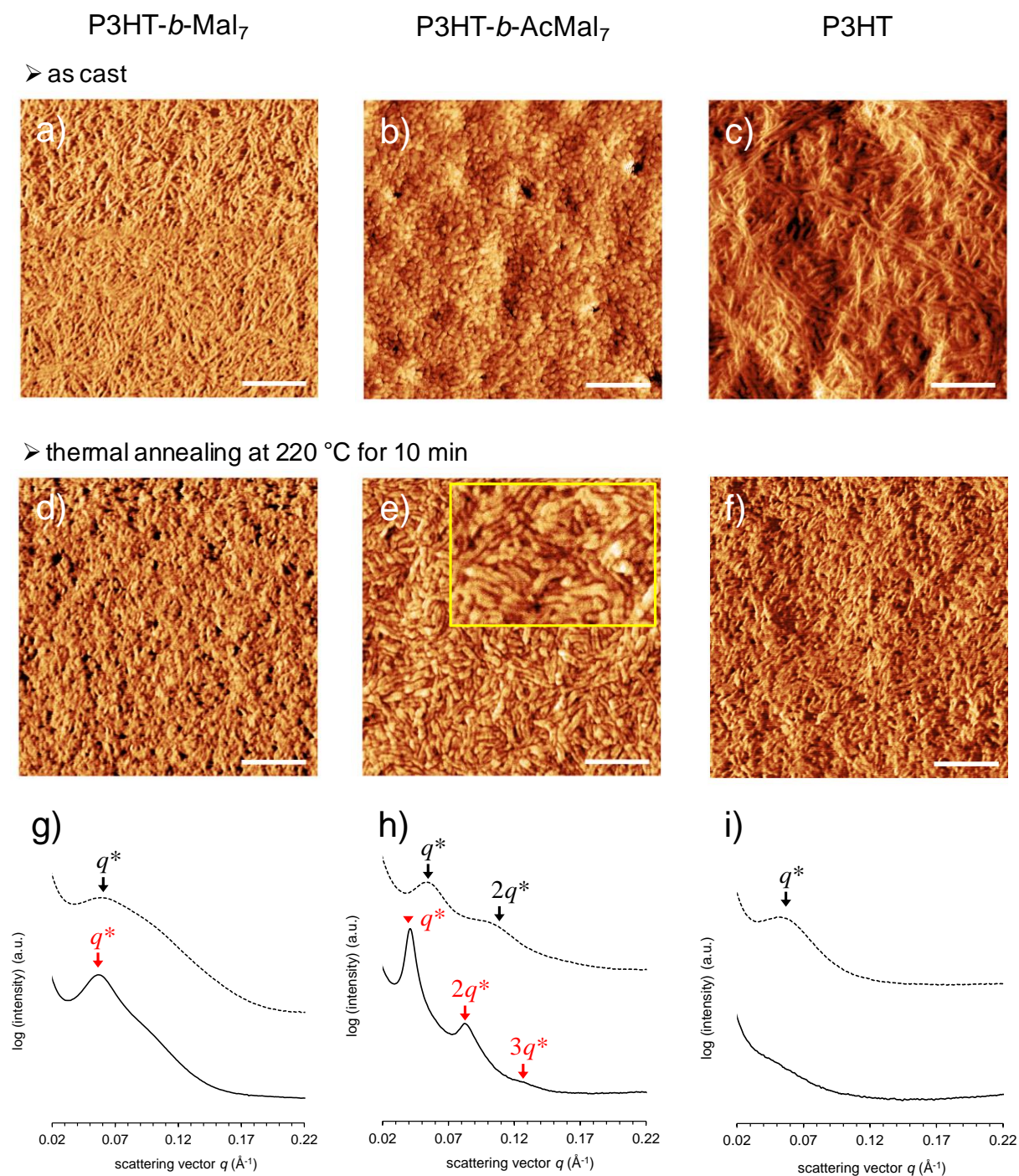
### III.5 Self-organization via thermal annealing

An alternative approach known as simple and cost effective technique for inducing the self-organization of block copolymers is thermal annealing. As mentioned in the above section, the applied temperature should be carefully chosen so as to be above the glass transition temperature ( $T_g$ ) or melting temperature ( $T_m$ ) of both segments to impart the mobility but below the decomposition temperature ( $T_d$ ) of the block copolymers. Therefore, the thermal properties of the block copolymers and each segment (AcMal<sub>7</sub>, Mal<sub>7</sub> and P3HT) were investigated by differential scanning calorimetry (DSC) and thermogravimetric analysis (TGA). The DSC gave the  $T_m$  of the ethynyl-P3HT **P1** ( $T_{m,P3HT-P1}$ ), P3HT-*b*-AcMal<sub>7</sub> ( $T_{m,P3HT(P1)-b-AcMal7}$ ), and P3HT-*b*-Mal<sub>7</sub> ( $T_{m,P3HT(P1)-b-Mal7}$ ) as 178 °C, 189 °C, and 189 °C, respectively. The  $T_g$  of AcMH ( $T_{g,AcMal7}$ ) was 115 °C, while the  $T_g$  of Mal<sub>7</sub> ( $T_{g,Mal7}$ ), which was reported to be around 150-160 °C,<sup>12</sup> was not observed in our experiments. The thermal decomposition temperatures for a 5 % weight loss ( $T_{d,5\%}$ ) of P3HT, P3HT-*b*-AcMal<sub>7</sub> and P3HT-*b*-Mal<sub>7</sub> were 422, 291 and 187 °C, respectively. The detailed discussion about the thermal properties of the block copolymers will be presented in the following chapter (refer to Chapter IV.I).

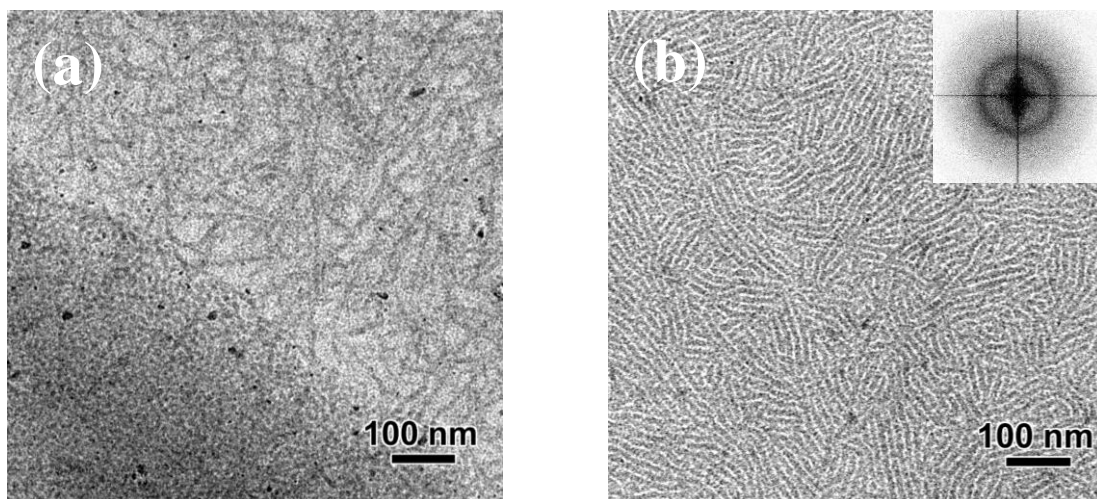
Thin films of the P3HT<sub>P1</sub>-*b*-Mal<sub>7</sub>, P3HT<sub>P1</sub>-*b*-AcMal<sub>7</sub>, and P3HT homopolymer were therefore annealed at 220 °C for 10 min under vacuum condition. This temperature was chosen based on the melting temperature of the P3HT-*b*-AcMal<sub>7</sub> and P3HT-*b*-Mal<sub>7</sub> ( $T_{m,P3HT(P1)-b-AcMal7} = T_{m,P3HT(P1)-b-Mal7} = 189$  °C) to melt the P3HT block and trigger the microphase separation of the block copolymers. After thermal annealing, the P3HT<sub>P1</sub>-*b*-Mal<sub>7</sub> film as well as the P3HT homopolymer film showed short-range fibril-like structures or rather disordered structures (representative images are shown in Figure 3.8d and 3.8f), indicating that the self-organization of P3HT<sub>P1</sub>-*b*-Mal<sub>7</sub> from molten state is dominated by the strong tendency of the P3HT to crystallize. Similar to the AFM observations, the corresponding SAXS profiles of the thermal annealed P3HT<sub>P1</sub>-*b*-Mal<sub>7</sub> bulk sample showed only a broad primary scattering peak ( $q^*$ ) arise from fibril-like P3HT crystalline structures (solid line in the Figure 3.8g). Thus, P3HT<sub>P1</sub>-*b*-Mal<sub>7</sub> could not be organized into periodic microphase separated structures by thermal annealing.

On the other hand, the AFM image of P3HT-*b*-AcMal<sub>7</sub> thin film showed clear morphological change toward well-defined periodic stripe pattern after thermal annealing as shown in Figure

3.8e. The SAXS profiles of the bulk P3HT<sub>P1</sub>-*b*-AcMal<sub>7</sub> samples after thermal annealing clearly support this morphological change (solid line in the Figure 3.8h), *i.e.*, sharp peaks in the SAXS profile after thermal annealing located at  $q^*$ ,  $2q^*$  and  $3q^*$  positions indicated a microphase separated lamellar phase with inter-domain spacing ( $d$ ) of 15.4 nm (half-pitch < 8 nm) determined from the  $q^*$  position using the Bragg equation:  $d = 2\pi/q^*$ . The TEM images of the thin film of P3HT<sub>P1</sub>-*b*-AcMal<sub>7</sub> before and after annealing are shown in Figure 3.9. Whereas the as-spun P3HT<sub>P1</sub>-*b*-AcMal<sub>7</sub> film (Figure 3.9a) showed regions of dot- and fibril-like structures, the thermally annealed sample (Figure 3.9b) displayed a well-ordered lamellar structure. The inter-domain spacing was estimated by Fast Fourier Transformation (FFT) of the TEM image and found to be *ca.* 14 nm, which is in good agreement with the inter-domain spacing calculated from the SAXS profile. Such domain features are one of the smallest sizes achieved to date by microphase separation of P3HT-based block copolymers.



**Figure 3.8** AFM phase images of as-cast films for (a) P3HT<sub>P1</sub>-*b*-Mal<sub>7</sub>, (b) P3HT<sub>P1</sub>-*b*-AcMal<sub>7</sub>, (c) ethynyl-P3HT **P1**, and thermally annealed films at 220 °C for 10 min for (d) P3HT<sub>P1</sub>-*b*-Mal<sub>7</sub>, (e) P3HT<sub>P1</sub>-*b*-AcMal<sub>7</sub>, (f) ethynyl-P3HT **P1**. Scale bars indicate 200 nm. SAXS profiles of neat samples in bulk (dotted line) and thermally annealed bulk samples (solid line) at 220 °C for 10 min for (g) P3HT<sub>P1</sub>-*b*-Mal<sub>7</sub>, (h) P3HT<sub>P1</sub>-*b*-AcMal<sub>7</sub> and (i) ethynyl-P3HT **P1**.



**Figure 3.9** TEM images of (a) as-spun and (b) thermally annealed (220 °C for 10 min) P3HT<sub>P1</sub>-*b*-AcMal<sub>7</sub> thin films. Fourier transform image of TEM image is given as the inset.

The P3HT<sub>P1</sub>-*b*-AcMal<sub>7</sub> has the ability to self-organize into periodic lamellar structure when the block copolymer obtained enough free mobility by heating to achieve the equilibrium state, while the structure formation of the P3HT<sub>P1</sub>-*b*-Mal<sub>7</sub> is mainly governed by the crystallization of the P3HT segment. In our previous studies on the unprotected oligo- and poly-saccharide-conjugated block copolymer systems, various types of well-organized nanostructures were achieved by thermal or solvent vapor annealing. To the contrary, the block copolymer consisting of P3HT and unprotected Mal<sub>7</sub> (P3HT<sub>P1</sub>-*b*-Mal<sub>7</sub>) did not self-organize, while the block copolymer of P3HT and acetyl-protected Mal<sub>7</sub> (P3HT<sub>P1</sub>-*b*-AcMal<sub>7</sub>) self-organized into a periodic lamellar structure.

Molecular properties of P3HT-*b*-AcMal<sub>7</sub> and P3HT-*b*-Mal<sub>7</sub> are summarized in Table 3.1. Based on the theory of block copolymer thermodynamics, the phase behavior of the rod-coil type of diblock copolymer is governed by following five factors: (i) the volume fractions of each block,  $f_A$  and  $f_B$  ( $f_A + f_B = 1$ ), (ii) the total degree of polymerization,  $N$  ( $N = N_A + N_B$ ), (iii) Flory-Huggins interaction parameter,  $\chi$ , which represents the degree of incompatibility between A and B blocks, (iv) Maier-Saupé interaction parameter,  $\mu$ , which represents the strength of rod-rod interaction (liquid crystalline interactions), and (v) the conformation asymmetry,  $\nu$  defined as a ratio of the radius of gyration of the coil and the rod length ( $\nu = R_{g, \text{coil}} / L_{\text{rod}}$ ) (Chapter I.3.1). The parameter  $\nu$

is known to affect the boundaries of the phase diagram, such as order-to-order transition and order-to-disorder transition. However, the relationship between the mismatch in the geometric distribution of both blocks ( $v$ ) and phase behavior is not fully understood so far.

Given the fact that the P3HT-*b*-AcMal<sub>7</sub> and P3HT-*b*-Mal<sub>7</sub> have same number of the monomer units and contain the same P3HT segments, there is no difference in the  $N$  and  $\mu$  parameter between the two block copolymer systems. For  $f_{\text{P3HT}}$ ,  $\chi$ , and  $v$ , quantitative or qualitative differences can be given between those of P3HT-*b*-AcMal<sub>7</sub> and P3HT-*b*-Mal<sub>7</sub>. From the point of view of phase segregation strength, the lower  $f_{\text{P3HT}}$  value for P3HT-*b*-AcMal<sub>7</sub> ( $f_{\text{P3HT}} = 0.66$ ) compared to that of P3HT-*b*-Mal<sub>7</sub> ( $f_{\text{P3HT}} = 0.80$ ) is advantageous because it is supposed to reduce the influence of P3HT crystallinity on the microphase separation. The  $\chi$  parameter (crucial driving force for the microphase separation) of the P3HT-*b*-AcMal<sub>7</sub> is presumed to be smaller than that of P3HT-*b*-Mal<sub>7</sub> because of the protection of hydroxyl groups by acetyl groups leading to a decrease in the hydrophilic-hydrophobic incompatibility between oligosaccharide and P3HT blocks.

To the best of our knowledge, the P3HT-*b*-AcMal<sub>7</sub> is the first example showing a well-ordered periodic nanostructure in the solid-state originated from the phase separation of the block copolymer with a peracetylated oligosaccharide component, while we have reported a variety of self-organized thin films of block copolymers with unprotected oligosaccharides. It is important to note that most of the previously reported unprotected oligosaccharide-containing block copolymer systems required a solvent vapor annealing process to induce the microphase separation. On the contrary, P3HT-*b*-AcMal<sub>7</sub> could be organized by thermal annealing rather than the solvent vapor annealing. A possible explanation for this is the difference of the multipolar interaction between oligosaccharide chains. The strong inter- and intra-chain hydrogen bonding between hydroxyl groups of the oligosaccharides restrain the mobility of oligosaccharidic block and hinder microphase separation of the block copolymers containing unprotected oligosaccharides even by heating above  $T_g$  or  $T_m$  of each block. Only when the block copolymers are treated with solvent vapors, sufficient mobility for achieving a thermodynamic equilibrium state will be given to the polymers by weakening the hydrogen bonds. In the case of P3HT-*b*-AcMal<sub>7</sub> system, such restriction of the chain mobility due to the polar interaction is reduced by the protection of the hydroxyl groups of Mal<sub>7</sub> by acetylation. Hence, P3HT-*b*-AcMal<sub>7</sub> acquired chain mobility by heating above its  $T_m$  and self-organized into lamellar structures even with the



lower hydrophilic-hydrophobic incompatibility between AcMal<sub>7</sub> block and P3HT compared to that between Mal<sub>7</sub> block and P3HT block.

Conversely, solvent vapor annealing applied for the P3HT-*b*-AcMal<sub>7</sub> system did not induce self-organization. This is probably because the solvent used for the annealing could not break down the crystals of the P3HT block. For similar reason, the solvent annealing for the P3HT-*b*-Mal<sub>7</sub> system did not lead to the microphase separation either.

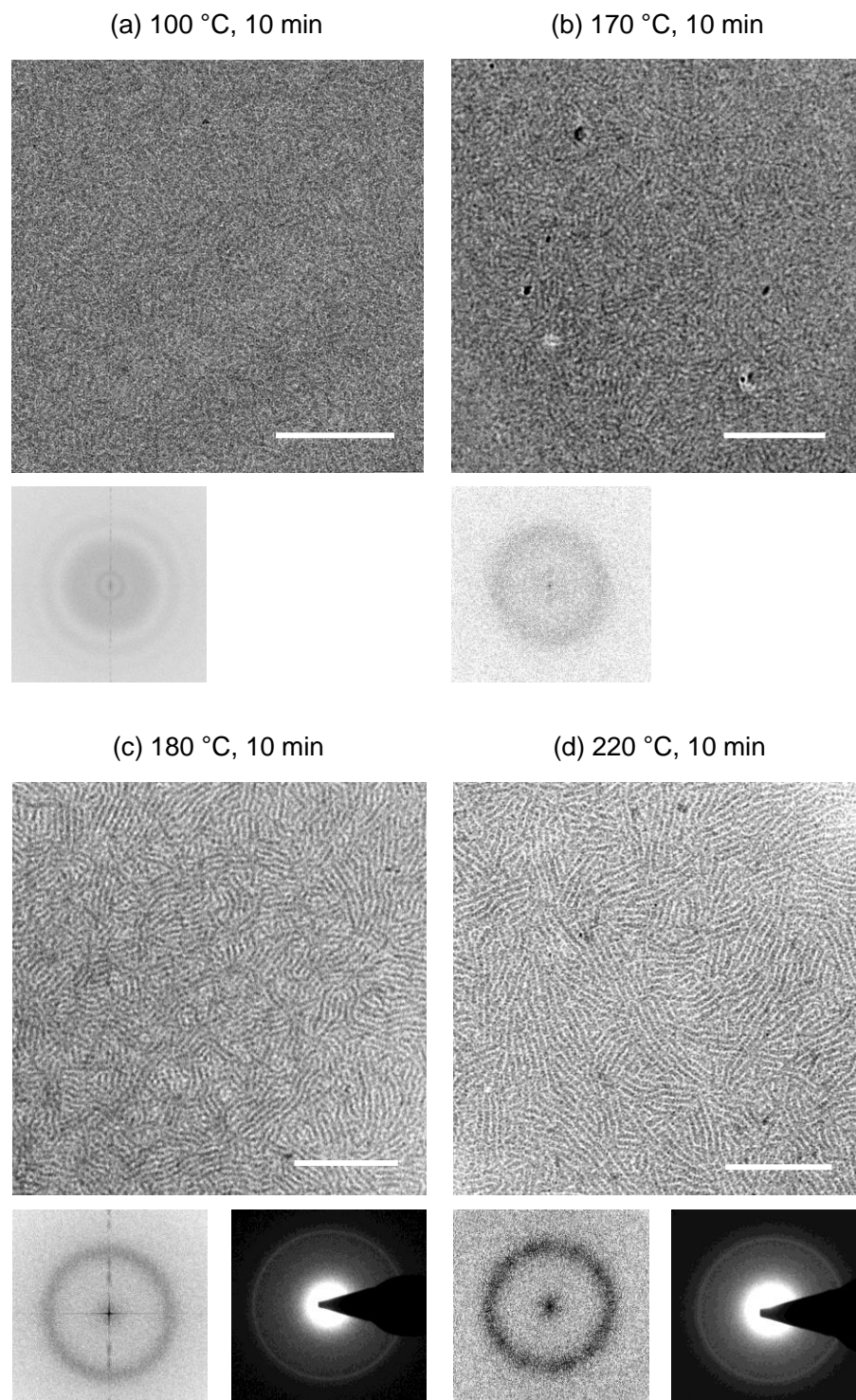
**Table 3.1** Molecular properties of P3HT-*b*-AcMal<sub>7</sub> and P3HT-*b*-Mal<sub>7</sub>

Possible factors that may affect the phase behavior of the block copolymers	P3HT- <i>b</i> -AcMal <sub>7</sub>		P3HT- <i>b</i> -Mal <sub>7</sub>
volume fraction	$f_{\text{P3HT}}$	<	$f_{\text{P3HT}}$
total number of monomer units	$N_{\text{P3HT-}b\text{-AcMal}_7}$	=	$N_{\text{P3HT-}b\text{-Mal}_7}$
Flory-Huggins interaction parameter	$\chi_{\text{P3HT-}b\text{-AcMal}_7}$	<	$\chi_{\text{P3HT-}b\text{-Mal}_7}$
Maier-Saupé interaction parameter	$\mu_{\text{P3HT-}b\text{-AcMal}_7}$	=	$\mu_{\text{P3HT-}b\text{-Mal}_7}$
conformation asymmetry	$\nu_{\text{P3HT-}b\text{-AcMal}_7}$	>	$\nu_{\text{P3HT-}b\text{-Mal}_7}$
thermal properties of the oligosaccharides	$T_{\text{g, AcMal}_7}$ : 115-120 °C < $T_{\text{g, Mal}_7}$ : 150-160 °C		
multipolar interaction of the oligosaccharides	weak	<	strong (hydrogen bond)

### Effect of annealing temperature on the morphology

To investigate the effect of the annealing temperature on the morphology, thin films of the P3HT<sub>P1</sub>-*b*-AcMal<sub>7</sub> were annealed at different temperatures for 10 min and characterized by TEM. At 100 °C where the temperature is below  $T_g$  of the AcMal<sub>7</sub> segment ( $T_{g, \text{AcMal}_7} = 115$  °C), no distinct ordered structure was observed as evidenced by FFT of the TEM image (Figure 3.10a). The beginning of the microphase separation was observed around 170 °C (Figure 3.10b). At 180 °C, which is slightly lower than melting temperature of the P3HT-*b*-AcMal<sub>7</sub> ( $T_{m, \text{P3HT(P1)-b-AcMal}_7} = 189$  °C), the periodic lamellae structure was clearly observed (Figure 3.10c). With a further temperature increase, a remarkable structural evolution in terms of the ordered domain size was observed (Figure 3.10d). In the temperature range above 180 °C, an obvious diffraction ring attributable to the  $\pi$ - $\pi$  stacking period of the P3HT main chains was observed in the electron diffraction patterns of the samples, indicating that the P3HT segments confined in the phase separated domains shows well-ordered crystalline structure. Thus, the annealing temperature must be at least near  $T_{m, \text{P3HT(P1)-b-AcMal}_7}$  for the formation of the well-ordered lamellar structure and a higher temperature is favorable in the range studied here.



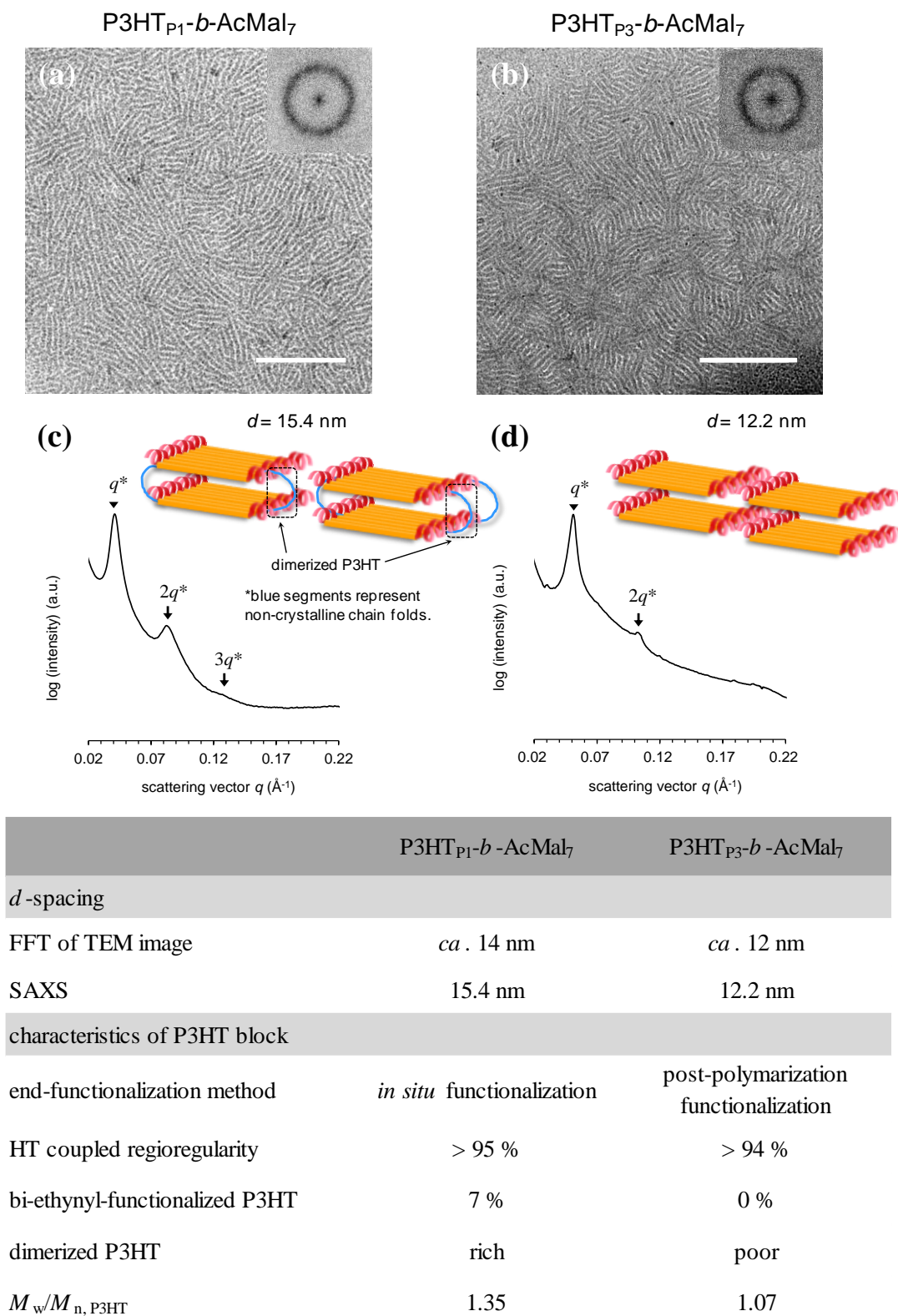


**Figure 3.10** TEM images of P3HTP<sub>1</sub>-*b*-AcMal<sub>7</sub> films obtained after thermal annealing at (a) 100 °C, (b) 170 °C, (c) 180 °C, and (d) 220 °C for 10 min. Scale bars indicate 200 nm. Fast Fourier transform (FFT) images and electron diffraction patterns are given bottom left and bottom right side of each TEM image, respectively.

### Comparison between P3HT<sub>P1</sub>-*b*-AcMal<sub>7</sub> and P3HT<sub>P3</sub>-*b*-AcMal<sub>7</sub>

The self-assembly behaviors of the P1 series (P3HT<sub>P1</sub>-*b*-AcMal<sub>7</sub> / P3HT<sub>P1</sub>-*b*-Mal<sub>7</sub>) and P3 series (P3HT<sub>P3</sub>-*b*-AcMal<sub>7</sub> / P3HT<sub>P3</sub>-*b*-Mal<sub>7</sub>) showed almost similar trend with a few exceptions. In both series, P3HT-*b*-Mal<sub>7</sub> block copolymer system did not exhibit any ordered periodic structures, while well-defined lamellar structures were obtained with the P3HT-*b*-AcMal<sub>7</sub> block copolymer system after thermal annealing. Figure 3.11a and 3.11b shows TEM images of the thermally annealed thin films of the P3HT<sub>P1</sub>-*b*-AcMal<sub>7</sub> and P3HT<sub>P3</sub>-*b*-AcMal<sub>7</sub>, respectively. Both samples display lamellae structure. The domain spacing of the P3HT<sub>P3</sub>-*b*-AcMal<sub>7</sub> estimated from the FFT of the TEM image was found to be *ca.* 12 nm which is slightly smaller than that of P3HT<sub>P1</sub>-*b*-AcMal<sub>7</sub> (*ca.* 14 nm). This deviation in domain spacing was further supported by SAXS analysis. Figure 3.11c and 3.11d shows the SAXS profiles of the thermally annealed bulk samples of the P3HT<sub>P1</sub>-*b*-AcMal<sub>7</sub> and P3HT<sub>P3</sub>-*b*-AcMal<sub>7</sub>, respectively. In both profiles, multiple scattering peaks located at integer multiples of the first peak position  $q^*$  were observed, indicative of the lamellar structure. The periodicity of the nanodomains calculated from the  $q^*$  peak position were 15.4 nm for the P3HT<sub>P1</sub>-*b*-AcMal<sub>7</sub> and 12.2 nm for the P3HT<sub>P3</sub>-*b*-AcMal<sub>7</sub>, respectively, showing good agreement with the TEM observations.

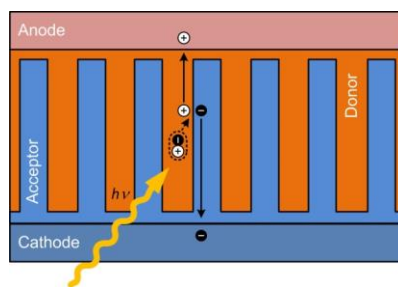
As described in the Chapter II.2.2, the post-polymerization functionalization method, which was employed for the preparation of the ethynyl-P3HT **P3**, enabled narrower molecular weight distribution, elimination of the bis-ethynyl-functionalized P3HT and suppression of the dimerized P3HTs formation (major differences between ethynyl-P3HT **P1** and ethynyl-P3HT **P3** are listed in the table below Figure 3.11). The difference in domain spacing between the P3HT<sub>P1</sub>-*b*-AcMal<sub>7</sub> and P3HT<sub>P3</sub>-*b*-AcMal<sub>7</sub> is most likely attributed to the amount of the dimerized P3HTs contaminated in the original P3HT homopolymers. The P3HT segments exhibit a fully extended chain conformation within the confined lamellar domain as will be demonstrated in the next section (Chapter III.6). Therefore, in order to allow the incorporation of the dimerized P3HT in the lamellar domain corresponding to the one polymer chain length, the dimerized P3HTs should fold back the chain as depicted in inset image of the Figure 3.11c. Since the bending parts cannot participate in the crystal formation, they form an amorphous region next to the crystalline layer. This non-crystalline chain folds might be responsible of the difference in the domain spacing.



**Figure 3.11** TEM images of (a) P3HT<sub>P1</sub>-*b*-AcMal<sub>7</sub> and (b) P3HT<sub>P3</sub>-*b*-AcMal<sub>7</sub> thin films obtained after thermal annealing at 220 °C for 10 min. Insets represent fast Fourier transform (FFT) images. Scale bars indicate 200 nm. SAXS profiles of (c) P3HT<sub>P1</sub>-*b*-AcMal<sub>7</sub> and (d) P3HT<sub>P3</sub>-*b*-AcMal<sub>7</sub> bulk samples obtained after thermal annealing at 220 °C for 10 min.

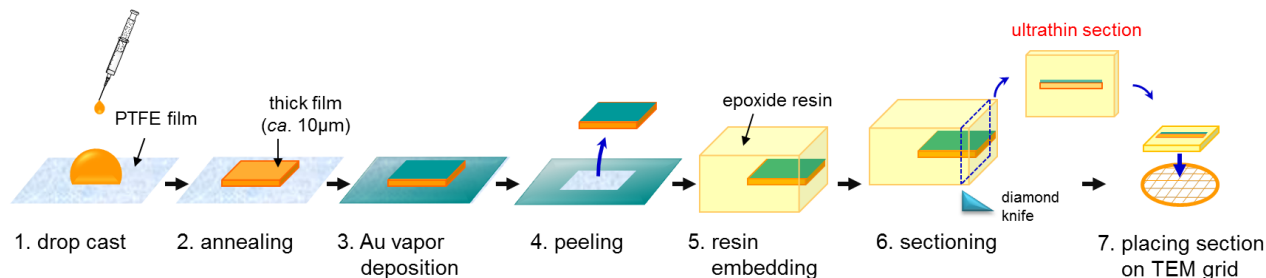
### Investigation of the internal structure of phase-separated P3HT-*b*-AcMal<sub>7</sub>

As described previously, the lamellae structure in which the electron donating and accepting materials are alternating at the sub-20 nm scale (comparable to the exciton diffusion length) is considered as the ideal active layer structure. In addition, to collect charge carriers efficiently, the donor and acceptor domains must form co-continuous pathways toward the respective electrodes (anode and cathode), namely the lamellae must stand perpendicular to the substrate as shown in Figure 3.12. Therefore, not only the morphology and size but also the orientation of lamellae is essential for high performance photovoltaic cells.



**Figure 3.12** An ideal structure for the active layer morphology of organic thin film solar cells.

In order to investigate the internal lamellae orientation, ultrathin sections of the phase-segregated P3HT<sub>P3</sub>-*b*-AcMal<sub>7</sub> were prepared and observed using TEM. Ultrathin section was prepared according to the procedure as shown in Figure 3.13. About 10 μm-thick P3HT<sub>P3</sub>-*b*-AcMal<sub>7</sub> film was prepared by drop casting from a concentrated polymer solution (solvent: THF) onto a PTFE substrate. After complete evaporation of the solvent, the resulting thick film was annealed at 220 °C for 10 min under vacuum to induce the structure formation. Gold was sputtered on top of the film to mark the interface between air and film surface. The thick film was then soaked in absolute ethanol overnight to dehydrate, and then embedded in an epoxy resin mixture. The hardened resin block was cut with a diamond knife to give ultrathin sections with thicknesses of less than 100 nm.



**Figure 3.13** Microtome procedure.

Figure 3.14 shows cross sectional TEM images of the thermally annealed P3HT<sub>P3</sub>-*b*-AcMal<sub>7</sub> films observed in the vicinity of the interface of air/film surface and film/PTFE substrate, respectively. In both cases, well-defined lamellar structure with a width of *ca.* 12 nm and a length of several tens to hundreds of nanometers was observed over the entire film.

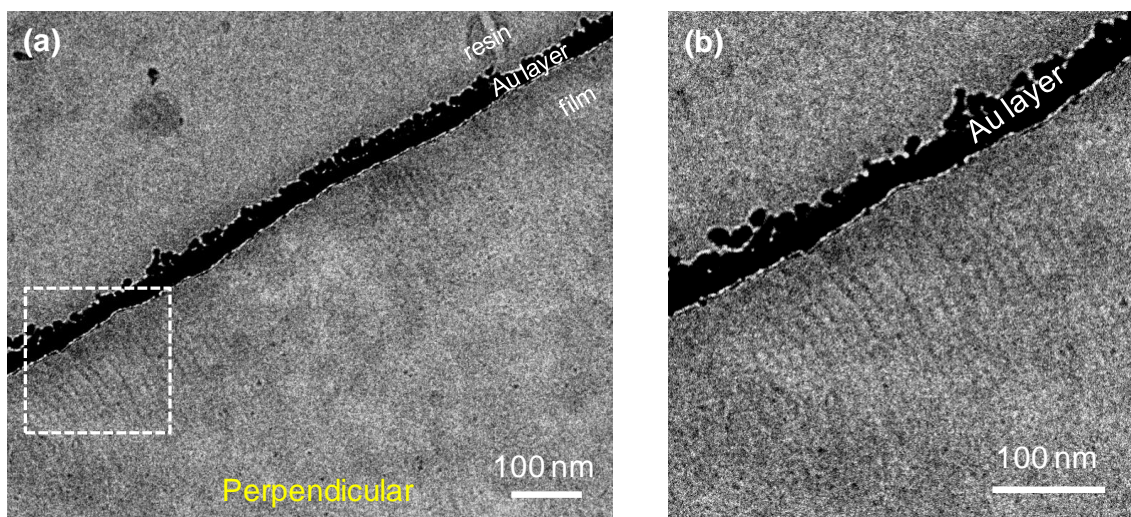
Regarding the lamellar orientation, at the bottom boundary, no preferential orientation was observed (Figure 3.14c). On the other hand, at the interface between air and the film top, perpendicularly oriented lamellae structure was exclusively observed in the region over more than 100 nm in depth from the film surface.

This observation was further confirmed by the Grazing incidence small-angle X-ray scattering (GISAXS) measurement. Figure 3.15 shows two-dimensional GISAXS pattern of thermally annealed P3HT<sub>P3</sub>-*b*-AcMal<sub>7</sub> thin film deposited on the Si substrate with a film thickness of *ca.* 35 nm. A clear spot parallel to the substrate is visible at *d*-spacing of 12.6 nm, indicating the perpendicular orientation.

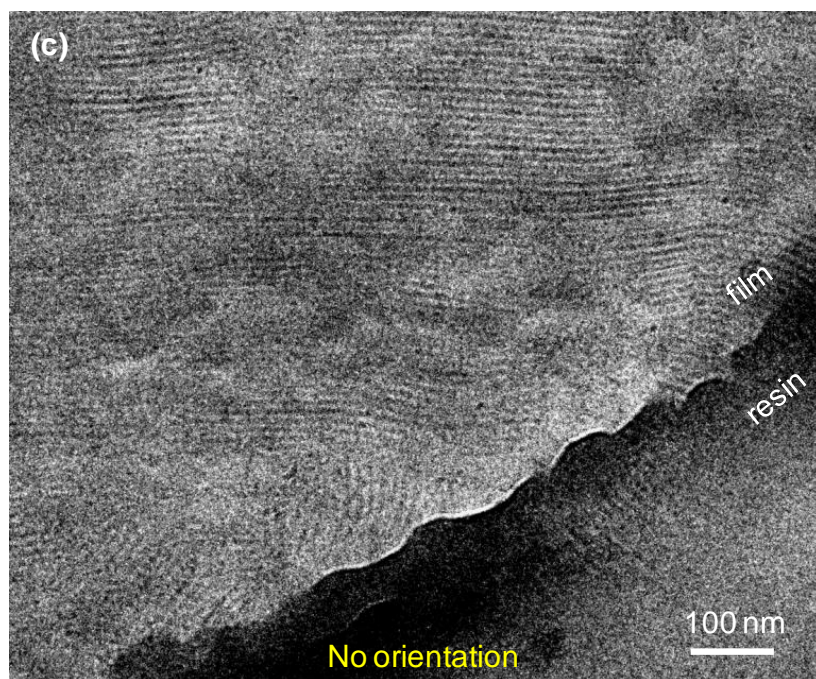
It is interesting that the P3HT-*b*-AcMal<sub>7</sub> tends to organize into perpendicularly oriented lamellae structure spontaneously at the air/film interface while at the bottom interface the domain orientation depends on the nature of the substrate. To understand this phenomenon, further investigations are needed.



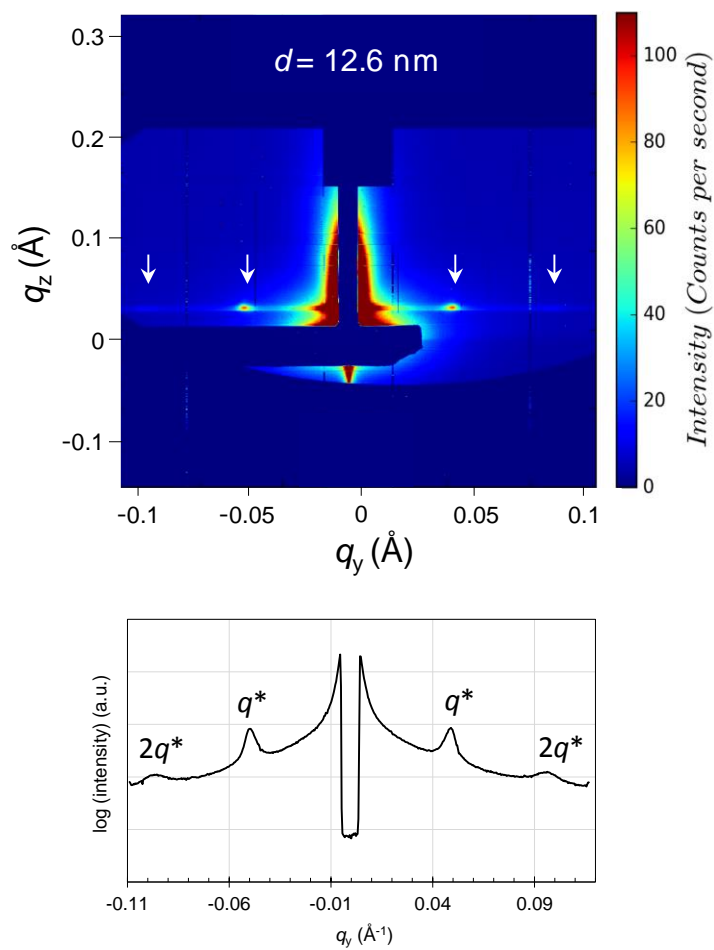
air/film interface



PTFE/film interface



**Figure 3.14** TEM images of the cross-section of thermally annealed P3HT<sub>P3</sub>-*b*-AcMal<sub>7</sub> films (annealing condition: 220 °C for 10 min). (a) Low magnification image of the air/film interface, (b) magnified image of the encircled area with dotted line in (a), and (c) low magnification image of the PTFE substrate/film interface.

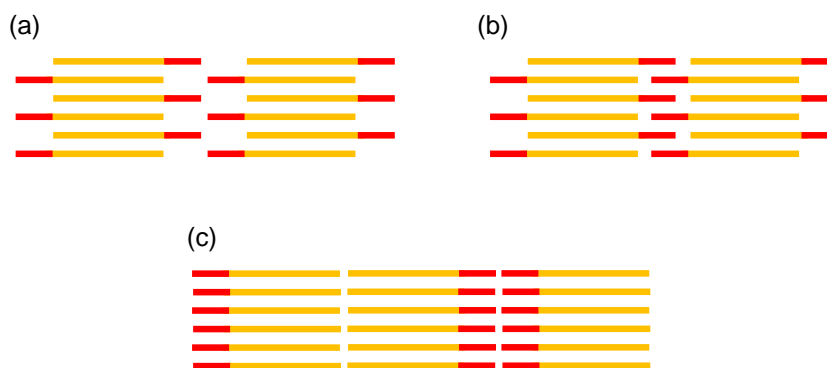


**Figure 3.15** Two-dimensional GISAXS pattern of P3HT<sub>P3</sub>-b-AcMal<sub>7</sub> thin film (*ca.* 35 nm) annealed at 200 °C for 10 min.

### III.6 Molecular Packing Model

How are the AcMal<sub>7</sub> and P3HT segments arranged in the phase-segregated lamellar domain? Basically, there are three possible arrangements as shown in Figure 3.16. The key differences in three models are; whether the block copolymers are aligned monolayers or bilayers and whether the AcMal<sub>7</sub> segments are interdigitated or not.

Whether the structure is based on monolayer or bilayer can be easily judged from the *d*-spacing of the lamellae structure. According to the SAXS measurement the *d*-spacing of the lamellae structure arisen from the phase separation of the P3HT<sub>P3</sub>-*b*-AcMal<sub>7</sub> was 12.2 nm. On the other hand, the *d*-spacing calculated from a broad primary scattering peak of the ethynyl-P3HT **P3** bulk was found to be 10.7 nm, which is indicative of the average width of the P3HT nanofiber (data are summarized in Table 3.2). Given the fact that the P3HTs having relatively low molecular weight tend to solidify into semi-crystalline structure with fully extended chain conformation, bilayer arrangement would not be possible because the length corresponding to the two P3HT polymer chains ( $10.7 \times 2 = 21.4$  nm) is already far beyond the experimental value (12.2 nm).



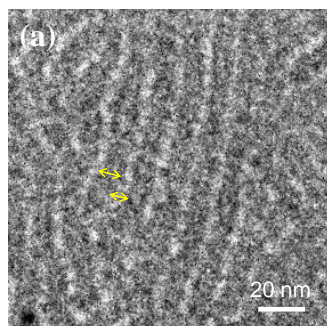
**Figure 3.16** Schematic images of possible packing models for lamellar structure of the P3HT-*b*-AcMal<sub>7</sub>, where orange and red lines represent the P3HT and AcMal<sub>7</sub> segments, respectively. (a) monolayer, non-interdigitated AcMal<sub>7</sub> packing (side-by-side arrangement), (b) monolayer, interdigitated AcMal<sub>7</sub> packing, and (c) bilayer, non-interdigitated AcMal<sub>7</sub> packing. For simplicity, scale and tilt of each block are disregarded here.



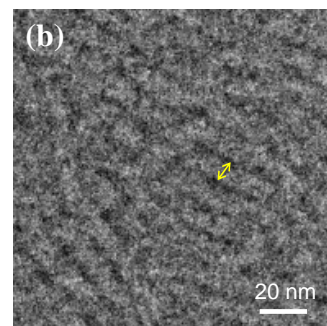
The individual domain sizes of the P3HT and AcMal<sub>7</sub> segments were estimated by close inspection of the TEM images. Magnified TEM image of the phase-separated P3HT-*b*-AcMal thin film and estimated domain sizes are presented in Table 3.2. Here, dark and bright regions observed in the TEM image can be attributed to the P3HT and AcMal<sub>7</sub> blocks, respectively. Note that no staining was applied prior to TEM observation of the P3HT-*b*-AcMal<sub>7</sub> thin film but sufficient diffraction contrast was obtained by filtering the scattered electron. This contrast arises from the difference in electron scattering power between crystalline P3HT block involving sulfur atoms (dark region) and AcMal<sub>7</sub> block (bright region). This contrast was further enhanced during the observation probably because the AcMal<sub>7</sub> is more sensitive to electron beam irradiation than the P3HT and easily damaged. The size of P3HT domain within the lamellar structure measured on the photograph was *ca.* 7.1 nm which is slightly smaller than the width of nanofibers consisted of the ethynyl-P3HT **P3** (10.7 nm (SAXS data), 8.7 nm (TEM data)). The AcMal<sub>7</sub> domain was about 5 nm.

**Table 3.2** Experimental structural parameters for P3HT<sub>P3</sub>-*b*-AcMal<sub>7</sub> and ethynyl-P3HT<sub>P3</sub>

		P3HT <sub>P3</sub> - <i>b</i> -AcMal <sub>7</sub> lamellar structures			ethynyl-P3HT <sub>P3</sub> nano fibrils
		total	P3HT <sub>P3</sub> block	AcMal <sub>7</sub> block	
SAXS <sup>a</sup>		12.2 nm	–	–	10.7 nm
TEM <sup>b</sup>	FFT	12.1 nm	–	–	10.6 nm
	visual estimation	12.1 ± 0.4 nm	7.1 ± 0.8 nm	5.0 ± 0.7 nm	8.7 ± 0.8 nm



- dark domain → P3HT
- bright domain → AcMal<sub>7</sub>



- P3HT nano fibrils

<sup>a</sup> *d*-spacings determined from primary scattering peak *q*\* in the corresponding SAXS profiles.

<sup>b</sup> The widths of each domain for the P3HT<sub>P3</sub>-*b*-AcMal<sub>7</sub> and P3HT nano fibrils were estimated by using inset TEM images (a) and (b), respectively.

Since the two blocks, the P3HT and AcMal<sub>7</sub>, are tethered each other, they must share the same lateral arrangement. In this context, the cross-sectional area of the P3HT and AcMal<sub>7</sub> segments, which can influence on the molecular conformation especially at interface of the two blocks, may provide crucial information to understand the packing mode of the block copolymer. The cross-sectional area of the P3HT segment was estimated based on the unit cell parameters proposed by Brinkmann *et al.*<sup>13</sup> On the other hand, the unit cell of the AcMal<sub>7</sub> is not available in the literature, because the maltoheptaose does not contain enough glucose units to form periodic helical structures which many other polysaccharides form, it rather shows amorphous structure. Thus, the unit cell parameters of model compound, amylose triacetate (form I), was used as reference values.<sup>14</sup> The amylose triacetate has exactly the same chemical structure as AcMal<sub>7</sub>, *i.e.* peracetylated linear  $\alpha$ -1,4 linked D-glucan, except for molecular weight. Here, the cross-sectional area ( $A$ ) is given by using unit cell parameters ( $a$ ,  $b$ , and  $\gamma$ ) as

$$A = \frac{a \times b \times \sin(\gamma)}{n}$$

where  $n$  is the number of molecules per unit cell. The obtained cross-sectional area of the P3HT ( $A_{\text{P3HT}}$ ) and AcMal<sub>7</sub> ( $A_{\text{AcMal7}}$ ) segments are 62 Å<sup>2</sup> and 103 Å<sup>2</sup>, respectively. The  $A_{\text{AcMal7}}$  is found to be 1.7 times larger than the  $A_{\text{P3HT}}$ . Considering the fact that a diffraction ring attributable to the  $\pi$ - $\pi$  stacking of the thiophene backbone (*ca.* 3.8 Å) has been observed in the electron diffraction pattern of the phase-separated P3HT-*b*-AcMal<sub>7</sub> thin film (Figure 3.9b), the P3HT segments should have a crystalline structure closely similar to the unit cell. In this case, the AcMal<sub>7</sub> segments cannot interdigitate each other due to their large molecular dimension compared with that of the P3HT segments. Therefore, the side-by-side arrangement (Figure 3.16a) seems the most likely model. The molecular length of AcMal<sub>7</sub> calculated based on the unit cell parameters is 2.7 nm. The AcMal<sub>7</sub> domain size estimated from TEM image (5.0 nm) roughly matches with the twice of the AcMal<sub>7</sub> length ( $2.7 \times 2 = 5.4$  nm). This coincidence in size corroborates the assumption of side-by-side arrangement. The contour length of the P3HT segment is given as the product of the number of repeating unit (DP = 23) times half value of lattice parameter  $c$  ( $c = 7.8$  Å), *i.e.* 9.0 nm ( $= 0.78 \text{ nm} \times 23$ ). This value is very close to the width of ethynyl-P3HT **P3** nanofibers (8.7 nm (data from TEM image)) but slightly larger than the single domain size of the P3HT segments estimated from TEM image ( $d_{\text{P3HT}} = 7.1$  nm). Considering the stiffness of the P3HT backbone and the proof of the  $\pi$ -stacked structure, a majority of the P3HT chains should be

fully extended in the phase-segregated nanodomain rather than shrinking. Based on this assumption, the discrepancy between the calculated polymer length and observed domain size can be reconciled by a model in which the P3HT segments are arranged in crystalline layer, with the main chains axes tilted to the lamellae planes (*i.e.* smectic C-like arrangement). Schematic image of the expected arrangement is depicted in Figure 3.17a. The tilt angle of the P3HT main chains relative to the lamellae plane ( $\theta$ ) can be calculated as

$$\theta \approx \arccos\left(\frac{7.1 \text{ nm}}{9.0 \text{ nm}}\right) \approx 38^\circ$$

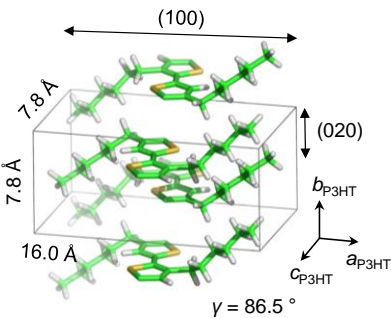
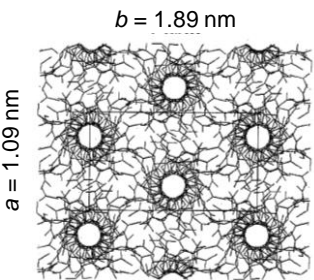
One explanation for this tilt arrangement can be provided on the basis of the space filling (density) argument. Non-polar molecules tend to fill the space avoiding free volumes, to reduce the enthalpy. Now suppose that the AcMal<sub>7</sub> segments first form a stable structure analogous to the crystal structure of the model compound (amylose triacetate). If the P3HT segments are aligned parallel to the AcMal<sub>7</sub> segment without tilt as shown Figure 3.17b, the  $\pi$ - $\pi$  stacking distance of the P3HT backbone would be determined by intermolecular distance of AcMal<sub>7</sub> (1.09 nm) because of the bulky structure of the AcMal<sub>7</sub>. In this case, the predicted density of the P3HT segment for this arrangement ( $\rho_{\text{P3HT, EX}} = 0.77 \text{ g/cm}^3$ ) is considerably lower than that of the crystal density ( $\rho_{\text{P3HT, crystal}} = 1.14 \text{ g/cm}^3$ ), indicating that the nontilted P3HT arrangement is thermodynamically unfavorable. In order to maintain the crystal density, the P3HT should be stacked with a stacking period of 0.78 nm per two chains equivalent to the lattice parameter  $c$ . Hence, the tilting of the P3HT main chain is the only solution to enable a thermodynamically stable arrangement. The expected structure is presented in Figure 3.17c. The tilt angle based on this model can be estimated as follows,

$$\theta \approx \arccos\left(\frac{0.78 \text{ nm}}{1.09 \text{ nm}}\right) \approx 44^\circ$$

This angle (44°) virtually coincides with the angle estimated from the geometric approach (38°).

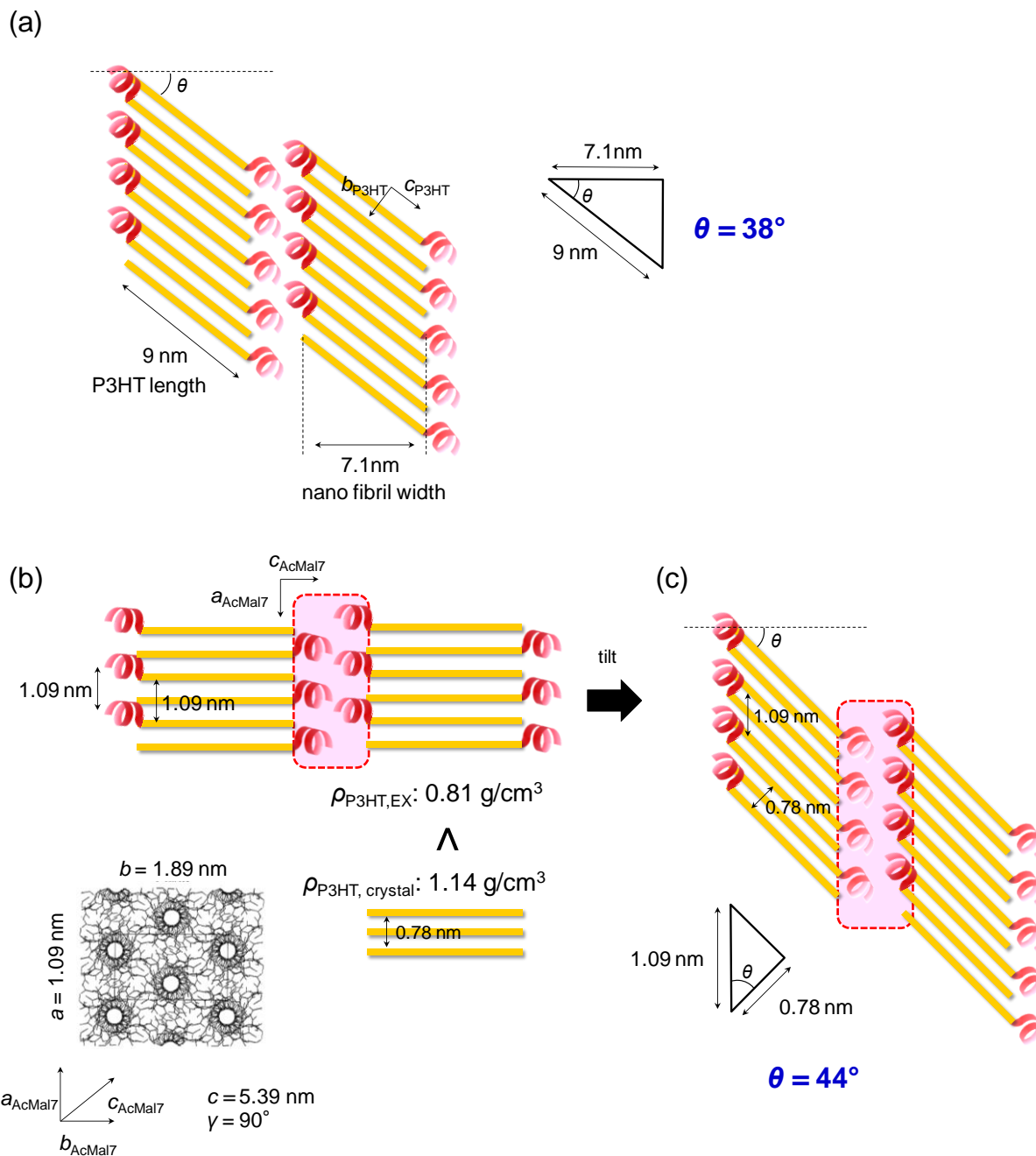
From the above considerations, it can be concluded that the P3HT and AcMal<sub>7</sub> segments are confined in the lamellae in which the AcMal<sub>7</sub> segments are aligned side-by-side (no interdigitation). The P3HT segments are tilting with respect to the lamellae plane and strongly  $\pi$ -stacked with an extended chain conformation in order to attain thermodynamically stable crystalline structure. An overall view of the proposed molecular packing model for the P3HT-*b*-AcMal<sub>7</sub> lamellar structure is depicted in Figure 3.18. This distinct molecular arrangement is attained as a result of the competition of multiple factors such as incompatibility between two blocks, strong  $\pi$ - $\pi$  interaction between P3HT backbones, geometrical mismatch between two blocks, space filling requirement and entropic penalties.

**Table 3.3** Structural parameters of P3HT and AcMal<sub>7</sub>

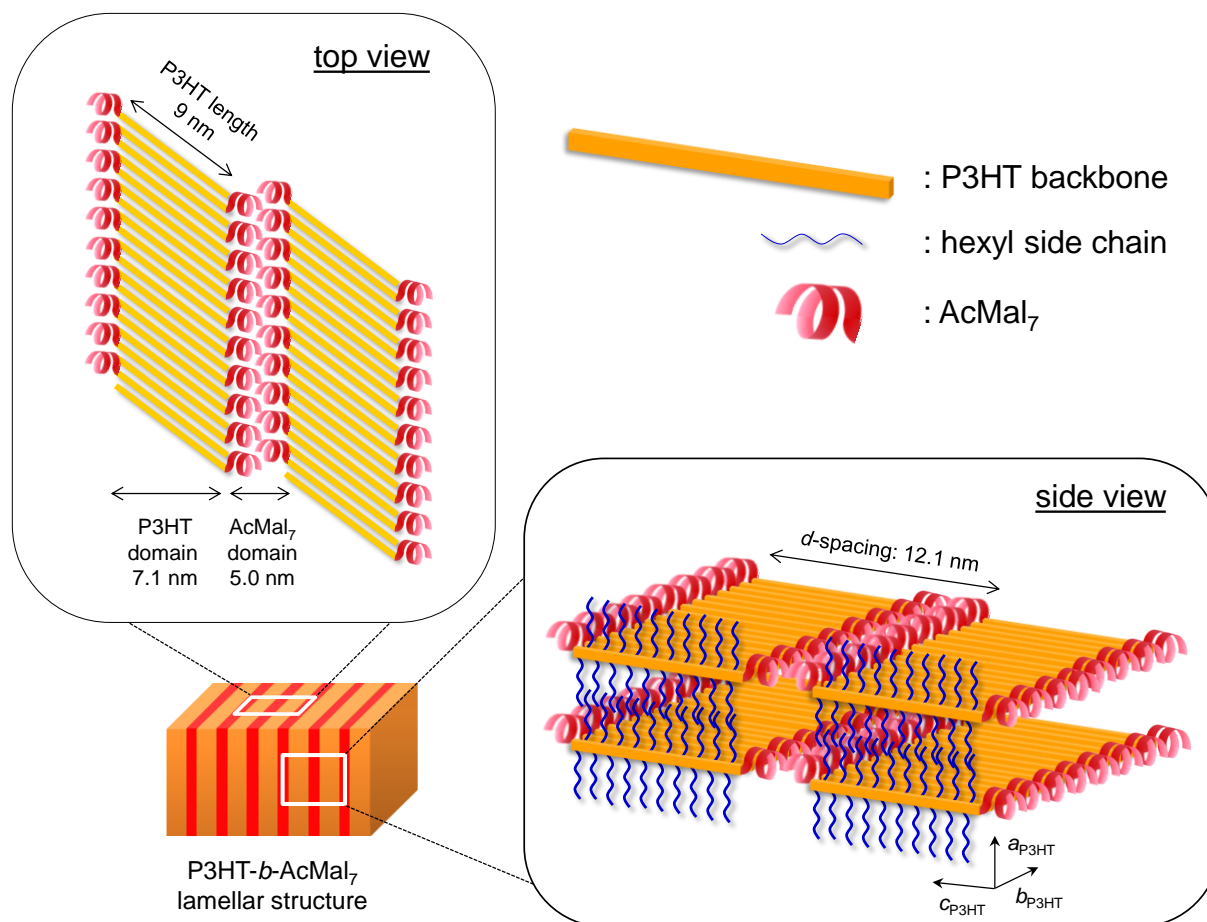
	P3HT <sub>P3</sub> (DP = 23)	AcMal <sub>7</sub> ≈ Amylose triacetate
unit cell parameters <sup>a</sup>		
cross-sectional area	62 Å <sup>2</sup>	103 Å <sup>2</sup>
monomer length	3.9 Å <sup>b</sup>	3.9 Å <sup>c</sup>
estimated molecular length	9.0 nm	2.7 nm
density	1.14 g/cm <sup>3</sup>	1.20 g/cm <sup>3</sup>

<sup>a</sup> Unit cell models for P3HT and AcMal<sub>7</sub> were referred from ref.13 and ref.14, respectively.

<sup>b</sup> Length of a 3-hexylthiophene unit. <sup>c</sup> Length of a glucose unit.



**Figure 3.17** Schematic illustrations of (a) expected arrangement estimated based on geometrical parameters, (b) hypothetical arrangement and density assuming P3HT segments are aligned parallel to the AcMal<sub>7</sub> segments, and (c) expected arrangement estimated based on space-filling (density) argument.



**Figure 3.18** Overall view of the proposed molecular packing model of P3HT-*b*-AcMal<sub>7</sub> lamellar structure, where orange bar, blue solid line and red helix represent the P3HT backbone, hexyl side-chain of P3HT, and AcMal<sub>7</sub>, respectively.

### III.7 Conclusion

The self-assembly behavior of synthesized block copolymers have been investigated by AFM, TEM, and SAXS analysis. The P3HT-*b*-AcMal<sub>7</sub> diblock copolymer was found to self-assemble into well-defined lamellar structure in sub-10 nm scale, which is one of the smallest domain sizes achieved by self-assembly of P3HT-based block copolymers, when the block copolymer obtained enough free mobility by heating to reach the equilibrium state.

Cross-sectional TEM observation and GISAXS measurement revealed that P3HT-*b*-AcMal<sub>7</sub> tends to organize into perpendicularly oriented lamellae structure spontaneously at the air/film interface while at the bottom interface the domain orientation depends on the nature of the substrate.

Based on the geometrical parameters and space-filling arguments, a molecular packing model for the self-assembled lamella structure of P3HT-*b*-AcMal<sub>7</sub> was proposed. The P3HT and AcMal<sub>7</sub> segments are confined in the lamellae in which the AcMal<sub>7</sub> segments are aligned side-by-side. The P3HT segments are tilting with respect to the lamellae plane and strongly  $\pi$ -stacked with an extended chain conformation in order to attain thermodynamically stable crystalline structure. This distinct molecular arrangement should be attained as a result of the competition of multiple factors such as segregation strength between P3HT and AcMal<sub>7</sub>, strong  $\pi$ - $\pi$  interaction of P3HT backbones, geometrical mismatch between two blocks, space filling requirement and entropic penalties.

### III.8 References

- (1) Liu, J.; Sheina, E.; Kowalewski, T.; McCullough, R. D. *Angew. Chemie Int. Ed.* **2002**, *41* (2), 329.
- (2) Craley, C. R.; Zhang, R.; Kowalewski, T.; McCullough, R. D.; Stefan, M. C. *Macromol. Rapid Commun.* **2009**, *30* (1), 11–16.
- (3) Higashihara, T.; Ueda, M. *Macromolecules* **2009**, *42* (22), 8794–8800.
- (4) Grancharov, G.; Coulembier, O.; Surin, M.; Lazzaroni, R.; Dubois, P. *Macromolecules* **2010**, *43* (21), 8957–8964.
- (5) He, L.; Pan, S.; Peng, J. *J. Polym. Sci. Part B Polym. Phys.* **2016**, *54* (5), 544–551.
- (6) Kim, S. H.; Misner, M. J.; Xu, T.; Kimura, M.; Russell, T. P. *Adv. Mater.* **2004**, *16* (3), 226–231.
- (7) Mokarian-Tabari, P.; Collins, T. W.; Holmes, J. D.; Morris, M. A. *ACS Nano* **2011**, *5* (6), 4617–4623.
- (8) Gotrik, K. W.; Hannon, A. F.; Son, J. G.; Keller, B.; Alexander-Katz, A.; Ross, C. A. *ACS Nano* **2012**, *6* (9), 8052–8059.
- (9) Cushen, J. D.; Otsuka, I.; Bates, C. M.; Halila, S.; Fort, S.; Rochas, C.; Easley, J. A.; Rausch, E. L.; Thio, A.; Borsali, R.; Willson, C. G.; Ellison, C. J. *ACS Nano* **2012**, *6* (4), 3424–3433.
- (10) Otsuka, I.; Tallegas, S.; Sakai, Y.; Rochas, C.; Halila, S.; Fort, S.; Bsiesy, A.; Baron, T.; Borsali, R. *Nanoscale* **2013**, *5* (7), 2637–2641.
- (11) Otsuka, I.; Zhang, Y.; Isono, T.; Rochas, C.; Kakuchi, T.; Satoh, T.; Borsali, R. *Macromolecules* **2015**, *48* (5), 1509–1517.
- (12) Imamura, K.; Sakaura, K.; Ohyama, K. I.; Fukushima, A.; Imanaka, H.; Sakiyama, T.; Nakanishi, K. *J. Phys. Chem. B* **2006**, *110* (31), 15094–15099.
- (13) Kayunkid, N.; Uttiya, S.; Brinkmann, M. *Macromolecules* **2010**, *43* (11), 4961–4967.
- (14) Takahashi, Y.; Nishikawa, S. *Macromolecules* **2003**, *36* (23), 8656–8661.





## **CHAPTER IV:**

# ***in situ* EVALUATION OF THERMALLY INDUCED STRUCTURAL EVOLUTION OF THE SEMICONDUCTING GLYCOCONJUGATED DIBLOCK COPOLYMERS**

## IV.1 Introduction

It is well-known that the optoelectronic properties of poly(3-hexylthiophene) (P3HT) in the solid-state are greatly dependent on its crystalline structure, which is governed not only by molecular properties of polymer but also by the film formation and post-treatment conditions.

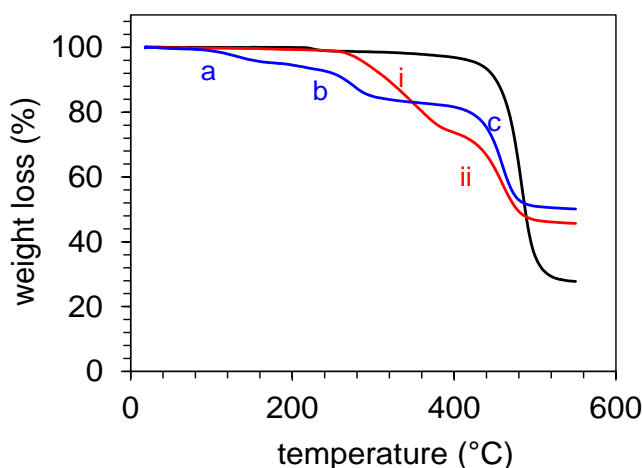
In chapter III, it was demonstrated that P3HT-*b*-AcMal<sub>7</sub> self-assembles into well-ordered periodic lamellar structure with a sub-10 nm scale after thermal annealing. Therefore, the crystal structure of P3HT segment formed in the phase-segregated P3HT-*b*-AcMal<sub>7</sub> nanodomain will be focused on this chapter. In addition, clarifying detailed nanostructure changes of the block copolymer during the thermal annealing process is of crucial importance to understand and control the crystallization of P3HT block and the microphase segregation behavior of the block copolymer.

In this chapter, a comprehensive study of the thermally-induced structural evolution of the P3HT-*b*-AcMal<sub>7</sub> will be discussed. Thermal stabilities and phase transition temperatures (such as glass transition  $T_g$ , melting  $T_m$ , crystallization  $T_c$ ) of the block copolymers (P3HT-*b*-AcMal<sub>7</sub> and P3HT-*b*-Mal<sub>7</sub>) and P3HT homopolymer were firstly examined by thermogravimetric analysis (TGA) and differential scanning calorimetry (DSC). Then, temperature dependent morphological changes of the P3HT-*b*-AcMal<sub>7</sub> in the course of thermal treatment was investigated by *in situ* small- and wide-angle X-ray scattering (SAXS/WAXS) analysis with step-wise heating and cooling. The obtained results from X-ray scattering were carefully interpreted together with the data from DSC.

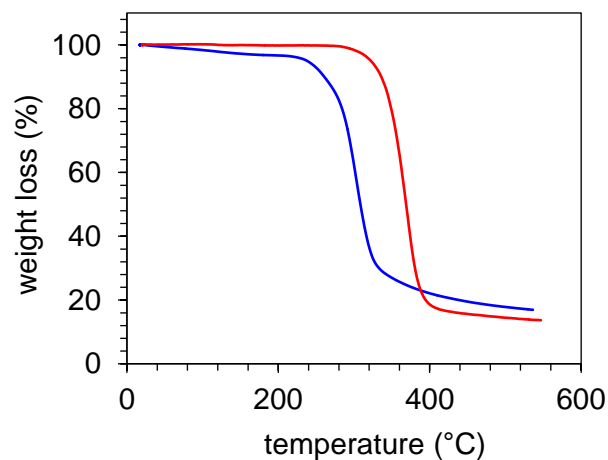
## IV.2 Thermal properties

### IV.2.1 Thermogravimetric analysis (TGA)

The thermal stability of diblock copolymers, P3HT-*b*-AcMal<sub>7</sub> and P3HT-*b*-Mal<sub>7</sub>, and P3HT homopolymer, was investigated by TGA as shown in Figure 4.1. The results are summarized in Table 4.1. The TGA curve of P3HT-*b*-AcMal<sub>7</sub> (red line) showed a two-stage weight loss behavior, corresponding to the thermal decomposition of AcMal<sub>7</sub> block (slope i), and the thermal decomposition of P3HT block (slope ii). The TGA curve of P3HT-*b*-Mal<sub>7</sub> (blue line) have multiple weight loss stages, corresponding to the loss of adsorbed water in the hydroxyl groups of Mal<sub>7</sub> (slope a), the thermal decomposition of Mal<sub>7</sub> block (slope b), and the thermal decomposition of P3HT block (slope c). The thermal decomposition temperatures for a 5 % weight loss ( $T_{d,5\%}$ ) of P3HT, P3HT-*b*-AcMal<sub>7</sub> and P3HT-*b*-Mal<sub>7</sub> were 422, 291 and 187 °C, respectively. Both diblock copolymers had lower  $T_{d, 5\%}$  values than that of the P3HT homopolymer, probably due to the low thermal stability of Mal<sub>7</sub> blocks (blue line in Figure 4.2). The thermal decomposition temperatures of the P3HT segment in both block copolymers are above 390 °C. This temperature can be considered as sufficiently high for optoelectronics applications, taking account of the fact that the non-conducting Mal<sub>7</sub> blocks will be eventually replaced with other conductive polymers after the microphase separation.



**Figure 4.1** TGA curves of ethynyl-P3HT, P3HT-*b*-AcMal<sub>7</sub> (red line) and P3HT-*b*-Mal<sub>7</sub> (blue line).



**Figure 4.2** TGA curves of AcMal<sub>7</sub> (red line) and Mal<sub>7</sub> (blue line).

**Table 4.1** Thermal properties of ethynyl-P3HT homopolymer, P3HT-*b*-AcMal<sub>7</sub>, and P3HT-*b*-Mal<sub>7</sub> obtained by TGA analysis

sample	TGA		
	temperature range of inclination <sup>a</sup>	factor	$T_{d, 5\%}$ (°C)
ethynyl-P3HT	400 - 530	decomposition of P3HT	422
P3HT- <i>b</i> -AcMal <sub>7</sub>	(i) 250 - 380	decomposition of AcMal <sub>7</sub>	291
	(ii) 400 - 500	decomposition of P3HT	
P3HT- <i>b</i> -Mal <sub>7</sub>	(a) 95 - 160	loss of water	187
	(b) 200 - 310	decomposition of Mal <sub>7</sub>	
	(c) 390 - 490	decomposition of P3HT	

<sup>a</sup> Temperature range of inclination of each slope shown in Figure 4.1.

## IV.2.2 Differential scanning calorimetry (DSC)

To investigate thermal property and crystallinity of P3HT, DSC measurements were performed on the P3HT homopolymer and the diblock copolymers. In order to achieve solvent evaporation conditions similar to that of the thin film samples prepared by the spin-coating method, all polymers were dissolved in THF followed by casting in aluminum DSC pans. These DSC samples were stored at 100 °C under vacuum for several hours prior to analysis.

The DSC thermograms recorded during the first cooling and the second heating cycles with the heating/cooling rates of 10 °C/min are shown in Figure 4.4. The detailed values are summarized in Table 4.2.

For the ethynyl-P3HT **P3** homopolymer (black line), an endothermic peak at 186 °C related to the melting temperature ( $T_m$ ) was observed in the heating cycle. The P3HT<sub>P3</sub>-*b*-Mal<sub>7</sub> (blue line) exhibits lower and broader  $T_m$  ( $T_{m, \text{P3HT-}b\text{-Mal7}} = 169$  °C) with respect to that of P3HT. The broad endothermic peak indicates a large distribution of the crystallite size, and the decrease in  $T_m$  reflects the low crystallinity (reduction in the crystallite thickness) of the P3HT segment (Gibbs-Thomson effect). Contrary to the P3HT<sub>P3</sub>-*b*-Mal<sub>7</sub>, the P3HT<sub>P3</sub>-*b*-AcMal<sub>7</sub> (red line) shows quite different melting behavior. Two endothermic peaks at 190 and 198 °C were observed in the heating cycle. These temperatures are higher than the  $T_m$  of the P3HT homopolymer, suggesting that the crystal state of the P3HT segment confined in the phase-separated P3HT<sub>P3</sub>-*b*-AcMal<sub>7</sub> is more ordered or more stable than that of the P3HT homopolymer. The bimodal endothermic peak implies a coexistence of two types of P3HT crystals having either different crystal structures or different degrees of crystal perfection.

The glass transition of the AcMal<sub>7</sub> segment ( $T_g$ ), that was clearly observed around 115-120 °C in the DSC thermogram of single constituent of AcMal<sub>7</sub> (Figure 4.3), was not identified in the thermogram of the P3HT<sub>P3</sub>-*b*-AcMal<sub>7</sub>, indicating that the AcMal<sub>7</sub> segment confined in the P3HT-*b*-AcMal<sub>7</sub> domain exhibits different thermal behavior from the bulk. In the cooling cycle, a similar tendency was observed in the peak shape and in the crystallization temperature ( $T_c$ ) expect for the  $T_c$  of the P3HT<sub>P3</sub>-*b*-AcMal<sub>7</sub>. P3HT<sub>P3</sub>-*b*-Mal<sub>7</sub> showed lower and broader exothermic peak at 136 °C compared to the P3HT ( $T_{c, \text{P3HT}} = 166$  °C). On the other hand, unlike the fact seen

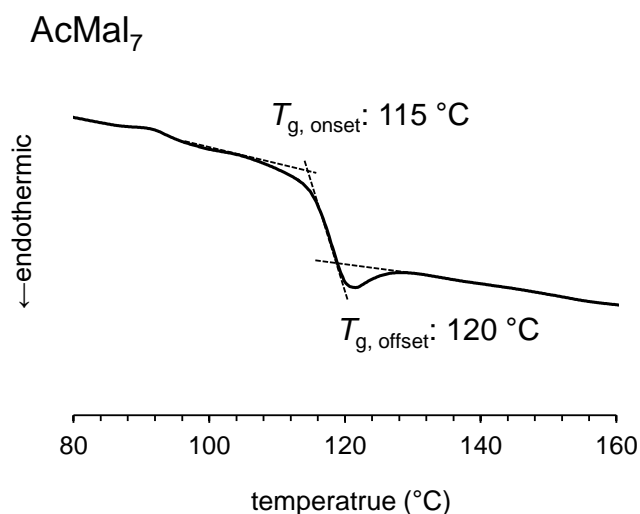
in the heating run, the  $T_c$  of the P3HT<sub>P3</sub>-*b*-AcMal<sub>7</sub> was slightly lower ( $T_{c, \text{P3HT-b-AcMal}_7} = 162\text{ }^\circ\text{C}$ ) than that of P3HT. For all the polymer samples, no peak corresponding to the melting or glass transition of the hexyl side chain was observed while some studies reported the melting of the side chain at around 55-60  $^\circ\text{C}$ .<sup>1,2</sup>

The melting enthalpy obtained by the integration of melting peak area normalized by the total sample weight ( $\Delta H_{m, \text{total}}$ ) for the P3HT homopolymer, P3HT<sub>P3</sub>-*b*-AcMal<sub>7</sub>, P3HT<sub>P3</sub>-*b*-Mal<sub>7</sub> were 14.1 J/g, 11.8 J/g and 9.3 J/g, respectively. However, since the melting enthalpy is directly associated with the required heat energy for breaking down the crystal structure, the weight fraction of P3HT in the block copolymer should be taken into account in order to evaluate the crystallinity of P3HT in an adequate manner. Hence, the melting enthalpies were corrected on the basis of the weight fraction of P3HT to give the amount of heat per P3HT unit weight.

The corrected melting enthalpy ( $\Delta H_{m, \text{P3HT}}$ ) for P3HT<sub>P3</sub>-*b*-AcMal<sub>7</sub> and P3HT<sub>P3</sub>-*b*-Mal<sub>7</sub> were calculated to be 18.1 J/g and 12.0 J/g, respectively. The relation of the  $\Delta H_{m, \text{P3HT}}$  for the respective polymers, *i.e.*, P3HT<sub>P3</sub>-*b*-AcMal<sub>7</sub> (18.1 J/g) > P3HT **P3** (14.1 J/g) > P3HT<sub>P3</sub>-*b*-Mal<sub>7</sub> (12.0 J/g) coincides with the order of the  $T_m$ , *i.e.*, P3HT<sub>P3</sub>-*b*-AcMal<sub>7</sub> (190  $^\circ\text{C}$  / 198  $^\circ\text{C}$ ) > P3HT **P3** (186  $^\circ\text{C}$ ) > P3HT<sub>P3</sub>-*b*-Mal<sub>7</sub> (169  $^\circ\text{C}$ ). This result also suggests that the crystal structure of the P3HT-*b*-AcMal<sub>7</sub> system was more stable than that of P3HT homopolymer while the P3HT<sub>P3</sub>-*b*-Mal<sub>7</sub> system showed the opposite result.

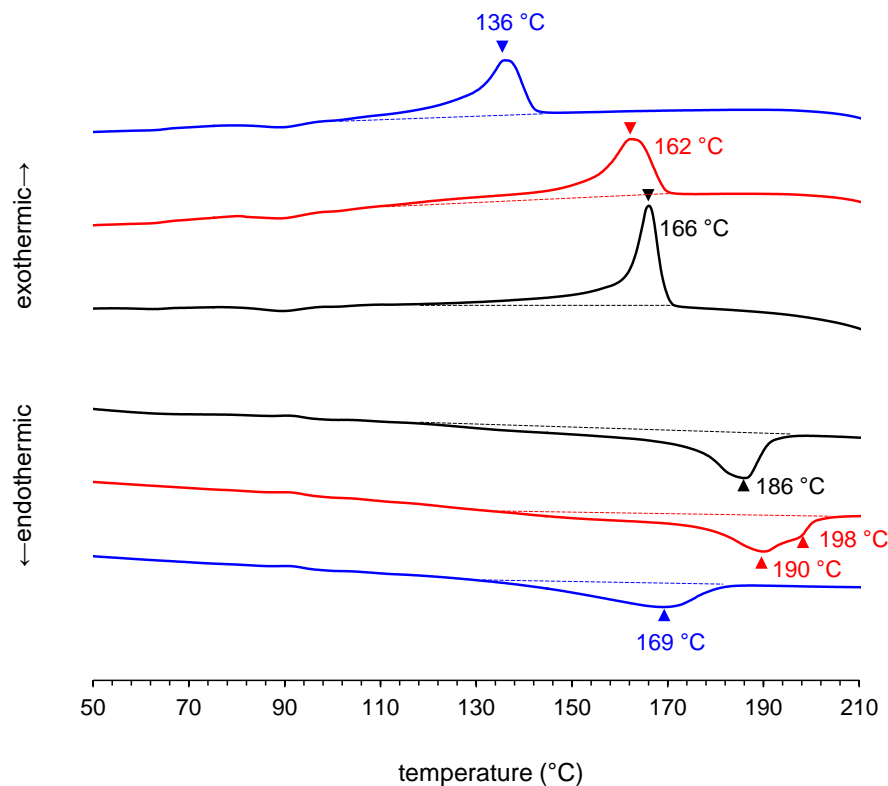
In the Chapter III.5, I raised a hypothesis on the origin of the absence of phase separation for the P3HT-*b*-Mal<sub>7</sub> system, *i.e.*, strong inter- and intra-chain hydrogen bonding of the Mal<sub>7</sub> would restrain the mobility of the Mal<sub>7</sub> block and hinders the microphase separation even above  $T_m$  of P3HT and  $T_g$  of Mal<sub>7</sub> (150-160  $^\circ\text{C}$ ).<sup>3</sup> Similarly, the hydrogen bonding would also affect the crystallization behavior of P3HT segment of the P3HT-*b*-Mal<sub>7</sub>. Since one chain-end of the P3HT is chemically tethered to the Mal<sub>7</sub>, a part of hexyl thiophene units near interface of two blocks cannot acquire the chain mobility necessary to rearrange into regular structures, leading to lower crystallinity of the P3HT-*b*-Mal<sub>7</sub> system. In contrast, when the P3HT<sub>P3</sub>-*b*-AcMal<sub>7</sub> system is heated above the  $T_m$  of P3HT (166 $^\circ\text{C}$ ) which is far beyond the  $T_g$  of AcMal<sub>7</sub> ( $T_{g, \text{AcMal}_7, \text{onset}} = 115\text{ }^\circ\text{C}$ ), the crystallization of the P3HT segment may occur from a pre-optimized nano-domain defined by the phase-segregated structure. The multipolar interactions between acetyl groups are much weaker than hydroxyl groups, allowing the chains to move and adapt the energetically

stable structure. As described in the Chapter III.6, the chain direction of the P3HT is not parallel to the lamellar plane. It is more likely that the P3HT segment adopts their stacking direction to lamellar structure by tilting in order to stabilizing their crystal state. In other words, an internal stress around boundary of the P3HT and AcMal<sub>7</sub> blocks is supposed to be minimized. Therefore, unlike the case of P3HT-*b*-Mal<sub>7</sub> system, the crystallinity of the P3HT segment is at least maintained, and further stabilized by the cohesion between AcMal<sub>7</sub>.



**Figure 4.3** DSC heating thermogram of AcMal<sub>7</sub> during heating cycle with a heating rate of 10 °C/min after cooling cycle with a cooling rate of 20 °C/min.





**Figure 4.4** DSC thermograms of ethynyl-P3HT **P3** (black line), P3HT<sub>P3</sub>-*b*-AcMal<sub>7</sub> (red line) and P3HT<sub>P3</sub>-*b*-Mal<sub>7</sub> (blue line) obtained during first cooling run and second heating run with a heating and cooling rate of 10 °C/min. Small changes around 90 °C found for the all samples are probably artifacts derived from the apparatus used.

**Table 4.2** Thermal properties of ethynyl-P3HT homopolymer, P3HT-*b*-AcMal<sub>7</sub>, and P3HT-*b*-Mal<sub>7</sub> obtained by DSC analysis

sample	$T_m$ (°C)		$T_c$ (°C)	$\Delta H_m$ (J/g)		$\Delta H_c$ (J/g)	
	1st peak	2nd peak		$\Delta H_{m, total}^a$	$\Delta H_{m, P3HT}^b$	$\Delta H_{c, total}^a$	$\Delta H_{c, P3HT}^b$
ethynyl-P3HT <b>P3</b>	186	–	166	14.1	14.1	14.8	14.8
P3HT <sub>P3</sub> - <i>b</i> -AcMal <sub>7</sub>	190	198	162	11.8	18.1	11.8	18.1
P3HT <sub>P3</sub> - <i>b</i> -Mal <sub>7</sub>	169	–	136	9.3	12.0	8.4	10.9

<sup>a</sup> The experimental values of total melting/crystallization enthalpy. <sup>b</sup> Calculated values based on the P3HT weight fraction.

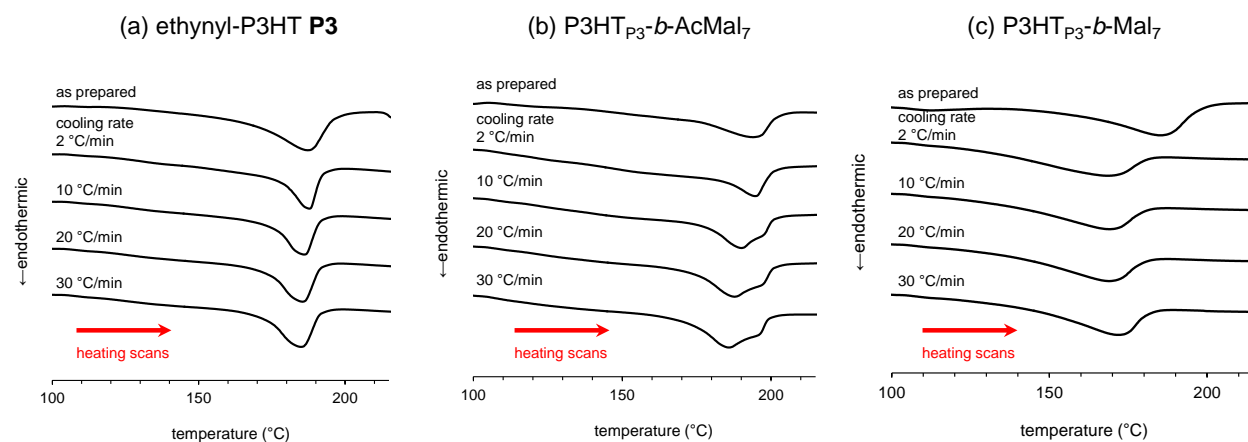
Figure 4.5 shows DSC heating traces of (a) ethyny-P3HT **P3**, (b) P3HT<sub>P3</sub>-*b*-AcMal<sub>7</sub>, and (c) P3HT<sub>P3</sub>-*b*-Mal<sub>7</sub> recorded after cooling process over the temperature range from 220 to 0 °C with different cooling rates from 2 °C/min to 30 °C/min. Heating rate of 10 °C/min was constant for all experiments. The melting enthalpy based on the total sample weight ( $\Delta H_{m, \text{total}}$ ) and corrected melting enthalpy ( $\Delta H_{m, \text{P3HT}}$ ) were taken from each thermograms. The detailed data are summarized in the Table 4.3.

For all heating traces of the P3HT homopolymer and P3HT<sub>P3</sub>-*b*-Mal<sub>7</sub>, single endothermic peak corresponding to the  $T_m$  of the P3HT segment was observed at almost same temperature irrespective of the cooling rate, except for the first heating run of the P3HT<sub>P3</sub>-*b*-Mal<sub>7</sub> sample that was solvent casted. The as-prepared sample of the P3HT<sub>P3</sub>-*b*-Mal<sub>7</sub> showed a relatively high  $T_m$  at 185 °C comparable to the  $T_m$  of the P3HT homopolymer (187 °C). After the subsequent heating cycles the melting transitions occurred at remarkably lower temperature over a wide range ( $T_m$ : 167-169 °C, transition temperature range: ~90 °C) compared to the initial  $T_m$ , namely the melting temperature of the solution-crystallized sample. This fact suggests that the crystallinity of the P3HT<sub>P3</sub>-*b*-Mal<sub>7</sub> receives a significant influence from the hydrogen-bonding of the Mal<sub>7</sub> segment when the polymer is crystallized from the molten state.

In a series of heating traces of the P3HT<sub>P3</sub>-*b*-AcMal<sub>7</sub>, an obvious change in the melting behavior was found cooling rate. In the first heating run and second heating run (after underwent the slow crystallization with the cooling rate of 2 °C/min), the single endothermic peak was observed at 193 and 194 °C, respectively. When the sample was crystallized at higher cooling rate, an additional endothermic peak appeared in the heating scans. For example, in case of the cooling rate of 10 °C/min, distinct bimodal peaks were observed at 190 and 198 °C. With the increase of the cooling rate, the former peak was shifted toward lower temperature from 190 to 186 °C, whereas the later peak remained in identical position. This observation implies that there are at least two crystal states which are formed through different crystallization process, *i.e.* the lower peak corresponds to the crystallization governed by kinetic factor and the higher peak corresponds to the crystallization governed by thermodynamic factor. If the crystallization rate is fast enough, the crystallization behavior may be governed by thermodynamic factor and is not susceptible to the cooling rate. On the contrary, if the crystallization rate is very slow, with increasing cooling rate, kinetic factor becomes dominant and it results in less ordered semi-crystalline structure because of an insufficient time to crystallize into thermodynamically

equilibrium structure. Therefore, it is reasonable to assume that the crystallization of the P3HT<sub>P3</sub>-*b*-AcMal<sub>7</sub> system takes place via two processes: slow and fast crystallization. The existence of these multi-crystallization processes might reflect the different environments for the P3HT segment in the P3HT<sub>P3</sub>-*b*-AcMal<sub>7</sub> melt, *i.e.*, chain-end tethered with AcMal<sub>7</sub> (low mobility, modest steric hindrance), middle part (highly crystalline part), and free chain-end (high mobility), etc.

Further characterization about the crystalline structure of the P3HT segment in the P3HT-*b*-AcMal<sub>7</sub> by using X-ray diffraction will be discussed in later section (Chapter IV.5).



**Figure 4.5** DSC heating thermograms of (a) ethynyl-P3HT P3, (b) P3HT<sub>P3</sub>-*b*-AcMal<sub>7</sub>, and (c) P3HT<sub>P3</sub>-*b*-Mal<sub>7</sub> obtained during heating cycles with a heating rate of 10 °C/min after cooling cycle with different cooling rate.

**Table 4.3** Thermal properties of ethynyl-P3HT homopolymer, P3HT-*b*-AcMal<sub>7</sub>, and P3HT-*b*-Mal<sub>7</sub> obtained by DSC analysis

sample	cooling rate (°C/min)	heating cycle			
		$T_m$ (°C)		$\Delta H_m$ (J/g)	
		1st peak	2nd peak	$\Delta H_{m, \text{total}}^a$	$\Delta H_{m, \text{P3HT}}^b$
ethynyl-P3HT <b>P3</b>	as prepared	187	–	–	–
	2 °C/min	188	–	15.5	15.5
	10 °C/min	186	–	14.1	14.1
	20 °C/min	185	–	13.9	13.9
	30 °C/min	185	–	12.9	12.9
P3HT <sub>P3</sub> - <i>b</i> -AcMal <sub>7</sub>	as prepared	193	–	–	–
	2 °C/min	194	–	12.3	18.9
	10 °C/min	190	198	11.8	18.1
	20 °C/min	188	198	11.9	18.2
	30 °C/min	186	197	11.4	17.5
P3HT <sub>P3</sub> - <i>b</i> -Mal <sub>7</sub>	as prepared	185	–	–	–
	2 °C/min	167	–	9.5	12.3
	10 °C/min	169	–	9.3	12.0
	20 °C/min	168	–	8.6	11.1
	30 °C/min	168	–	8.2	10.6

<sup>a</sup> The experimental values of total melting enthalpy. <sup>b</sup> Calculated values based on the P3HT weight fraction.

### IV.3 Step-wise heating and cooling SAXS measurements

An *in situ* small-angle X-ray scattering (SAXS) analysis during the heating and cooling was performed on the bulk sample of the P3HT and P3HT-*b*-AcMal<sub>7</sub>. The bulk samples were stepwise heated from room temperature to 220 °C with an interval of 10°C using thermal controller and then cooled to below 100 °C by simple heat dissipation.

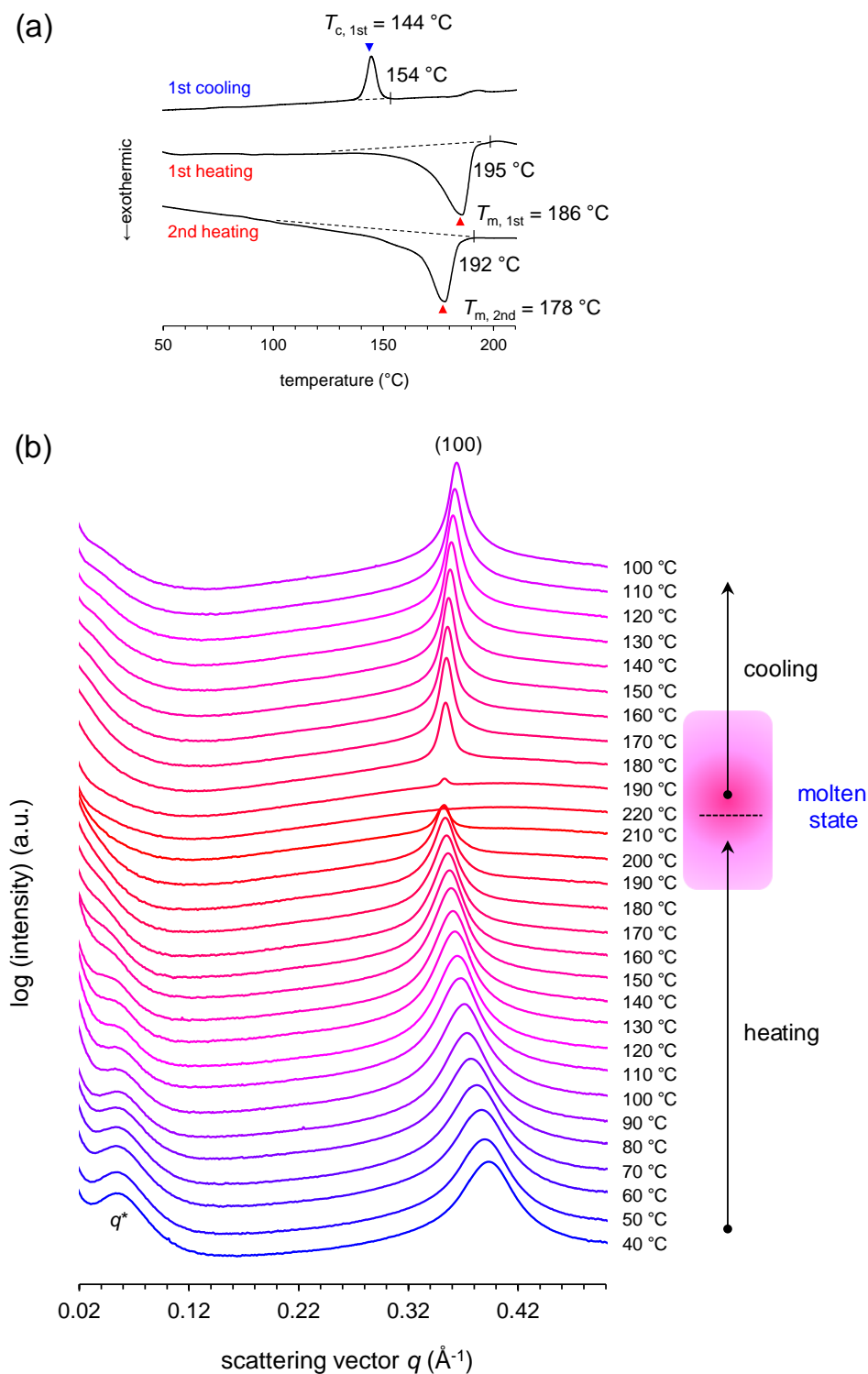
#### P3HT homopolymer

Figure 4.6 presents a variation of SAXS profiles of the P3HT homopolymer sample during the heating and cooling. In the low temperature range, two broad peaks related to the P3HT nanofiber structure (hereinafter called Peak<sub>fiber</sub>) and the (100) reflection of the P3HT crystal structure (hereinafter called Peak<sub>100</sub>) were observed at  $q = 0.055 \text{ \AA}^{-1}$  and  $q = 0.393 \text{ \AA}^{-1}$ , respectively. Corresponding periodicities for the Peak<sub>fiber</sub> and Peak<sub>100</sub> are 11.4 and 1.60 nm, respectively ( $d = 2\pi/q$ ).

As the temperature increased to 190 °C, the Peak<sub>fiber</sub> clearly broadened and slightly shifted toward a lower angle, accompanying a significant decrease in the intensity of the Peak<sub>fiber</sub>. Above the 180 °C, *i.e.*, in the temperature range where the majority of the P3HT chains melt ( $T_{m, \text{P3HT, 1st heat}} = 186 \text{ °C}$ ), no diffraction peak was observed, indicating that the nanofibers that had ordered internal structure at lower temperature turned into a disordered state. In the cooling cycle, the Peak<sub>fiber</sub> did not show up, in agreement with the previously presented SAXS profile taken at room temperature for the thermally annealed P3HT sample (see Figure 3.8i). These results indicate that the P3HT could not rearrange into the semi-defined nanofibers that was obtained by initial sample preparation (solution-crystallization). On the other hand the Peak<sub>100</sub>, corresponding to the interlayer distance separated by the hexyl side chain, became sharper and shifted toward lower  $q$  region from 0.393 to  $0.351 \text{ \AA}^{-1}$  during the heating. The shift is due to the thermal expansion of the hexyl side chains, and the sharpening reflects an increasing long-range order, at the expense of fibril morphology.

At 220 °C, the diffraction completely disappeared, meaning that polymer is completely melted. Upon cooling from the molten state, the Peak<sub>100</sub> appeared again and shifted back toward its original position while the peak width broadened. This reversible change in the peak position of

the Peak<sub>100</sub> corroborates the thermal expansion of the hexyl side chains. The broadening of the Peak<sub>100</sub> during the cooling is counter-intuitive but the shrinking of the hexyl groups might have introduced internal strain. The detailed discussion about the crystal structure of the P3HT will be described in a later section (Chapter IV.2).

**ethynyl-P3HT P1**

**Figure 4.6** (a) DSC thermograms of ethynyl-P3HT **P1** during 1st heating, 1st cooling, and 2nd heating cycles with a heating rate of 10 °C/min and cooling rate of 2.5 °C/min. (b) SAXS profiles of ethynyl-P3HT **P1** bulk sample taken during *in situ* heating, holding, and cooling measurement.

**P3HT-*b*-AcMal<sub>7</sub>**

The same type of experiment was performed on the P3HT-*b*-AcMal<sub>7</sub> bulk sample and a temperature evolution of the SAXS profiles are presented in Figure 4.7. First, overall trends extracted from Figure 4.7 will be described, and then some detailed discussions about *d*-spacing and ordered domain size will be made in a later paragraph.

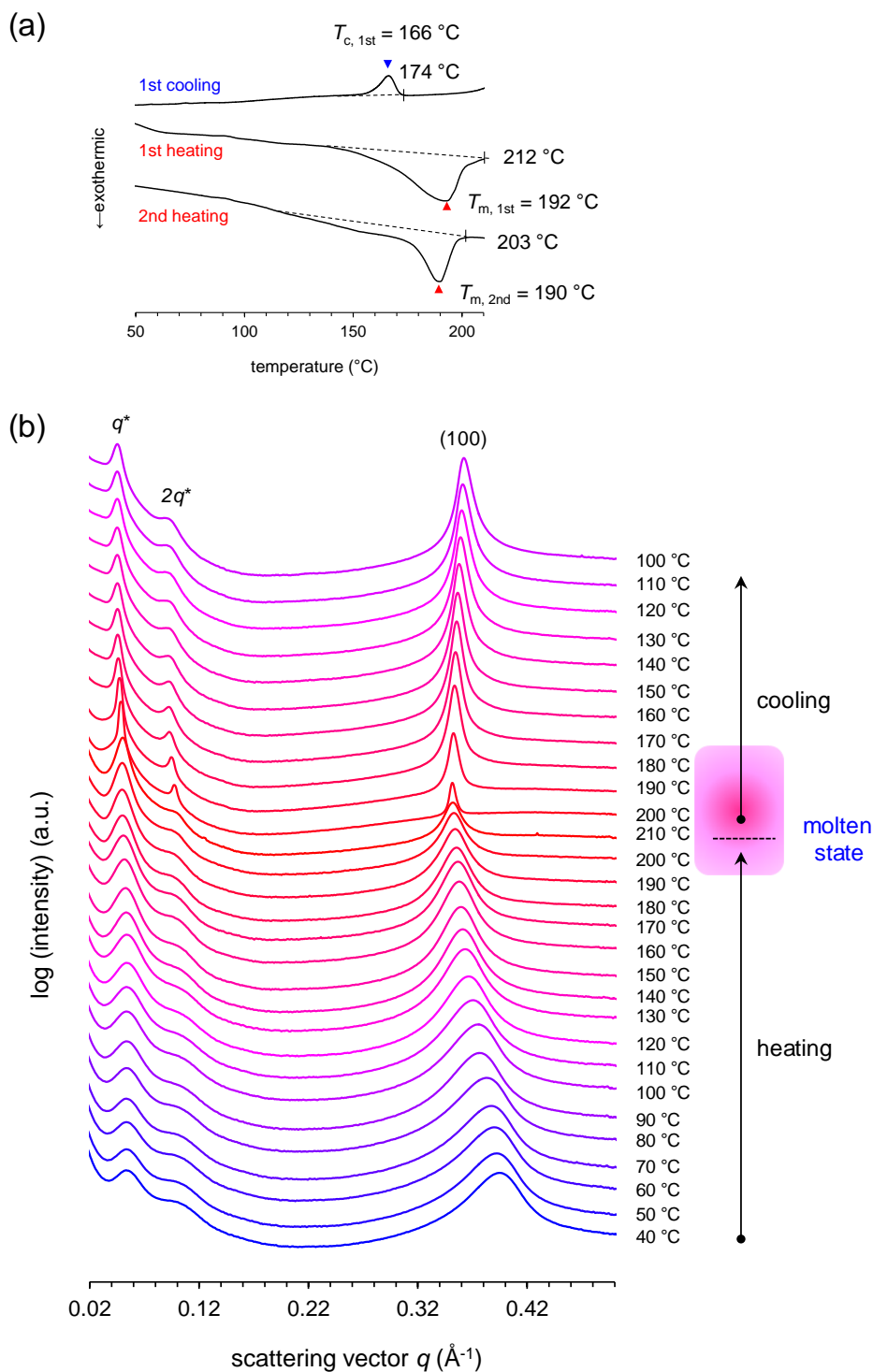
Overall trends

In a *q*-range between 0.04 and 0.13 Å<sup>-1</sup>, two broad peaks, *q*\* and 2*q*\*, corresponding to the lamellar structure derived from the micro-phase separation of the P3HT-*b*-AcMal<sub>7</sub>, were observed before heating. Another broad peak indexed as (100) reflection was also observed at *q* = 0.395 Å<sup>-1</sup>. As the temperature increases up to 210 °C, the *q*\* and 2*q*\* peaks become more intense and sharper. Then, in the initial stage of cooling process (between 210 to 180 °C), *i.e.* above the crystallization temperature of the polymer (*T*<sub>c, P3HT-*b*-AcMal<sub>7</sub></sub> = 174 °C) and glass transition of the AcMal<sub>7</sub> (*T*<sub>g, AcMal<sub>7</sub>, onset</sub> = 115 °C), a drastic sharpening of the *q*\* and 2*q*\* peaks was observed, indicating that the P3HT-*b*-AcMal<sub>7</sub> displayed well-ordered lamellar structure in the molten state, which can be assimilated as liquid crystals. This is a direct evidence that the P3HT-*b*-AcMal<sub>7</sub> system possesses strong segregation strength (*χN*) between P3HT and AcMal<sub>7</sub> segments. At the same time, the peak related to the (100) reflection of P3HT block exhibited similar thermal behavior as that of P3HT homopolymer expect for the fact that the (100) peak was still observed at 220 °C, meaning that a higher temperature is required to melt the P3HT crystalline structure when AcMal<sub>7</sub> is attached to the P3HT segment. This fact is in good agreement with the DSC analysis results described before (Chapter IV.2).

The P3HT block of the P3HT-*b*-AcMal<sub>7</sub> system is confined within the lamellar structure and anchored by AcMal<sub>7</sub> segment. Thus the entropy gain of melting would be reduced due to the reduced degree of freedom, leading to the high melting temperature. Also, the appearance of long-range order of lamellar structure of alternating P3HT and AcMal<sub>7</sub> blocks preceded the intensity increase of (100) peak of P3HT, meaning that the crystallization of P3HT proceeded within the lamellar gap.

Upon further cooling, the peak widths of the *q*\* and 2*q*\* became broader while the peak position remain constant. The reason of the broadening is not clear for the moment.

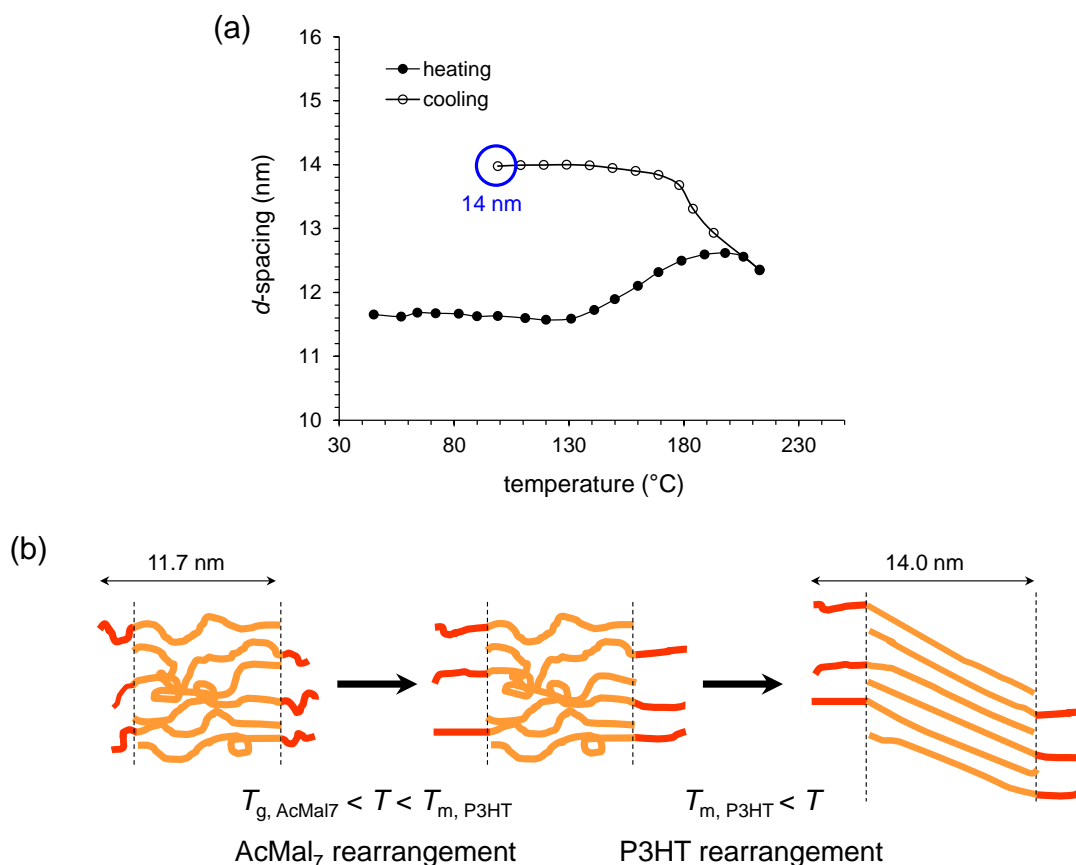


**P3HT<sub>P1</sub>-*b*-AcMal<sub>7</sub>**

**Figure 4.7** (a) DSC thermograms of P3HT<sub>P1</sub>-*b*-AcMal<sub>7</sub> during 1st heating, 1st cooling, and 2nd heating cycles with a heating rate of 10 °C/min and cooling rate of 2.5 °C/min. (b) SAXS profiles of P3HT<sub>P1</sub>-*b*-AcMal<sub>7</sub> bulk sample taken during *in situ* heating, holding, and cooling measurement.

Variation of  $d$ -spacing of the lamellar structure

The variation of  $d$ -spacing of the lamellar structure calculated from the peak position of the  $q^*$  is shown in Figure 4.8a. Starting from room temperature, the  $d$ -spacing remained unchanged up to 130 °C, then above this temperature gradually increased from 11.7 to 12.6 nm. In the cooling cycle, the  $d$ -spacing further increased to 13.8 nm in the temperature range between 220 and 170 °C. After that, the  $d$ -spacing showed only a slight increase to 14.0 nm between 170 and 130 °C, then, became constant. The first increase of the  $d$ -spacing began in the vicinity of the glass transition of the AcMal<sub>7</sub> ( $T_{g, \text{AcMal}_7, \text{offset}} = 120$  °C). The second remarkable increase observed in the cooling cycle (from 220 to 170 °C) took place in the fully molten state ( $T_{c, \text{P3HT-}b}$



**Figure 4.8** (a) Evolution of  $d$ -spacing of P3HTP<sub>1</sub>-*b*-AcMal<sub>7</sub> during *in situ* measurement. (b) Schematic illustration of P3HTP<sub>1</sub>-*b*-AcMal<sub>7</sub> conformation, where orange and red lines represent P3HT and AcMal<sub>7</sub> segments, respectively. Scale and the tilt angle of each block are disregarded here.

AcMal<sub>7</sub>, onset = 174 °C). Thus, it is likely that the domain expansion is caused by molecular rearrangements of both AcMal<sub>7</sub> and P3HT segments. In particular, taking the molecular packing model of the P3HT-*b*-AcMal<sub>7</sub> nanostructure into consideration (see Chapter III.6), the P3HT polymer is assumed to exhibit fully extended chain conformation. If it is so, this conformation can be achieved in the course of thermal treatment particularly above  $T_{m, P3HT}$  while adapting the polymer chain within the phase-segregated melt composition.

#### Variation of ordered domain size

It is known that there is a correlation between full width at half maximum (FWHM) ( $\beta$ ) of the reflection peak and crystallite size ( $\tau$ ) expressed by following formula (so-called Scherrer equation);

$$\tau = \frac{K\lambda}{\beta \cos \theta} \quad (\text{Eq. 4.1})$$

where  $K$  is a shape factor (Scherrer constant) which usually takes the value of 0.9,  $\lambda$  is the incident X-ray wavelength, and  $\theta$  is the diffraction angle. The peak width  $\beta$  is inversely proportional to the crystallite size  $\tau$  (schematic illustration is given in below).

#### Determination of average size of the ordered domains

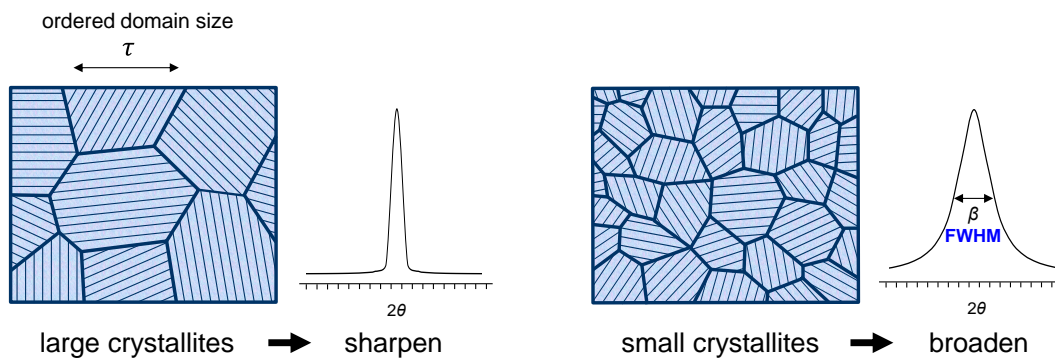
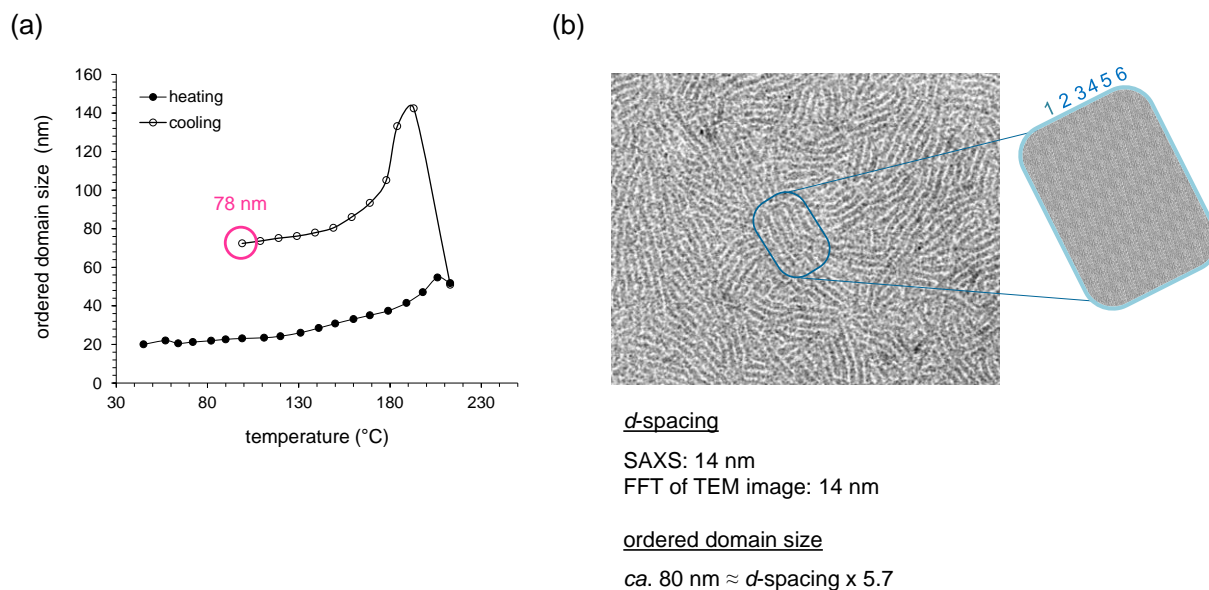


Figure 4.9a presents a variation of the ordered domain size  $\tau_{\text{lamellar}}$  (*i.e.* size of lamellar domain), estimated from the peak width of  $q^*$ , as a function of the temperature. Starting from the room

temperature, the  $\tau_{\text{lamellar}}$  increased steadily up to 220 °C from 20 to 55 nm, then jumped up to 142 nm during the period where the temperature was hold at 220 °C for about 5 min. Upon cooling the  $\tau_{\text{lamellar}}$  drastically decreased in the temperature range between 220 and 170 °C, and then below  $T_c$ , gradually decreased to 78 nm with lower inclination. This value is roughly equal to a domain size observed in the TEM image of the thermally annealed P3HT-*b*-AcMal<sub>7</sub>, though no explanation could be found for the drop in domain size during cooling.

On the basis of the SAXS analysis, it is revealed that a slow solidification from the phase-separated melt or long-time annealing in the vicinity of the melting temperature may allow improving the self-organizing network with a long periodic lamellar structure.



**Figure 4.9** (a) Evolution of ordered domains size of P3HT<sub>P1</sub>-*b*-AcMal<sub>7</sub> during *in situ* measurement. (b) TEM image of P3HT<sub>P1</sub>-*b*-AcMal<sub>7</sub> thin film obtained after thermal annealing at 220 °C for 10 min.

## IV.4 Step-wise heating and cooling WAXS measurements

### Special remark

The SAXS / WAXS measurements reported in this thesis were performed at different occasions on the different series of homopolymer and diblock copolymer, *i.e.* series 1 (P3HT **P1** / P3HT<sub>P1</sub>-*b*-AcMal<sub>7</sub>) and series 3 (P3HT **P3** / P3HT<sub>P3</sub>-*b*-AcMal<sub>7</sub>). Unfortunately, these experiments could not be performed under the same conditions due to the experimental settings that changed depending on the requirements of experimentalist sharing the beam time. Due to the structure formation at large range of length scale, ideally a  $q$ -range spanning from 0.02 to 2 Å<sup>-1</sup> is needed to draw a picture of the system. However, only part of the  $q$ -ranges could be obtained due to the limited beamtime, and the  $q$ -range differed from a series of samples to another. However, taken into consideration a similarity in the molecular parameters (see Table 4.4), thermal behaviors, and diffraction patterns of each polymer derived from series 1 and series 3, the polymers of the two series should be regarded as essentially the identical. For example, Figure 4.12a shows two diffraction patterns corresponding to the P3HT **P1** ( $q$ -range: from 0.05 to 1.50 Å<sup>-1</sup>) and P3HT **P3** ( $q$ -range: from 0.55 to 2.80 Å<sup>-1</sup>) recorded with different camera lengths. Although an overlapping area is limited, it is obvious that the both samples have a very similar crystal structure by showing their characteristic reflection peaks (200 and 300) due to the P3HT crystal structure at very close position. Thus, in this section, a series of diffraction data are presented under an assumption that the polymers having the same chemical structure but synthesized by different routes as the same substance.

**Table 4.4** Molecular parameters of P3HT homopolymer and P3HT-*b*-AcMal<sub>7</sub>

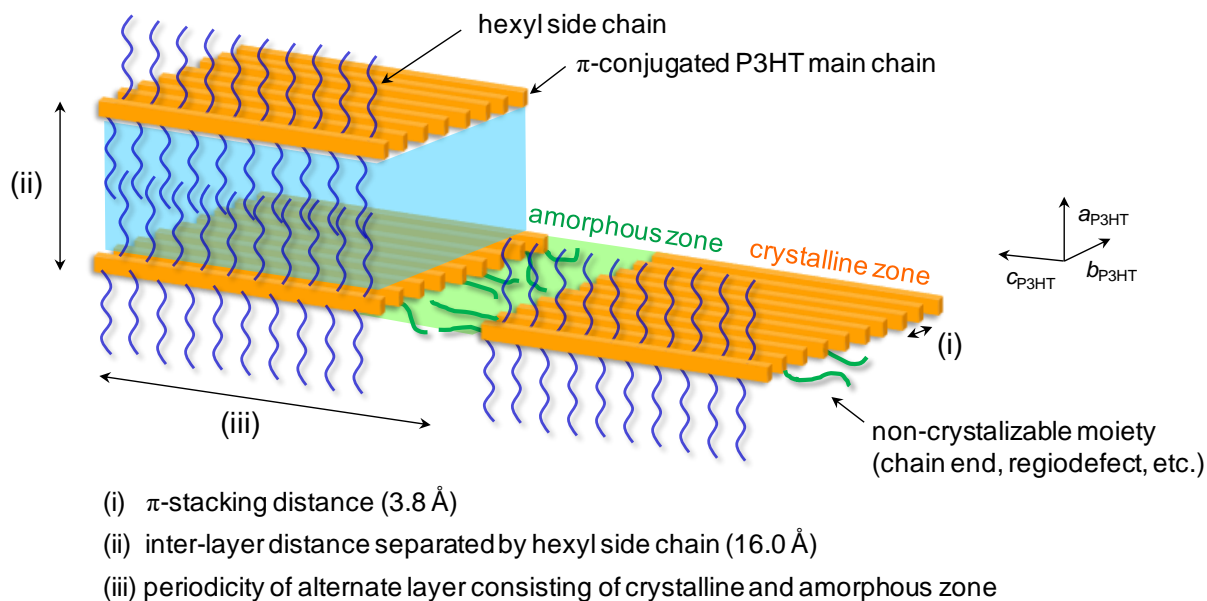
sample	category	P3HT			block copolymer	
		$M_{p, \text{MALDI, P3HT}}^a$ (g/mol)	$M_w/M_n, \text{P3HT}^b$	% HT <sup>c</sup>	$M_{p, \text{MALDI, P3HT}}^a$ (g/mol)	$\phi_{\text{P3HT}}^e$ (%)
ethynyl-P3HT P1	series 1	3596	1.35	> 95 %		
ethynyl-P3HT P3	series 3	3850	1.07	> 94 %		
P3HT <sub>P1</sub> - <i>b</i> -AcMal <sub>7</sub>	series 1				5656	0.64
P3HT <sub>P3</sub> - <i>b</i> -AcMal <sub>7</sub>	series 3				5910	0.66

<sup>a</sup> Molecular weight at the peak maximum determined by MALDI-TOF MS. <sup>e</sup> Dispersity of the P3HT estimated by SEC in THF based on PS standards. <sup>c</sup> HT coupling regioregularity determined by <sup>1</sup>H NMR. <sup>d</sup> Dispersity of the block copolymers estimated by SEC in THF based on PS standards. <sup>e</sup> Volume fraction of P3HT in copolymers calculated by using density values 1.16 g/cm<sup>3</sup> for P3HT, 1.36 g/cm<sup>3</sup> for Mal<sub>7</sub> and 1.20 g/cm<sup>3</sup> for AcMal<sub>7</sub>.

### Crystal structure of as-prepared P3HT homopolymer – at room temperature

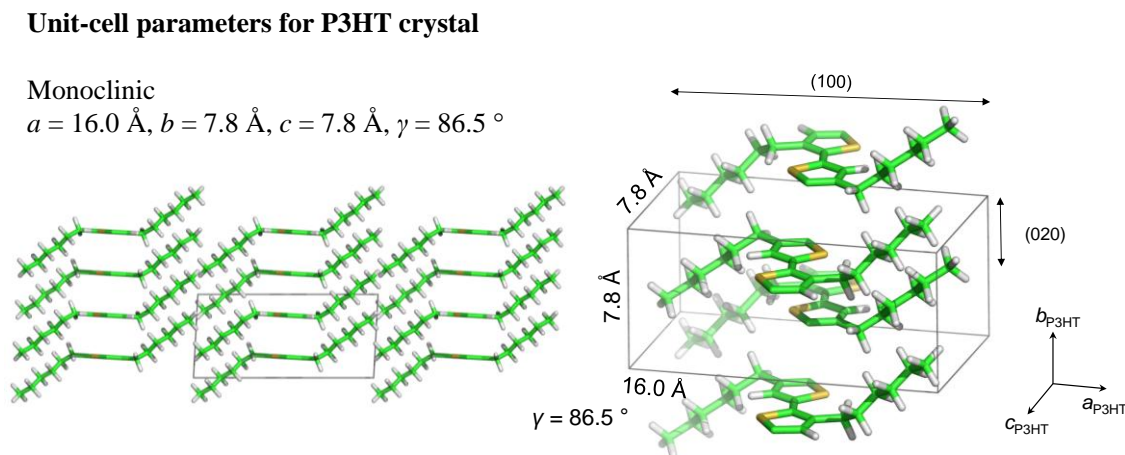
Prior to analyze the temperature dependence of the P3HT-*b*-AcMal<sub>7</sub>, the crystal structure of the synthesized P3HT homopolymers was first investigated by WAXS analysis at room temperature.

The basic spatial orders of P3HT are well-documented in the literature. As illustrated in the Figure 4.10, the P3HT exhibits a semi-crystalline structure involving several characteristic periodic distances spanning three orders of magnitude, *i.e.* (i) inter-molecular distance of P3HT main chains ( $\pi$ - $\pi$  stacking period, *ca.* 3.8 Å), (ii) inter-layered lamellar distance separated by hexyl side chains (*ca.* 16 Å), and (iii) alternating arrangement consisting of crystalline and amorphous domains (roughly equal to nanofiber width in the present study). This fundamental structure has been revealed by several groups by using X-ray diffraction, electron diffraction, and molecular modeling, etc., and various structural models were proposed.<sup>4-7</sup>



**Figure 4.10** Schematic illustration of the hierarchical semi-crystalline structure of P3HT.

Figure 4.12a shows diffraction patterns of as-prepared bulk samples of P3HT homopolymer. As a reference, positions of strong reflections estimated based on the unit cell proposed by Brinkmann *et al.*<sup>8</sup> (unit cell parameters are given in Figure 4.11) were depicted with gray dashed lines in the Figure 4.12a together with corresponding Miller indices. All reflection positions were plotted with purple marks as well.



**Figure 4.11** Projection of the P3HT crystal structure along  $c$  axes and the unit cell proposed by Brinkmann *et al.*<sup>8</sup>

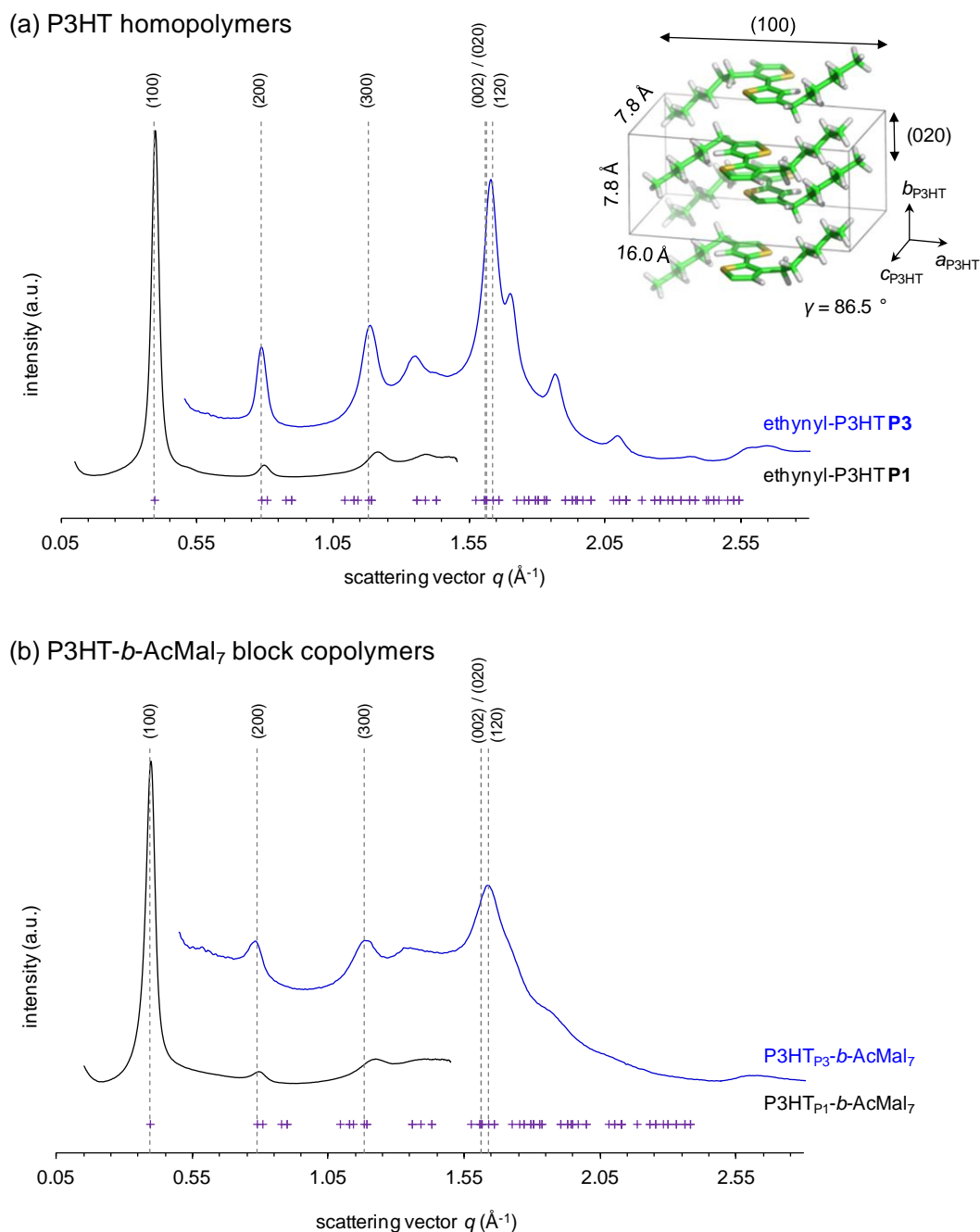
At least ten distinct diffraction peaks were observed in the  $q$ -range from  $0.05$  to  $2.08 \text{ \AA}^{-1}$ . All experimental peaks are found in the vicinity of the predicted reflection positions, indicating that the P3HT synthesized in this study have a similar crystal structure to the reported unit cell. The three intense reflection peaks in the lower  $q$ -range, *i.e.* at  $0.39$ ,  $0.80$ , and  $1.21 \text{ \AA}^{-1}$ , can be indexed to  $(100)$ ,  $(200)$ , and  $(300)$ , respectively, which reflects the inter layer distance of the hexyl side chains. The  $d_{100}$ -spacing calculated from  $(100)$  peak position ( $15.93 \text{ \AA}$ ) is almost consistent with the predicted value ( $15.97 \text{ \AA}$ ) (Table 4.5). Another intense peak at  $1.63 \text{ \AA}^{-1}$  might be a superimposition of the  $(002)$  and  $(020)$  peaks because calculated those peaks were found in very close vicinity. At the moment the individual contribution of the  $(002)$  and  $(020)$  peaks to the diffraction intensity is unknown, but this peak is considered to include structural information along the  $b$ -axis that represents the  $\pi$ - $\pi$  staking of main chain. For other peaks found in the higher  $q$ -range, it was difficult to index to unique peak due to the presence a large number of predicted peaks.

**Initial crystal structure of P3HT segment in the P3HT-*b*-AcMal<sub>7</sub> – at room temperature**

Figure 4.12b presents diffraction patterns of as-prepared bulk samples of the P3HT-*b*-AcMal<sub>7</sub>. Three distinct reflection peaks located at 0.39, 0.78, and 1.20 Å<sup>-1</sup>, which correspond to the (*h*00) reflections, and another peak located at 1.64 Å<sup>-1</sup> assignable to the combined reflections of the (002) and (020) were observed. However, other small peaks observed in the diffraction pattern at higher *q*-range of P3HT homopolymer, were extremely broadened. The peaks indexed to the (*h*00) and (002)/(020) were relatively broader compared to those observed in the diffraction pattern of P3HT homopolymer. This indicates the crystallite size of P3HT-*b*-AcMal<sub>7</sub> is smaller than that of P3HT homopolymer.

The small crystallite size might appear inconsistent with the result of DSC analysis, where the *T<sub>m</sub>* and corrected melting enthalpy ( $\Delta H_{m, \text{P3HT}}$ ) of the P3HT segment of the P3HT-*b*-AcMal<sub>7</sub> were higher than those of P3HT homopolymer. Smaller crystallite size implies higher contribution of surface energy, and in general leads to a lower melting temperature and enthalpy. One possible explanation for this contradiction is that the stabilization effect induced by the anchoring of the P3HT with AcMal<sub>7</sub> segment may be sufficiently high even considering the compensation of this surface energy. The crystallinity is difficult to estimate due to the broad amorphous halo of the AcMal<sub>7</sub> segment underneath the crystalline peak since the weight fraction of AcMal<sub>7</sub> segment is significant (35 % of the total weight).



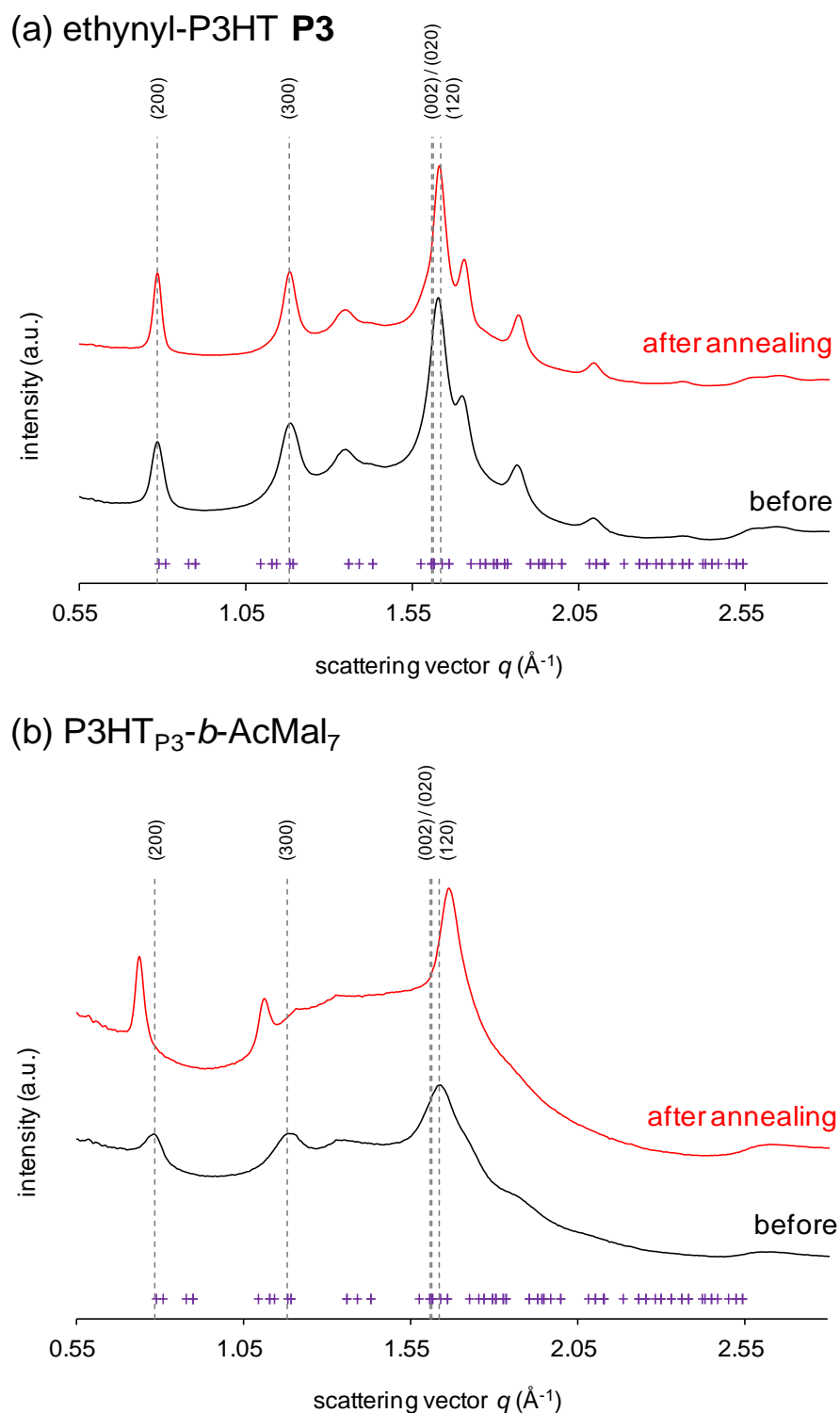


**Figure 4.12** WAXS profiles of (a) P3HT homopolymers and (b) P3HT-*b*-AcMal<sub>7</sub> block copolymers measured at room temperature. Black and blue profiles represent P1 and P3 series, *i.e.* ethynyl-P3HT **P1**/P3HT<sub>P1</sub>-*b*-AcMal<sub>7</sub> and ethynyl-P3HT **P3**/P3HT<sub>P3</sub>-*b*-AcMal<sub>7</sub>, respectively. Positions of strong reflections estimated based on the unit cell proposed by Brinkmann *et al.* were depicted with gray dashed lines together with corresponding Miller indices. All reflection positions were plotted with purple marks.

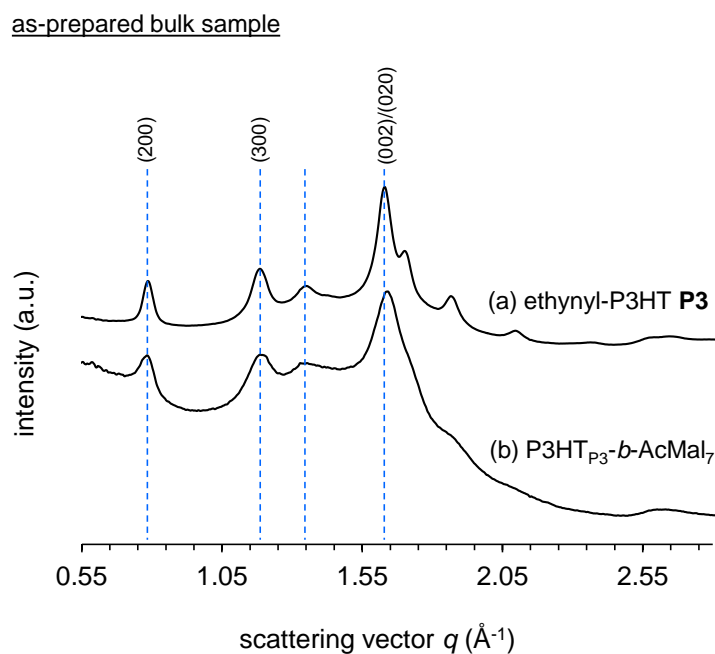
### Structural change of P3HT homopolymer and P3HT-*b*-AcMal<sub>7</sub> after thermal annealing –at room temperature

A comparison of the diffraction patterns, recorded at room temperature, before and after thermal annealed ethynyl-P3HT **P3** samples is shown in Figure 4.13a. It was found that the entire diffraction peaks became sharper after thermal annealing at 210 °C for 10 min, while the peak positions remained almost analogous to that of non-treated one. Table 4.5 summarized the *d*-spacings determined from each peak position of the non-annealed and annealed sample. In the P3 series, the *d*-spacings did not vary after thermal annealing. In other words, thermal annealing lead to larger crystallite sizes (*i.e.* the size of ordered domain consisting of the periodic P3HT backbones separated by hexyl side chains), while the crystal lattice was not changed through the thermal annealing process.

In contrast, P3HT<sub>P3</sub>-*b*-AcMal<sub>7</sub> sample showed changes not only in the width of the peaks but also in the peak positions (Figure 4.13b). The (200) and (300) reflections corresponding to the interlayer distance of the hexyl side chains shifted toward lower *q* after thermal treatment. For instance, the *d*-spacing of (200) peak increased from 8.02 to 8.50 Å through the thermal treatment, which corresponds to an expansion by 6% perpendicular to the layer composed of  $\pi$ -stacked chains. On the other hand, a broad reflection peak centered at  $q = 1.64 \text{ \AA}^{-1}$ , corresponding to the combined reflections of (002) and (020), shifted to a higher *q*-range region at around  $q = 1.67 \text{ \AA}^{-1}$ . This reflects a shrinking of the lattice spacing from 3.83 to 3.77 Å that is equivalent to a reduction in size by 1.6 %. For a monoclinic system, this reduction can be due to either (i) shrinking of *c*-axis = chain shrinkage, (ii) reduction in the  $\pi$ -stacking distance = shortening of the *b*-axis or (iii) change in the monoclinic angle. Since the backbone is quite rigid, and no explanation can be found to reduce the  $\pi$ -stacking distance with increased temperature, scenario (iii) seems to be the most probable. Molecularly it represents a shift between layers composed of  $\pi$ -stacked chains that can be induced by the change in the tilt angle of hexyl groups. In any case, the P3HT segment in the P3HT<sub>P3</sub>-*b*-AcMal<sub>7</sub> experienced a structural transition from the crystal structure analogous to that of P3HT homopolymer (direct structural comparison between P3HT homopolymer and the P3HT<sub>P3</sub>-*b*-AcMal<sub>7</sub> is given in Figure 4.14) to thermodynamically more stable structure by adopting its crystal conformation to the phase-separated nano-domain in the course of thermal treatment.



**Figure 4.13** Comparison between before (black) and after (red) thermal annealed bulk samples. (a) ethynyl-P3HT **P3** and (b) P3HT<sub>P3</sub>-*b*-AcMal<sub>7</sub>. Positions of strong reflections estimated based on the unit cell proposed by Brinkmann *et al.* were depicted with gray dashed lines together with corresponding Miller indices. All reflection positions were plotted with purple marks.



**Figure 4.14** Comparison of diffraction patterns between as-prepared bulk samples of (a) ethynyl-P3HT **P3** and (b) P3HT<sub>P3</sub>-*b*-AcMal<sub>7</sub>.

**Table 4.5** Predicted and experimental  $d$ -spacings

$hkl$	$d_{calc}^a$ ( $\text{\AA}$ )	ethynyl-P3HT <b>P1</b>	ethynyl-P3HT <b>P3</b>		P3HT <sub>P1</sub> - <i>b</i> -AcMal <sub>7</sub>	P3HT <sub>P3</sub> - <i>b</i> -AcMal <sub>7</sub>	
		as-prepared ( $\text{\AA}$ )	as-prepared	after annealing ( $\text{\AA}$ )	as-prepared ( $\text{\AA}$ )	as-prepared	after annealing ( $\text{\AA}$ )
100	15.97	15.93	—	—	15.94	—	—
200	7.99	7.90	7.99	7.98	7.93	8.02	8.50
300	5.32	5.18	5.30	5.32	5.17	5.27	5.64
002/020	3.90/3.89	—	3.85	3.85	—	3.83	3.77

<sup>a</sup>  $d$ -spacings estimated based on the unit cell proposed by Brinkmann *et al*,  $a = 16.0 \text{ \AA}$ ,  $b = 7.8 \text{ \AA}$ ,  $c = 7.8 \text{ \AA}$ , and  $\gamma = 86.5^\circ$ .

**Structural evolution of P3HT-*b*-AcMal<sub>7</sub>—during the annealing**

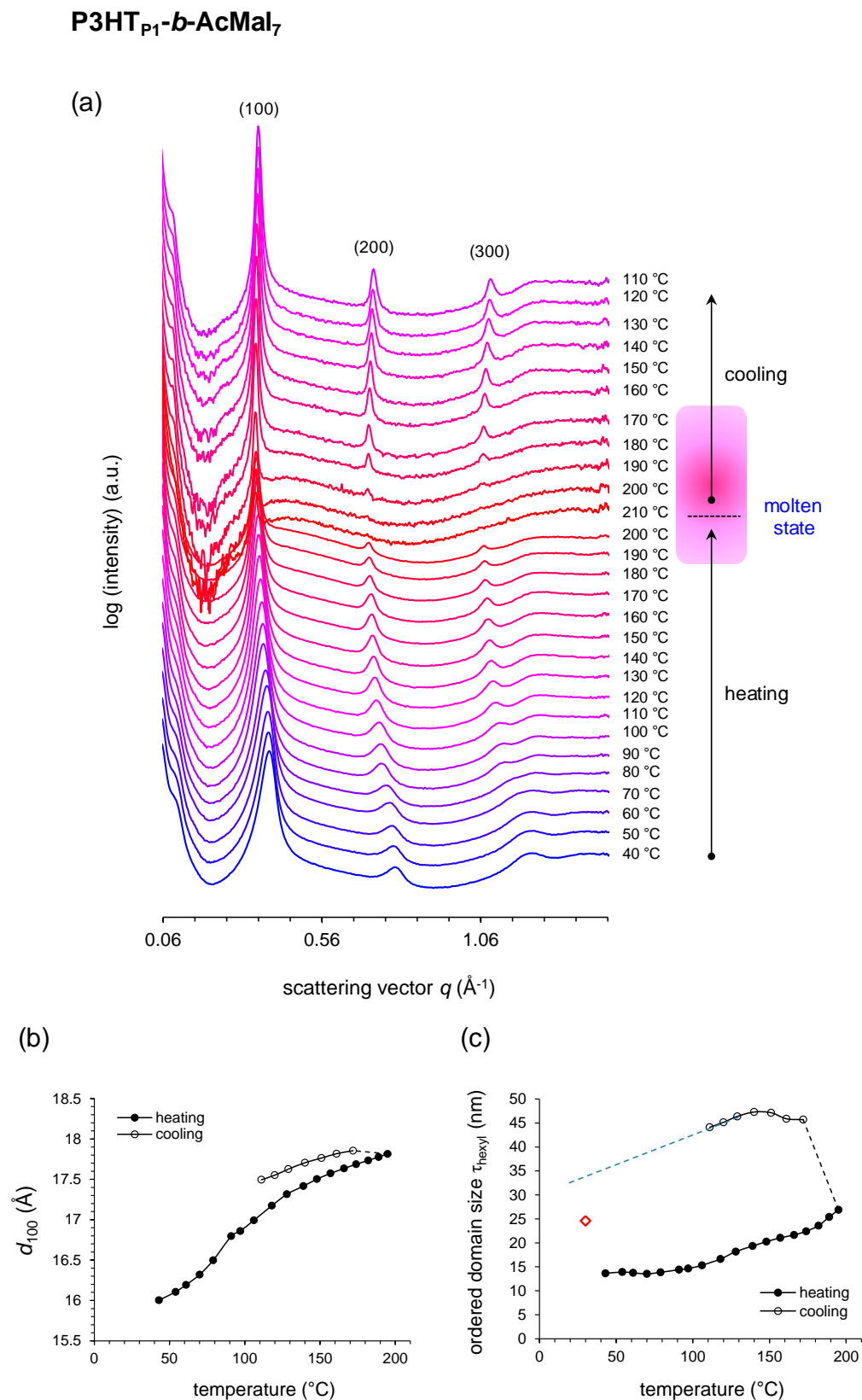
Figure 4.15 and 4.16 present the evolution of WAXS profiles during the annealing process of the P3HT<sub>P1</sub>-*b*-AcMal<sub>7</sub> and P3HT<sub>P3</sub>-*b*-AcMal<sub>7</sub>, respectively. The overall behavior of (*h*00) peaks can be observed in the Figure 4.15a covering the *q*-range from 0.05 to 1.50 Å<sup>-1</sup>. The evolution of *d*-spacing calculated from the (100) peak position (*d*<sub>100</sub>-spacing) and ordered domain size consisting of the periodic P3HT backbones separated by hexyl side chains ( $\tau_{\text{hexyl}}$ ) estimated from the FWHM of the (100) peak are also presented in Figure 4.15b and 4.15c. As the temperature increased up to 200 °C, the (*h*00) peaks continuously shifted toward a lower *q*-range, accompanying a sharpening of the peaks. Above 200 °C, both (200) and (300) peaks diminished while the primary (100) peak remained during whole heating process. Upon cooling, the (200) and (300) peaks showed up at 190 °C which is higher than *T<sub>c</sub>* of the P3HT<sub>P1</sub>-*b*-AcMal<sub>7</sub> determined by DSC (*T<sub>c</sub>*, onset = 174 °C, *T<sub>c</sub>*, peak top = 166 °C). The difference in the crystallization temperature can be partly attributed to the difference of the cooling rate between DSC (10°C/min) and WAXS (cooling by simple heat dissipation) measurements because, in general, the crystallization temperature decreases with increasing cooling rate. With further cooling, the (*h*00) peaks shifted back toward higher *q*-range. Again, this reversible variation in the (*h*00) peak positions supports previous explanation, *i.e.* thermal expansion of the hexyl side chain.

The  $\tau_{\text{hexyl}}$  value increased steadily from 13.7 to 26.9 nm, and jumped up to 45.7 nm during the holding period at 210 °C. During cooling the  $\tau_{\text{hexyl}}$  value decreased slightly. The decrease of the crystallite size during the cooling is counter-intuitive but two explanations are possible: (i) the shrinking of the hexyl groups might have introduced internal strain or (ii) the crystal forming at lower temperature have to grow between limited spaces available, and even the small crystal germ persists at lower temperature leading to smaller average crystallite sizes. The final  $\tau_{\text{hexyl}}$  estimated from the diffraction pattern which was recorded at 110 °C in the cooling cycle (no data below 110 °C) was 44.1 nm. This value corresponds to about 28 times the period of inter layer distance separated by hexyl side chain (*d*<sub>100</sub>-spacing = 1.6 nm) (44.1 nm ~ 1.6 nm × 28). For comparison, the  $\tau_{\text{hexyl}}$  calculated from the diffraction pattern of the P3HT<sub>P1</sub>-*b*-AcMal<sub>7</sub> that underwent a standard thermal treatment (210 °C for 10 min followed by rapid quenching to room temperature) was plotted in Figure 4.15c with red square. The red square seems to somewhat deviate from an extrapolation of the  $\tau_{\text{hexyl}}$  slope of the cooling cycle (plotted with open circle).

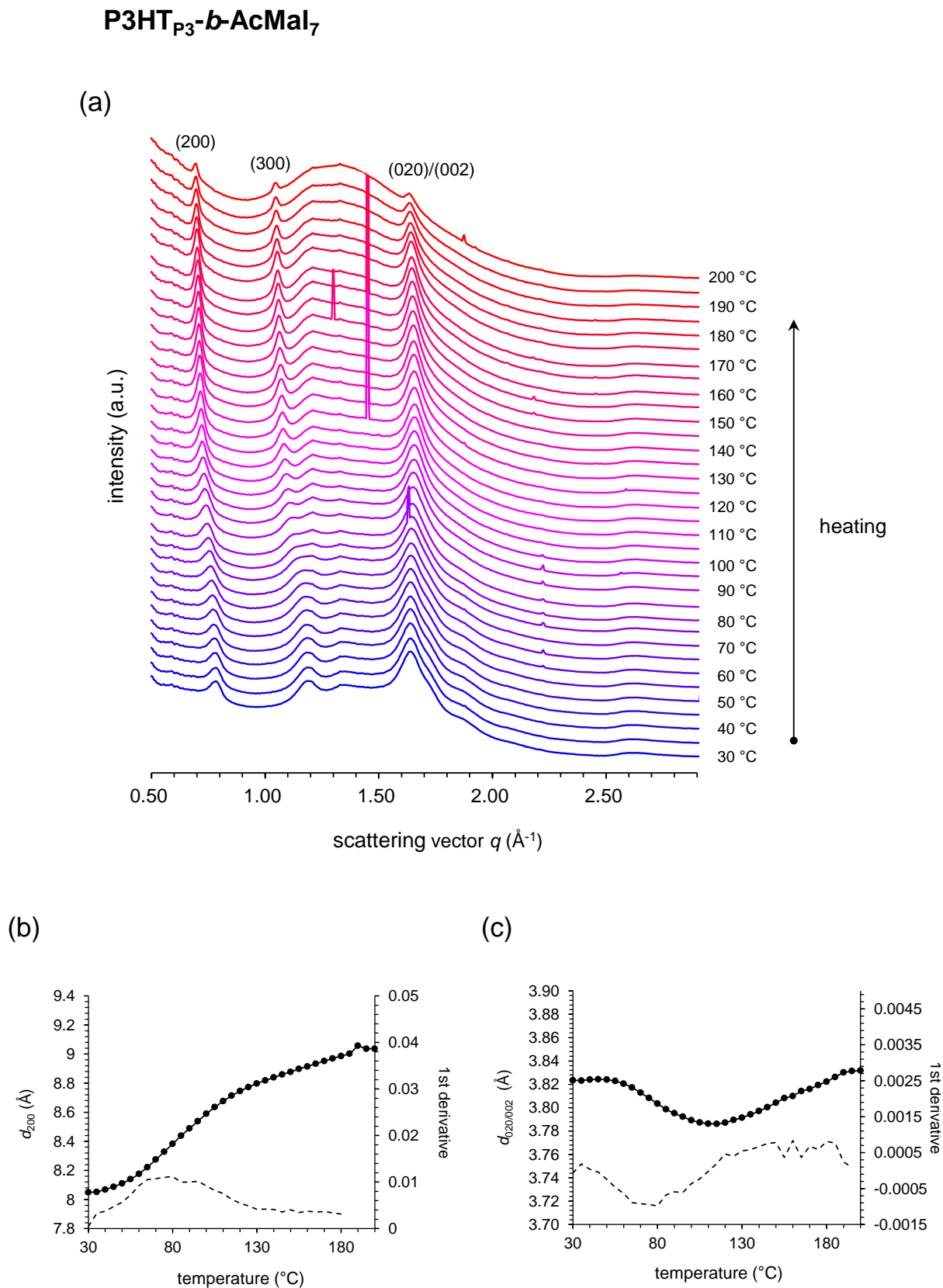
This indicates that the rapid cooling prevented the long-range ordering of the P3HT segment of the P3HT<sub>P1</sub>-*b*-AcMal<sub>7</sub>.

Figure 4.16a covers a higher  $q$ -range. With the temperature increases up to 120 °C, the (020)/(002) peak slightly shifts toward higher  $q$ -range, which is opposite to the shift of ( $h$ 00) peaks, then shifts back to lower  $q$  by further heating above 120°C. Figure 4.16b and Figure 4.16c shows a variation of the  $d$ -spacing calculated from the peak position of (200) reflection ( $d_{200}$ ) and one calculated from the peak position of (020)/(002) reflection ( $d_{020/002}$ ), respectively, together with the first temperature derivatives of the corresponding  $d$ -spacing. The  $d_{200}$  follows a similar trend as  $d_{100}$  as expected, with a slow transition between 60 and 110°C superimposed with a linear thermal expansion of about 800 ppm/K. The transition is accompanied by about 6 % increase in  $d_{200}$ . The  $d_{020/002}$  also shows a similar trend with a thermal expansion of 100 ppm/K and the transition between 60 and 110°C which induces a decrease of  $d$ -spacing of about 1 %. The first derivatives of  $d_{200}$  showed a close similarity in shape to that of  $d_{020/002}$  but with opposite sign, supporting the phase transition occurring between 60 and 110°C.

The *in-situ* X-ray scattering experiment revealed the difference between the annealed and as cast samples of P3HT-*b*-AcMal<sub>7</sub> comes from the phase transition occurring between 60 and 110 °C during the first heating, where the basic arrangement of P3HT segment slightly changes. This phase transition was not accompanied little change in internal energy as no heat-flow could be detected in the DSC thermogram. If the  $d_{100}$  increased by 6 % and  $d_{020}$  shrunk by 1 % during the phase transition, the net density of P3HT segments decreased which should lead to an increase in internal energy. This might have been compensated by the densification and rearrangement of AcMal<sub>7</sub> segment, which was not detectable due to its amorphous nature. In the solution casting, the P3HT segment starts to crystallize prior to complete evaporation of the solvent THF, and the structure formation might be dictated by the crystallization tendency of P3HT leading the AcMal<sub>7</sub> in high-energy packing situation. In the complete absence of solvent, the thermal annealing would soften the P3HT segments allowing the AcMal<sub>7</sub> segment to relax imposing some constraint on P3HT that transform into other crystalline form. The net enthalpy would be almost zero as the conversion is simply a transfer of internal energy from AcMal<sub>7</sub> segments to P3HT segments.



**Figure 4.15** (a) WAXS profiles of P3HT<sub>P1</sub>-*b*-AcMal<sub>7</sub> bulk sample and variation of (b)  $d_{100}$  and (c) crystallite size during *in situ* heating and cooling process.



**Figure 4.16** (a) WAXS profiles of P3HT<sub>P3</sub>-*b*-AcMal<sub>7</sub> bulk sample and variation of (b)  $d_{200}$  and (c)  $d_{020/002}$  during *in situ* heating process from 30 to 200  $^{\circ}\text{C}$ .



## IV.5 Conclusion

In this chapter, thermal properties and thermally-induced structural evolution of P3HT-*b*-AcMal<sub>7</sub> have been systematically investigated by TGA, DSC, and *in situ* step-wise heating and cooling X-ray scattering analysis comparing with those of P3HT homopolymer.

The temperature dependent *in situ* SAXS experiments revealed that the P3HT-*b*-AcMal<sub>7</sub> exhibits microphase separation above  $T_g$  of AcMal<sub>7</sub> and  $T_m$  of P3HT segment. The multiple scattering peaks located at integer multiples of the first peak position indicates the existence of lamellar structure in molten state, which is quite reasonable morphology considering the phase diagram and the volume fraction of P3HT segment ( $f_{\text{P3HT}} = 0.66$ ). Although order-disorder transition of the lamellar phase could not be observed in the experimental temperature range (*i.e.*  $T_{\text{ODT}} > 210\text{ }^{\circ}\text{C}$ ), the P3HT-*b*-AcMal<sub>7</sub> can be considered as strong segregation system.

In the crystalline-rubber block copolymer system whose  $T_c$  is in between the  $T_{\text{ODT}}$  and  $T_g$  ( $T_{\text{ODT}} > T_c > T_g$ ), crystallization precedes solidification of rubber block upon cooling. Hence, when the segregation strength between crystalline and rubber blocks is not sufficiently high, microphase-separated structure existed in molten state will be destroyed due to the strong crystallization tendency of crystalline block. Contrary to such case, crystallization of the P3HT segments of P3HT-*b*-AcMal<sub>7</sub> took place within the phase-separated nanodomains while retaining initial lamellar morphology, indicating that P3HT and AcMal<sub>7</sub> are strongly segregated throughout whole structure formation process.

The reliability of this confined crystallization phenomenon was further corroborated by DSC analysis. The P3HT-*b*-AcMal<sub>7</sub> showed more complex melting behavior compared with the P3HT homopolymer. In particular, when the block copolymer was solidified rapidly from the molten state, a bimodal endothermic peak, corresponding to the melting transition of P3HT segments, was observed in the heating thermogram. This bimodal peak implies a coexistence of two different crystal states which formed through different crystallization process, *i.e.* (i) metastable crystal formed under the control of kinetic factors and (ii) stable crystal formed under the control of thermodynamic factors. The origin of such behavior can be attributed to tethering effect of P3HT with AcMal<sub>7</sub> which leads to the different chemical and geometrical environments for the P3HT segments (low mobile chain-end anchored by AcMal<sub>7</sub>, highly crystallizable middle part,

and highly mobile free chain-end, *etc.*). Thus, it is quite likely that the crystallization of P3HT segment proceeds in the confined space where the contribution of tethering effect cannot be avoided.

## IV.6 References

- (1) Wu, Z.; Petzold, A.; Henze, T.; Thurn-Albrecht, T.; Lohwasser, R. H.; Sommer, M.; Thelakkat, M. *Macromolecules* **2010**, *43* (10), 4646–4653.
- (2) Yuan, Y.; Zhang, J.; Sun, J.; Hu, J.; Zhang, T.; Duan, Y. *Macromolecules* **2011**, *44* (23), 9341–9350.
- (3) Imamura, K.; Sakaura, K.; Ohyama, K. I.; Fukushima, A.; Imanaka, H.; Sakiyama, T.; Nakanishi, K. *J. Phys. Chem. B* **2006**, *110* (31), 15094–15099.
- (4) Prosa, T. J.; Winokur, M. J.; Moulton, J.; Smith, P.; Heeger, a. J. *Macromolecules* **1992**, *25* (17), 4364–4372.
- (5) Mårdalen, J.; Samuelsen, E. J.; Gautun, O. R.; Carlsen, P. H. *Synth. Met.* **1992**, *48* (3), 363–380.
- (6) Prosa, T. J.; Winokur, M. J.; McCullough, R. D. *Macromolecules* **1996**, *29* (10), 3654–3656.
- (7) Brinkmann, M.; Wittmann, J. C. *Adv. Mater.* **2006**, *18* (7), 860–863.
- (8) Kayunkid, N.; Uttiya, S.; Brinkmann, M. *Macromolecules* **2010**, *43* (11), 4961–4967.



## **CHAPTER V:**

# **APPROACHES TOWARD APPLICATION OF THE SEMICONDUCTING GLYCOCONJUGATED DIBLOCK COPOLYMERS TO PHOTOVOLTAIC CELLS**

## V.1 Introduction

To address the ultimate objective of this project, *i.e.*, fabrication of OPV devices having an ideal lamellar structure derived from the self-assemble of block copolymers, two approaches were conducted.

First, selective etching of oligosaccharide domain from phase-separated P3HT-*b*-AcMal<sub>7</sub> film was carried out (Chapter V.2). The cavity obtained as a result of the selective etching will be filled with acceptor compound to give a practical active layer in which donor and acceptor domains are arranging alternatively in sub-10 nm scale, so that it will provide ideal active layer morphology in terms of efficient exciton dissociation and low probability of charge carrier recombination. Here, we demonstrate two methods for preparing nano-patterned film consisting of well-defined P3HT-based lamellar structure; *i.e.* (i) dry etching (plasma etching) method and (ii) wet chemical etching method.

Second, a small molecule consisting of AcMal<sub>7</sub> and electronically active fullerene derivative (AcMal<sub>7</sub>-C<sub>61</sub>) is newly designed and synthesized as an alternative acceptor compound with the aim to control location of fullerenes. In this method, selective etching of the oligosaccharide segment is not intended. The phase-separated semi-active P3HT-*b*-AcMal<sub>7</sub> film can be utilized as it is by blending with AcMal<sub>7</sub>-C<sub>61</sub> as acceptor. Since AcMal<sub>7</sub> segment of AcMal<sub>7</sub>-C<sub>61</sub> is assumed to be incorporated within the AcMal<sub>7</sub> segment of the P3HT-*b*-AcMal<sub>7</sub>, C<sub>61</sub> moiety is expected to arrange along a boundary of P3HT domains. In the Chapter V.3, the synthesis of AcMal<sub>7</sub>-C<sub>61</sub> and detailed characterization is reported. Additionally, preliminary characterization of blend films of the P3HT-*b*-AcMal<sub>7</sub> (as an electron donating moiety) and AcMal<sub>7</sub>-C<sub>61</sub> (as an electron accepting moiety) is also reported with particular emphasis on their morphology.

## V.2 Selective etching of oligosaccharidic block

### V.2.1 Plasma etching

Etching technology is generally classified into two categories, namely wet chemical etching and dry etching processes. The former is an etching method that uses liquid chemicals such as acid and alkaline solutions. The latter, also known as plasma etching, is a method where the material removal process occurs in the gas phase. In this process, the active species (ions, electrons, radicals and neutral particles, etc.) play an essential role in etching off the target materials. The etching reaction takes place either via chemical (chemical plasma etching), physical (sputtering, ion beam milling), or combination of chemical/physical (reactive ion etching) reaction mechanisms. These modes can be controlled by radio frequency (RF) power, etchant gasses, and process pressure, etc.

Among the various evaluation criteria such as etch uniformity, etch profile (isotropy or anisotropy), and resolution etc., etching selectivity (S) is one of the most critical parameters which is defined as the relative etch rate of the target material (etching object) A ( $R_a$ ) to the another material B ( $R_b$ ).

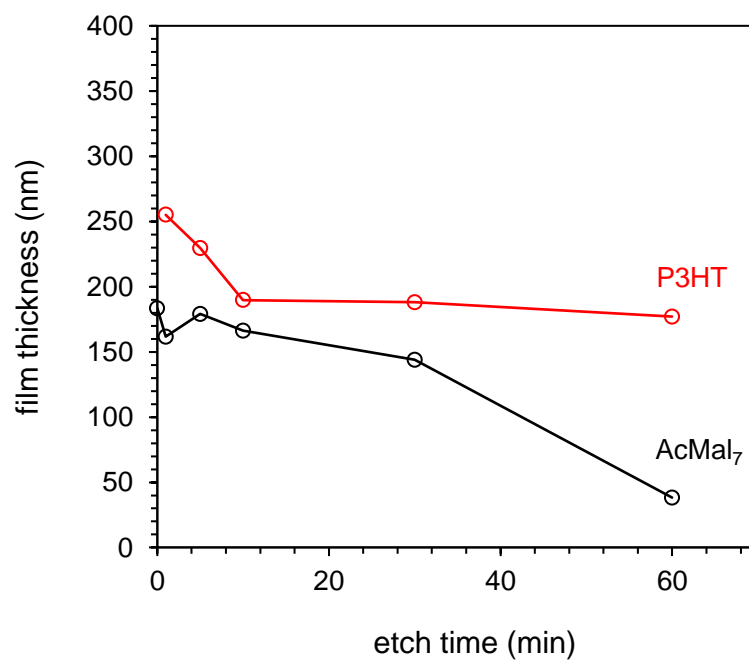
$$\text{Etching selectivity: } S_{ab} = \frac{R_a}{R_b}$$

In the present study, high selectivity between P3HT block and sacrificial AcMal<sub>7</sub> block is required to achieve a well-defined P3HT-based lamellar pattern.

For the semi-crystalline polymers, it is known that there is a strong correlation between crystallinity and etch rate,<sup>1</sup> where higher crystallinity results in a less susceptibility to plasma etching. Thus, in our current system the non-crystalline AcMal<sub>7</sub> domain is expected to be preferentially removed during etching process.

As a first experiment, plasma etching with oxygen/argon etchant gas was carried out using a PVA Tepla IoN 3 MHz. plasma system. The thick films (> 180 nm) of the P3HT and AcMal<sub>7</sub> were exposed to the oxygen/argon plasma in the same etching sequence to ensure the both samples undergo etch process under identical conditions. The thickness of the initial films and remaining films was measured by AFM.

Although several parameters were varied to find the appropriate etching conditions, it was not possible with this apparatus to determine the etching rate since both segments were completely etched away in few seconds even under the mildest conditions (13.56 MHz, 15 W, 0.8 Torr, O<sub>2</sub> flow rate: 50 cm<sup>3</sup>/min, Ar flow rate: 60 cm<sup>3</sup>/min). Thus, alternatively, PELCO easiGlow<sup>TM</sup> GlowDischarge Cleaning System was used for subsequent experiments, which was capable of lowering the operation power with a variation from 1 W to 30 W. The thick films were exposed to air plasma at low pressure of 0.3 Torr with 5W at room temperature. Figure 5.1 shows the film thickness of the P3HT (red circle) and AcMal<sub>7</sub> (black circle) as a function of the etching time. The thickness of AcMal<sub>7</sub> film decreased almost linearly with the etch rate of 2.1 nm/min. On the other hand, the etch rate of P3HT shows two regimes. In the first stage, the P3HT film was etched away faster than AcMal<sub>7</sub> with the etch rate of 7.3 nm/min and then suddenly became stable (etch rate in the second stage: 0.3 nm/min). Indeed, we found some differences regarding etching behaviors between crystalline P3HT and amorphous AcMal<sub>7</sub>, but no significant etching selectivity was obtained. In addition, a deterioration of the electronic property of P3HT cannot be avoided because the P3HT film is also somewhat damaged by plasma irradiation. Thus, the plasma etching technique is not suitable for the selective etching of the P3HT-*b*-AcMal<sub>7</sub> system.



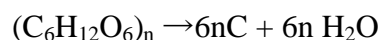
**Figure 5.1** Film thickness of the P3HT (red circle) and AcMal<sub>7</sub> (black circle) as a function of etching time.



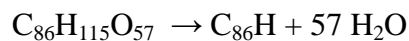
### V.2.2 Wet etching by concentrated sulfuric acid

A selective etching of sugar domain via a wet process was performed using concentrated sulfuric acid. Wet etching is the process that removes materials by immersing in a liquid bath (chemical etchant bath) in which the chemical reacts with only target materials. Due to its simple setup, low cost, high chemical selectivity, and high etching rate, the wet etching process is widely used in the printing and semiconductor fabrication industries.

Concentrated sulfuric acid is well-known as a strong dehydrating agent.<sup>2</sup> Due to its strong affinity with water, concentrated sulfuric acid extract hydrogen and oxygen in form of water from other compounds such as carbohydrates and sugars and afford carbonized residue. For instance, the addition of concentrated sulfuric acid to the starch  $(C_6H_{12}O_6)_n$  will result in the elemental carbon and water as shown in a following chemical reaction formula:



In the current system sugar is easily dehydrated and carbonized by concentrated sulfuric acid, while P3HT would not be affected by sulfuric acid as it does not contain an oxygen atom. Therefore, we applied the concentrated sulfuric acid to the selective elimination/degradation of the AcMal<sub>7</sub> domain from the P3HT-*b*-AcMal<sub>7</sub> film. The dehydration reaction on the AcMal<sub>7</sub> can represent as following.

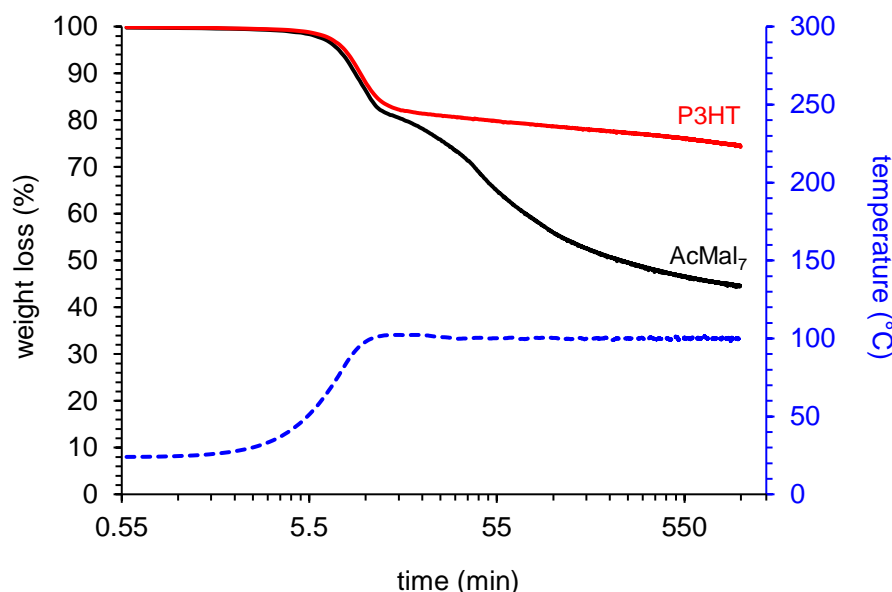


The empty space that is formed as a result of elimination of the AcMal<sub>7</sub> segment can be used as a vessel for electron acceptor compounds. Besides, if the reaction proceeds without side reaction though some side reactions may occur, such as emission of CO<sub>2</sub> and CO, etc., the AcMal<sub>7</sub> turns into almost completely carbonized compound C<sub>86</sub>H (the carbon content: > 99 wt%) after removal of water. The resultant residue consisting of a carbon skeleton is expected to have a good affinity with typical electron acceptor compounds, such as [6,6]-phenyl-C<sub>61</sub>-butyric acid methyl ester (PC<sub>61</sub>BM) and indene-C<sub>60</sub> bisadduct (ICBA), because the basic structures of those compounds are fullerene that is also entirely composed of carbon.

This method is technically and environmentally favorable for manufacturing production. As is usual with wet etching process, developing and/or washing step is often regarded as troublesome due to contamination of etch residues on the film surface. In addition, a collapse of the fine pattern sometimes takes place during washing step. By contrast, since our strategy affords just water as a reaction product, any complex treatment is not needed. Immersing films in water is enough to clean.

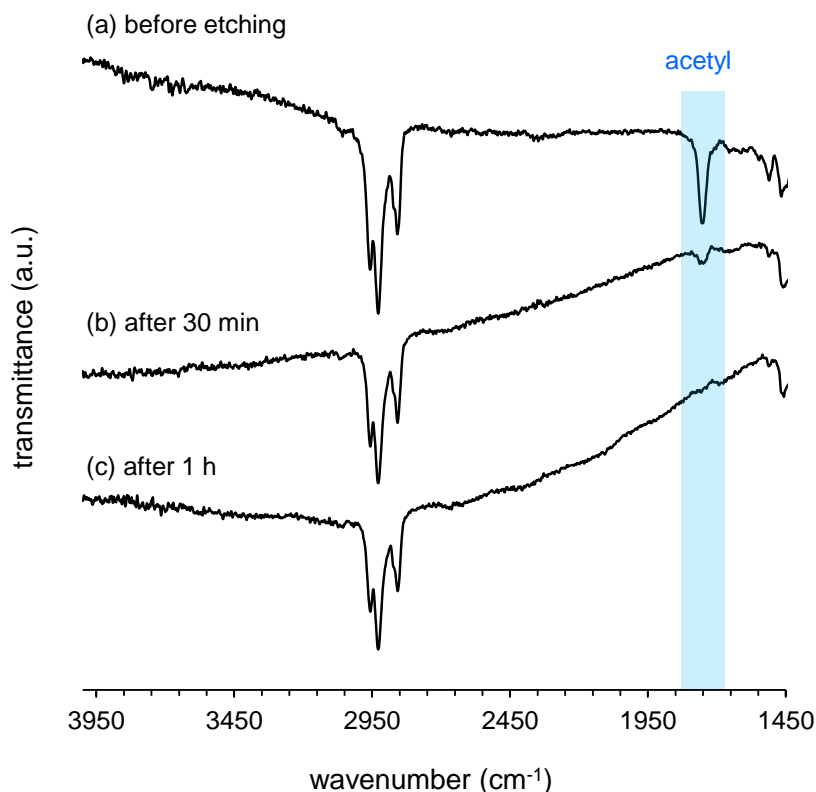
First, in order to examine the dehydration action of the concentrated sulfuric acid, thermogravimetry analysis (TGA) was carried out on sulfuric acid-impregnated powder samples of AcMal<sub>7</sub> and P3HT individually. The powder samples of the AcMal<sub>7</sub> and P3HT were weighted accurately and placed to a sample pan. The dilute sulfuric acid solution was added to the pan so as the sulfuric acid content to be 5 % (ratio by weight) with respect to the sample weight. Here, dilute sulfuric acid was used to impregnate into the powder samples sufficiently in a homogeneous manner. Low concentration of sulfuric acid causes no problem because the solution will be concentrated by a subsequent heating in the course of TGA measurement. The sulfuric acid-impregnated samples were heated to 100 °C at a heating rate of 10 °C/min under nitrogen flow and then the temperature was hold at 100 °C for 24 h. The isothermal hold temperature of 100 °C was chosen as above the boiling point of water, but below the  $T_g$  of P3HT ( $T_{g,P3HT}$ ). At this temperature, dehydration reaction would be enhanced by evaporating initial water (it leads an increase of H<sub>2</sub>SO<sub>4</sub> concentration) and the water extracted from AcMal<sub>7</sub> segment. But no collapse of the lamellar structure may occur because the P3HT segment remain in a solid-state below the  $T_{g,P3HT}$ .

The weight loss behaviors of the sulfuric acid-impregnated AcMal<sub>7</sub> and P3HT samples are shown in Figure 5.2. At the first stage below 100 °C, weight loss due to evaporation of water was observed for the both samples. AcMal<sub>7</sub> sample showed a significant weight loss during the isothermal heating at 100 °C whereas P3HT sample showed only a small weight loss. This result suggests that there is a strong possibility of selective etching of sugar domains from the phase-separated P3HT-*b*-AcMal<sub>7</sub> films by wet etching using concentrated sulfuric acid.



**Figure 5.2** Weight loss profiles obtained by thermogravimetry of sulfuric acid-impregnated AcMal<sub>7</sub> (black line) and P3HT (red line) powders as a function of time during heating process from room temperature to 100 °C with heating rate at 10 °C/min following isothermal heat treatment at 100 °C.

Wet etching of the sugar block using sulfuric acid was then carried out on the thermally annealed P3HT<sub>P3</sub>-*b*-AcMal<sub>7</sub> thick films. The dehydration reaction was monitored by FT-IR spectrometry. The thick film samples with the thickness of *ca.* 250 nm were prepared by spin-coating from concentrated THF solution of the polymer onto Si wafer so as to gain sufficient spectral intensity. After thermal annealing at 200 °C for 10 min, the thick films were treated with concentrated sulfuric acid at 100 °C for different time. The treated films were then carefully rinsed with deionized (DI) water for several times using a pipette in order to remove sulfuric acid. The films containing water were then subjected to solvent substitution with ethanol and dried overnight at room temperature under reduced pressure. Figure 5.3 shows FT-IR spectra of the before and after etching P3HT<sub>P3</sub>-*b*-AcMal<sub>7</sub> films. The FT-IR spectrum of the resulting film after 1 hour etching demonstrates the complete removal of acetyl groups of the AcMal<sub>7</sub> segment as proven by a complete disappearance of the characteristic signal at 1750 cm<sup>-1</sup> corresponding to a carbonyl stretching. In contrast, the characteristic signals corresponding to the P3HT block observed in the range of 3050 to 2860 cm<sup>-1</sup> remain unchanged, indicating that P3HT block is not subjected to

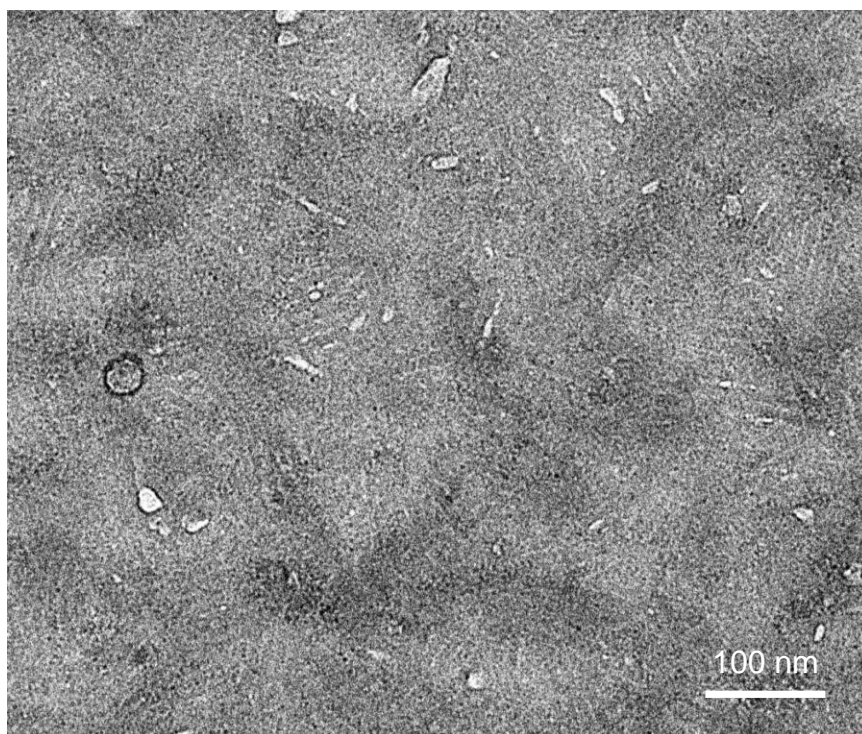


**Figure 5.3** FT-IR spectra of the P3HT<sub>P3</sub>-*b*-AcMal<sub>7</sub> films (a) before etching and after sulfuric acid etching at 100 °C for (b) 30 min and (c) 1h. The film was prepared by spin-coating on Si wafer with the thickness of *ca.* 250 nm.

dehydration action from concentrated sulfuric acid. To investigate the morphology of etched thick film, AFM measurement was conducted, but unfortunately we could not obtain clear surface image by AFM. This is probably due to a high surface roughness that was formed during the film preparation and washing process with water. The thick film used in AFM was prepared from 3 wt % polymer solution in THF by spin-coating method. A high concentration and heterogeneous evaporation of highly volatile of THF may cause roughness of the resulting film. Secondly, washing process with water resulted in a film peeling from Si substrate. A high surface tension of water might affect the adhesive strength between the polymer layer and substrate and caused a film distortion.

TEM measurement was carried out to visualize the morphology of the etched film. Thin film of P3HT<sub>P3</sub>-*b*-AcMal<sub>7</sub> with a thickness about 30 nm was prepared for the express purpose of TEM observation. After etching and washing process, the thin film was carefully placed into a water receiver to float out the film from Si substrate. Floating film was collected using a TEM grid and excess water was removed with paper filter and dried in the oven under reduced pressure. TEM image of the etched film shows successful selective etching of sugar block (Figure 5.4). The lamellar morphology consisting of P3HT matrix maintained after the wet etching as observed with dark contrast. A bright thin region observed between the P3HT structures is either carbonized sugar domains or voids after the removal of those domains by washing. The strong bright contrast that can be seen as white spots suggests the absence of the elements in this domain.

Thus, all of the above results revealed that the concentrated sulfuric acid is a very effective agent for preparing the pattern etched films via selective etching of sugar domain from microphase separated P3HT-*b*-AcMal<sub>7</sub> block copolymer film.



**Figure 5.4** TEM image of the P3HT<sub>P3</sub>-b-AcMal<sub>7</sub> thin film, obtained after sulfuric acid etching at 100 °C for 1h.

Although this strategy is promising for the selective etching of sugar domain, there is an issue concerning weak adhesive strength of coating film with substrate. The concentrated sulfuric acid reacts efficiently and selectively with the sugar domain but coincidentally reduce the film adhesiveness with Si substrate. When the films were placed into water for washing, the films were easily peeled off from the substrate. In addition, evaluation of electronic properties of the resulting film is one of the most important aspects for the practical applications. To be free from a deterioration of the conductivity of P3HT is an indispensable prerequisite. In this respect, (i) investigation of electronic properties of the etched film, (ii) a more accurate parameter control (such as initial concentration of sulfuric acid, operation time and temperature) and (iii) exploring better process that does not cause peeling, are the tasks to be addressed in the future.

### V.3 Synthesis and characterization of fullerene-conjugated oligosaccharide

This section aims to realize an assembly with well-defined nanostructure including the electron-donating P3HT and electron-accepting fullerene derivatives in which both materials are arranged mutually.

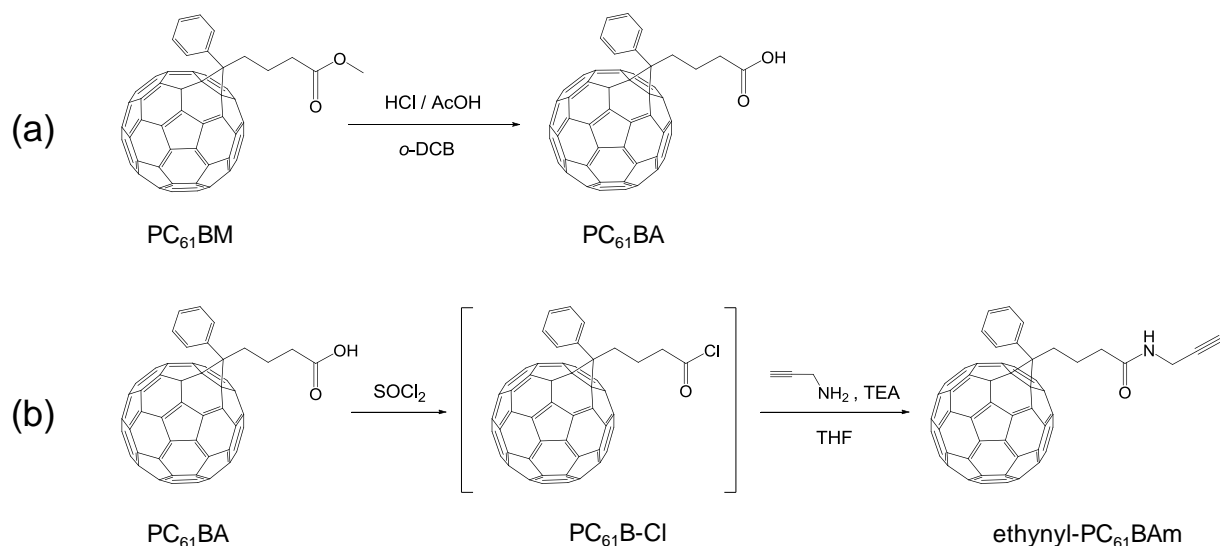
Some of the most inherent drawbacks of the conventional bulk-heterojunction systems such as P3HT:PC<sub>61</sub>BM are a precise control of the blend structure at nanoscale and morphological instability. For instant, large aggregates of acceptor compounds or macro phase segregation between donor and acceptor compounds are often found in the blend films through post-treatment process like thermal or solvent annealing. Various attempts for morphological control have been made to enhance the efficiency and stability.<sup>3-5</sup> Among them, immobilization of the acceptor compound via chemical or physical interaction to selected domain is thought as an effective way to localize and stabilize acceptor moiety.

For this purpose the synthesis of fullerene attached P3HT-*b*-Mal<sub>7</sub> block copolymers was initially attempted with the aim of preparing electronically active donor-*b*-acceptor block copolymers. However, contrary to our expectations, all attempts eventuated in failure mainly due to a low solubility of fullerene derivatives, inaccessibility to the reactive hydroxyl group of the Mal<sub>7</sub> (P3HT-*b*-Mal<sub>7</sub> formed nanoparticles in the reaction mixture), and complex purification process, etc.

Therefore, fullerene-conjugated AcMal<sub>7</sub> (AcMal<sub>7</sub>-C<sub>61</sub>) was newly designed as an acceptor compound suitable for the current P3HT-*b*-AcMal<sub>7</sub> system. The purpose of this approach is to provide conceptually optimal donor-acceptor architecture in which a location of the acceptor moiety is well controlled by intermolecular interaction. Not only a perfect miscibility between AcMal<sub>7</sub> segments of the AcMal<sub>7</sub>-C<sub>61</sub> and P3HT-*b*-AcMal<sub>7</sub> but also a high incompatibility between AcMal<sub>7</sub>-C<sub>61</sub> and P3HT segments may provide a major contribution to the localization of the acceptor moiety. AcMal<sub>7</sub>-C<sub>61</sub> is thought to easily penetrate in the AcMal<sub>7</sub> domain but be excluded from P3HT crystalline packing without destroying the lamellar structure.

### V.3.1 Synthesis of alkyne-functionalized fullerene derivative

Alkyne-functionalized “clickable” fullerene derivative was synthesized in two steps as shown in Scheme 5.1. First, (6,6)-phenyl C<sub>61</sub> butyric acid (PC<sub>61</sub>BA) was prepared via hydrolysis of PC<sub>61</sub>BM by using HCl and acetic acid according to the reported procedure (Scheme 5.1a).<sup>6</sup> The reaction progress was monitored by TLC until complete disappearance of the starting material. The product was then characterized by FT-IR and MALDI-TOF MS analysis. MALDI-TOF MS spectrometry gave the molecular ion [M-H]<sup>-1</sup> at  $m/z = 896.0$  in negative mode as shown Figure 5.5. IR spectrum of the product displayed a characteristic absorption band at 1702 cm<sup>-1</sup> indicative of the carboxylic acid group of the PC<sub>61</sub>BA (Figure 5.6b). Thus, resulting product was identified as PC<sub>61</sub>BA. The solubility of PC<sub>61</sub>BA was significantly changed after hydrolysis, and PC<sub>61</sub>BA turned insoluble in most of organic solvents.





Subsequently, PC<sub>61</sub>BA was reacted with thionyl chloride (SOCl<sub>2</sub>) under reflux (Scheme 5.1b). In the general procedure, carbon disulfide (CS<sub>2</sub>) has been used as a solvent because it is one of the few solvent in which PC<sub>61</sub>BA is slightly soluble.<sup>6-8</sup> However, in our experiment, it was found that the use of solvent was not indispensable. PC<sub>61</sub>BA became soluble in the SOCl<sub>2</sub> in the course of the reaction. Moreover, taking into account for the boiling point of SOCl<sub>2</sub> ( $T_{b, \text{SOCl}_2} = 75\text{ }^{\circ}\text{C}$ ) and CS<sub>2</sub> ( $T_{b, \text{CS}_2} = 46\text{ }^{\circ}\text{C}$ ), the absence of the CS<sub>2</sub> is more favorable to promote the reaction by heating the mixture until near  $T_{b, \text{SOCl}_2}$ . After approximately 6 hours, the PC<sub>61</sub>BA was almost completely converted into PC<sub>61</sub>B-Cl reactive intermediate as evidenced by FT-IR spectroscopy.

IR spectrum of the reaction mixture clearly shows an appearance of the peak at 1793 cm<sup>-1</sup> due to the C=O stretching of the carbonyl chloride and an absence of the peak at 1702 cm<sup>-1</sup> corresponding to the C=O stretching of carboxylic acid group of the PC<sub>61</sub>BA (Figure 5.6c).

After the mixture was cooled to the room temperature, thionyl chlorid was removed from the reaction system by vacuum pump. Then, propargylamine and dry trimethylamine were added to the PC<sub>61</sub>B-Cl to yield the *N*-propargyl (6,6)-phenyl C<sub>61</sub> butyramido (ethynyl-PC<sub>61</sub>BAm). The resulting product was soluble in THF and hardly soluble in toluene, CHCl<sub>3</sub>, and *o*-DCB. The product was characterized by means of <sup>1</sup>H NMR, FT-IR, and MALDI-TOF MS spectrometry.

Figure 5.7 shows <sup>1</sup>H NMR spectra of the PC<sub>61</sub>BM and resultant product recorded in CDCl<sub>3</sub> and THF-*d*<sub>8</sub>, respectively. (Different deuterated solvents were used for the present comparative experiment because no common good deuterated solvent could be found for the both compounds) The spectrum of the resultant product exhibits new proton resonances at 7.34 ppm, 3.93 ppm, and 2.53 ppm corresponding to the ethynyl functional group, which is a clear evidence of the successful introduction of the ethynyl group to the fullerene derivative (Figure 5.7b). Additionally, the degree of substitution was quantified from the <sup>1</sup>H NMR integrals to be 100 %.

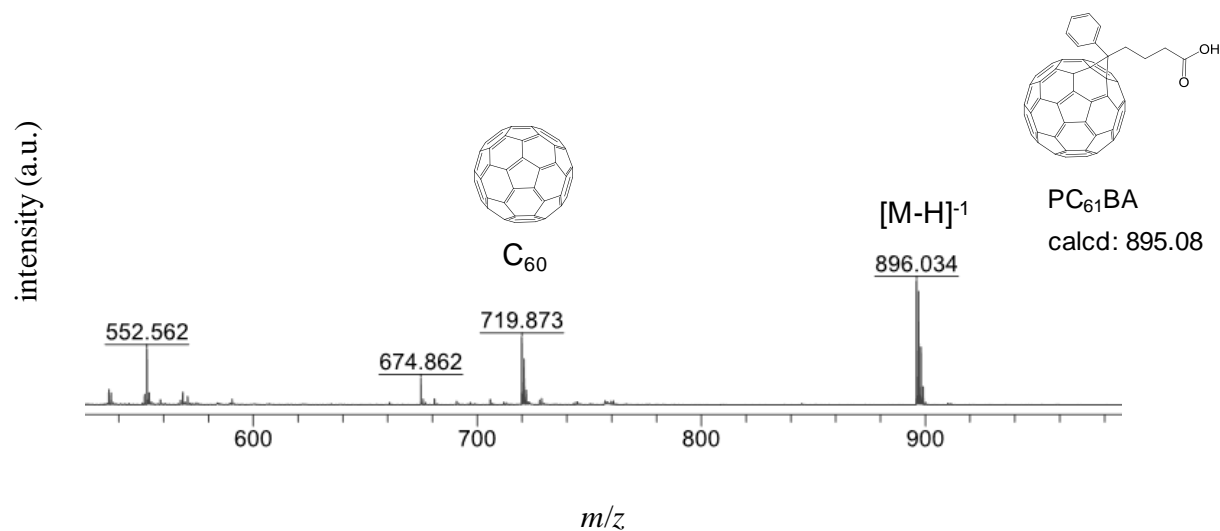
Figure 5.6d shows IR spectrum of the obtained product. The characteristic absorption band of the C=O stretching of the carbonyl chloride at  $1793\text{ cm}^{-1}$  completely disappeared, while a relatively wide absorption band at  $1646\text{ cm}^{-1}$  appeared. This wide absorption band is assignable to the C=O of amide group because C=O stretching band of amide group is generally observed at lower wavenumbers region than that of regular C=O ( $\text{R}-\text{C}=\text{O}-\text{R}'$ ) due to delocalization of electrons as shown below (resonance effect).



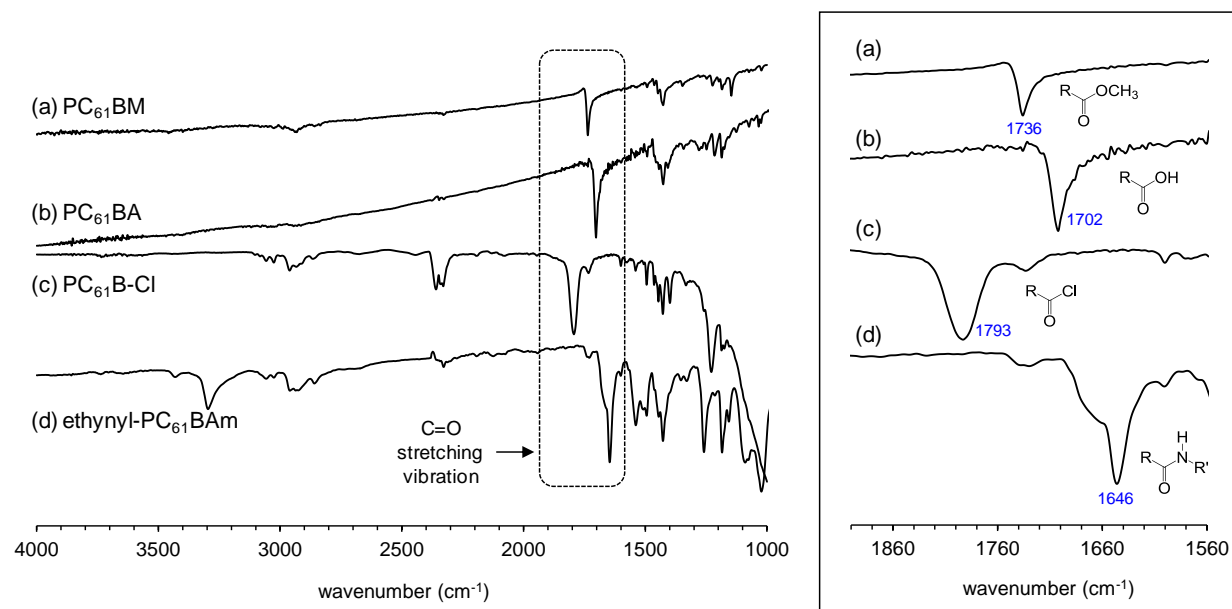
Here it should be noted that a small peak at  $1736\text{ cm}^{-1}$  derived from the C=O stretching of PC<sub>61</sub>BM was observed in the spectrum of the resulting product, indicating that negligible amount of PC<sub>61</sub>BM remained as an impurity in the product.

MALDI-TOF MS measurement provides further evidence for the chemical structure of the product as shown Figure 5.8. The most intense peak at  $m/z$  932.9 was assigned to the molecular ion peak  $[\text{M}-\text{H}]^-$ . Another peak at  $m/z$  719.7 was assigned to  $\text{C}_{60}^-$  which is presumably due to a fragmentation of the product or an impurity contaminated from the beginning in the starting material.

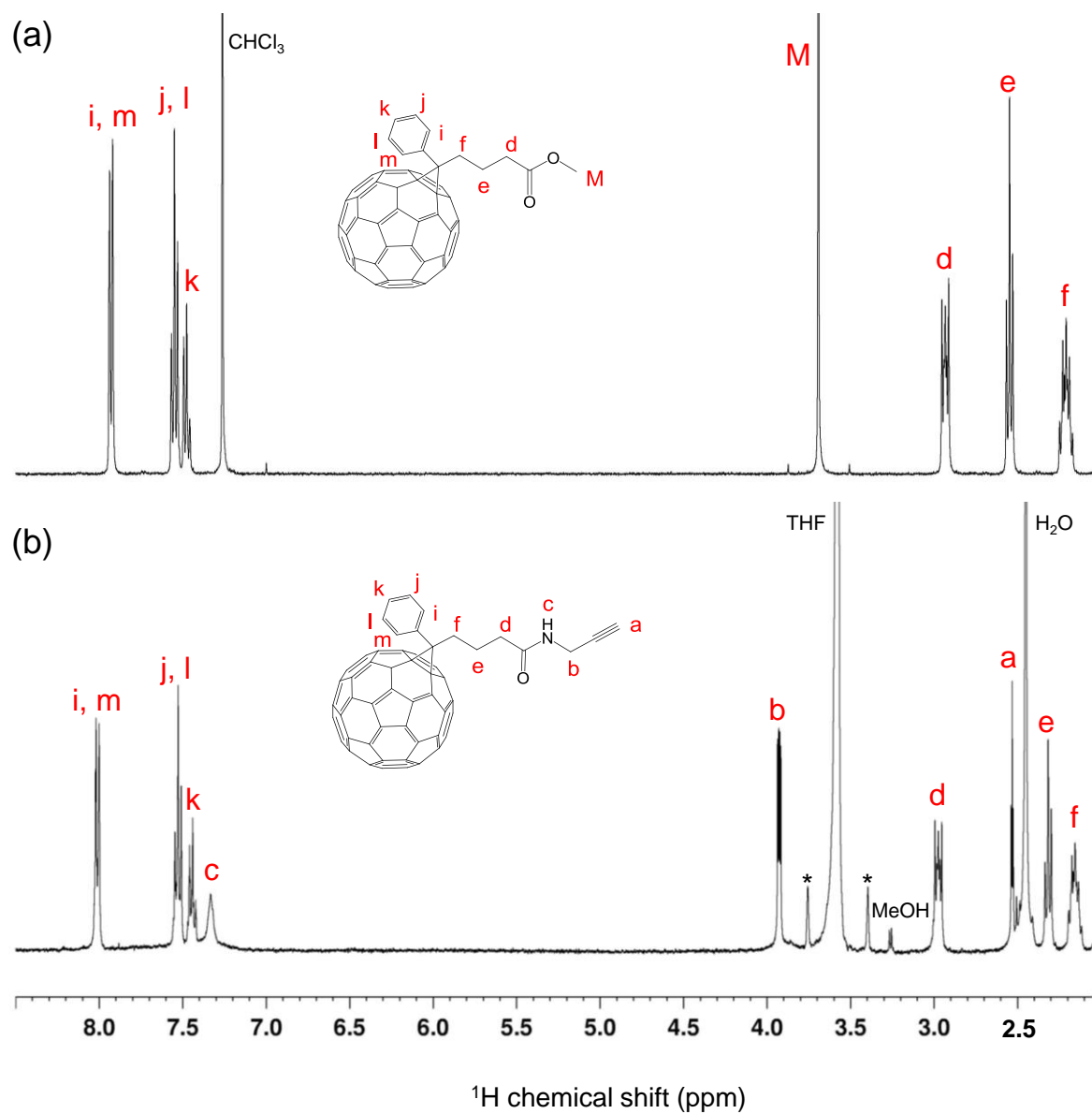
All of these results clearly indicate that the ethynyl group was quantitatively introduced to the fullerene derivatives.



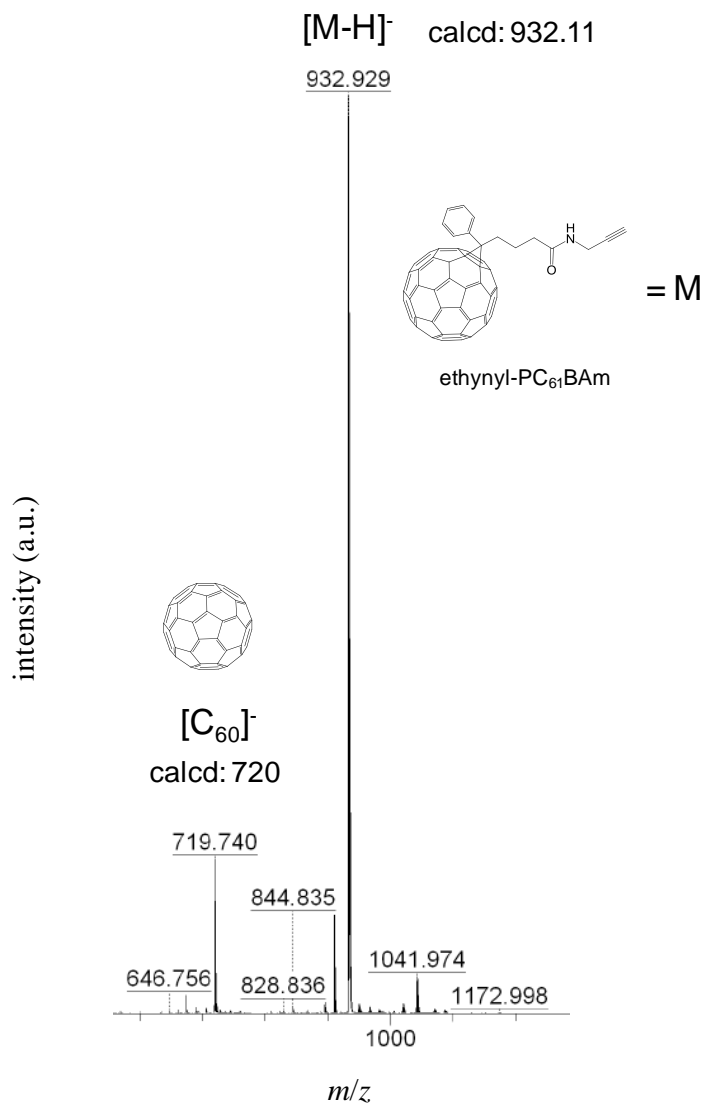
**Figure 5.5.** MALDI-TOF MS spectrum of PC<sub>61</sub>BA in the negative mode.



**Figure 5.6** FT-IR spectra of (a) PC<sub>61</sub>BM, (b) PC<sub>61</sub>BA, (c) PC<sub>61</sub>B-Cl, and (d) ethynyl-PC<sub>61</sub>BAm.

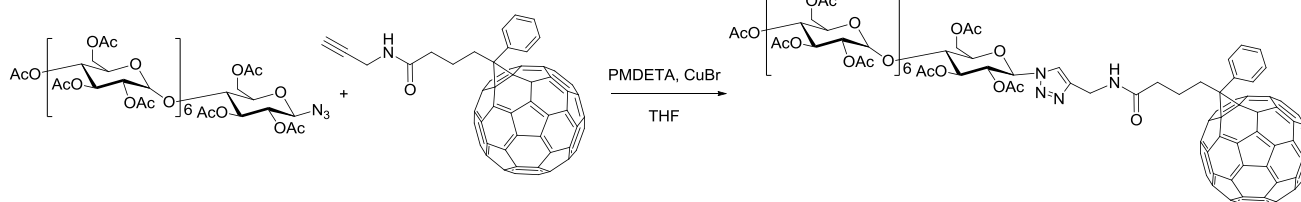


**Figure 5.7**  $^1\text{H}$  NMR spectrum of (a)  $\text{PC}_{61}\text{BM}$  in  $\text{CDCl}_3$  and (b) ethynyl- $\text{PC}_{61}\text{BAm}$  in  $\text{THF}-d_8$ .



**Figure 5.8** MALDI-TOF MS spectrum of ethynyl-PC<sub>61</sub>BAm in negative mode.

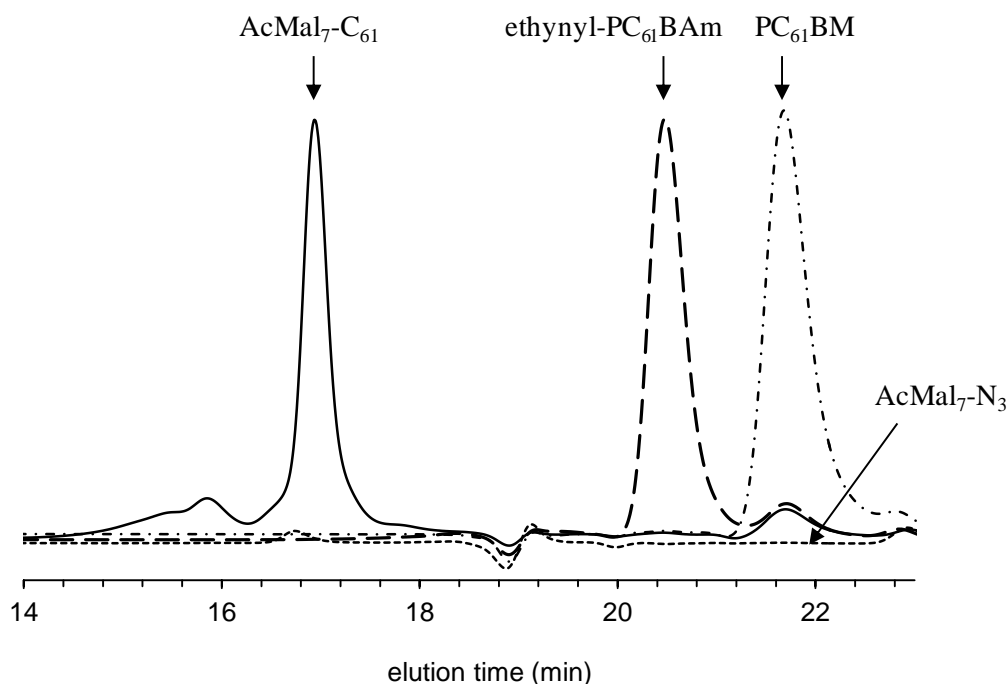
### V.3.2 Synthesis of fullerene-conjugated AcMal<sub>7</sub> (AcMal<sub>7</sub>-C<sub>61</sub>)



**Scheme 5.2** Synthesis of fullerene-conjugated AcMal<sub>7</sub>.

Finally, “click” reaction between “clickable” ethynyl-PC<sub>61</sub>BAM and previously synthesized AcMal<sub>7</sub>-N<sub>3</sub> (see chapter II.4.2) was carried out in THF (Scheme 5.2). To avoid a complex removal process of unreacted raw materials, a stoichiometric amount of AcMal<sub>7</sub>-N<sub>3</sub> was added to ethynyl-PC<sub>61</sub>BAM (1 equiv.). Reaction progress was monitored by FT-IR and SEC. After confirming the complete consumption of the AcMal<sub>7</sub>-N<sub>3</sub>, the crude product was purified by passing through a neutral alumina column and precipitated into cold methanol to afford the product as a brown solid with 58 % yield. The resultant product was well soluble in THF, CHCl<sub>3</sub>, *o*-DCB, and acetone and slightly soluble in toluene. The product was characterized by <sup>1</sup>H NMR, FT-IR, SEC, and MALDI-TOF MS spectrometry.

Figure 5.9 shows SEC traces of the resulting product and raw materials recorded using UV detector. The SEC trace of the product exhibits a clear shift to higher molecular weight region as compared to the starting material: ethynyl-PC<sub>61</sub>BAM. Here, it should be noted that no peak was observed in the SEC trace of AcMal<sub>7</sub> by UV detection, whereas an elution peak was observed at a retention time of 16.85 min by RI detection (data not shown). This is because AcMal<sub>7</sub> does not absorb UV light at the wavelength used for this analysis ( $\lambda = 257$  nm). By contrast, the SEC trace of the obtained product by UV detection showed an elution peak at 16.93 min, which is a clear evidence of successful functionalization of AcMal<sub>7</sub> with UV-detectable fullerene derivative.



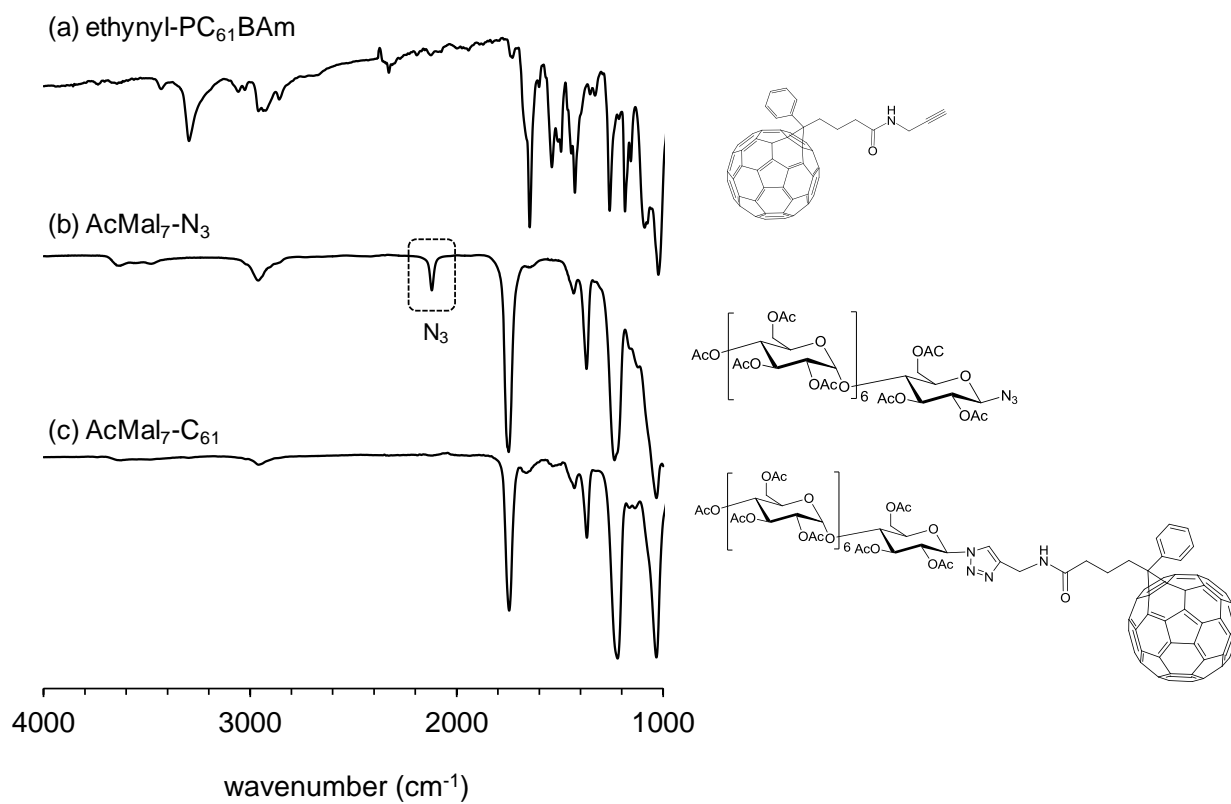
**Figure 5.9** SEC traces of PC<sub>61</sub>BM (alternate long and short dashed line), ethynyl-PC<sub>61</sub>BAm (dashed line), AcMal<sub>7</sub>-N<sub>3</sub> (dotted line), and AcMal<sub>7</sub>-C<sub>61</sub> (solid line) recorded by UV detector.

The FT-IR spectrum of the product clearly shows a complete consumption of azide groups of the AcMal<sub>7</sub>-N<sub>3</sub> as the diagnostic peak of the azide group is absent at 2100 cm<sup>-1</sup> (Figure 5.10c).

Figure 5.11 shows MALDI-TOF MS spectrum of the resulting product performed in negative mode. Good agreement between theoretical and experimental molecular weight was obtained. The most intense peak at  $m/z$  3059.7 was assigned to the target molecule with sodium ion [M+Na]<sup>+</sup>.

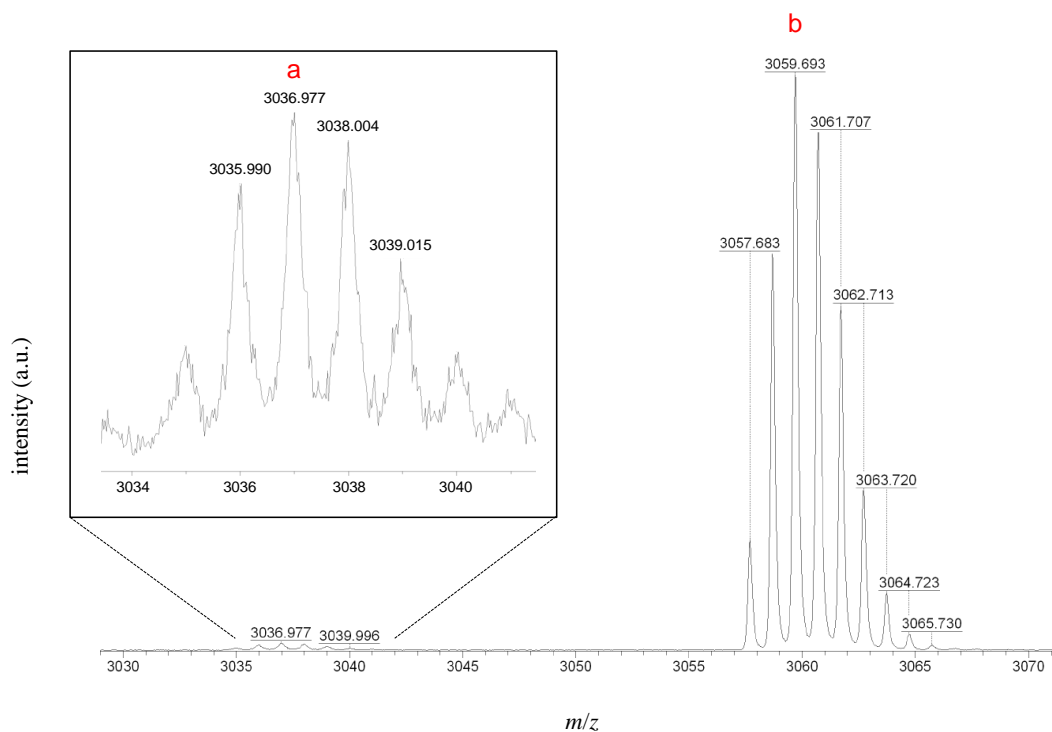
The successful formation of the AcMal<sub>7</sub>-C<sub>61</sub> was elucidated by <sup>1</sup>H DOSY NMR experiment (Figure 5.12). <sup>1</sup>H DOSY NMR spectra of the product displays a unique population related to the proton resonances of AcMAL<sub>7</sub> and PC<sub>61</sub>BAm, indicating that both substances are covalently linked. The diffusion coefficient of the product:  $D = 3.2 \times 10^{-10}$  m<sup>2</sup>/s is slightly smaller than that of AcMal<sub>7</sub>-N<sub>3</sub> ( $3.9 \times 10^{-10}$  m<sup>2</sup>/s) and remarkably smaller than that of ethynyl-PC<sub>61</sub>BAm ( $2.0 \times 10^{-9}$  m<sup>2</sup>/s). These values showed a good correlation with a molecular weight of each compound.

On the basis of all the data, the obtained product was identified as the targeted AcMal<sub>7</sub>-C<sub>61</sub>.



**Figure 5.10** FT-IR spectra of (a) ethynyl-PC<sub>61</sub>BAm, (b) AcMal<sub>7</sub>-N<sub>3</sub>, and (c) AcMal<sub>7</sub>-C<sub>61</sub>.



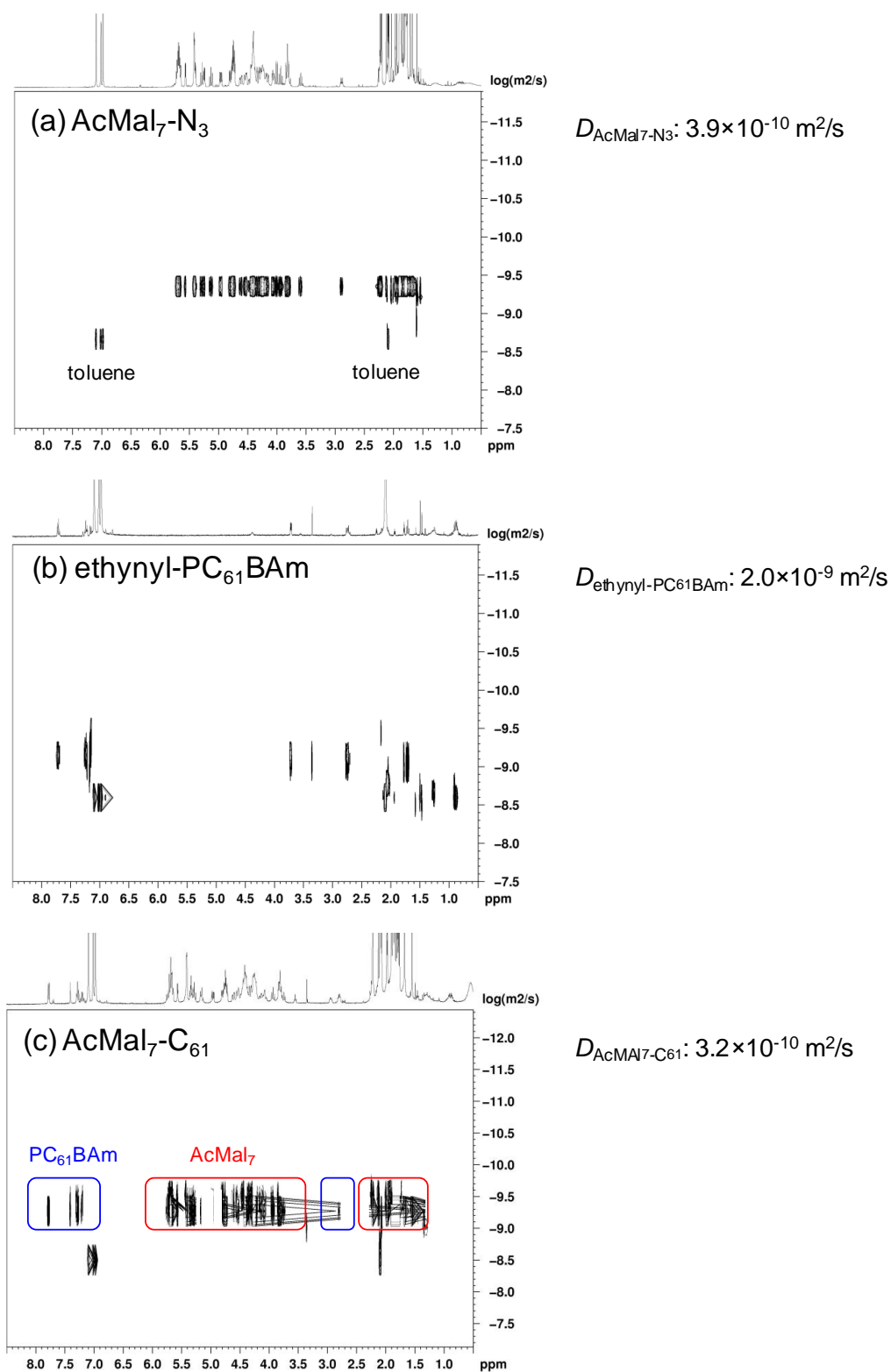


**Figure 5.11** MALDI-TOF MS spectrum of AcMal<sub>7</sub>-C<sub>61</sub> in positive mode.

**Table 5.1** Structural assignments of peaks observed in MALDI-TOF MS spectrum of AcMal<sub>7</sub>-C<sub>61</sub>

peak code <sup>a</sup>	structure	added ion	mass ( <i>m/z</i> )	
			calculated	observed
a		H <sup>+</sup>	3036.75	3036.98
b		Na <sup>+</sup>	3058.73	3059.69

<sup>a</sup> Peak codes are shown in Figure 5.11.



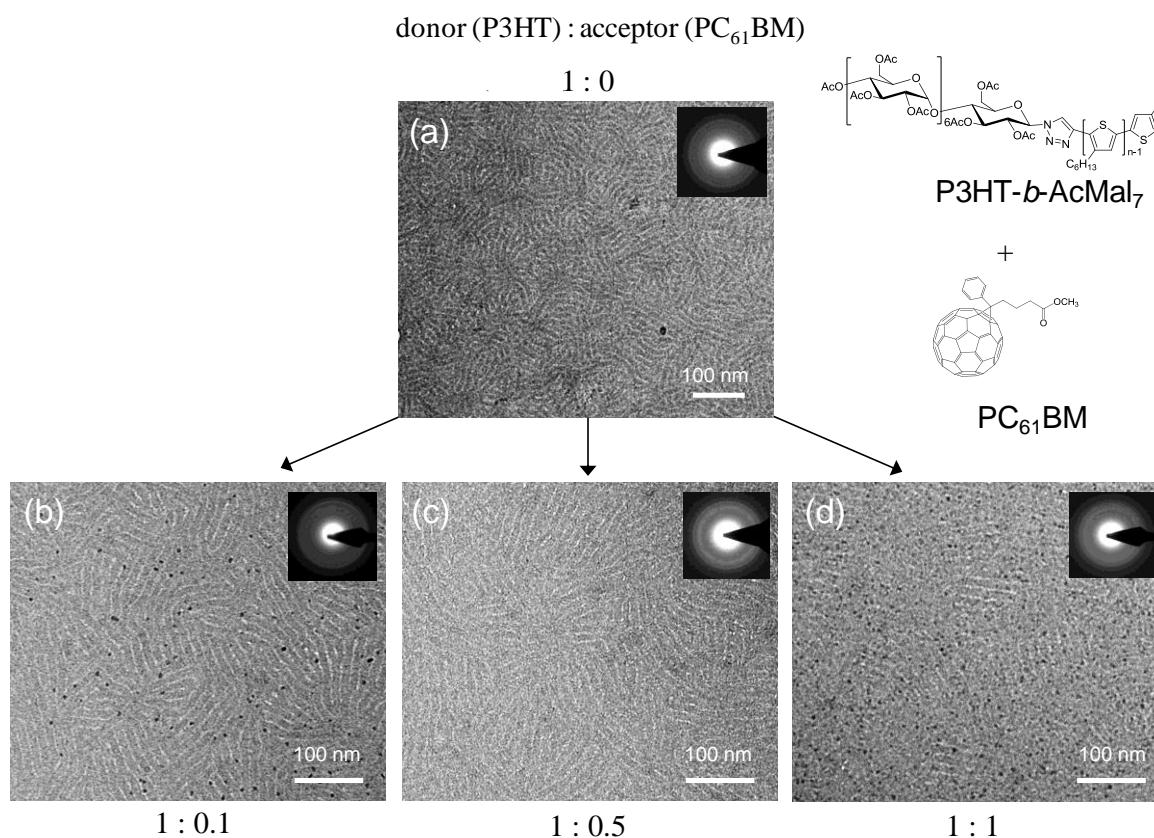
**Figure 5.12**  $^1\text{H}$ -DOSY spectrum of (a) AcMal<sub>7</sub>-N<sub>3</sub>, (b) ethynyl-PC<sub>61</sub>BAm, and (c) AcMal<sub>7</sub>-C<sub>61</sub> (solvent: toluene-*d*<sub>8</sub>).

### V.3.3 Morphologies of the blend of P3HT-*b*-AcMal<sub>7</sub>:AcMal<sub>7</sub>-C<sub>61</sub>

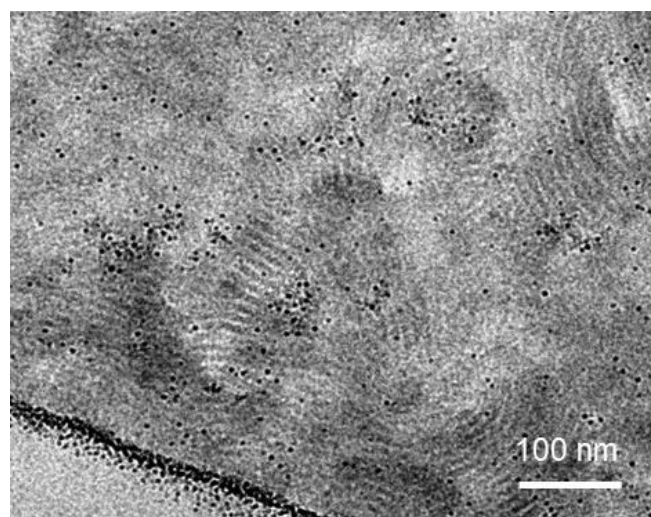
This section describes the morphological investigation of the microstructure of the blend film of synthesized P3HT-*b*-AcMal<sub>7</sub> and AcMal<sub>7</sub>-C<sub>61</sub>.

As a comparative experiment, the morphology of the blend film of P3HT<sub>P3</sub>-*b*-AcMal<sub>7</sub>:PC<sub>61</sub>BM were examined by TEM. The thin films on copper grid were prepared by spin coating from the mix solution of P3HT<sub>P3</sub>-*b*-AcMal<sub>7</sub> and PC<sub>61</sub>BM in chloroform. A weight ratio of donor: acceptor (*i.e.* proportion of total amount of P3HT segment in the P3HT<sub>P3</sub>-*b*-AcMal<sub>7</sub> to PC<sub>61</sub>BM by weight) was varied from 1:0.1 to 1:1. These blended films were subsequently annealed at 210 °C for 10 min to induce the microphase separation.

TEM images of the non-blended single block copolymer film and the blend films with various donor:acceptor ratio are presented in Figure 5.13. Well-defined lamellar pattern attributable to the self-organization of the P3HT-*b*-AcMal<sub>7</sub> was visible in all the images. PC<sub>61</sub>BM molecule (or PC<sub>61</sub>BM cluster) observed as small black spots did not show obvious aggregates or crystal structure in the blend film. Hence, it was found that PC<sub>61</sub>BM was well incorporated to the phase-segregated P3HT-*b*-AcMal<sub>7</sub> film without destroying a lamellar structure up to a blend ratio of P3HT:PC<sub>61</sub>BM = 1:1 (wt:wt) (beyond this ratio needs to be tested). However, an important point to be emphasized here is that there is no restraining factor to control the localization of PC<sub>61</sub>BM for this blend system. PC<sub>61</sub>BM was found in the both P3HT and AcMal<sub>7</sub> domains. A similar behavior was observed by internal observation of the blend film. Figure 5.14 shows TEM image of the cross section of thermally annealed P3HT<sub>P3</sub>-*b*-AcMal<sub>7</sub>:PC<sub>61</sub>BM blend film in the vicinity of the interface of the film and PTFE substrate (see procedure of cross section preparation, chapter VI.2.2). No preferential localization of PC<sub>61</sub>BM was observed except for the film/substrate interface. It is clear that PC<sub>61</sub>BM spontaneously migrated to the hydrophobic surface of the PTFE substrate in the course of thermal annealing.



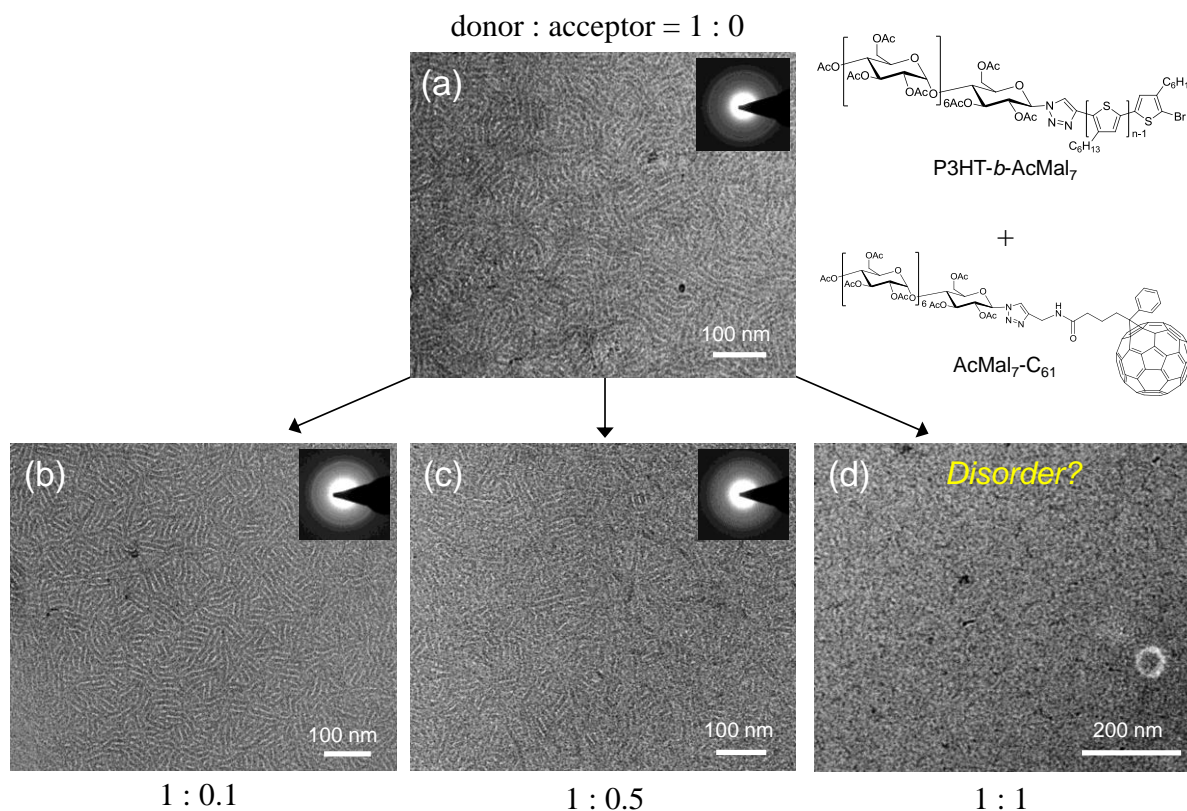
**Figure 5.13** TEM images of thermally annealed thin films of (a) P3HT<sub>P3</sub>-*b*-AcMal<sub>7</sub> and the blend of P3HT<sub>P3</sub>-*b*-AcMal<sub>7</sub> and PC<sub>61</sub>BM with donor: acceptor ratio of (b) 1:0.1, (c) 1:0.5 and (d) 1:1 (annealing condition: 210 °C for 10 min).



**Figure 5.14** TEM images of the cross section of thermally annealed P3HT<sub>P3</sub>-*b*-AcMal<sub>7</sub>: PC<sub>61</sub>BM blend film (1:1) (annealing condition: 220 °C for 10 min) at the interface of PTFE substrate/film.

The morphology of the blend film consisting of the P3HT<sub>P3</sub>-*b*-AcMal<sub>7</sub> and newly synthesized AcMal<sub>7</sub>-C<sub>61</sub> was investigated. A donor:acceptor weight ratio was calculated based on the total amount of P3HT moiety in the block copolymer with respect to that of acceptor moiety in the AcMal<sub>7</sub>-C<sub>61</sub>.

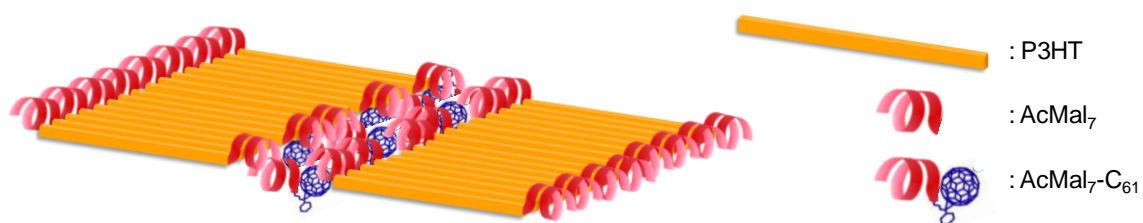
TEM images of the P3HT<sub>P3</sub>-*b*-AcMal<sub>7</sub>:AcMal<sub>7</sub>-C<sub>61</sub> blend films annealed at 210 °C for 10 min are presented in Figure 5.15. TEM observation showed different morphologies of the films with the blending ratio changed. At low loading ratio of AcMal<sub>7</sub>-C<sub>61</sub> (donor: acceptor = 1:0.1), the blend film (Figure 5.15b) exhibited well-defined periodic lamellar structure almost identical to that of P3HT<sub>P3</sub>-*b*-AcMal<sub>7</sub> single film (Figure 5.15a), indicating that the addition of the AcMal<sub>7</sub>-C<sub>61</sub> at



**Figure 5.15** TEM images of thermally annealed thin films of (a) P3HT<sub>P3</sub>-*b*-AcMal<sub>7</sub> and the blend of P3HT<sub>P3</sub>-*b*-AcMal<sub>7</sub> and AcMal<sub>7</sub>-C<sub>61</sub> with donor: acceptor ratio of (b) 1:0.1, (c) 1:0.5 and (d) 1:1 (annealing condition: 210 °C for 10 min).

low concentration did not disturb P3HT crystallization. Electron diffraction diagram inserted in Figure 5.15b also supports this finding by showing a sharp reflection corresponding to the  $\pi$ -stacking of the P3HT crystal with the stacking period of *ca.* 0.38 Å. Upon increasing the loading ratio up to 1:0.5, the reflection pattern became less intense while TEM image showed still definite lamellar structure (Figure 5.15c). At a blending ratio of donor:acceptor = 1:1, this system probably reached order-disorder transition as the blend film showed no trace of ordered structure (Figure 5.15d). Accordingly, no distinctive reflective pattern was observed by electron diffraction.

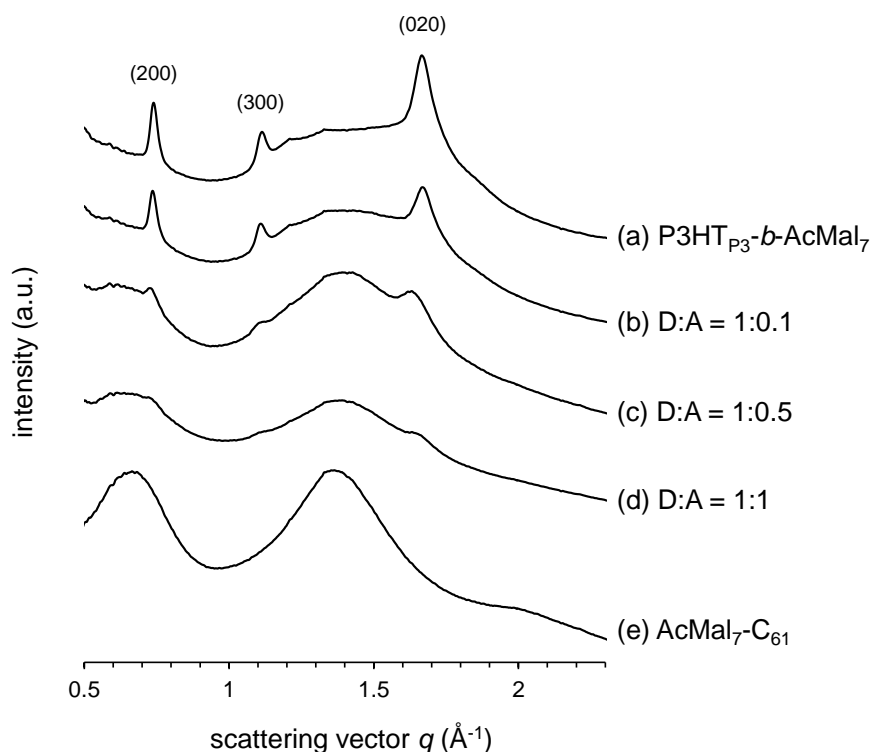
Unfortunately the present experiments did not provide the location of AcMal<sub>7</sub>-C<sub>61</sub>. However we expect that AcMal<sub>7</sub>-C<sub>61</sub> are incorporated in the AcMal<sub>7</sub> domain so that terminal fullerenes are aligned along the domain boundary of P3HT and AcMal<sub>7</sub> segments as depicted in Figure 5.16, in the case where the lamellar structure is maintained at low loading ratio of AcMal<sub>7</sub>-C<sub>61</sub>.



**Figure 5.16** Schematic representation of nanostructure of the blend film of P3HT-*b*-AcMal<sub>7</sub> and AcMal<sub>7</sub>-C<sub>61</sub>.

To obtain further information about the microscopic distribution of AcMal<sub>7</sub>-C<sub>61</sub> and crystal state of P3HT, structural analysis of the blend films was carried out by means of WAXS measurement. Figure 5.17 shows WAXS profiles of the thermally annealed bulk samples of the blend of P3HT-*b*-AcMal<sub>7</sub>:AcMal<sub>7</sub>-C<sub>61</sub> with different blending ratio and that of single substances, *i.e.* P3HT-*b*-AcMal<sub>7</sub> and AcMal<sub>7</sub>-C<sub>61</sub>. For all blend samples, (*h*00) and (020) peaks related to the P3HT crystalline structure are visible while their intensities decrease with increasing acceptor ratio. It indicates that addition of AcMal<sub>7</sub>-C<sub>61</sub> disturbs P3HT crystal structure to some extent but not completely. Note that a broad amorphous halo centered at 5.5 nm was observed in the WAXS

profile of the AcMal<sub>7</sub>-C<sub>61</sub> due to the short range order of molecular arrangement of AcMal<sub>7</sub>-C<sub>61</sub> (5.5 nm is nearly equal to the molecular size of AcMal<sub>7</sub>-C<sub>61</sub> (5.4 nm) estimated from the molecular length of AcMal<sub>7</sub> (3.9 nm), triazole+CH<sub>2</sub> linker (0.5 nm) and PCBM (1 nm)<sup>9</sup>). Therefore, the WAXS profiles of the blend samples are surely superimposed on the broad amorphous halo; as a consequence, characteristic reflection peaks of the P3HT crystal structure might be hidden.



**Figure 5.17** WAXS profiles of the thermally annealed bulk samples of the single substance of (a) P3HT<sub>P3</sub>-*b*-AcMal<sub>7</sub> and (e) AcMal<sub>7</sub>-C<sub>61</sub>, and the thermally annealed bulk samples of the blend of P3HT-*b*-AcMal<sub>7</sub> and AcMal<sub>7</sub>-C<sub>61</sub> with donor:acceptor ratio of (b) 1:0.1, (c) 1:0.5, and (d) 1:1 (Annealing condition: 210 °C for 10 min).

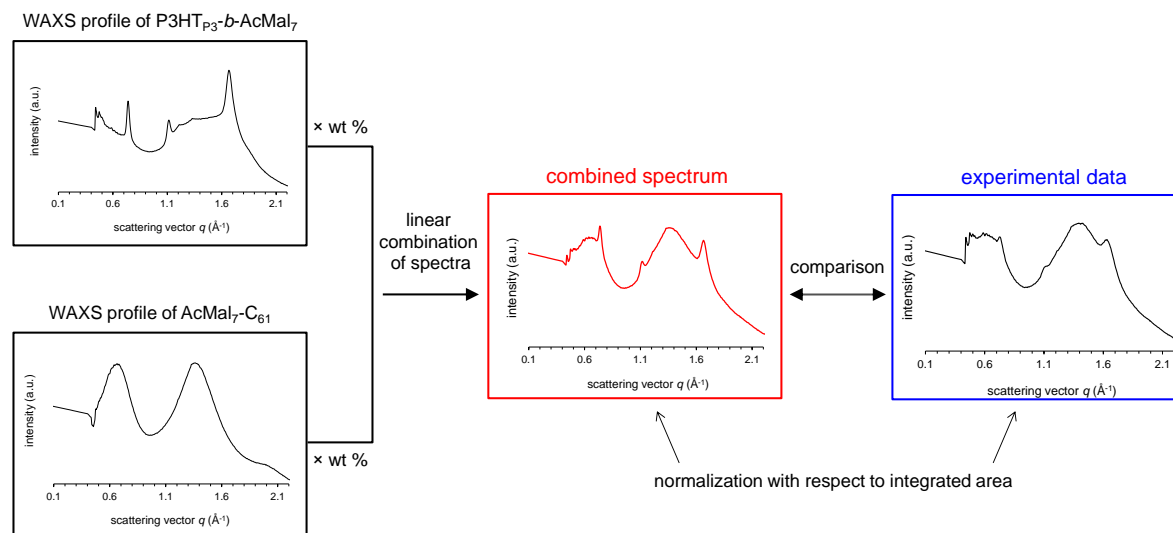
If the addition of AcMal<sub>7</sub>-C<sub>61</sub> does not affect the crystal structure of P3HT segment in the blend film, the scattering intensity should be expressed by a linear combination of two reference WAXS profiles of single substances (P3HT-*b*-AcMal<sub>7</sub> and AcMal<sub>7</sub>-C<sub>61</sub>) as illustrated in Figure 5.18. For a weight fraction of P3HT-*b*-AcMal<sub>7</sub>,  $\alpha$  in the blend system, the expected scattering intensity,  $I_{cal}$  is given as:

$$I_{cal} = \alpha I_{donor} + (1 - \alpha) I_{acceptor}$$

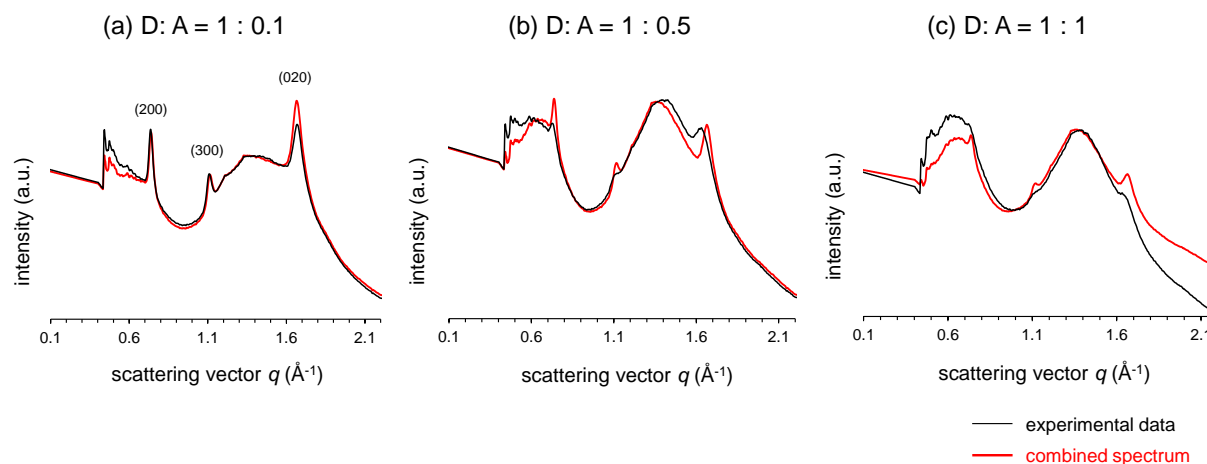
where  $I_{donor}$  and  $I_{acceptor}$  are scattering intensities of P3HT-*b*-AcMal<sub>7</sub> and AcMal<sub>7</sub>-C<sub>61</sub>, respectively.

The normalized both spectra were presented in Figure 5.19. At low loading ratio of donor: acceptor = 1:0.1, experimental profile shows almost same figure as combined one expect for the intensity of (020) peak. At higher ratio, all the peaks of (*h*00) and (020) broadened and shifted to a small angle region, indicating that intermolecular distance corresponding to the hexyl side chain and P3HT backbone ( $\pi$ -stacking period) were gradually separated with increasing loading ratio. Hence, it was revealed that the absence of intense peaks related to the P3HT crystal structure in the experimental data is attributable not only to superposition of the scattering pattern of AcMal<sub>7</sub>-C<sub>61</sub> but also to intrinsic structural change of the P3HT domain. This structural change might be direct consequence of the addition of the voluminous AcMal<sub>7</sub>-C<sub>61</sub> molecules to the existing well-packed lamellar structure. Therefore, for addressing this problem, certain actions such as addition of P3HT homopolymer and optimization the blend ratio are indispensable.





**Figure 5.18** Methodology used for evaluation of the mixed state of P3HT-*b*-AcMal<sub>7</sub> and AcMal<sub>7</sub>-C<sub>61</sub>.



**Figure 5.19** WAXS profiles (black) and combined spectra (red) of the thermally annealed samples of the blend of P3HT-*b*-AcMal<sub>7</sub> and AcMal<sub>7</sub>-C<sub>61</sub> with donor/acceptor ratio of (a) 1/0.1, (b) 1/0.5, and (c) 1/1 (Annealing condition: 210 °C for 10 min). The combined spectra were normalized with respect to integrated area of corresponding WAXS profiles.

## V.4 Conclusion

The selective elimination of the oligosaccharide block from phase-separated films has been investigated via two approaches; (i) dry etching and (ii) wet etching.

In the first strategy, plasma etchings were carried out using either oxygen or air as etchant gas. Although several parameters were varied to find the appropriate etching conditions, no significant etching selectivity between P3HT and AcMal<sub>7</sub> was obtained.

In the second strategy, the concentrated sulfuric acid was successfully employed on the fabrication of nanopatterned P3HT films. The concentrated sulfuric acid showed highly selective decomposition of AcMal<sub>7</sub> block via dehydration and carbonization of oligosaccharides without affecting the preexisting lamellae structure as proven by TEM observation. The resultant void consisting of carbon skeleton is expected to have a good affinity with typical electron acceptor compounds, such as [6,6]-phenyl-C<sub>61</sub>-butyric acid methyl ester (PC<sub>61</sub>BM) and indene-C<sub>60</sub> bisadduct (ICBA), because the basic structures of those materials are also entirely composed of carbon.

The fullerene attached AcMal<sub>7</sub> (AcMal<sub>7</sub>-C<sub>61</sub>) was successfully synthesized via CuAAC "click" reaction of alkyne-functionalized fullerene and azido-functionalized AcMal<sub>7</sub> for the purpose of location control of acceptor materials in the nano-patterned donor/acceptor blend films. A preliminary morphological investigation on the blend films made of the P3HT-*b*-AcMal<sub>7</sub> (electron-donating compound) and AcMal<sub>7</sub>-C<sub>61</sub> (electron-accepting compound) suggested that the AcMal<sub>7</sub>-C<sub>61</sub> molecules are incorporated in the phase-separated AcMal<sub>7</sub> domain so that terminal fullerenes are aligned along the domain boundary of P3HT and AcMal<sub>7</sub> segments, leading to the prevent of segregation of acceptor compound upon heating. The phase-separated lamellar and P3HT crystal structures were maintained up to the blending ratio of donor:acceptor = 1:0.5.

## V.5 References

- (1) Yasuda, T. *Text. Res. J.* **1992**, 62, 474–480.
- (2) Kim, D.; Nishiyama, Y.; Wada, M.; Kuga, S. *Cellulose* **2001**, 8 (1), 29–33.
- (3) Lin, Y.; Lim, J. A.; Wei, Q.; Mannsfeld, S. C. B.; Briseno, A. L.; Watkins, J. J. *Chem. Mater.* **2012**, 24 (3), 622–632.
- (4) Stalmach, U.; Boer, B. De; Videlot, C.; Hutten, P. F. Van; Hadziioannou, G. *J. Am. Chem. Soc.* **2000**, 122 (23), 5464–5472.
- (5) Laiho; Ras, R. H. A.; Valkama, S.; Ruokolainen, J.; Österbacka, R.; Ikkala, O. *Macromolecules* **2006**, 39 (22), 7648–7653.
- (6) Knight, B. W.; Wudl, F. *J. Org. Chem* **1995**, 60 (21), 532–538.
- (7) Wei, Q.; Nishizawa, T.; Tajima, K.; Hashimoto, K. *Adv. Mater.* **2008**, 20 (11), 2211–2216.
- (8) Miyanishi, S.; Zhang, Y.; Hashimoto, K.; Tajima, K. *Macromolecules* **2012**, 45 (16), 6424–6437.
- (9) Paternò, G.; Warren, A. J.; Spencer, J.; Evans, G.; Sakai, V. G.; Blumberger, J.; Cacialli, F. *J. Mater. Chem. C* **2013**, 1 (36), 5619.

## **CHAPTER VI:**

### **EXPERIMENTAL SECTION**

## VI.1 Synthesis

### VI.1.1 Materials

Maltoheptaose was purchased from Hayashibara Biochemical Laboratories, Inc., Japan, and used as received. (6,6)-phenyl C<sub>61</sub> butyric acid methyl ester (PC<sub>61</sub>BM) is gift from PCAS, and used as received. All other reagents were purchased from Sigma-Aldrich Chemicals Co. Tetrahydrofuran (THF), *o*-dichlorobenzene (*o*-DCB), *tert*-butylmagnesium chloride (2.0 M in diethyl ether), [1,2-bis(diphenylphosphino)propane] dichloronickel(II) (Ni(dppp)Cl<sub>2</sub>), ethynylmagnesium bromide (0.5 M in THF), tris(dibenzylideneacetone)dipalladium(0) (Pd<sub>2</sub>(dba)<sub>3</sub>), bis(tri-*tert*-butylphosphine)palladium(0) (Pd(P(*t*-Bu)<sub>3</sub>)<sub>2</sub>), ethynyltributylstannaane, magnesium turnings, iodine, (5-chloro-1-pentynyl) trimethylsilane, tetrabutylammonium fluoride trihydrate (TBAF·3H<sub>2</sub>O), 2-bromoethylamine hydrobromide, sodium azide (NaN<sub>3</sub>), 2-chloro-1,3-dimethylimidazoliumchloride (DMC), *N,N*-diisopropylethylamine (DIPEA), 4-(dimethylamino)pyridine (DMAP), acetic anhydride, pyridine, *N,N,N',N'',N''*-pentamethyldiethylenetriamine (PMDETA) and copper (I) bromide (CuBr), hydrochloric acid (HCl), thionyl chloride (SOCl<sub>2</sub>), propargylamine, sodium hydroxide (NaOH), sodium chloride (NaCl), sodium sulfate anhydrous (Na<sub>2</sub>SO<sub>4</sub>) were used as received. Lithium chloride (LiCl) was dried *in vacuo* at 140 °C before use. 2, 5-Dibromo-3-hexylthiophene, 1-hexene, and triethylamine were stirred overnight over CaH<sub>2</sub> and distilled prior to use.

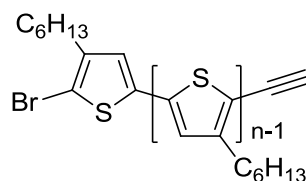
### VI.1.2 Instruments

<sup>1</sup>H and <sup>13</sup>C NMR spectra were recorded using a Bruker Avance DRX 400 MHz spectrometer operating at a frequency of 400.13 MHz for <sup>1</sup>H and 100.62 MHz for <sup>13</sup>C. The two-dimensional NMR (2D-NMR) experiments, including Heteronuclear single-quantum correlation (HSQC) spectroscopy, Heteronuclear multiple-bond correlation (HMBC) spectroscopy and Diffusion ordered spectroscopy (DOSY) were performed with a 3267.91 Hz spectral width, 1024 data points, 0.155s acquisition time, 1 s relaxation delay. Solid-state <sup>13</sup>C NMR experiments were performed with a Bruker Avance DSX 400 MHz spectrometer operating at 100.62 MHz, using the combination of cross-polarization (CP), high-power proton decoupling and magic angle spinning (MAS) method. The spinning speed was set at 12 Hz, sweep width 29761 Hz, and recycle delay 2s. The spectra were averaged over 23000 scans. The <sup>13</sup>C chemical shifts were

calibrated with glycine carboxyl group (176.03 ppm). Infrared (IR) spectra were recorded using a Perkin-Elmer Spectrum RXI FTIR Spectrometer. Matrix assisted laser desorption ionization mass spectrometry (MALDI-TOF MS) measurements were performed on a Bruker Daltonics Autoflex apparatus using dithranol as the matrix. Size Exclusion Chromatography (SEC) was performed at 30 °C using a Agilent 390-MDS system (290-LC pump injector, ProStar 510 column oven, 390-MDS refractive index detector) equipped with Knauer Smartline UV detector 2500 and two Agilent PLgel 5 $\mu$ m MIXED-D 300 \* 7.5 mm columns (Part No: PL1110-6504) in THF at the flow rate of 1.0 ml/min.

### VI.1.3 Synthesis of P3HT-*b*-oligosaccharide block copolymers

#### Synthesis of ethynyl-P3HT



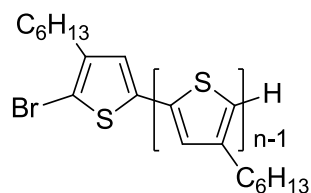
#### Method 1: *in situ* end-functionalization via GRIM polymerization

Ethynyl-terminated poly (3-hexylthiophene) (ethynyl-P3HT) was prepared by a modified Grignard metathesis (GRIM) method described in the literature<sup>1</sup> under an argon atmosphere using oven-dried glassware. THF was refluxed and distilled from sodium benzophenone ketyl prior to use. In a dry 100 ml Schlenk flask, LiCl (0.83 g, 19.4 mmol, 26 equiv.) was introduced and dissolved in freshly distilled dry THF (37 ml). The solution was stirred under argon at room temperature until LiCl was completely dissolved. Then 2, 5-dibromo-3-hexylthiophene (4 ml, 18.7 mmol, 25 equiv.) and *tert*-butylmagnesium chloride (9 ml, 18.0 mmol, 24 equiv.) were transferred to the flask via syringe under an argon atmosphere and stirred at room temperature overnight in order to complete the metal-halogen exchange reaction. In another dry 500 ml Schlenk flask, Ni (dppp) Cl<sub>2</sub> (0.39 g, 0.8 mmol, 1 equiv.) was added and flame dried, and then 145 ml of dry THF was added. The activated Grignard monomer solution was transferred into a 500 ml Schlenk flask using a cannula and stirred for 30 min at room temperature, and then cooled

to 0 °C. 1-Hexene (94 ml, 752 mmol, 1008 equiv.) was added to the reaction mixture before the termination step according to a previous report<sup>2</sup> in order to obtain the monofunctional polymer. The termination reaction and functionalization were carried out in a one-shot addition of ethynylmagnesium bromide (15 ml, 7.5 mmol, 10 equiv.). The mixture was stirred for 3 min and then poured into cold MeOH for quenching. The precipitate was re-dissolved in THF and the insoluble solid was removed by filter paper. The filtrate was recovered from successive precipitations in cold methanol, dried under reduced pressure to afford ethynyl-P3HT as a purple solid (2.11 g, 68%). <sup>1</sup>H NMR (400 MHz, CDCl<sub>3</sub>):  $\delta$  (ppm): 7.06-6.80 (m, 1H, aromatic), 3.53 (s, -C $\equiv$ C-H), 2.90-2.48 (m, 2H,  $\alpha$ -CH<sub>2</sub>), 1.71 (m, 2H,  $\beta$ -CH<sub>2</sub>), 1.54-1.15 (m, 6H, -CH<sub>2</sub>-CH<sub>2</sub>-CH<sub>2</sub>-CH<sub>3</sub>), 0.92 (br, 3H, -CH<sub>3</sub>). <sup>13</sup>C NMR (400 MHz, CDCl<sub>3</sub>):  $\delta$  (ppm): 140.06, 133.88, 130.66, 128.77, 31.85, 30.66, 29.62, 29.41, 22.81, 14.27. SEC:  $M_w$  = 5330 g/mol,  $M_n$  = 3490 g/mol, PDI = 1.35. FT-IR (CaF<sub>2</sub>): 3312 cm<sup>-1</sup> (H-C  $\equiv$  C) and 2096 cm<sup>-1</sup> (C  $\equiv$  C).

## Method 2: Post-polymerization functionalization

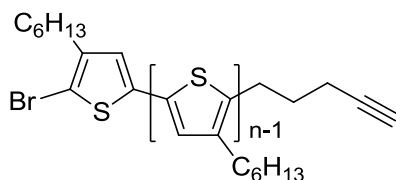
### (i) Synthesis of Br/H-terminated P3HT<sup>3</sup>



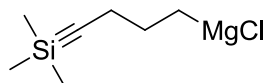
The Br/H-terminated P3HT was synthesized by the similar procedure as described above expect for the termination reaction and purification. To quench the reaction, 5N HCl was added to the reaction mixture at room temperature and the mixture was stirred for 30 min and then poured into cold methanol. The precipitate was fractionated by successive Soxhlet extraction by using MeOH, Hexane, and DCM in this order. DCM fraction was collected for subsequent reaction. After removal of the solvent, the product was re-solved in THF and precipitated into cold MeOH and dried under reduced pressure to afford Br/H-capped P3HT as a purple solid (yield: 59 %). <sup>1</sup>H NMR (400 MHz, CDCl<sub>3</sub>):  $\delta$  (ppm): 7.06-6.80 (m, 1H, aromatic), 2.83-2.48 (m, 2H,  $\alpha$ -CH<sub>2</sub>), 1.71 (m, 2H,  $\beta$ -CH<sub>2</sub>), 1.48-1.34 (m, 6H, -CH<sub>2</sub>-CH<sub>2</sub>-CH<sub>2</sub>-CH<sub>3</sub>), 0.92 (br, 3H, -CH<sub>3</sub>). SEC:  $M_w$  = 6652 g/mol,  $M_n$  = 6233 g/mol, PDI = 1.07.

**(ii) Synthesis of ethynyl-functionalized P3HT**

The Br/H-terminated P3HT (1.1 g,  $2.7 \times 10^{-4}$  mol, 1 equiv.),  $\text{Pd}_2(\text{dba})_3$  (15 mg,  $1.6 \times 10^{-5}$  mol, 0.06 equiv.), and  $\text{Pd}(\text{P}(\text{t-Bu})_3)_2$  (22 mg,  $4.2 \times 10^{-5}$  mol, 0.16 equiv.) were added to a flask and dissolved in dry THF (160 ml) under argon. Ethynyltributylstannaane (2.6 g,  $8.2 \times 10^{-3}$  mol, 31 equiv.) was added to the flask and the mixture was stirred at room temperature for 24 h under an argon atmosphere. The mixture was then precipitated into cold methanol to give mono-ethynyl-functionalized P3HT as a dark purple solid (yield: 62 %).  $^1\text{H}$  NMR (400 MHz,  $\text{CDCl}_3$ ):  $\delta$  (ppm): 7.05-6.85 (m, 1H, aromatic), 3.53 (s,  $-\text{C}\equiv\text{C}-\text{H}$ ), 2.84-2.50 (m, 2H,  $\alpha\text{-CH}_2$ ), 1.71 (m, 2H,  $\beta\text{-CH}_2$ ), 1.48-1.34 (m, 6H,  $-\text{CH}_2\text{-CH}_2\text{-CH}_2\text{-CH}_3$ ), 0.92 (br, 3H,  $-\text{CH}_3$ ). SEC:  $M_w = 6919$  g/mol,  $M_n = 6452$  g/mol, PDI = 1.07.

**Synthesis of pentynyl-P3HT**

Pentynyl-terminated poly (3-hexylthiophene) (pentynyl-P3HT) was synthesized via the following three steps described in the literature<sup>4</sup>:

**(i) Preparation of the Grignard reagent: (5-chloromagnesio-1-pentynyl) trimethylsilane**

Magnesium turnings (0.31 g, 13 mmol, 1.5 equiv.) and small piece of iodine were added to a dry 100 ml Schlenk flask equipped with a reflux condenser, and flame dried under vacuum and back-filled with dry argon. The 4.2 ml of dry THF was added to the flask via syringe and (5-chloro-1-pentynyl) trimethylsilane (1.5 ml, 8.4 mmol, 1 equiv.) was added dropwise. The mixture was stirred for 2 days under argon at 40 °C.



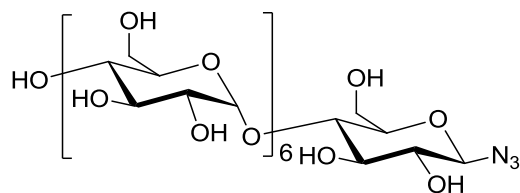
## (ii) Polymerization

The end-functionalized P3HT was synthesized by the same procedure as described above except for the Grignard reagent. (5-chloromagnesio-1-pentynyl) trimethylsilane was used for the termination reaction and functionalization.

## (iii) Deprotection of TMS group

The polymer protected with TMS group was dissolved in 60 ml of THF, and the solution was cooled to -20 °C. 0.2 M solution of TBAF·3H<sub>2</sub>O in THF (10 equiv. based on the chain end) was added dropwise and the mixture was stirred at -20 °C for 30 min and then at room temperature for 4 h. The mixture was passed through a short silica column to remove excess TBAF and then precipitated into cold MeOH. The polymer was collected via filtration and dried under vacuum at room temperature to afford pentynyl-P3HT as a dark purple solid (yield: 77%). <sup>1</sup>H NMR (400 MHz, CDCl<sub>3</sub>):  $\delta$  (ppm): 7.06-6.81 (m, 1H, aromatic), 3.75 (-C $\equiv$ C-H), 2.90-2.70 (m, 2H,  $\alpha$ -CH<sub>2</sub>), 2.59-2.51 (m, -CH<sub>2</sub>-C<sub>2</sub>H<sub>4</sub>-C $\equiv$ CH), 2.32-2.26 (m, -CH<sub>2</sub>-CH<sub>2</sub>-CH<sub>2</sub>-C $\equiv$ CH), 1.91-1.84 (m, -CH<sub>2</sub>-CH<sub>2</sub>-CH<sub>2</sub>-C $\equiv$ CH), 1.71 (m, 2H,  $\beta$ -CH<sub>2</sub>), 1.48-1.26 (m, 6H, -CH<sub>2</sub>-CH<sub>2</sub>-CH<sub>2</sub>-CH<sub>3</sub>), 0.92 (br, 3H, -CH<sub>3</sub>). SEC:  $M_w$  = 4451 g/mol,  $M_n$  = 3689 g/mol, PDI = 1.20. FT-IR (CaF<sub>2</sub>): 3314 cm<sup>-1</sup> (H-C  $\equiv$  C).

## Synthesis of azido-functionalized maltoheptaose

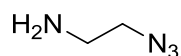


Azido-functionalized maltoheptaose (Mal<sub>7</sub>-N<sub>3</sub>) was synthesized by using a direct anomeric azidation method according to the previous reported procedure<sup>5</sup> with minor modification. To a solution of maltoheptaose (2.00 g, 1.7 mmol, 1 equiv.) and NaN<sub>3</sub> (28.12 g, 433 mmol, 250 equiv.) in water (200 mL) were added DMC (7.32 g, 43.3 mmol, 25 equiv.) and DIPEA (16.84 g, 130 mmol, 75 equiv.). The mixture was stirred at room temperature until the TLC (eluent: acetonitrile/water = 7/3) showed complete disappearance of the starting material. The mixture

was first dialyzed against water using a dialysis membrane (Spectra/Por, Biotech CE tubing, MWCO: 100-500D), and then freeze-dried to afford Mal<sub>7</sub>-N<sub>3</sub> as a white solid (1.64 g, 80 %). <sup>1</sup>H NMR (400 MHz, D<sub>2</sub>O):  $\delta$  (ppm): 5.48-5.41 (m, 6H, H-1<sup>II-VII</sup>), 4.70 (d, 1H, H-1<sup>I</sup>), 4.07-3.59 (m, 40H), 3.46 (t, 1H) and 3.34 (t, 1H). <sup>13</sup>C (400 MHz, D<sub>2</sub>O):  $\delta$  (ppm): 100.09, 99.93, 90.30, 77.08, 77.03, 76.81, 76.55, 73.69, 73.23, 73.06, 72.09, 71.90, 71.83, 71.54, 69.68, 60.83, and 60.77. MALDI-TOF MS (m/z): calcd for [M+Na]<sup>+</sup>: 1200.38, found: 1200.37. FT-IR (CaF<sub>2</sub>): 3660-3020 cm<sup>-1</sup> (OH, sugars), 2120 cm<sup>-1</sup> (N<sub>3</sub>).

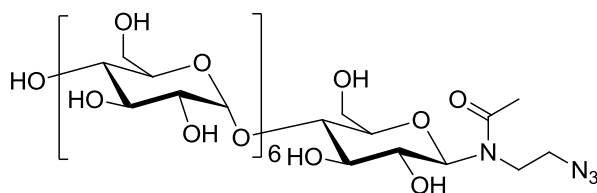
## Synthesis of *N*-( $\beta$ -Maltoheptaosyl)-*N*-(2-azidoethyl)-acetoamide (Mal<sub>7</sub>-N<sub>3</sub>-Ac-C<sub>2</sub>H<sub>4</sub>-N<sub>3</sub>)

### (i) Preparation of 2-azidoethylamine



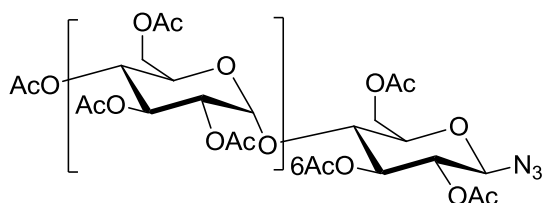
In a flask equipped with a reflux condenser, NaN<sub>3</sub> (23.8 g, 366 mmol, 3 equiv.) was added to a solution of 2-bromoethylamine hydrobromide (25 g, 122 mmol, 1 equiv.) in water (200 ml). The mixture was heated to 75 °C and stirred for 24 h and then cooled down to room temperature. NaOH (29.3 g, 733 mmol, 6 equiv.) was added to the mixture while cooling with ice to reach basic pH. The mixture was purified by extraction employing diethyl ether and saturated NaCl for three times. The organic phase was dried over anhydrous Na<sub>2</sub>SO<sub>4</sub> and removed only organic solvent by evaporator to afford 2-azidoethylamine as a light yellow liquid (6.62 g, 63%). <sup>1</sup>H-NMR (400 MHz, CDCl<sub>3</sub>):  $\delta$  (ppm) 3.36 (t, 2H, -CH<sub>2</sub>-N<sub>3</sub>) and 2.88 (t, 2H, -CH<sub>2</sub>-NH<sub>2</sub>). FT-IR (KCl): 2101 cm<sup>-1</sup> (N<sub>3</sub>).

### (ii) Synthesis of Mal<sub>7</sub>-N<sub>3</sub>-Ac-C<sub>2</sub>H<sub>4</sub>-N<sub>3</sub>



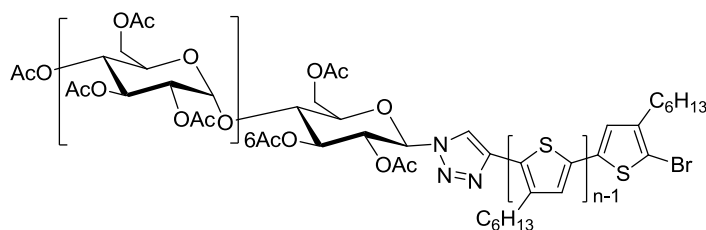
A suspension of maltoheptaose (502 mg, 0.43 mmol, 1 equiv.) in neat 2-azidoethylamine (781 mg, 9.1 mmol, 21 equiv.) was stirred vigorously at room temperature. The reaction progress was monitored by TLC (eluent: BuOH/EtOH/H<sub>2</sub>O = 1/3/1). After complete disappearance of the starting material, the mixture was dissolved in MeOH (4ml) and then precipitated into CH<sub>2</sub>Cl<sub>2</sub>. The solid was filtered and washed with a mixture of MeOH / CH<sub>2</sub>Cl<sub>2</sub> (1/3). A solution of Ac<sub>2</sub>O in MeOH (Ac<sub>2</sub>O/MeOH = 1/20, 50 ml) was added to the solid and stirred for 18 h at room temperature until the TLC (eluent: BuOH/EtOH/H<sub>2</sub>O = 1/3/1) showed complete disappearance of the starting material. The solvent was then removed by co-evaporation with a mixture of toluene and MeOH (1/1). The resulting solid was dissolved in water and lyophilized to afford *N*-(β-Maltoheptaosyl)-*N*-(2-azidoethyl)-acetoamide (Mal<sub>7</sub>-N<sub>3</sub>-C<sub>2</sub>H<sub>4</sub>-N<sub>3</sub>) as a white solid (443 mg, 81 %). <sup>1</sup>H-NMR (400 MHz, D<sub>2</sub>O): δ (ppm) 5.47-5.43 (m, 6H, H-1<sup>II-VII</sup>), 5.09, 5.07 (d, 1H, H-1<sup>I</sup><sub>β</sub>), 4.02-3.43 (m, 46H, H-2,3,4,5,6<sup>I-VII</sup> and -CH<sub>2</sub>-CH<sub>2</sub>-N<sub>3</sub>) and 2.32, 2.29 (2xs, rotamers, -CO-CH<sub>3</sub>). MALDI-TOF MS (m/z): calcd for [M+Na]<sup>+</sup>: 1285.44, found: 1285.44. FT-IR (KBr): 2111 cm<sup>-1</sup> (N<sub>3</sub>).

### Synthesis of peracetylated azido-functionalized maltoheptaose (AcMal<sub>7</sub>-N<sub>3</sub>)



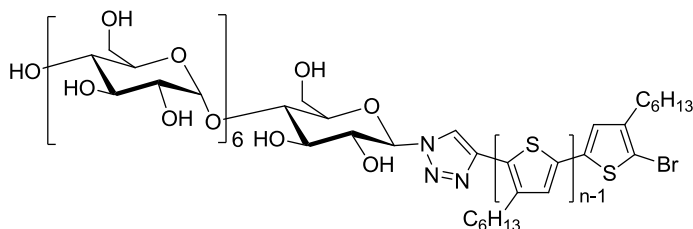
Mal<sub>7</sub>-N<sub>3</sub> (1.00 g, 83.3 mmol) was peracetylated with acetic anhydride in pyridine (acetic anhydride: pyridine = 1:2 (v/v), 30 mL) in the presence of catalytic amount of DMAP. The mixture was stirred overnight at room temperature until the TLC (eluent: ethyl acetate/ether = 7/3) showed complete disappearance of the starting material. The solvent was then evaporated and re-dissolved in ethyl acetate. The solution was washed with 1M HCl, saturated NaHCO<sub>3</sub> and water. Then the organic layer was dried over anhydrous Na<sub>2</sub>SO<sub>4</sub> and concentrated by evaporation to afford peracetylated azido-functionalized maltoheptaose (AcMal<sub>7</sub>-N<sub>3</sub>) as a yellow solid (1.52 g, 86%). <sup>1</sup>H-NMR (400 MHz, CDCl<sub>3</sub>): δ (ppm) 6.18 – 3.75 (m, 49H) and 2.20 – 1.98 (m, 66H, CH<sub>3</sub> acetyl group). MALDI-TOF MS (m/z): calcd for [M+Na]<sup>+</sup>: 2124.61, found: 2124.67. FTIR (CaF<sub>2</sub>): 2120 cm<sup>-1</sup> (N<sub>3</sub>), 1750 cm<sup>-1</sup> (C=O, esters).

### Synthesis of poly (3-hexylthiophene)-*b*-peracetylated maltoheptaose (P3HT-*b*-AcMal<sub>7</sub>)



In a two-neck round-bottom flask (flask 1), AcMal<sub>7</sub>-N<sub>3</sub> (1.05 g, 0.5 mmol, 1.8 equiv.) and PMDETA (88  $\mu$ L, 0.4 mmol, 1.5 equiv.) were dissolved in THF (10 mL), degassed by bubbling with argon for 5 min and stirred at room temperature. In a second two-neck round-bottom flask (flask 2), alkyne-P3HT (1.00 g, 0.3 mmol, 1 equiv.) and CuBr (0.06 g, 0.4 mmol, 1.5 equiv.) were dissolved in THF (90 mL), degassed by bubbling with argon for 5 min and stirred at room temperature. The content of flask 1 was transferred to flask 2 via cannula under argon atmosphere. The reaction mixture was stirred at room temperature for 4h until the SEC traces showed complete disappearance of the peak of starting material. The solution was passed through a neutral alumina column in order to remove copper salt. After concentration, the product was recovered by precipitation in cold acetone and dried under reduced pressure to yield the P3HT-*b*-AcMal<sub>7</sub> block copolymer as a purple solid (1.05 g, 67%). <sup>1</sup>H-NMR (400 MHz, CDCl<sub>3</sub>):  $\delta$ (ppm): 7.77 (s, triazole), 7.06-6.80 (m, aromatic), 5.96 – 3.87 (m, sugar), 2.90-2.48 (m,  $\alpha$ -CH<sub>2</sub>), 2.20 – 1.98 (m, CH<sub>3</sub> acetyl group), 1.71 (m,  $\beta$ -CH<sub>2</sub>), 1.54-1.15 (m, -CH<sub>2</sub>-CH<sub>2</sub>-CH<sub>2</sub>-CH<sub>3</sub>), 0.92 (br, -CH<sub>3</sub>). SEC:  $M_w$  = 12200 g/mol,  $M_n$  = 9480 g/mol, PDI = 1.29. FTIR (CaF<sub>2</sub>): 1750 cm<sup>-1</sup> (C=O, esters).

### Deacetylation: synthesis of poly (3-hexylthiophene)-*b*-maltoheptaose (P3HT-*b*-Mal<sub>7</sub>)

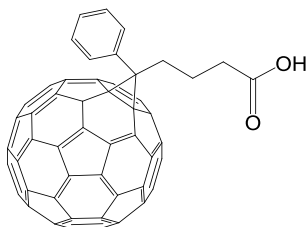


In a round-bottom flask, P3HT-*b*-AcMal<sub>7</sub> (0.95 g, 1 equiv.) was dissolved in THF (188 mL) and stirred at room temperature. A solution of 1M sodium methoxide in methanol (7.3 mL, 2 equiv.

compared to acetyl groups) was dissolved in THF (33 mL) and added dropwise to the copolymer solution under stirring. The mixture was stirred overnight at room temperature until the FT-IR spectrum showed complete disappearance of the signal due to the acetyl groups ( $1750\text{ cm}^{-1}$ ). Then the mixture was evaporated and dissolved in THF. The product was recovered from successive precipitations in a mixture of methanol and water (9:1). The precipitate was filtrated and dried under reduced pressure to afford the P3HT-*b*-Mal<sub>7</sub> block copolymer as a purple solid (0.72 g, 90%). SEC:  $M_w = 9530\text{ g/mol}$ ,  $M_n = 6850\text{ g/mol}$ , PDI = 1.39. FTIR (CaF<sub>2</sub>):  $3660\text{--}3110\text{ cm}^{-1}$  (OH, sugars).

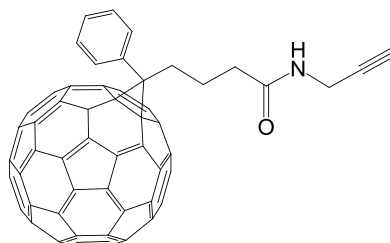
#### VI.1.4 Synthesis of fullerene-conjugated AcMal<sub>7</sub>

##### Synthesis of (6,6)-phenyl C<sub>61</sub> butyric acid (PC<sub>61</sub>BA)



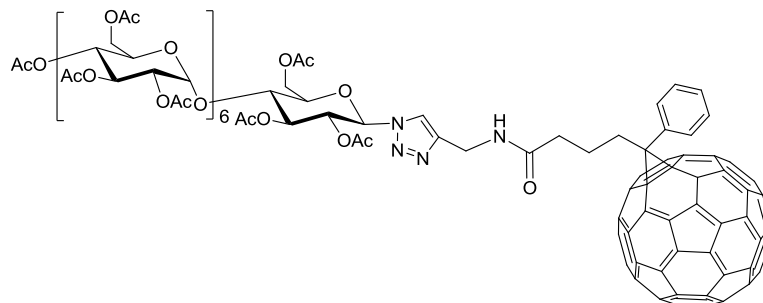
To a solution of (6,6)-phenyl C<sub>61</sub> butyric acid methyl ester (PC<sub>61</sub>BM) (99.2 mg, 0.11 mmol) in *o*-dichlorobenzene (20 ml) was refluxed for 3h. HCl (12M, 4 ml) and acetic acid (10 ml) were introduced to the solution in one portion. The reaction mixture was refluxed for 5 days until the TLC (eluent: toluene) showed complete disappearance of the starting material. The solvent was removed under reduced pressure and the residual solid was purified by centrifugation with MeOH and toluene to afford (6,6)-phenyl C<sub>61</sub> butyric acid (PC<sub>61</sub>BA) as a brown solid (73.4 mg, 75 %). MALDI-TOF MS ( $m/z$ ): calcd for  $[M-H]^+$ : 895.08, found: 896.03. FT-IR (KBr):  $1702\text{ cm}^{-1}$  (C=O, carboxylic acid).

## Synthesis of *N*-propargyl (6,6)-phenyl C<sub>61</sub> butyramido (ethynyl-PC<sub>61</sub>BAm)



In a dry 100 ml three-neck round-bottom flask equipped with a reflux condenser (flask 1), PC<sub>61</sub>BA (200 mg, 0.22 mmol, 1 equiv.) and thionyl chloride (4 ml) were introduced, and the mixture was refluxed at 70 °C under an argon atmosphere until the IR spectrum showed complete disappearance of the peak at 1702 cm<sup>-1</sup> corresponding to the C=O stretching vibration of carboxylic acid group in the PC<sub>61</sub>BA. After the mixture was cooled to the room temperature, thionyl chloride was evaporated by vacuum pump. In another dry 50 ml flask (flask 2), propargylamine (42.8 µl, 0.67 mmol, 3 equiv.), dry triethylamine (0.19 µl, 0.13 mmol, 6 equiv.) and THF (12 mL) were added and the solution was degassed by bubbling with argon for 5 min and stirred at room temperature. The content of flask 2 was transferred to flask 1 via syringe under argon atmosphere. The reaction mixture was stirred at room temperature for 4h until the IR spectrum showed complete disappearance of the peak at 1793 cm<sup>-1</sup> corresponding to the C=O stretching vibration of the carbonyl chloride group. After concentration, the product was purified by precipitation in cold methanol and dried under reduced pressure to yield the *N*-propargyl (6,6)-phenyl C<sub>61</sub> butyramido (ethynyl-PC<sub>61</sub>BAm) as a brown solid (88.5 mg, 43%). <sup>1</sup>H-NMR (400 MHz, THF-*d*<sub>8</sub>): δ(ppm) 8.01 (d, 2H, *o*-H aromatic), 7.53 (t, 2H, *m*-H aromatic), 7.44 (t, 1H, *p*-H aromatic), 7.34 (br, 1H, -NH-), 3.93 (m, 2H, -CH<sub>2</sub>-C≡CH), 2.97 (m, 2H, -CH<sub>2</sub>-CO-NH-), 2.53 (1H, -C≡CH), 2.32 (t, 2H, Ph-C-CH<sub>2</sub>-), 2.16 (m, 2H, -CH<sub>2</sub>-CH<sub>2</sub>-CO-NH-). MALDI-TOF MS (*m/z*): calcd for [M-H]<sup>-</sup>: 932.11, found: 932.93. FT-IR (ATR): 1646 cm<sup>-1</sup> (C=O, butyramido).

## Synthesis of fullerene-conjugated AcMal<sub>7</sub> (AcMal<sub>7</sub>-C<sub>61</sub>)



In a 250 ml flask, ethynyl-PC<sub>61</sub>BAm (0.40 g, 0.43 mmol, 1 equiv.) and CuBr (91.6 mg, 0.64 mmol, 1.5 equiv.) were dissolved in THF (60 ml), degassed by bubbling with argon for 5 min, and stirred at room temperature. In another 100 ml flask, AcMal<sub>7</sub>-N<sub>3</sub> (0.90 g, 0.43 mmol, 1 equiv.) and PMDETA (134  $\mu$ l, 0.64 mmol, 1.5 equiv.) were dissolved in THF (20 ml), degassed by bubbling with argon for 5 min, and stirred at room temperature. The solution of AcMal<sub>7</sub>-N<sub>3</sub> was transferred to the stirred solution of ethynyl-PC<sub>61</sub>BA via cannula under argon atmosphere. The reaction mixture was stirred at room temperature for 12h until the FT-IR spectrum showed complete disappearance of the signal corresponding to the azide group of AcMal<sub>7</sub>-N<sub>3</sub>. The reaction mixture was passed through a neutral alumina column in order to remove copper salt with a THF eluent. After concentration of the eluent, the crude product was purified by precipitation in cold methanol. The product was collected by centrifugation and dried under reduced pressure to give the AcMal<sub>7</sub>-C<sub>61</sub> as a brown solid (0.76 g, 58%). MALDI-TOF MS ( $m/z$ ): calcd for [M+H]<sup>+</sup>: 3036.75, found: 3036.98.

## VI.2 Characterization

### VI.2.1 Thermal properties

Thermogravimetry analysis (TGA) was performed using a SETARAM 92-12 TGA apparatus at a heating rate of 5 °C/min up to 800 °C under nitrogen atmosphere. Differential scanning calorimetry (DSC) analysis was performed using a TA Instruments DSC Q200 equipped with RCS 90 cooling unit. The samples (*ca.* 5 mg) were firstly dissolved in THF and deposited on the aluminum DSC pan followed by slow evaporation of the solvent. These DSC samples were stored at 100 °C under vacuum for several hours prior to analysis. The measurements were carried out under a nitrogen atmosphere at a scan rate of 10 °C/min.

## VI.2.2 AFM and TEM measurements

Atomic force microscopy (AFM) phase images were realized in tapping mode by using a Picoplus microscope (Molecular Imaging, Inc., Tempe, AZ). Transmission electron microscopy (TEM) observations were carried out using CM200 Philips microscope (Hillsboro, OR) operating at 80 kV.

### Polymer thin film (AFM/TEM)

Polymer thin films were prepared by spin-coating for both AFM and TEM measurements. First, the polymer was dissolved in organic solvent and stirred for at least 3 h at room temperature. Then, the solution was filtered through a 0.45  $\mu\text{m}$  PTFE filter by using glass syringe prior to use. In case of the samples for AFM measurement, the solution was deposited onto Si wafer. The Si wafers should be cleaned in ethanol under ultrasonic treatment for 20 min and then rinsed with ethanol and acetone 3 times for each solvent and dried with  $\text{N}_2$  flow prior to use. For TEM measurement, carbon-coated copper grids were used as a substrate. The grid was placed on the center of a glass support which was fixed to the spin coater and the adequately diluted polymer solution was deposited on it. In the typical experiments, the deposition of the polymer solutions were carried out by spin coater with rotation speed of 3000 rpm for 30 sec in both cases. Then these thin films were annealed either via solvent annealing or/and via thermal annealing method under different conditions. Annealing temperatures were verified by measuring the surface temperature of the oven using a thermometer.

### Ultrathin section (TEM)

About 10  $\mu\text{m}$ -thick  $\text{P3HT}_{\text{P3}}\text{-}b\text{-AcMal}_7$  film was prepared by drop casting from a concentrated polymer THF solution onto a PTFE substrate. After complete evaporation of the solvent, obtained thick film was annealed at 220  $^\circ\text{C}$  for 10 min under vacuum to induce the microphase separation. Au vapor deposition was carried out on top of the film to mark the interface between air and film surface. The thick film was then soaked in absolute ethanol overnight to dehydrate, and then embedded in an epoxy resin mixture (Embed-812). The hardened resin block was set on an ultramicrotome with the film plane being orthogonal to the sectioning direction. Ultrathin sections with the thickness of less than 100 nm were obtained using a 35 $^\circ$  diamond knife with a clearance angle of 6 $^\circ$ , and mounted onto carbon-coated copper grid.



**Donor: acceptor blend film (TEM)**

P3HT-*b*-AcMal<sub>7</sub> and acceptor compound (PC<sub>61</sub>BM or C<sub>61</sub>-AcMal<sub>7</sub>) were dissolved in chloroform at the total concentration of 0.1 wt%. The solution was stirred at room temperature for 24h then passed through a 0.45 µm PTFE filter. The deposition onto copper grid was carried out by spin coating with rotation speed of 3000 rpm for 30 sec. Then the blend film was annealed via thermal annealing at 210 °C for 10 min to induce microphase separation. A weight ratio of donor/acceptor was calculated based on total amount of P3HT segment in the P3HT-*b*-AcMal<sub>7</sub> and total amount of PC<sub>61</sub>BM or acceptor moiety in the C<sub>61</sub>-AcMal<sub>7</sub>. The donor/acceptor ratio was varied from 1/0.1 to 1/1.

**VI.2.3 SAXS and WAXS measurements**

Small-angle X-ray scattering (SAXS) and wide-angle X-ray scattering (WAXS) experiments were performed on the BM02 beamline of the European Synchrotron Radiation Facility (ESRF, Grenoble, France). All the samples for SAXS and WAXS measurements were prepared by drop casting from concentrated polymer solution (*ca.* 3%) onto a PTFE substrate. THF or chloroform was used as a solvent. The polymer solutions were filtered through a 0.45 µm PTFE filter by using glass syringe prior to deposit. After complete evaporation of the solvent, about 10 µm-thick films were treated under optional annealing conditions. The annealed bulk samples were then peeled off from PTFE substrate and finely crashed to put into 1.5 nm diameter glass capillaries. The capillaries were sealed with hot-melt adhesive by mean of a STEINEL hot-melt glue applicator. These samples were placed in sample holders equipped with an integrated heating system. The experiments were performed using 15 keV ( $\lambda = 0.083$  nm). In case of the step-wise heating and cooling experiments, the samples were heated at 5 or 10 °C intervals and cooled by natural air cooling. Scattered intensities were recorded during 2-5 s exposures on a CCD detector (Popper Scientific). The scattering intensities were corrected for grid distortion, the detector response, dark current, empty cell scattering, and sample transmission. A silver behenate and lanthanum hexaboride were used for SAXS and WAXS experiments, respectively, to calibrate the  $q$  scale of the detector.

## **VI.3 Selective etching of oligosaccharidic block**

### **VI.3.1 Plasma etching**

Oxygen/argon plasma etching and air plasma etching were performed using a PVA Tepla IoN 3 MHz. plasma system at a pressure of 0.8 Torr and PELCO easiGlow<sup>TM</sup> GlowDischarge Cleaning System at a pressure of 0.3 Torr, respectively. P3HT and AcMal<sub>7</sub> thick films (> 180 nm) were placed to the plasma system and exposed to the oxygen or air plasma for various operation times. The thickness of the initial films and remaining films was measured by AFM.

### **VI.3.2 Wet etching by concentrated sulfuric acid**

Thermogravimetry analysis (TGA) was performed using a SETARAM 92-12 TGA apparatus. The powder samples of the AcMal<sub>7</sub> and P3HT were weighted accurately and placed to a TGA sample pan. The dilute sulfuric acid solution was added to the pan so as the sulfuric acid content to be 5 % (ratio by weight) with respect to the sample weight. The sulfuric acid-impregnated samples were heated to 100 °C at a heating rate of 10 °C/min under nitrogen flow and then the temperature was hold at 100 °C for 24 h.

Infrared (IR) spectra were recorded using a Perkin-Elmer Spectrum RXI FTIR Spectrometer. The thick film samples with the thickness of *ca.* 250 nm were prepared by spin-coating from concentrated THF solution (*ca.* 3 wt%) of the P3HT<sub>P3</sub>-*b*-AcMal<sub>7</sub> onto Si wafer. After thermal annealing at 200 °C for 10 min under reduced pressure, the thick films were treated with concentrated sulfuric acid at 100 °C for different time. The treated films were then carefully rinsed with deionized (DI) water for several times using a pipette in order to remove sulfuric acid. The films containing water were then subjected to solvent substitution with ethanol and dried overnight at room temperature under reduced pressure.

For TEM measurement, P3HT-*b*-AcMal<sub>7</sub> thin film was prepared by spin-coating onto Si wafer. Thermal annealing was applied to obtain a phase separated nanostructure at 200 °C for 10 min under vacuum. Then, the thin film was subjected to sulfuric acid etching in order to selectivity remove/carbonize sugar block. After etching and washing process, the thin film was carefully placed into a water receiver to float out the film from Si substrate. Floating film was collected using a TEM grid and excess water was removed with paper filer and dried in the oven under

reduced pressure. TEM measurement was carried out using CM200 Philips microscope (Hillsboro, OR) operating at 80 kV.

## VI.4 References

- (1) Jeffries-El, M.; Sauvé, G.; McCullough, R. D. *Macromolecules* **2005**, *38* (25), 10346–10352.
- (2) Kochemba, W. M.; Kilbey, S. M.; Pickel, D. L. *J. Polym. Sci. Part A Polym. Chem.* **2012**, *50* (14), 2762–2769.
- (3) Park, J.; Moon, H. C.; Kim, J. K. *J. Polym. Sci. Part A Polym. Chem.* **2013**, *51* (10), 2225–2232.
- (4) Urien, M.; Erothu, H.; Cloutet, E.; Hiorns, R. C.; Vignau, L.; Cramail, H. *Macromolecules* **2008**, *41* (19), 7033–7040.
- (5) Tanaka, T.; Nagai, H.; Noguchi, M.; Kobayashi, A.; Shoda, S. *Chem. Commun.* **2009**, 23, 3378–3379.



## GENERAL CONCLUSION

This study has demonstrated the validity of the use of novel semiconducting glycoconjugated diblock copolymers for fabrication of the ideal nanopatterned active layer in photovoltaics via their self-assembly. By taking advantage of strong incompatibility between the oligosaccharide and  $\pi$ -conjugated semicrystalline blocks, the sub-10 nm scale periodic lamellar structure has been achieved.

First, a new class of glycoconjugated P3HT-based block copolymers, P3HT-*b*-Mal<sub>7</sub> and P3HT-*b*-AcMal<sub>7</sub>, were successfully synthesized using a combination of synthetic strategies involving controlled polymerization (GRIM method), one-step end-functionalization of oligosaccharide, and CuAAC "click" reaction. The chemical structures of the obtained block copolymers were precisely identified by MALDI-TOF MS, SEC, IR, and liquid- and solid-state NMR (Chapter II).

The self-assembly behavior of these block copolymers have been investigated by AFM, TEM, and SAXS analysis. The P3HT-*b*-AcMal<sub>7</sub> block copolymer self-assembled into well-defined lamellar structure in sub-10 nm scale, which is one of the smallest domain sizes achieved by self-assembly of P3HT-based block copolymers, when the block copolymer obtained enough free mobility by heating to reach the equilibrium state (Chapter III.5).

Cross-sectional TEM observation and GISAXS analysis revealed that P3HT-*b*-AcMal<sub>7</sub> tends to self-organize into perpendicularly oriented lamellae structure spontaneously at the air/film interface while at the bottom interface the domain orientation depends on the nature of the substrate (Chapter III.5).

Based on the geometrical parameters and space-filling arguments, a molecular packing model for the self-assembled lamella structure of P3HT-*b*-AcMal<sub>7</sub> was proposed. The P3HT and AcMal<sub>7</sub> segments are confined in the lamellae in which the AcMal<sub>7</sub> segments are aligned side-by-side. The P3HT segments are tilting with respect to the lamellae plane and strongly  $\pi$ -stacked with an extended chain conformation in order to attain thermodynamically stable crystalline structure. This distinct molecular arrangement should be attained as a result of the competition of multiple factors such as segregation strength between P3HT and AcMal<sub>7</sub>, strong  $\pi$ - $\pi$  interaction of P3HT

backbones, geometrical mismatch between two blocks, space filling requirement and entropic penalties (Chapter III.6).

The temperature dependent *in situ* SAXS experiments revealed that the P3HT-*b*-AcMal<sub>7</sub> exhibits microphase separation even in molten state. It was also revealed that the crystallization of P3HT segments of P3HT-*b*-AcMal<sub>7</sub> takes place within the phase-separated nanodomains while retaining initial lamellar morphology (confined crystallization), indicating that P3HT and AcMal<sub>7</sub> are strongly segregated throughout structure formation process (Chapter IV.3).

The DSC analysis indicated that the self-organization of the P3HT-*b*-AcMal<sub>7</sub> provides more stable or ordered P3HT crystal state, which is a crucial aspect for photovoltaic applications, than that of P3HT homopolymer due to the nanoconfinement effect (Chapter IV.2).

The feasibility of pattern transfer from phase-separated block copolymer template has been demonstrated. The wet etching of the self-organized P3HT-*b*-AcMal<sub>7</sub> film using concentrated sulfuric acid showed the selective decomposition of AcMal<sub>7</sub> block via dehydration and carbonization of oligosaccharides without affecting the preexisting lamellae structure. The resultant void consisting of carbon skeleton is expected to have a good affinity with typical electron acceptor compounds such as [6,6]-phenyl-C<sub>61</sub>-butyric acid methyl ester (PCBM) because the basic structures of those materials are also entirely composed of carbon (Chapter V.2).

In the last part of this study, the fullerene linked AcMal<sub>7</sub> (AcMal<sub>7</sub>-C<sub>61</sub>) was synthesized and used for the purpose of location control of acceptor materials in the nano-patterned donor/acceptor blended films. A preliminary morphological investigation on the blended films made of the P3HT-*b*-AcMal<sub>7</sub> (electron-donating compound) and AcMal<sub>7</sub>-C<sub>61</sub> (electron-accepting compound) suggested that the AcMal<sub>7</sub>-C<sub>61</sub> molecules are incorporated in the phase-separated AcMal<sub>7</sub> domain, so that terminal fullerenes are aligned along the domain boundary of P3HT and AcMal<sub>7</sub> segments (Chapter V.3).

In conclusion, this thesis proved that the self-assembly of semiconducting carbohydrate-based diblock copolymers is a promising strategy to realize ideal active layer structures for organic photovoltaic cells. The results and knowledge obtained in this study are believed to provide an opportunity for further advances and innovation in organic photovoltaics.